Quantum dynamics of ballistic coherent conductors : quantum switch and photo-assisted transport

Matthieu Santin

NNT : 2017SACLS169

Thèse de doctorat de l'Université Paris-Saclay préparée A l'Université Paris-Sud

Ecole doctorale n°564
Physique en Ile-de-France
Spécialité de doctorat: Physique
par

M. Matthieu Santin

Dynamique quantique dans des conducteurs balistiques et cohérents : interrupteur quantique et transport photo-assisté

Thèse présentée et soutenue à L'Orme des Merisiers, CEA Saclay, le 30 juin 2017.

Composition du Jury :

M.	Claude PASQUIER	Professeur *LPS, Université Paris-Sud*	Président du jury
M.	Christopher BÄUERLE	Directeur de recherche *Institut Néel, CNRS*	Rapporteur
M.	Thierry MARTIN	Professeur des universités *Université Aix-Marseille*	Rapporteur
M.	Christophe CHAUBET	Professeur *Université Montpellier II*	Examinateur
Mme.	Inès SAFI	Chargé de recherche *LPS, CNRS*	Examinateur
M.	Marc SANQUER	Directeur de recherche *INAC, CEA Grenoble*	Examinateur
M.	Preden ROULLEAU	Chargé de recherche *SPEC, CEA Saclay*	Codirecteur de thèse
M.	Christian GLATTLI	Directeur de recherche *SPEC, CEA Saclay*	Directeur de thèse

"Parce que tu m'as vu, Thomas, tu as cru. Heureux ceux qui n'ont pas vu et qui ont cru."

Jean 20,28

"La vie de tout homme présente deux faces ; celle de sa vie personnelle, d'autant plus libre que ses intérêts sont abstraits, et celle de sa vie élémentaire, la vie de ruche où l'homme obéit inéluctablement aux lois qui lui sont prescrites."

Léon Tolstoï, *Guerre et Paix*

"Il ne faut pas oublier qu'un accélérateur de particules est quelque chose que nous ne fabriquons pas avec quelques morceaux de bois, mais quelque chose qui implique un effort social considérable."

Alexandre Grothendieck, 1972

Remerciements

Je souhaite remercier tout d'abord les membres de mon jury d'avoir accepté de juger ce travail de thèse : Christopher Bäuerle et Thierry Martin, pour avoir accepté d'être rapporteurs et de corriger (malgré les nombreuses coquilles !) mon manuscrit. Je remercie également les examinateurs, Chistophe Chaubet, Inès Safi, Marc Sanquer et plus particulièrement Claude Pasquier, qui n'hésite pas à prendre du temps pour aider les étudiants en tant que directeur de l'ED.

Je tiens à témoigner ma gratitude à mon directeur de thèse, Christian Glattli, qui a accepté que j'effectue ma thèse dans son équipe. J'ai apprécié sa passion pour la physique ainsi que son expertise scientifique qui m'a éclairé de nombreuses fois.

Grâce à mes deux compagnons successifs de manip, Benoît Roche et Maëlle Kapfer, les journées de trvail se sont toujours déroulées dans une ambiance détendue : ce ne sont plus simplement des collègues, mais des amis. Merci Benoît pour m'avoir formé aux nombreuses difficultés de cette manip, de la cryogénie à Labview, toujours avec une extrême rigueur. Merci Maëlle, avec qui je me suis si bien entendu, malgré nos divergences sur à peu près n'importe quel sujet. Tu as repris dignement la suite des expériences, je te souhaite bon courage pour la suite.

Merci à Patrick Pari, Philippe Forget et Mathieu de Combarieu du groupe Cryogénie qui nous ont maintes fois aidé (et sauvé) par leur expertise et leur gentillesse à toute épreuve face aux caprices du cryostat et de sa bobine. Encore merci PP pour m'avoir fait partagé ta passion pour l'automobile au rétrofestival de Caen et de m'avoir fait découvrir la Normandie !

Je remercie Patrice Jacques pour son travail d'orfèvre et ses compétences techniques qui m'ont permis de faire toutes les modifications nécessaires à la manip et de réparer mes erreurs... Un grand merci à Patrice Roche, "Patoche sans filtre", qui a pris du temps pour m'aider pendant des moments difficiles de la rédaction et dont j'admire la rigueur, la pédagogie et la franchise. La solidarité du motard (jusqu'aux contraventions !) s'est vérifiée avec François Parmentier malgré son obstination à vouloir rouler sur avec des motos italiennes bruyantes et peu fiables ! Évidemment, je remercie aussi tous les membres du GNE, en particulier Claudine et Fabien, ainsi qu'Ambroise pour nos discussions passionnées mais aussi Carlès, Ramiro...

Je ne doute pas que sans la patience et la gentillesse de Pief, la microfabrication aurait

été bien plus difficile ! Je te remercie aussi pour m'avoir autorisé à me laisser faire mes quelques projets perso. Je remercie aussi tous les gens de l'atelier pour leur disponibilité et leur sympathie, de m'avoir laissé faire mes propres pièces ! Je pense aussi en particulier à Vincent et Dom, qui ont pris du temps pour m'aider à réparer les petits soucis de la Yam. Un grand merci au secrétariat : Nathalie, Corinne, qui m'ont permis de ne pas lutter avec l'administration parfois kafkaïenne du CEA... Je remercie aussi François Daviaud et Myriam Pannetier-Lecoeur qui ont su efficacement m'aider durant certains moments difficiles.

Je remercie mon directeur de stage de Master 2, Xavier Waintal, avec qui j'ai pu découvrir la physique mésoscopique et m'a donné le goût de continuer de faire une thèse. Ce stage a été extrêmement enrichissant pour moi d'un point de vue humain et scientifique, et je te remercie d'avoir eu la gentillesse de m'aider à trouver une thèse.

J'ai une pensée pour les thèsards qui m'ont précédé, Thibaut dont le travail de thèse a été un fil directeur tout au long de la mienne ; et Andrey pour ses discussions et ses précieux conseils. Je souhaiterais remercier mes compagnons de galère, en thèse ou en post-doc, avec qui j'ai partagé de bons moments en pause, en manip ou autour d'un verre : Camille J., Vincent, Jean-Yves, Olivier, Chloé, Rebeca, PAG... Mais aussi aux "footeux" du rendez-vous incontournable du vendredi soir, qui ont dû supporter ma technique du jeu plus proche de Chabal que de Messi : Amal, Fawaz, Sebastian, Yi, Romain, Sylvio, Stefan...

J'ai une pensée aussi pour mes anciens camarades de prépa et de l'ENS, avec qui je partage de si bons moments : Baydir, Fred, Amandine, Nadia, Romain, Christopher, Carmelo, Thibaut, Clément, Aurélien et Cécile... Je tiens à remercier tout particulièrement ma famille, mes parents, mon grand-père, Anne et Damien, qui m'ont toujours soutenu indéfectiblement et avec qui je passe de si bons moments lorsque je retourne à Claix... Et un merci à mes amis Grenoblois de longue date, toujours là quand il le faut : Jérémy, Alex, Manon, Quentin, Kévin.

Et, pour terminer ces remerciements, une tendre pensée à Laure qui m'a tant encouragé et qui occupe désormais une place particulière dans ma vie... Merci !

Contents

Résumé en Français

Introduction

La motivation générale de ce travail est de manipuler des électrons individuellement dans des circuit électroniques. Contrairement à un ordinateur ou à un circuit classique, où l'information est codée sous la forme d'impulsion de courants macroscopiques, nous voulons ici réduire des impulsions au strict minimum, c'est-à-dire un seul électron. Au-delà de l'avantage de la miniaturisation du support de l'information, réduit à une particule élémentaire, les aspects quantiques de la matière commencent à être atteints. De tels effets ont été déjà observés dans les expériences d'optique quantique électronique, analogues aux expériences d'optique quantique mais en utilisant des électrons dans des solides, comme par exemple l'interféromètre de Mach-Zehnder électronique [67, 107], les expériences de Hong-Ou-Mandel [37] ou de Hanbury Brown et Twiss [13].

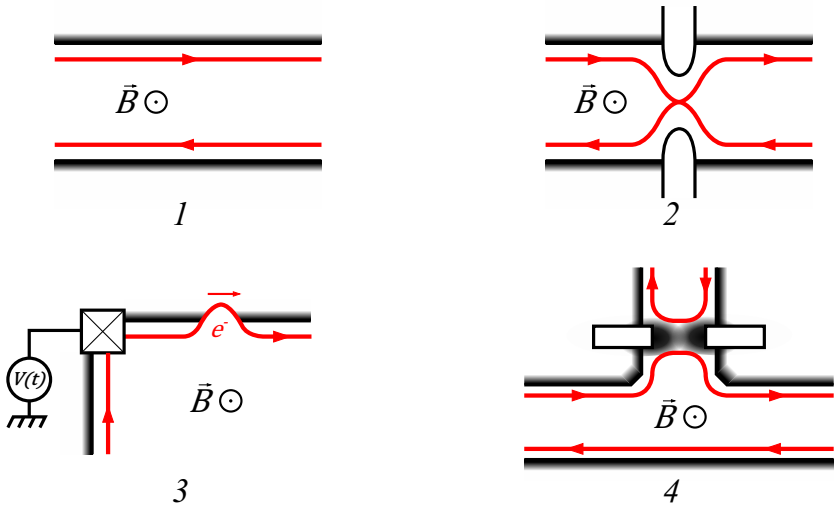

Figure 1: Éléments nécessaire aux expériences d'optique quantique électroniques. 1 - Le rail quantique, l'équivalent de la fibre optique. 2- La lame séparatrice, permettant de transmettre ou de réfléchir les électrons avec une certaine probabilité. 3 - La source d'électrons à la demande, permettant d'injecter quelques électrons dans les rails quantiques. 4 - Le routeur ou interrupteur quantique, guidant les électrons dans les différentes parties du circuit. Ces deux derniers éléments seront l'objet d'étude de cette thèse.

Il est légitime alors de se demander si, en utilisant des électrons soumis aux lois de la

mécanique quantique, il est possible de réaliser du calcul quantique avec de tels objets. Une proposition serait de coder l'information sur les trajectoires balistiques des électrons dans des conducteurs balistiques et cohérents, communément appelés "flying qu-bits" [64]. Dans ces conducteurs, les électrons se déplacent sans collisions sur des dizaines de micromètres et gardent leur cohérence quantique (la distance sur laquelle les effets quantiques se manifestent) le long de leur trajectoire. On peut ainsi réaliser des rails quantique (figure 1, 1), ou l'équivalent de la fibre optique pour électrons, en plongeant un conducteur balistique et cohérent sous un champ magnétique intense appliqué perpendiculairement à sa surface : on observe alors l'effet Hall quantique et le transport électronique a alors lieu dans les canaux de bord, des trajectoires unidimensionnelles qui suivent le contour de l'échantillon. On peut aussi créer des lames séparatrices en déposant des grilles électrostatiques qui créent une barrière de potentiel pour les électrons, qui auront une certaine probabilité de la traverser par effet tunnel (figure 1, 2). Des contacts ponctuels quantiques [126] (*Quantum Point Contact*, ou QPC, en anglais) réalisent ce genre de système.

Pour manipuler des électrons individuellement, il est alors nécessaire de disposer des sources d'électrons et des "routeurs" ou un "interrupteur" quantique (figure 1, 3 et 4). La source d'électrons va permettre d'envoyer un à un et à la demande de l'utilisateur tandis que l'interrupteur va permettre de guider les électrons à travers les différents parties du circuit. Ces deux éléments seront l'objet d'étude de cette thèse : formellement et expérimentalement proches, nous les étudierons d'un point de vue théorique et expérimental. La suite de cette présentation s'organisera en deux partie : la première sur les sources d'électrons et la seconde sur l'interrupteur.

Vers des sources d'électrons à la demande dans des rails quantiques : Étude du bruit photo-assisté en effet Hall Quantique entier

Comment injecter exactement un électron parmi les nombreux autres qui peuplent un conducteur ? Si différentes sources à un électron ont déjà été réalisées [102, 61], nous intéressons ici aux sources qui injectent un électron dans un état quantique bien déterminé. La première source de ce genre a été réalisée au LPA en 2007 et utilise une capacité mésoscopique jouant le rôle de puit quantique, chargé et déchargé à l'aide d'une électrode extérieure [41]. Ainsi, un électron puis un trou sont injectés successivement à une énergie bien définie dans le conducteur, mais l'instant d'émission n'est pas déterminé par l'utilisateur. Dans un autre type de source complémentaire, les sources à impulsion de tension, l'émission d'électron est déclenchée par l'application d'une impulsion de tension directement appliquée sur le conducteur. Plus particulièrement, c'est cette type de source sera étudiée dans cette thèse.

Quel est l'effet d'une impulsion de tension appliquée sur un conducteur ?

On s'intéresse ainsi à réaliser une source d'électron dans un conducteur quantique que j'ai réalisé dans le laboratoire, dont la vue au MEB est présentée sur la figure 2. Le conducteur quantique, représenté en bleu, est un gaz bidimensionnel d'électron formé dans une hétérostructure d'AsGa/AsGaAl. Il y a six contacts sur lesquels on va pouvoir appliquer un potentiel extérieur (en orange) ainsi que de grilles électrostatique (en noir) qui vont réaliser un QPC et contrôler les coefficient de transmission τ et de réflexion ρ des électrons émis par les contacts 0 et 3 vers les contacts 1 et 4. Fonctionnant dans l'effet Hall quantique, les trajectoires électroniques sont représentées en rouge.

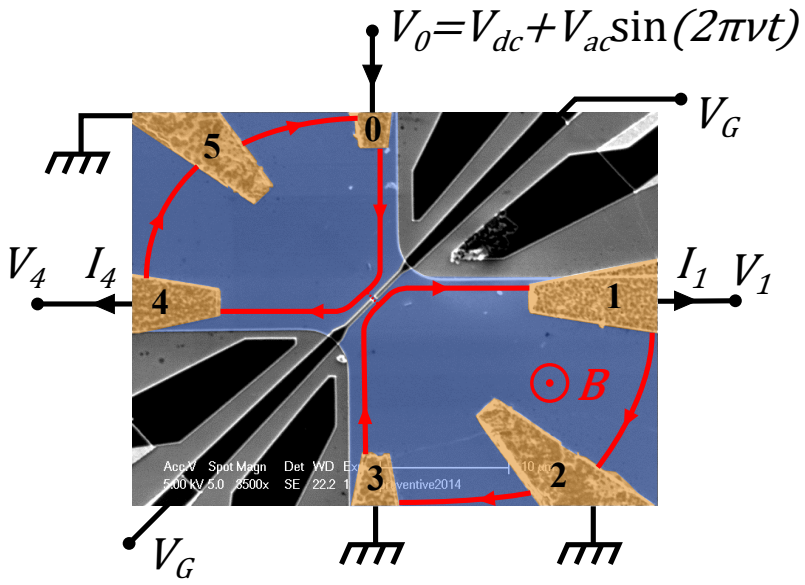

Figure 2: Vue au MEB de l'échantillon utilisé durant cette thèse pour l'étude du transport photo-assisté dans le régime de l'effet Hall quantique entier. Le conducteur quantique est représenté en bleu, les contacts en orange et les grilles électrostatiques en noir. Le but de l'expérience est d'injecter des électrons à partir d'impulsion de tensions sinusoïdales appliquées sur le contact 0, et de mesurer le courants et ses fluctuations à travers les contacts 1 et 4.

Pour réaliser une source d'électrons, une première idée serait d'appliquer un potentiel DC V_{dc} sur un conducteur quantique. Dans ce cas là, le potentiel chimique du contact 0 est augmenté d'une quantité eV_{dc} au-dessus de l'énergie de Fermi et des électrons sont émis en moyenne à des intervalles de temps $t = h/eV_{dc}$, et le courant injecté s'écrit ainsi comme $I_0 = \frac{e^2}{h}V_{dc}$, où $\frac{e^2}{h}$ est le quantum de conductance. Cependant, cela ne forme pas une source à la demande d'électrons, car ils sont émis de manière continue sans connaître le moment d'émission.

Par conséquent, une idée pour déclencher le moment où les électrons sont émis serait d'appliquer un potentiel qui dépend du temps, soit une impulsion de tension : $V_0 =$

$V_{dc} + V_{ac}(t)$, où V_{ac} est une tension purement alternative de fréquence ν. Comme la relation précédente entre le courant et la tension est toujours valable, l'intégration de cette relation sur une période nous permet de voir qu'on injecte $n = \frac{e}{h}\int dt V_0(t)$ charges dans le conducteur[1]. Cependant, appliquer une impulsion de tension sur un conducteur quantique n'est pas anodin : l'ensemble des électrons de la mer de Fermi ressentant le potentiel alternatif, on génère une excitation collective [83], modélisée par l'opérateur de seconde quantification $\hat{A}_0$ qui décrit les états électroniques émis par le réservoir 0 *pulsé* : $\hat{A}_0(\varepsilon) = \sum_l p_l \hat{a}_0(\varepsilon - lh\nu)$, où $\hat{a}_0(\varepsilon)$ sont les opérateurs de seconde quantification qui décrivent les états électroniques émis par le réservoir 0 *lorsqu'il n'est pas pulsé* et les coefficients p_l sont les coefficients de Fourier de $e^{-i\phi(t)}$, avec $\phi(t)$ la phase acquise par les électrons lors du pulse. Cette excitation collective s'interprète comme la présence de N_e électrons (resp. N_h trous) au-dessus (resp. en-dessous) de la mer Fermi en superposition cohérente et n'est pas un état quantique bien défini, susceptible de générer des fluctuation de courant dans le circuit. Ce type de transport dynamique est appelé "photo-assisté" car un électron a une probabilité $|p_l|^2$ d'absorber l quanta d'énergie $h\nu$. Néanmoins, Levitov et al. [74] ont montré que lorsque le pulse de tension est lorentzien et porte une charge n entière, aucun trou n'est crée et on injecte exactement une excitation quantique élémentaire de charge n, appelée *leviton*. Cette propriété fondamentale a été montrée expérimentale en 2013 dans notre laboratoire durant les thèse de J. Dubois et T. Jullien, dans le cas où il n'y a pas de champ magnétique.

Le premier objectif de cette thèse est de montrer qu'il est possible d'injecter des levitons dans des rails quantiques, c'est à dire montrer la validité du transport photo-assisté dans le cadre de l'effet Hall quantique. Pour cela, nous allons nous intéresser au bruit de courant en excès, créé par le partitionnement des excitations électron-trou sur la barrière du QPC, qui permet de compter le nombre total d'excitations $N_e + N_h$. Plus particulièrement, nous allons mesurer ces fluctuations, quantifiées par la densité spectrale de puissance S_I, en fonction de la tension DC : $S_I(V_{dc}) = \sum_l |p_l|^2 S_I^{dc}(V_{dc} - lh\nu/e)$, où S_I sont les fluctuations sans pulses appliqués sur le réservoir 0, ce qui nous permettra de remonter à la distribution des p_l qui décrivent le transport photo-assisté. On se focalisera dans nos expériences sur des impulsions sinusoïdales, les plus simple à réaliser, afin de valider ces résultats pour d'autre type de pulses, comme les pulse lorentzien qui permettront d'injecter des levitons dans les canaux de bords.

[1] Pour une impulsion de 1 ns de durée et de 4 μV d'amplitude, on injecte un électron dans le conducteur.

Interrupteur quantique : bruit de charge fondamental généré par le processus d'ouverture et de fermeture

Que se passe t-il lorsque la mer de Fermi est brutalement coupée en deux parties distinctes ? C'est la question qui se pose lorsqu'on s'intéresse à la possibilité de réaliser un interrupteur quantique. On considère un conducteur élémentaire séparé par une barrière électrostatique, par exemple un QPC, faisant varier les coefficients de réflexion $\rho(t)$ et de transmission $\tau(t)$ au cours du temps (figure 3). Ainsi, lorsque $\tau = 1$, $\rho = 0$ (resp. $\tau = 0$, $\rho = 1$), tous les électrons émis par le réservoir de gauche sont transmis (resp. réfléchis) vers le réservoir de droite (resp. de gauche), ce qui correspond à un interrupteur fermé (resp. ouvert). Pendant le temps où la barrière s'ouvrent, les électrons se délocalisent dans l'espace disponible de part et d'autre de la barrière et s'intriquent (figure 3). Au moment où la barrière se referme, de l'entropie d'intrication quantique est créée due au manque d'information sur la position des électrons, dont la fonction d'onde se projette soit d'un côté soit de l'autre. Cela se manifeste à travers des fluctuations de courant [76] dans les canaux de conductions qui peuvent être mesurées à travers les contacts du conducteurs. Ces fluctuations sont *fondamentales*, dans le sens où elles ne sont dues uniquement au processus d'ouverture et de fermeture de l'interrupteur, même à température nulle et à l'équilibre.

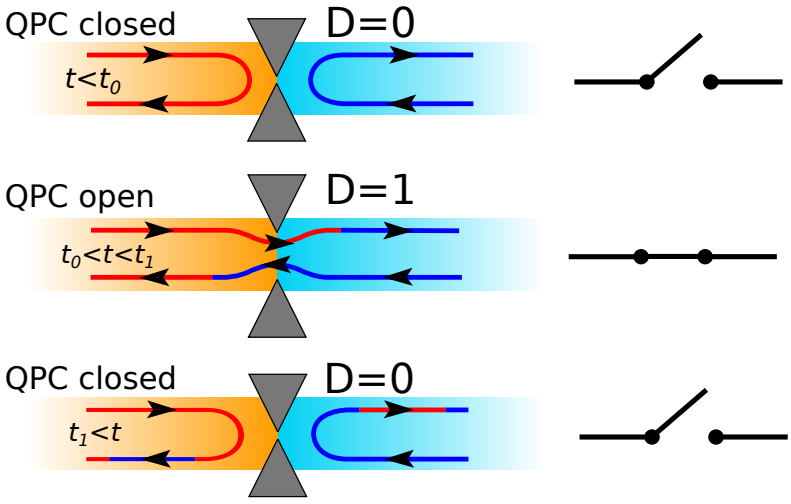

Figure 3: Schéma d'un interrupteur quantique. Une grille électrostatique (en gris) impose une barrière électrostatique qui autorise ou non le passage des électrons de part et d'autre. Un interrupteur quantique peut être réalisé à partir d'un QPC, comme celui présenté sur la figure 2 à l'aide du potentiel de grille V_G. Le processus d'ouverture et de fermeture de l'interrupteur génère de l'entropie d'intrication quantique entre les deux réservoirs et des fluctuations de courants aux bornes du conducteurs. Ces fluctuations sont fondamentales car elles sont uniquement liés à ce processus d'ouverture/fermeture.

Le second objectif de cette thèse est de mesurer ces fluctuations générées par le fonc-

tionnement d'un interrupteur quantique. Nous utilisons un QPC, comme celui présenté présenté sur la figure 2, mais où la tension sinusoïdale est appliquée sur les grilles afin de réaliser le processus d'ouverture et de fermeture de l'interrupteur au cours du temps. Les fluctuations de courant sont mesurées à travers les contacts 1 et 4, alors que tous les autres sont au potentiel de la masse.

Introduction

The purpose of this thesis is to explore the dynamics of electronic quantum transport, thanks to two experiments of current noise measurements across a coherent ballistic conductor, implemented by a Quantum Point Contact (QPC). We studied in a first part the Photo-assisted properties of a sine excitation applied on the lead of a QPC in the Quantum Hall Effect and in a second part the most elementary switch of a conductance channel implemented by the potential barrier of a QPC, which plays the role of a quantum switch.

Quantum transport in mesoscopic physic

The work presented here belongs to the field of mesoscopic physics. Thanks to the development of micro-fabrication and cryogenic techniques during the last three decades, it has been possible to implement artificial systems of intermediate scale between the macroscopic world and the atomic scale, and whose properties are governed by the quantum laws. One of the first striking manifestation was the Aharonov-Bohm oscillations measured in a gold ring of 800 nm diameter at 10 mK[130]. Surprisingly, this experiment demonstrates that the length in which electrons preserve their quantum phase coherence, also called the coherence length, is much larger than the crystal lattice despite the interactions with impurities and the chaotic motion of electrons. Thanks to the development of the 2 Dimensional Electron Gas (2DEG) in GaAs heterostructures[124] for the high speed electronics, the large coherence length can be combined with the ballistic motion of electrons[60], over distances of tens of microns. In these materials, electrons behave like free quantum particles with a low effective mass in a 2D plane: condensed matter physicists can now perform experiments of a quantum pool, where billiard balls have been replaced by electrons[123]! Furthermore, it is possible to implement unidimensional ballistic coherent conductors in 2DEG using surface gates, whose electrostatic barrier potential confine electrons in one direction[126]. For instance, the number of lateral modes in a quantum wire can be controlled in a Quantum Point Contact (QPC) thanks to its tunable barrier, allowing to evidence the quantification of conductance[132, 127]. The DC transport properties in such devices have been widely studied experimentally and theoretically, in particular thanks to the formalism developed by Landauer, Martin and

Büttiker[21, 19, 86].

Dynamical transport for electronic optic experiments and quantum computation using flying qu-bits

From that, one can ask if the large coherence lengths and ballistic trajectories of electrons in such devices could be used in order to perform the experiments of quantum optics, such as Hong-Ou-Mandel[63] or Bell's inequality[6] experiments. Indeed, the fermionic nature of electron make their emission one-per-one easier, in principle, than photons used in quantum optics which tend to be emitted by packets[42]. Moreover, the possibility of controlling electrons through the Coulomb interaction is of a great interest for quantum computation, by using "flying qu-bits" where the information is coded on the electronic trajectories[64][95]. But how manipulate only one electron among billions in a crystal? This major difficulty has been overcame in the nineties with the first manipulation of unique charges, performed into a serie of metallic islands, where the Coulomb blockade allows to transfer electron one-per-one[51, 102]. Another approach is to use the piezo-electric properties of the GaAs in order to generate Surface Acoustic Waves (SAW), which create a moving potential for electrons in a depleted 1D wire. It enables to transfer an electron above the Fermi sea from a quantum dot to another[61, 89]. An important step forward for the implementation of flying qu-bits was the realisation of coherent electron sources by injecting an electron just above the Fermi sea in a quantum wire. The first has been realized in 2007[41] thanks to a mesoscopic capacitor playing the role of a quantum dot[46], which injects an electron at a well defined energy above the Fermi sea. Another idea is to use voltage pulses for the injection of a leviton, a single charge wavepacket with a Lorentzian shape for which the extra electron-hole excitations created when an arbitrary voltage is applied on the lead of a quantum wire[74] are cancelled. This has been experimentally demonstrated in our group[37] and we discuss below about the perspectives explored in this thesis. Thanks to these coherent electron sources, it has been possible to perform the electron tomography and Hong-Ou-Mandel experiments [70, 71, 12]. In parallel, the framework has been built thanks to the theoretical study of the dynamic of quantum transport in coherent ballistic conductors [16, 24, 27, 25, 20, 1, 110] and stimulates numerical simulations, for instance the study of the propagation of time-resolved pulses in quantum wires [49, 50].

We propose in this thesis to go forward in the study of AC transport in coherent ballistic conductors and in the realisation of quantum circuits for flying qu-bits. To achieve this, we demonstrate in the first part the first step validating the possibility to implement a voltage-pulse electron source in the Quantum Hall Effect (QHE) in order to use the edge channels as quantum rails for levitons. In the second part, we study the experimental realisation of a quantum switch, a required element for the manipulation of

the flying qu-bits in a quantum circuit and connect the problem of a switch in a single conductance mode with more general physics, such as the measurement of entanglement entropy.

Photo-assisted shot-noise in quantum Hall effect

The first part of this thesis is devoted to the study of Photo-Assisted Shot-Noise (PASN) in the QHE. Its observation is the first necessary step which validates the possibility to implement a voltage pulse source in this regime. The principle is simple: a voltage pulse applied on the contact of a quantum wire injects a charge $q = \frac{e^2}{h}\int dt\ V(t)$ that corresponds to one electron for a carefully chosen $V(t)$ area. If an arbitrary voltage shape induces photo-assisted extra electron-hole excitations[39], Levitov and al. shown that the Lorentzian shape send in the wire a single electron above the Fermi sea with no extra excitations[83, 74, 66, 81]: a leviton, realizing a clean electron source suitable for flying qu-bits. This has been experimentally realized in our group[37] in the absence of magnetic field.

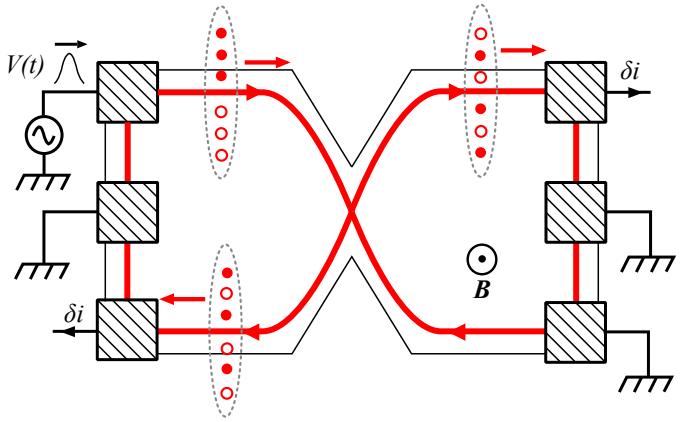

Figure 4: The Photo-Assisted Shot-Noise experiment in the Quantum Hall Effect regime. A time-dependant voltage is applied on a contact of a QPC acting as a beam-splitter. The effect of the AC voltage is to create coherent electron-hole excitations whose number is counted through current fluctuations $\overline{\delta i^2}$ measured on the transmitted and reflected channels. The understanding of those excitations is required for the implementation of a single electron source in the QHE.

However, the control of the leviton trajectory is required for quantum computation and this can be done by using the chiral propagation in the QHE, where edge channels play the role of quantum rails for levitons. Therefore, it is crucial to ensure that the physics of photo-assisted processes leading to the remarkable property (no extra electron-hole excitations) of Lorentzian pulses demonstrated without magnetic field is still valid in the QHE regime. To achieve this, we count the number of extra electron-hole excitations through the photo-assisted shot noise generated by their partitioning on the potential

barrier of a 6-contacts QPC acting as a beam-splitter, as illustrated in the figure 4. To test the photo-assisted physics the study is restricted to a sine pulse which is more convenient: there are no relative phase shifts or amplitudes to control. This experiments remains an experimental challenge: one has to send RF voltages at very low temperature, while the noise measurement is disturbed by the parasitic interferences provided by the presence of the 14 T magnet. The results presented in chapter 4 show a good agreement between the Photo-Assisted theory, paving the way for an implementation of levitons in the QHE regime.

Quantum switch

In the second part of this thesis, we study the fundamental charge noise generated by an elementary switch on a single mode of conduction: a quantum switch. Indeed, a quantum switch could enable the control of the trajectory of the flying qu-bits in the QHE regime in quantum circuits. However, during the switching process, current fluctuations due to the creation of extra electron-holes is generated and can disturb the computational process. Therefore, understanding of those fluctuations is essential and is also connected to more general physics we detail below.

The problem is the following: a coherent unidimensional conductor is separated in two parts thanks to a punctual scatter of transmission $D(t)$, for instance a QPC which plays the role of a switch. The transmission varies quickly in time, connecting and disconnecting the right and left sides of the quantum wire and this generates intrinsic current fluctuations. This noise is fundamental: even in the limit of zero temperature without partitioning on the QPC, fluctuations appears as soon as the transmission is suddenly modified.

Originally proposed by Levitov[76], this problem can be viewed in terms of entanglement entropy. This picture is illustrated on the figure 5: two reservoirs of a quantum wire are initially spatially separated ($D = 0$) and are suddenly connected ($D = 1$) at time t_0. During a time t_1, electrons of both reservoirs delocalize in the whole available space, making the two reservoirs entangled. Then, the left and right sides are again disconnected, creating entropy due to the loss of information about the electron location during the time t_1. This entanglement entropy creation[119] is directly related to the current fluctuations: indeed, a delocalized electron is projected either on the right or the left side after the final separation. This induces fluctuations of the number of charges between both sides and then generates a charge noise. Moreover, the problem can also be described in terms of entangled electron-hole excitations in the Fermi sea produced during the switching process[133, 32].

Therefore, we propose in this thesis to derive the QS noise according to the photo-assisted theory developed for the PASN and to provide expressions well adapted for a

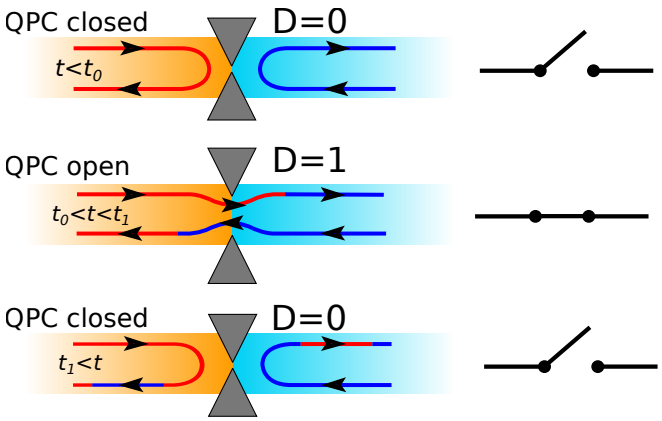

Figure 5: The Quantum Switch experiment. A single mode quantum conductor is initially separated by a fast tunable barrier in its middle which plays the role of a switch. During a time t_1, the barrier opens and electrons from one part delocalize in the other part making the two previously disconnected parts entangled. Then, the closing of the switch generates fundamental charge fluctuations in the conductor, which are measurable. This picture is inspired from [76].

comparison with experimental data, by taking in account the realistic time-dependence of the transmission. Then, we performed experimentally the first measurements of the QS noise implemented thanks to a QPC where the AC voltage is now applied on the gates. The results are found in a good agreement with the expected theoretical noise for both in the absence of magnetic field and in the QHE regime, evidencing the experimental signature of the Quantum Switch.

Outline

This manuscript is organized as follows. In chapter 1, we first review the basics of DC transport in quantum conductor for two types of sample: the 2-contacts and the 6-contacts geometries, used in the experimental work. The Floquet formalism is presented in order to derive the expressions of PASN and to interpret the results in terms of electrons-hole excitations. Then, we apply this powerful formalism in the case of a time-dependent transmission of the scatter and an elegant expression of the QS noise is obtained. The chapter 2 and 3 are devoted to the experimental aspects of this thesis. In chapter 2, we present the general feature of the QPC and the sample fabrication thanks to our facilities of our laboratory and also a simple model in order to design the gate adapted for the PASN or the QS experiments. The measurement set-up, RF wire engineering and the calibration are detailed in chapter 3. The experimental results of the PASN in the QHE are reported in chapter 4 in which we highlight the good agreement with the expected theory, except an offset in the noise that we attempt to explain. The last chapter presents the QS noise measurements: without magnetic field, the experimental results are

remarkably well described by a QS noise combined with PASN resulting of a parasitic AC drain-source voltage that we understood. The results in the QHE regime exhibits an unexpected behaviour of the conductance, while the measured noise is consistent with the QS noise.

Chapter 1

AC-transport in quantum conductors

The purpose of this chapter is to study the theoretical aspects of the AC transport in a quantum wire with a tunable scatter. Starting from the DC description of the current and the noise in this system, we recall both the theoretical framework for the PASN experiment, in which the AC potential in the lead is periodically driven and for the QS experiment where the transmission of the scatter is periodically driven. Thus, it allows us to understand the mechanisms of the photo-assisted process occurring in the AC transport and to derive direct formulas of the current and the noise for a comparison with the experimental data presented in chapter 4 and 5. The formalism used for the description of electrons in coherent ballistic conductor is strongly inspired from the work of M. Büttiker, R. Landauer, T. Martin[19, 86, 85] and the Master course of D. C. Glattli of Mesoscopic physics.

This chapter is organized as follows: in section 1, we first review the DC transport for the two types of quantum conductors used in our experiments. Then, we study in section 2 the effects of a periodic voltage applied on a quantum wire thanks to the Floquet formalism and we obtain the expressions of the photo-assisted shot-noise. In section 3, we describe the properties of the periodic modulation of a scatterer in a quantum wire, which plays the role of a switch.

1.1 DC transport in unidimensional quantum conductors

1.1.1 Scattering theory in quantum conductors

We consider a quantum conductor, represented in the figure 1.1, composed of N quantum wires indexed by $\alpha \in [0 \dots N-1]$ each of them connected to a thermal reservoir (or contacts) R_α. A reservoir plays the role of electron thermal bath: an electron moving toward a reservoir is absorbed with a probability 1 and can be re-emitted at a random

energy and phase. The energy distribution of electrons emitted by the reservoir α at temperature T is characterized by the Fermi distribution[36]:

$$f_\alpha(\varepsilon) = \frac{1}{1 + e^{\beta(\varepsilon - \mu_\alpha)}} \tag{1.1}$$

where $\beta = 1/k_B T$ and μ_α is the chemical potential of the reservoir, which is equal to the Fermi energy ε_F at thermal equilibrium. When a DC voltage V_{dc} is applied on it, it increases the chemical potential by $\mu_\alpha = \varepsilon_F + eV_{dc}$[3].

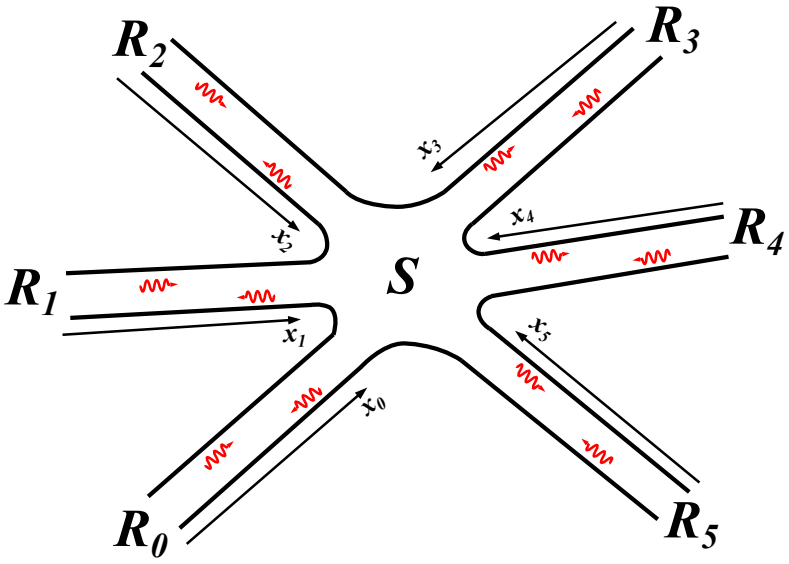

Figure 1.1: A quantum conductor composed of $N = 6$ quantum wires α, each of them are connected to a thermal reservoir R_α, which emit or absorb electrons (red arrows). All wires are connected to the elastic scatterer S in the center.

In the conductor leads, the electron motion is ballistic and quantum coherence is preserved along its trajectory. An elastic scatterer S placed in the center can reflect or transmit an electron emitted by the reservoir α to an other reservoir β, with a probability amplitude $S_{\beta\alpha}$. It is convenient to define S by the scattering matrix $\mathbf{S} = (S_{\alpha\beta})_{\alpha,\beta\in[0\ldots N-1]}$[18]. Electrons in the quantum wire α are fully described by the Fermi operator[1] $\hat{\Psi}_\alpha$:

$$\hat{\Psi}_\alpha(x_\alpha, t) = \int \frac{d\varepsilon}{\sqrt{2\pi\hbar v(\varepsilon)}} \left(\hat{\mathbf{a}}_\alpha(\varepsilon) e^{ik(\varepsilon)x_\alpha} + \sum_{\beta=0}^{N-1} S_{\alpha\beta} \hat{\mathbf{a}}_\beta e^{-ik(\varepsilon)x_\alpha} \right) e^{-i\varepsilon t/\hbar} \tag{1.2}$$

where $v(\varepsilon) = \hbar k(\varepsilon)/m^*$ is the velocity of an electron of energy[2] ε. The term $\hat{\mathbf{a}}_\alpha(\varepsilon) e^{ik(\varepsilon)x_\alpha}$ represents the annihilation operator of an electron emitted by R_α propagating into the increasing x_α. Terms $S_{\alpha\beta}\hat{\mathbf{a}}_\beta e^{-ik(\varepsilon)x_\alpha}$ represents the annihilation operator of an electron emitted by R_β scattered by $\mathbf{S}$ toward R_α with a probability amplitude $S_{\alpha\beta}$ which propa-

[1] In the following, integrals with no integral interval denoted corresponds to indefinite integrals.
[2] m^* is the effective mass. The dispersion equation is thus $\varepsilon = \hbar^2 k^2 / 2m^*$.

gates into the decreasing x_α. Note that $1/2\pi\hbar v(\varepsilon)$ is a normalisation term. The annihilation operator $\hat{\mathbf{a}}$ and the creation operator $\hat{\mathbf{a}}^\dagger$ verify: $\langle \hat{\mathbf{a}}^\dagger_\alpha(\varepsilon_1)\hat{\mathbf{a}}_\beta(\varepsilon_2)\rangle = f_\alpha(\varepsilon_1)\delta(\varepsilon_1-\varepsilon_2)\delta_{\alpha\beta}$, where $\langle \ldots \rangle$ is a statistical and quantum average. The Fermi operator $\hat{\Psi}_\alpha$ is the basic tool for current and noise calculations presented in this chapter. Indeed, the current operator defined as:

$$\hat{\mathbf{I}}_\alpha(x_\alpha,t) = \frac{e\hbar}{2m^*}\left(\frac{1}{i}\hat{\Psi}^\dagger_\alpha\frac{d\hat{\Psi}_\alpha}{dx_\alpha} - \frac{1}{i}\frac{d\hat{\Psi}^\dagger_\alpha}{dx_\alpha}\hat{\Psi}_\alpha\right) \tag{1.3}$$

It represents the total current created by the flows of incoming and outgoing electrons in the quantum wire α. The time and space arguments (x_α, t) are kept in the expression of $\hat{\mathbf{I}}_\alpha$ in order to highlight the propagation in the AC transport regime considered in section 4.2. The current noise, or current fluctuations, are described through the Power Spectral Density (PSD) of the current operator, defined as:

$$S_{I_\alpha\times I_\beta}(\omega) = 2\int dt' e^{i\omega t'}\left(\langle\overline{\hat{\mathbf{I}}_\alpha(t)\hat{\mathbf{I}}_\beta(t+t')}\rangle - \langle\overline{\hat{\mathbf{I}}_\alpha(t)}\rangle\langle\overline{\hat{\mathbf{I}}_\beta(t+t')}\rangle\right) \tag{1.4}$$

where $\overline{\ldots}$ is the time average over t. This average is performed only for time-dependant problems, for instance in AC transport. In the case of $\alpha \neq \beta$, eq. 1.4 is the correlation[3] between current fluctuations of contacts α and β. This quantity, sometimes denoted S_I, quantizes the fluctuations of the current around its mean value at a given frequency. More details about noise properties can be found in the phD thesis of Laure-Hélène Reydellet [11].

The case of several modes in a quantum wire is easily generalised from the framework presented here. We assume that each mode is independent from another[4], so that the resulting current or noise is the sum over all modes possible, except if they are mixed by the scatterer[5]. For simplicity, it will not be taken in account in the notation and we will directly generalize from one to several mode in the following calculations.

The present framework is here applied for two types of quantum conductors: the 2-contacts and 6-contacts geometries, corresponding to the experimental devices used in this thesis and presented in chapter 2. All the information about the geometry of a system is included in the scattering property, described by the scattering matrix $\mathbf{S} = (S_{\alpha\beta})_{\alpha,\beta\in[1\ldots N-1]}$ defined previously. We detail in the following the calculation of current and noise for both geometries.

1.1.2 2-contacts geometry

The first geometry studied is a Quantum Point Contact (QPC) with 2-contacts presented in figure 1.2. It is the simplest geometry for quantum transport experiments. The quan-

[3] Also called cross-correlation.

[4] We neglect for instance interaction between edge channels in the QHE regime.

[5] The case of mixed modes are studied in this chapter

tum conductor (in blue) is connected to the reservoirs (also called contacts or leads) L and R (in yellow). A scatterer S is placed into the constriction in the central part. An electron emitted by L or by R has an amplitude probability ρ to be reflected and a probability τ to be transmitted through the scatterer. We assume that these amplitudes are independent of the energy of the incoming electron[6]. The scatterer is tunable[7] so that electrons can be completely reflected (QPC closed) or completely transmitted (QPC open).

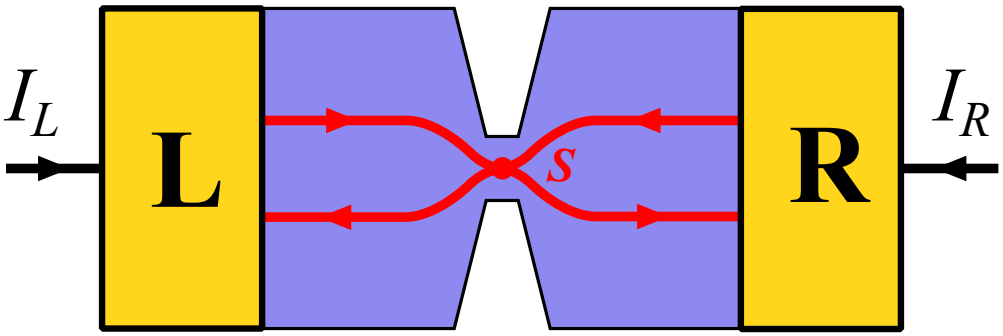

Figure 1.2: A 2-contacts geometry quantum point contact. The blue part in the quantum conductor, the yellow parts are the reservoirs left L and right R. A constriction in the middle with a tunable potential barrier scatters the incoming electrons emitted by the left or right reservoirs.

For this geometry, the scattering matrix $\mathbf{S}$ is:

$$\mathbf{S} = \begin{pmatrix} \rho & \tau \\ \tau & -\rho \end{pmatrix} \tag{1.5}$$

This holds only for $B = 0$ as $\mathbf{S}^T = \mathbf{S}$. It is implicitly supposed that scatterer is perfectly centered in the quantum conductor so that the phase accumulated by the wave function of electrons does not appear in $\mathbf{S}$. The unitary of the matrix is equivalent to the current conservation:

$$\mathbf{S}^\dagger\mathbf{S} = \mathbf{S}\mathbf{S}^\dagger = \mathbb{1} \Leftrightarrow |\rho|^2 + |\tau|^2 = 1 \tag{1.6}$$

In the following the probability of reflection and transmission are denoted D and R and are respectively given by:

$$D = |\tau|^2 \tag{1.7}$$

$$R = |\rho|^2 \tag{1.8}$$

This scattering matrix of the 2-contacts QPC does not change when a magnetic field is applied. Thus, formulas of current and noise derived in the following stay unchanged

[6]This is a good approximation for energies closed to the Fermi sea. This assumption will be justified in the chapter 2.

[7]In chapter 2, we describe more precisely how we experimentally tune the barrier of the QPC.

without external magnetic field or in the quantum Hall effect.

Current operator

Starting from the scattering matrix of the 2-contacts geometry, the expression of the Fermi operator $\hat{\Psi}_L$ is:

$$\hat{\Psi}_L(x_L,t) = \int \frac{d\varepsilon}{\sqrt{2\pi\hbar v(\varepsilon)}} \left(\hat{\mathbf{a}}_L(\varepsilon)e^{ik(\varepsilon)x_L} + (\rho\hat{\mathbf{a}}_L(\varepsilon) + \tau\hat{\mathbf{a}}_R(\varepsilon))e^{-ik(\varepsilon)x_L}\right) e^{-i\varepsilon t/\hbar} \tag{1.9}$$

Therefore, using eq. 1.3, the operator $\hat{\mathbf{I}}_L(x,t)$ of the current flowing from the left to the right at time t at the position x_L reads:

$$\begin{aligned}\hat{\mathbf{I}}_L(x_L,t) = \frac{e}{h}\int d\varepsilon_1 d\varepsilon_2 \Bigg(&\hat{\mathbf{a}}_L^\dagger(\varepsilon_1)\hat{\mathbf{a}}_L(\varepsilon_2) - \rho^2\hat{\mathbf{a}}_L^\dagger(\varepsilon_1)\hat{\mathbf{a}}_L(\varepsilon_2) - \tau^2\hat{\mathbf{a}}_R^\dagger(\varepsilon_1)\hat{\mathbf{a}}_R(\varepsilon_2) \\ &+ \tau\rho\hat{\mathbf{a}}_L^\dagger(\varepsilon_1)\hat{\mathbf{a}}_R(\varepsilon_2) - \tau\rho\hat{\mathbf{a}}_R^\dagger(\varepsilon_1)\hat{\mathbf{a}}_L(\varepsilon_2)\Bigg) e^{-i(\varepsilon_1-\varepsilon_2)(t-x_L/v_F)/\hbar}\end{aligned} \tag{1.10}$$

This full development will be used for the noise computation in the following. The current $\hat{\mathbf{I}}_R(x_R,t)$ flowing from the right to the left has an identical expression by replacing terms indexed $\ldots_L$ by $\ldots_R$. Only the terms $\hat{\mathbf{a}}_L^\dagger\hat{\mathbf{a}}_L$ and $\hat{\mathbf{a}}_R^\dagger\hat{\mathbf{a}}_R$ of the quantum average of the current, denoted I_L, are non-zero and give:

$$I_L = \langle\hat{\mathbf{I}}_L(x_L,t)\rangle = \frac{2e}{h}\int d\varepsilon \cdot D\left[f_L(\varepsilon) - f_R(\varepsilon)\right] \tag{1.11}$$

We take in account the spin degeneracy through the factor 2. The mean current is uniform and stationary. I_L depends only on the difference of population between the reservoirs L and R. At equilibrium, $\mu_L = \mu_R = \varepsilon_F$, the current flowing from L to R is equal to the current flowing from R to L so that the total current is zero. If the left reservoir is polarised with a DC voltage V_{dc}, it increases its chemical potential of $\mu_L = \varepsilon_F + eV_{dc}$ and the flow does not compensate each other. Then, the current reads[8]:

$$I = \frac{2e^2}{h}DV_{dc} \tag{1.12}$$

This relation exhibits the quantum of conductance $G_Q = (e^2/h)^{-1} \simeq 25812\ \Omega$ that depends only on the physical constant h and e and not on the nature of the wire or its geometry. It is interesting to note that even for a fully transparent conductor ($D = 1$), a quantum wire has a conductance bounded to $2e^2/h$, despite the absence of dissipation processes. The effect of a voltage applied on a reservoir is that there are more electrons

[8]The Fermi energy in our samples is $\varepsilon_F \simeq 6.5$ meV, voltages applied are typically $eV_{dc} \simeq 200\ \mu$eV and temperature of electrons is $T \simeq 3.5\ \mu$eV. Thus, it is reasonable to assume: $eV_{dc}, k_BT \ll \varepsilon_F$. Consequently, $f(\varepsilon + eV_{dc}) = f(\varepsilon) + eV_{dc}\frac{df}{d\varepsilon}$ and $\frac{df}{d\varepsilon} \simeq \delta(\varepsilon - \varepsilon_F)$. More details can be found in [22].

flowing from the left to the right than from the right to the left.

The case of several modes in the QPC is easily deduced from eq. 1.12. Each mode is independent from an another. It is equivalent to m quantum wires in parallel, each of them having a conductance $2e^2/h$. Transmission and reflection of the mode k are $|\tau_k|^2$ and $|\rho_k|^2$. The conductance is then simply the sum of all contributions:

$$I = \frac{2e^2}{h} \sum_{k=1}^{m} |\tau_k|^2 \tag{1.13}$$

The values of transmission coefficients depend on the potential of the scatterer. This will be discuss in detail in chapter 2.

Current fluctuations

The noise is computed using the current-current operators and expression 1.4. It is possible to compute and measure the auto-correlation at contact L, $\langle \hat{\mathbf{I}}_L \hat{\mathbf{I}}_L \rangle$, and R, $\langle \hat{\mathbf{I}}_R \hat{\mathbf{I}}_R \rangle$, and the cross-correlation $\langle \hat{\mathbf{I}}_L \hat{\mathbf{I}}_R \rangle$. The experimental interest of these three contributions measurement will be explained in detail in chapter 3. In this section, we deal with the noise generated by DC voltages that does not depends on time. Consequently, the average in 1.4 is only a statistical average and time t has no importance. Using expression of current $\langle \hat{\mathbf{I}}_L \rangle$ in eq. 1.10 and eq. 1.4, the noise on the contact L reads:

$$\begin{aligned}
&S_{I_L \times I_L}(\omega) = 2 \int dt' \; e^{i\omega t'} \langle \hat{\mathbf{I}}_L(0,0) \hat{\mathbf{I}}_L(0,t') \rangle \\
=&2\frac{e^2}{h^2} \int dt' \int d\varepsilon_1 d\varepsilon_2 d\varepsilon_3 d\varepsilon_4 \Big(|\tau|^4 \langle \hat{\mathbf{a}}_L^\dagger(\varepsilon_1) \hat{\mathbf{a}}_L(\varepsilon_4) \rangle \langle \hat{\mathbf{a}}_L(\varepsilon_2) \hat{\mathbf{a}}_L^\dagger(\varepsilon_3) \rangle + |\tau|^4 \langle \hat{\mathbf{a}}_R^\dagger(\varepsilon_1) \hat{\mathbf{a}}_R(\varepsilon_4) \rangle \langle \hat{\mathbf{a}}_R(\varepsilon_2) \hat{\mathbf{a}}_R^\dagger(\varepsilon_3) \rangle \\
&+ |\rho|^2 |\tau|^2 \langle \hat{\mathbf{a}}_L^\dagger(\varepsilon_1) \hat{\mathbf{a}}_L(\varepsilon_4) \rangle \langle \hat{\mathbf{a}}_R(\varepsilon_2) \hat{\mathbf{a}}_R^\dagger(\varepsilon_3) \rangle + |\rho|^2 |\tau|^2 \langle \hat{\mathbf{a}}_R^\dagger(\varepsilon_1) \hat{\mathbf{a}}_R(\varepsilon_4) \rangle \langle \hat{\mathbf{a}}_L(\varepsilon_2) \hat{\mathbf{a}}_L^\dagger(\varepsilon_3) \rangle \Big) e^{i\omega t' + i(\varepsilon_3 - \varepsilon_4)t'/\hbar}
\end{aligned} \tag{1.14}$$

The time t is chosen to be zero because processes are stationary in the DC case. Only non zero terms are written and four operator averages are decomposed thanks to Wick's theorem[9]. In the following, we only consider the limit of low-frequency fluctuations, corresponding to $\hbar\omega \ll k_B T$ and all noise calculations will be done at[10] $\omega = 0$. In other

[9] Wick's theorem for four annihilation and creation operators is $\langle \hat{a}^\dagger(\varepsilon_1) \hat{a}(\varepsilon_2) \hat{a}^\dagger(\varepsilon_3) \hat{a}(\varepsilon_4) \rangle = \langle \hat{a}^\dagger(\varepsilon_1) \hat{a}(\varepsilon_2) \rangle \langle \hat{a}^\dagger(\varepsilon_3) \hat{a}(\varepsilon_4) \rangle + \langle \hat{a}^\dagger(\varepsilon_1) \hat{a}(\varepsilon_4) \rangle \langle \hat{a}(\varepsilon_2) \hat{a}^\dagger(\varepsilon_3) \rangle$

[10] At the temperature of 25 mK, $k_B T \simeq 0.5$ GHz and noise measurements are performed at the MHz regime. Experimentally, we have only access to the limit $\omega \longrightarrow 0$ of the noise.

words, for $\hbar\omega \ll k_B T$, the noise is a white noise. Then, we obtain:

$$S_{I_L \times I_L}(\omega = 0) = \frac{2e^2}{h} \int d\varepsilon \Big(D^2 f_L(\varepsilon)(1 - f_L(\varepsilon)) + D^2 f_R(\varepsilon)(1 - f_R(\varepsilon)) \\ + RD f_L(\varepsilon)(1 - f_R(\varepsilon)) + RD f_R(\varepsilon)(1 - f_L(\varepsilon)) \Big) \tag{1.15}$$

The first line of eq. 1.15 corresponds to thermal fluctuations of each reservoirs and the second line 1.15 exhibits the partitioning of electrons over the Fermi sea, highlighted by the term RD. An analytical integration gives a simpler formula:

$$S_{I_L \times I_L} = 4k_B T \frac{2e^2}{h} \left(D^2 + RD \frac{eV_{dc}}{2k_B T} \coth \left(\frac{eV_{dc}}{2k_B T} \right) \right) \tag{1.16}$$

where V_{dc} is the potential applied on the reservoir R_L. At equilibrium ($V_{dc} = 0$), the noise reduces to $S_{I_L \times I_L} = 4k_B T D \frac{2e^2}{h}$, which is the usual Johnson-Nyquist formula with conductance $D\frac{2e^2}{h}$[79], corresponding to the thermal fluctuations of the reservoirs. For voltages $eV_{dc} > 2k_B T$, fluctuations are mostly provided by the partitioning of electrons through the scatterer, highlighted by the term $RD f_L(\varepsilon)(1 - f_R(\varepsilon))$ in the expression 1.15: an electron emitted by L at an energy ε meets a hole emitted[11] by R_R and is either reflected or transmitted. The rate of partitioned particles is proportional to V_{dc}, so the noise tends towards a linear function: $S_I \longrightarrow 4RD\frac{2e^2}{h} eV_{dc}$ in this case.

Because of the symmetry, fluctuations are the same on both contacts R_L and R_R. Thus, auto-correlation noise on R gives exactly the same expression:

$$S_{I_L \times I_L} = S_{I_R \times I_R} \tag{1.17}$$

The cross-correlation term involves not the same terms of $\hat{\mathbf{I}}_L$ and $\hat{\mathbf{I}}_R$ (in eq. 1.10) for the calculation of the noise, but the result is found identical, except to the minus sign:

$$S_{I_L \times I_R} = -S_{I_L \times I_L} \tag{1.18}$$

Minus sign evidences the fact that fluctuations in R and L are anti-correlated. This results from the current conservation in the low frequency limit. Cross-correlated noise has several advantages compared to the auto-correlation: for instance, the contribution of the experimental set-up to the noise is considerably reduced.

[11] Because of Fermi exclusion principle, partitioning occurs only when an electron is scattered in an empty outgoing state, corresponding to a hole.

1.1.3 6-contacts geometry

We propose here to compute expressions of current and noise for a 6-contacts QPC, presented in figure 1.3. Contacts are now denoted from index 0 to 5. This geometry is relevant in the Quantum Hall Effect (QHE) using the chirality of edge channels[12]. In the following, the 6-contacts QPC is supposed to work in the QHE regime and electrons follow the trajectories drawn in figure 1.3. Similarly to the 2-contacts QPC, a scatterer S reflects or transmits electrons emitted by contacts 0 and 3.

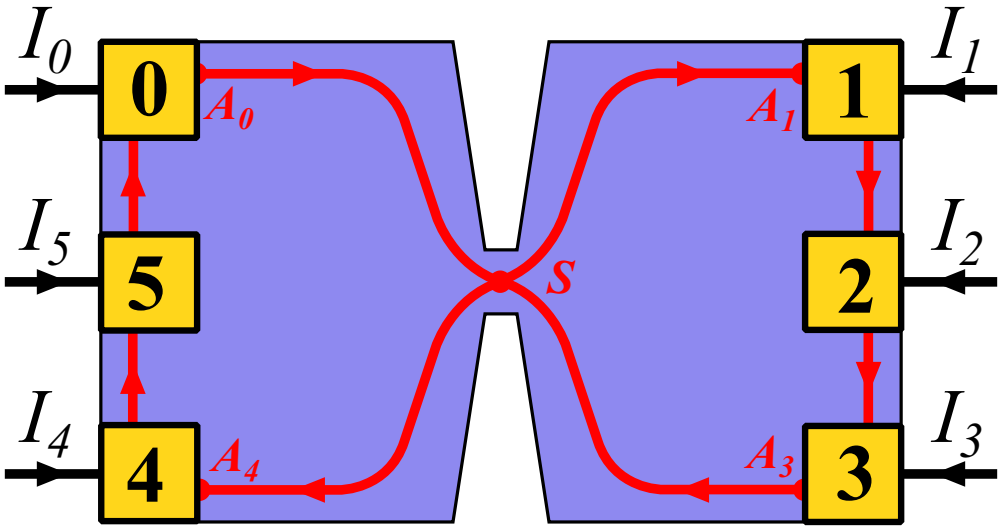

Figure 1.3: A 6-contacts QPC working in the QHE regime. Edge channels are represented by the red lines. Partitioning of electrons emitted by the reservoir R_0 and R_3 occurs in the scatter **S**. Contrary to appearances, this geometry is topologically equivalent to the schematic quantum conductor presented in the figure 1.1.

The scattering matrix **S** for a 6-contact QPC is now a 6×6 dimensional matrix and reads :

$$\mathbf{S} = \begin{pmatrix} 0 & 0 & 0 & 0 & 0 & e^{i\varphi_{05}} \\ i\tau e^{i\varphi_{01}} & 0 & 0 & i\tau e^{i\varphi_{13}} & 0 & 0 \\ 0 & e^{i\varphi_{12}} & 0 & 0 & 0 & 0 \\ 0 & 0 & e^{i\varphi_{23}} & 0 & 0 & 0 \\ \rho e^{i\varphi_{04}} & 0 & 0 & \rho e^{i\varphi_{34}} & 0 & 0 \\ 0 & 0 & 0 & 0 & e^{i\varphi_{45}} & 0 \end{pmatrix} \tag{1.19}$$

where τ and ρ are respectively transmission and reflection coefficients of the scatterer S. Terms $e^{i\varphi_{ij}}$ are Aharonov-Bohm phases accumulated between the contacts i and j, proportional to the path length travelled on the edge channels. Some of these phases

[12] On the contrary of the 2-contact QPC, there is no interest to perform experiments without magnetic field. More details are given in chapter 2.

verify an interesting relation:

$$\varphi_{01} - \varphi_{13} + \varphi_{04} - \varphi_{34} = 0 \tag{1.20}$$

Indeed, φ_{ij} is proportional to the path length travelled on the edge channels between contacts i and j, denoted A_iA_j, as shown of figure 1.3. If the coefficient of proportionality between phases and distances is denoted a, we obtain:

$$\varphi_{01} - \varphi_{13} = a(A_1A_0 - A_3A_1) = a(A_0S + SA_1 - A_3S - SA_1) = a(A_0S - A_3S) \tag{1.21}$$
$$\varphi_{04} - \varphi_{34} = a(A_4A_0 - A_4A_3) = a(A_4S + SA_0 - A_4S - SA_3) = -a(A_0S - A_3S) \tag{1.22}$$

where S is the position of the scatterer. The eq. 1.20 highlights that trajectories converge on the point S, giving the name of "Quantum Point Contact" to these devices.

The unitary of $\mathbf{S}$ must be verified here: $\mathbf{S}^\dagger\mathbf{S} = \mathbb{1}$, because of the current conservation $\rho^2 + \tau^2 = R + D = 1$. Scattering matrix is obviously not Hermitian unlike the 2-contact geometry. Indeed, time-reversal symmetry is not longer true: travelling trajectories in the opposite direction is topologically different, which is easy to visualise in figure 1.3, by reversing the direction of red arrows[13].

Current operator

In this geometry, it is interesting to compute the currents $\hat{\mathbf{I}}_0$, $\hat{\mathbf{I}}_1$ and $\hat{\mathbf{I}}_4$ when a DC polarisation V_{dc} is applied on the contact 0. We suppose that no potential is applied on the other contacts. Using the Fermi operator[14] $\hat{\Psi}_0$ and eq. 1.3, the current in the wire 0 $\hat{\mathbf{I}}_0$ is:

$$\hat{\mathbf{I}}_0(x_0,t) = \frac{e}{h}\int d\varepsilon_1 d\varepsilon_2 \left(\hat{\mathbf{a}}_0^\dagger(\varepsilon_1)\hat{\mathbf{a}}_0(\varepsilon_2) - \hat{\mathbf{a}}_5^\dagger(\varepsilon_1)\hat{\mathbf{a}}_5(\varepsilon_2)\right) e^{-\frac{i}{\hbar}(\varepsilon_1-\varepsilon_2)(t-x_0/v_F)} \tag{1.24}$$

[13] Time reversing is also equivalent to change $\vec{B}$ into $-\vec{B}$.

[14] In this case, $\hat{\Psi}_0$ reads:

$$\hat{\Psi}_0(x_0,t) = \int \frac{d\varepsilon}{\sqrt{2\pi\hbar v(\varepsilon)}} \left(\hat{\mathbf{a}}_0(\varepsilon)e^{ik(\varepsilon)x_0} + \hat{\mathbf{a}}_5(\varepsilon)e^{i\varphi_{05}}e^{-ik(\varepsilon)x_0}\right) e^{-i\varepsilon t/\hbar} \tag{1.23}$$

where x_0 is the axis[15] of incoming and outgoing currents in contact 0. The current operator in the wire 1 is composed of partitioning terms and reads:

$$\hat{\mathbf{I}}_1(x_1,t) = \frac{e}{h}\int d\varepsilon_1 d\varepsilon_2 \Big(\hat{\mathbf{a}}_1^\dagger(\varepsilon_1)\hat{\mathbf{a}}_1(\varepsilon_2) - \rho^2\hat{\mathbf{a}}_0^\dagger(\varepsilon_1)\hat{\mathbf{a}}_0(\varepsilon_2) - \tau^2\hat{\mathbf{a}}_3^\dagger(\varepsilon_1)\hat{\mathbf{a}}_3(\varepsilon_2) \\ - \tau\rho e^{-i\varphi_{10}+i\varphi_{13}}\hat{\mathbf{a}}_0^\dagger(\varepsilon_1)\hat{\mathbf{a}}_3(\varepsilon_2) - \tau\rho e^{-i\varphi_{13}+i\varphi_{10}}\hat{\mathbf{a}}_3^\dagger(\varepsilon_1)\hat{\mathbf{a}}_0(\varepsilon_2)\Big) e^{-\frac{i}{\hbar}(\varepsilon_1-\varepsilon_2)(t-x_1/v_F)} \tag{1.25}$$

Current $\hat{\mathbf{I}}_4$ is identical to expression 1.25, by replacing index $\ldots_1 \longleftarrow \ldots_4$ and $\ldots_0 \longleftarrow \ldots_3$. Averaged currents are denoted I_0, I_1 and I_4. Similarly to the calculation of the 2-contact geometry, the integrated forms read:

$$I_0 = \frac{e^2}{h}V_0 \tag{1.26}$$

$$I_1 = \frac{e^2}{h}(V_1 - DV_0 - RV_3) \tag{1.27}$$

$$I_4 = \frac{e^2}{h}(V_4 - RV_0 - DV_3) \tag{1.28}$$

where V_1, V_3 and V_4 are the voltages on contacts 1, 3 and 4. The quantum of conductance $G_Q = e^2/h$ appears as a factor of proportionality between currents and voltages. In the QHE, there is no spin degeneracy, so the factor 2 does not appear. The current emitted from the contact 0 does not depend on R or D and is diverted either toward the contact 1 or the contact 4. Thus, it is more relevant in this geometry to deals with the transmission and reflection coefficients D and R rather than the conductance of the sample. Experimental aspects of conductance of the 6-contacts geometry are treated in chapter 2 and 3.

The case of several modes correspond to an integer filling factor $\nu > 1$. Contributions of each edge channel add independently to the current, so the previous expressions 1.28 become:

$$I_0 = \frac{e^2}{h}\nu V_0 \tag{1.29}$$

$$I_1 = \frac{e^2}{h}(\nu V_1 - V_0\sum_k D_k - \sum_k R_k V_3) \tag{1.30}$$

$$I_4 = \frac{e^2}{h}(\nu V_4 - \sum_k R_k V_0 - \sum_k D_k V_3) \tag{1.31}$$

where T_k and R_k are in this case the transmission and the reflection of each mode k. In that case, the conductance of the sample with QPC fully opened is now the Hall

[15] One can note that edge channel in the figure 1.3 from contact 0 to 1 has no the same axis of current from contact 5 to 0. However, the 6-contacts geometry presented in figure 1.3 is topologically equivalent to the general quantum conductor of figure 1.1, so that it is correct to reduce the problem to one axis x_0.

conductance, $G_H = \nu G_Q = \nu e^2/h$.

Current fluctuations

We compute here the auto-correlations $\langle \hat{\mathbf{I}}_1 \hat{\mathbf{I}}_1 \rangle$ and $\langle \hat{\mathbf{I}}_4 \hat{\mathbf{I}}_4 \rangle$ and the cross-correlation $\langle \hat{\mathbf{I}}_1 \hat{\mathbf{I}}_4 \rangle$ of currents in the wires 1 and 4. Contact 2 (respectively contact 5) allows to disconnect contact 1 and 3 (respectively 4 and 0), so that fluctuations of 1 and 3 (respectively 4 and 0) are uncorrelated. The noise calculation is similar to the previous computation in eq. 1.14 and is not developed here. For the 6-contacts geometry, the auto-correlation reads:

$$\begin{aligned} S_{I_1 \times I_1} = \frac{2e^2}{h} \int d\varepsilon \Big(& f_1(\varepsilon)(1 - f_1(\varepsilon)) + D^2 f_0(\varepsilon)(1 - f_0(\varepsilon)) + R^2 f_3(\varepsilon)(1 - f_3(\varepsilon)) \\ & + RD f_0(\varepsilon)(1 - f_3(\varepsilon)) + RD f_3(\varepsilon)(1 - f_0(\varepsilon)) \Big) \end{aligned} \tag{1.32}$$

Thermal terms appears in the first line while partitioning time with factor RD are written in the second line. If the contact 0 is polarised such that $V_0 = V_{dc}$ and $V_3 = 0$, the noise is:

$$S_{I_1 \times I_1} = S_{I_4 \times I_4} = 2k_B T \frac{e^2}{h} \left(1 + D^2 + R^2 + 2RD \frac{eV_{dc}}{2k_B T} \coth \left(\frac{eV_{dc}}{2k_B T} \right) \right) \tag{1.33}$$

Auto-correlations on contact 1 and 4 are identical. Expression is slightly different from eq. 1.14 of the 2-contacts geometry because of the spatial separation of edge channels.

For the case of several modes, at filling factor ν, an edge channel can be partitioned at once. Thus, the contribution of $\nu - 1$ other edge channel in the noise reduces to the thermal terms. The auto-correlation noise at filling factor ν then reads:

$$S_{I_1 \times I_1} = S_{I_4 \times I_4} = 2k_B T \frac{e^2}{h} \left(2\nu - 1 + D^2 + R^2 + 2RD \frac{eV_{dc}}{2k_B T} \coth \left(\frac{eV_{dc}}{2k_B T} \right) \right) \tag{1.34}$$

The Johnson-Nyquist noise is recovered for $V_{dc} = 0$: $S_{I_1 \times I_1} = 4k_B T \nu e^2/h$. It corresponds to the thermal noise generated by a conductance of $\nu e^2/h$ that does not depend on the transmission D of the scatterer. It highlights that for this geometry, the conductance seen by every contact is the Hall conductance $G_Q = \nu e^2/h$.

The cross-correlation expression between contact 1 and 4 is different from auto-correlations, contrary to the 2-contacts geometry. The filling factor does not appears in the final integrated form:

$$S_{I_1 \times I_4} = -4k_B T \frac{e^2}{h} RD \left(1 + \frac{eV_{dc}}{2k_B T} \coth \left(\frac{eV_{dc}}{2k_B T} \right) \right) \tag{1.35}$$

Indeed, only thermal fluctuations of the partitioned edge channel is non equal to zero. It is interesting to note that fluctuations vanishes when the QPC is either open or closed: in that case, contacts 1 and 4 are completely uncorrelated.

1.2 Photo-assisted shot-noise

In this section, we study the effects of a periodic voltage, of fundamental frequency ν, applied on a quantum wire. First, we present the Floquet formalism[44] in order to describe the electronic states under an alternative (AC) voltage. In this formalism, electronic wavefunctions become a superposition of states of energy shifted by quanta $h\nu$, giving the name of "photo-assisted" to the properties deduced from this process. The computation of the current operator allows to recover the number of charges injected in the quantum wire per period. The partition noise generated in this regime, or photo-assisted shot-noise, is a direct measure of the total number of excitations in the Fermi sea.

1.2.1 Floquet Formalism

Effect of an AC voltage on the Fermi sea

What is the response of electrons in the quantum wire when a periodic voltage $V_{ds}(t)$ is applied on it? A first assumption would be to consider the adiabatic continuity of the static case studied before. A DC voltage applied on a reservoir increases chemical potential of a quantity eV_{dc}, thus, a time-dependant voltage drives the chemical potential $\mu = \varepsilon_F + eV_{ds}(t)$ and transport properties are adiabatically modulated. For example, resulting noise would be the adiabatic temporal average of the DC-noise:

$$S_I^{ad.} = \nu \int_0^{1/\nu} dt \cdot S_I^{DC}(V_{ds}(t)), \tag{1.36}$$

where ν is the fundamental frequency of $V(t)$ and S_I^{DC} the expression of shot-noise 1.15 by replacing V_{dc} by $V_{ds}(t)$.

In the following, we are going to show that this classical picture corresponds to the low frequency limit of the Floquet formalism presented here. The later has been developed first by Moskalets and Büttiker[93, 94] for quantum charge pumping where charge carriers are scattered by an oscillating scatterer. We apply this formalism to a reservoir driven by a periodic potential and interpret the result as electron-hole excitations. We also apply it for the quantum switch study in the next section, where the transmission of the scatterer is periodically driven.

The voltage $V_{ds}(t)$ is decomposed on its static and alternative components: $V_{ds}(t) = V_{dc} + V_{ac}(t)$, such that $\overline{V_{ds}(t)} = V_{dc}$. The effect of the DC voltage is to shift the chemical potential of the Fermi sea, $\mu_L = \varepsilon_F + eV_{dc}$. The pure alternative part $V_{ac}(t)$ adds a time-dependant $\hat{\mathbf{V}}_{ac}(t)$ potential in the leads from the contact to the QPC and is supposed to be spatially uniform far from the scatterer, and decreases slowly to zero be fore the

scatterer. Solving the Schrödinger's equation, single-particle Hamiltonian is:

$$\hat{\mathbf{H}} = \frac{\hat{\mathbf{P}}^2}{2m^*} - e\hat{\mathbf{V}}_{ac}(t) \tag{1.37}$$

The eigen wave functions are still plane waves, but with a supplementary time-dependant phase $\phi(t)$:

$$\Psi(x,t) = \frac{e^{i(k(\varepsilon)x - \varepsilon t/\hbar) - i\phi(t)}}{\sqrt{L}}, \quad \phi(t) = \frac{e}{\hbar}\int_{-\infty}^{t} dt' V_{ac}(t') \tag{1.38}$$

The voltage $V_{ac}(t)$ adds a phase $\phi(t)$ to the wavefunction of electron at all energies. As $V_{ac}(t)$ is a periodic function of fundamental frequency ν whose the mean value is 0, $e^{-i\phi(t)}$ is also a ν-periodic function, so it can be developed as a Fourier serie:

$$e^{-i\phi(t)} = \sum_{l=-\infty}^{+\infty} p_l e^{-2\pi i \nu l t}, \tag{1.39}$$

Where p_l are the Fourier coefficients[16] of $e^{i\phi(t)}$. Writing the Fourier serie in the expression 1.38, the wave function finally exhibits a superposition of state at energies shifted by $lh\nu$:

$$\Psi(x,t) = \sum_{l=-\infty}^{+\infty} p_l \frac{e^{ik(\varepsilon)x}}{\sqrt{L}} e^{-i(\varepsilon + lh\nu)t/\hbar} \tag{1.41}$$

The electron in a driven Fermi sea is in a discrete quantum superposition of the previous eigen state. It can be interpreted as follows: an electron at energy ε has a probability $P_l = |p_l|^2$ to absorb (resp. emit) l quanta of energy $h\nu$ for $l > 0$ (resp. $l < 0$). This process is similar to an absorption or an emission of a photon, giving the name "photo-assisted". The Fourier coefficients verify an interesting property[129]: taking modulus square of 1.39, we obtain the equality:

$$\sum_{l=-\infty}^{+\infty} p_l^* p_{l+m} = \delta_{m,0} \tag{1.42}$$

In particular, for $m = 0$, $\sum_l |p_l|^2 = 1$ results from the conservation of the current where the probabilities are $P_l = |p_l|^2$. Note that if the sum of non-diagonal terms is zero, they are not necessary zero, $p_l^* p_{l+k} \neq 0$.

Values of the serie $\{p_l\}_{l\in\mathbb{Z}}$ obviously depends on the temporal shape of $V_{ds}(t)$ during one period. For a sine signal $V_{ds}(t) = V_{ac}\sin(2\pi\nu t)$, Fourier coefficients are $p_l = j_l(\alpha)$, where $j_l(\alpha)$ is the l^{th}-Bessel function and its argument α is the dimensionless amplitude

[16] Coefficients p_l are given by :

$$p_l = \frac{1}{T}\int_0^T dt\ e^{2i\pi l t/T} e^{-i\phi(t)} \tag{1.40}$$

$\alpha = eV_{ac}/h\nu$[100].

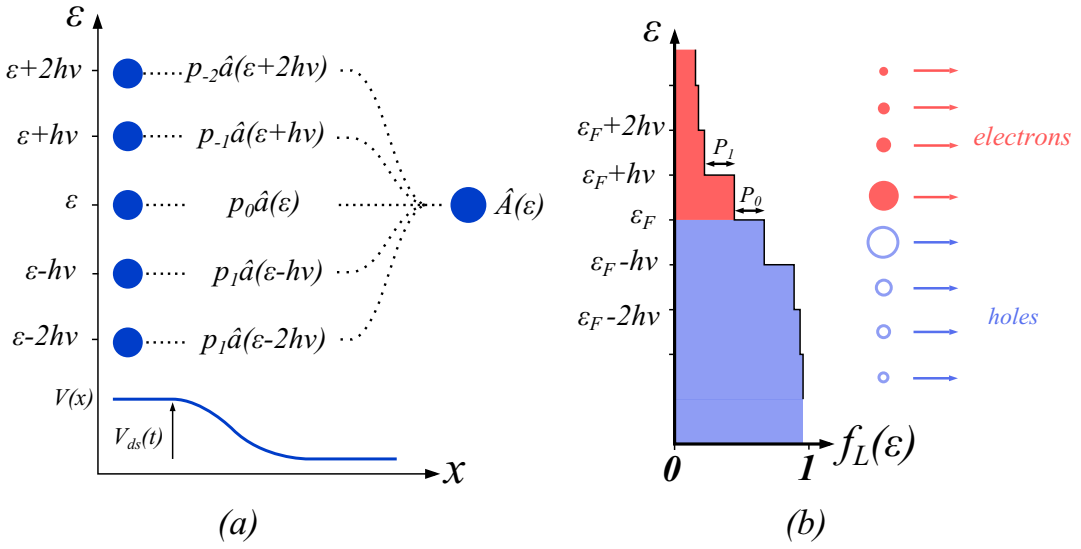

Figure 1.4: *(a)* An electron in a alternative potential $eV_{ds}(t)$ of period $1/\nu$ is in a superposition of state at energy $\varepsilon + l h\nu$. *(b)* The whole Fermi sea of reservoir R_L submitted to $V_{ds}(t)$ at $T = 0K$. It exhibits coherent electron-hole excitations.

For the calculation of operators, we need to write down the annihilation and creation operators in the driven reservoir, denoted with a capital: $\hat{\mathbf{A}}$ and $\hat{\mathbf{A}}^\dagger$, $\hat{\mathbf{a}}$ and $\hat{\mathbf{a}}^\dagger$. Figure 1.4 details how it is build. The annihilation operator $\hat{\mathbf{A}}(\varepsilon)$ describes the amplitude probability to find an electron at energy ε after emission/absorption of quanta $h\nu$. For example, the contribution of an electron emitted by the reservoir at energy $\varepsilon - l h\nu$ is $p_l \hat{\mathbf{a}}_\alpha(\varepsilon - l h\nu)$ Then, for the reservoir α driven by $V(t)$, it reads:

$$\hat{\mathbf{A}}_\alpha(\varepsilon) = \sum_{k=-\infty}^{+\infty} p_l \hat{\mathbf{a}}_\alpha(\varepsilon - l h\nu) \tag{1.43}$$

where $\hat{\mathbf{a}}_\alpha$ is the annihilation operator describing an electron of the reservoir α without modulation. Consequently, for a periodically driven reservoir, we only have to replace $\hat{\mathbf{a}}_\alpha \longleftarrow \hat{\mathbf{A}}_\alpha$ in the calculation of noise and current. The modulated quantum field operators allows to understand how the whole Fermi sea is affected by the AC potential. The quantum and statistical average reads:

$$\langle \hat{\mathbf{A}}_\alpha^\dagger(\varepsilon) \hat{\mathbf{A}}_\beta(\varepsilon') \rangle = \sum_{k,l} p_l^* p_k f_\alpha(\varepsilon - l h\nu) \delta(\varepsilon - \varepsilon' - (l-k)h\nu) \delta_{\alpha\beta} \tag{1.44}$$

The DC properties (through V_{dc}) are included in the Fermi distribution f_α and the AC properties are reflected in the sum over the p_l coefficients. This sum on the Fermi function f_L translated of $l h\nu$ corresponds to a distribution of electron and hole excitations[128]. The occupation number, plotted in figure 1.4 *(b)*, has a staircase structure of height equal

to the quanta of energy $h\nu$ with a width P_l at energy $\varepsilon + lh\nu$: electrons are excited above the Fermi sea and holes under it. In the limit $T = 0$ and in the case of a pure AC voltage, the number of electron above the Fermi sea is simply given by:

$$N_e = \sum_{l=0}^{+\infty} lP_l \tag{1.45}$$

and the number of holes, under the Fermi sea:

$$N_h = -\sum_{l=-\infty}^{-1} lP_l \tag{1.46}$$

Note that N_e and N_h are equal when $\overline{V_{ds}} = 0$ (pure AC voltage) in order to respect the current conservation. Electrons and holes are in a coherent superposition. Indeed, diagonal factors $p_l^* p_k \neq 0$ are not necessary zero[57, 56]. This situation differs radically of an incoherent Fermi sea.

1.2.2 Current operator and charge injection

We compute in this section the current operator and their averages in the framework of Floquet theory for both geometries of QPC considered in section 1.1.

2-contacts geometry

We consider the case of a periodic voltage $V_{ds}(t)$ applied only on the left reservoir R_L of QPC presented on figure 1.2. As said previously, the DC operators $\hat{\mathbf{a}}_L$ are replaced in that case by the Floquet operators $\hat{\mathbf{A}}_L$ defined in 1.43. Similarly to the expression 1.10, we obtain:

$$\begin{aligned}\hat{\mathbf{I}}_L(x,t) = \frac{e}{h}\int d\varepsilon_1 d\varepsilon_2 \Big(&\hat{\mathbf{A}}_L^\dagger(\varepsilon_1)\hat{\mathbf{A}}_L(\varepsilon_2) - \rho^2 \hat{\mathbf{A}}_L^\dagger(\varepsilon_1)\hat{\mathbf{A}}_L(\varepsilon_2) - \tau^2 \hat{\mathbf{a}}_R^\dagger(\varepsilon_1)\hat{\mathbf{a}}_R(\varepsilon_2) \\ &- i\tau\rho \hat{\mathbf{A}}_L^\dagger(\varepsilon_1)\hat{\mathbf{a}}_R(\varepsilon_2) + i\tau\rho \hat{\mathbf{a}}_R^\dagger(\varepsilon_1)\hat{\mathbf{A}}_L(\varepsilon_2)\Big) e^{-i(\varepsilon_1-\varepsilon_2)(t-x/v_F)/\hbar}\end{aligned} \tag{1.47}$$

Using eq. 1.44, the average gives:

$$\begin{aligned} I_L(x,t) = \langle \hat{\mathbf{I}}_L(x,t)\rangle =& \frac{2e}{h}\int d\varepsilon |\tau|^2 \left(\sum_{l,m} p_l^* p_m f_L(\varepsilon - lh\nu) e^{i(l-m)(t-x/v_F)/\hbar} - f_R(\varepsilon)\right) \\ =& \frac{2e^2}{h} D V_{ds}(t - x/v_F) \end{aligned} \tag{1.48}$$

Finally, we recover the formula 1.12 extended to the case of a time-dependant voltage. The current propagates in the wire at the Fermi velocity v_F with an amplitude proportional

to the AC voltage.

6-contacts geometry

For the 6-contacts geometry, the voltage $V_0(t) = V_{ds}(t) = V_{dc} + V_{ac}(t)$ is applied on the contact 0. There is no external potential is applied on the other contacts. The computation is performed similarly than what have been done in section 1.2.2, by using the expression of currents 1.24 or 1.25 of the 6-contacts geometry. In the framework of Floquet formalism, the operators $\hat{\mathbf{a}}_0$ are replaced by $\hat{\mathbf{A}}_0$ defined in 1.43. Then, the average gives:

$$\begin{aligned} I_0(x_0,t) = \langle \hat{\mathbf{I}}_0(x,t) \rangle =& \frac{e}{h} \int d\varepsilon \left(|\tau|^2 \sum_{l,m} p_l^* p_m f_0(\varepsilon - lh\nu) e^{i(l-m)(t-x_1/v_F)/\hbar} - f_5(\varepsilon) \right) \\ =& \frac{e^2}{h} V_0(t - x_0/v_F) \end{aligned} \tag{1.49}$$

Similarly, the currents in the wire 1 and 4 are:

$$I_1(x_1,t) = \frac{e^2}{h} D V_0(t - t' - x_1/v_F) \tag{1.50}$$

$$I_4(x_4,t) = \frac{e^2}{h} R V_0(t - t' - x_4/v_F) \tag{1.51}$$

where $t' = A_0 S/v_F$ is the delay accumulated from contact 0 to the scatterer. The voltage $V_0(t)$ generates a propagative sine currents in the wire 0 which is split by S into a superposition of a reflected and a transmitted currents. Finally, transport properties in the quantum wire in the quantum Hall effect are identical to the case of zero magnetic field, except the spatial separation of the propagation.

1.2.3 Current fluctuations

Photo-assisted processes are not explicit in the expression of currents developed in the previous section, which is equivalent to an adiabatic modulation of the DC current in both geometries, propagation excepted. On the contrary, noise reveals characteristics of the Floquet states, that strongly differs from a trivial adiabatic modulation[82, 108, 128]. Photo-assisted shot-noise has been measured in ballistic [106] and diffusive[115] coherent conductors. The figure 1.5 shows how remarkable structure of photo-assisted Fermi sea impacts the partitioning noise.

Electrons excited above the Fermi sea of the left reservoir meet empty states (of electrons) of the right reservoir, generating a partitioning noise. Same process occurs with holes created under the Fermi sea. This partitioning of electron-holes excitation is modulated by shifting the whole right Fermi sea with an additional DC voltage V_{dc}. The

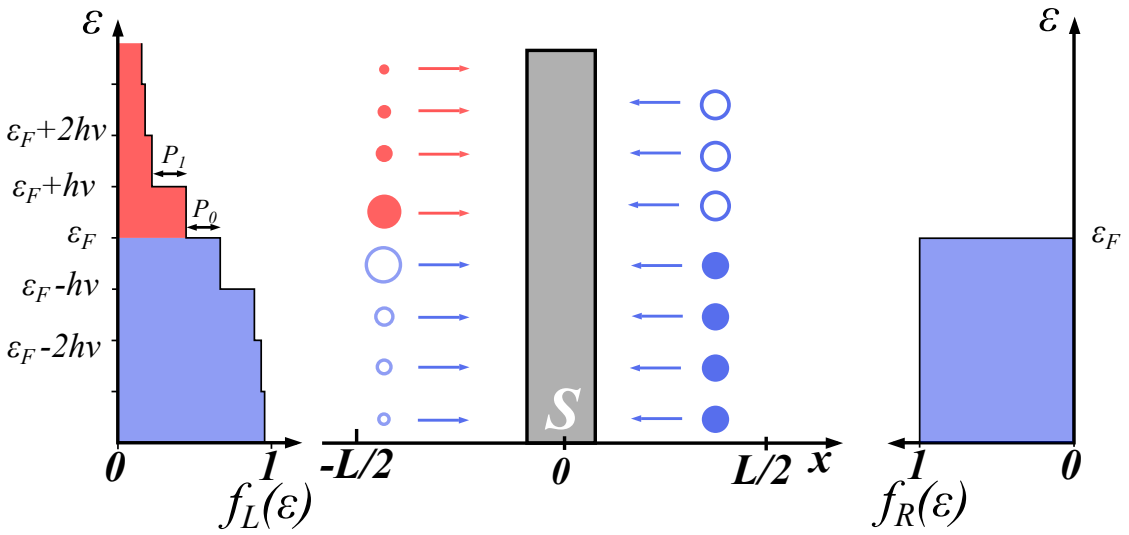

Figure 1.5: Photo-assisted shot-noise schematic. Temperature is 0 K. The right reservoir R_R sends only electrons under the Fermi sea whereas an AC voltage applied on R_L creates an electron-hole superposition. Partitioning of electrons (respectively holes) occurs above (resp. under) the Fermi sea.

partitioning noise increases by step while we jump from step to an another of the staircase structure of the Fermi sea. We propose here to derive formula of the noise with a driven reservoir, called photo-assisted shot-noise, for the two geometries studied.

2-contacts geometry

In the 2-contacts geometry, voltage $V_{ds}(t) = V_{dc} + V_{ac}\cos(2\pi\nu t)$ is applied on the left reservoir. Current fluctuations are derived from expression of $\hat{\mathbf{I}}_L(x,t)$ using eq. 1.4. Main differences with the DC case is that the current-current operator is periodic with time t and is averaged over one period. Calculation is the same of eq. 1.14, by replacing $\hat{\mathbf{a}}_L$ with $\hat{\mathbf{A}}_L$. Expressions are heavy and not written here for simplicity. Then, the noise reads:

$$S_{I_L\times I_L} = \frac{2e^2}{h}\sum_{l=-\infty}^{+\infty}|p_l|^2\int d\varepsilon\Big(D^2 f_L(\varepsilon)(1-f_L(\varepsilon)) + D^2 f_R(\varepsilon)(1-f_R(\varepsilon)) \\ + RDf_L(\varepsilon - lh\nu)(1-f_R(\varepsilon)) + RDf_R(\varepsilon)(1-f_L(\varepsilon - lh\nu))\Big) \tag{1.52}$$

Thermal terms in the first line stays unchanged from the DC case despite the modulation of the left reservoir. Photo-assisted signatures appear in the partitioned contributions in the second line where Fermi distributions of the left and right reservoir are compared. The resulting integrated form is finally a sum of DC shot-noise shifted of $lh\nu$ toward V_{dc}, with a probability $|p_l|^2$. The auto-correlation $S_{I,R\times I_R}$ of the right reservoir is identical

and cross-correlation is opposite. The integrated form reads:

$$S_{I_L \times I_L} = \sum_{l=-\infty}^{+\infty} |p_l|^2 4k_B T \frac{2e^2}{h} \left(D^2 + RD \frac{eV_{dc} - lh\nu}{2k_B T} \coth \left(\frac{eV_{dc} - lh\nu}{k_B T} \right) \right) \tag{1.53}$$

In particular, the DC shot-noise is recovered at $V_{ac} = 0$.

6-contacts geometry

In the case of the 6-contact geometry, the voltage $V_{ds}(t)$ is applied on the contact 0. Then, the auto-correlation on the contact 1 of the 6-contacts geometry is:

$$S_{I_1 \times I_1} = 4k_B T \frac{e^2}{h} \left(2\nu - 1 + D^2 + R^2 + RD \sum_{l=-\infty}^{+\infty} |p_l|^2 \frac{eV_{dc} - lh\nu}{2k_B T} \coth \left(\frac{eV_{dc} - lh\nu}{k_B T} \right) \right) \tag{1.54}$$

Expression of $S_{I_4 \times I_4}$ is identical. The cross-correlation is:

$$S_{I,1\times 4} = -4k_B T \frac{e^2}{h} RD \left(1 + \sum_{l=-\infty}^{+\infty} |p_l|^2 \frac{eV_{dc}}{2k_B T} \coth \left(\frac{eV_{dc}}{k_B T} \right) \right) \tag{1.55}$$

It is interesting to note that the expressions of PASN developed previously are written as a superposition of DCSN translated of quanta $lh\nu$, for both geometries or for the auto and cross-correlation. This results has been shown in [31] by Crépieux and al. in the case of a filling factor $\nu = 1$. In the general case, the photo-assisted shot-noise S_I^{PASN} is connected to the DC shot-noise S_I^{PASN} by the relation:

$$S_I^{PASN}(V_{dc}) = \sum_{l=-\infty}^{+\infty} |p_l|^2 S_I^{DC}(V_{dc} - lh\nu/e) \tag{1.56}$$

Experimentally, this expression is convenient to evidence photo-assisted processes. The noise is measured at $V_{ac} = 0$ and $V_{ac} \neq 0$ and measurements obtained are compared according to eq. 1.56. An analytical expression of the DCSN is not required. More surprisingly, J. Rech and al. [105] has shown that a similar expression 1.56 describes also photo-assisted processes in the fractional quantum Hall regime in the case of strong back-scaterring regimes ($D >> 1$), where the theoretical framework is radically different. Note that a similar expression has been derived by I. Safi and E.V. Sukhorukov[111, 109] also for the expression of the current: $I^{PASN}(V_{dc}) = \sum_l |p_l|^2 I^{DC}(V_{dc} - lh\nu/e)$, which is consistent with the results of eq. 1.49 and 1.51[17].

[17] The photo-assisted process does not directly appears in the expression of current because it is a linear function of the drain-source voltage on the contrary of the noise. Photo-assisted processes manifest for current measurement in the fractional quantum Hall effect, where the where the conductance is strongly non-linear.

Excess noise and electron-hole excitations

Unlike the current, the contributions of the partitioning electrons and holes are cumulative in the PASN. Thus, the noise counts the total number of electron-hole excitations generated by an arbitrary voltage $V_{ds}(t)$. More precisely, we are interested in the excess number of particles, denoted ΔN_{e-h}, in addition to the injected charge q. In the limit $T = 0$, it is connected to the excess noise ΔS through[18]:

$$\Delta S_I = S_I(V_{ac} \neq 0) - S(V_{ac} = 0) \tag{1.57}$$

$$= 2\frac{e^2}{h} RDh\nu \sum_{l=-\infty}^{+\infty} |p_l|^2 \left(|q+l| - |q|\right) \tag{1.58}$$

$$= 2\frac{e^2}{h} RDh\nu \Delta N_{e-h} \tag{1.59}$$

ΔN_{e-h} represents the number of particles injected in addition to the number of charges q, and it strongly depends on the time-dependence of $V_{ds}(t)$. For instance, the excess number of particle vanishes for a Lorentzian profile for integer values of q: the leviton[66, 74]. Also, the total number of holes and electrons in the Fermi sea is recovered at $q = 0$: $\Delta N_{e-h} = N_e + N_h$. Note that this situation differs from the electron-hole excitations successively emitted over a period from a mesocopic capacitance[41] where a similar formula is found and have been experimentally verified [13].

1.2.4 Photo-Assisted Shot-Noise as a function of DC drain-source voltage

As explained in figure 1.5, the shot-noise versus the DC polarisation reflects the properties of the set of $|p_l|^2$. It corresponds to probe the energy distribution of the excited Fermi-sea, or to perform an energy spectroscopy. Figure 1.6 shows the photo-assisted noise as a function of the reduced charge $q = eV_{dc}/h\nu$ (proportional to the DC-voltage) at several reduced amplitudes $\alpha = eV_{ac}/h\nu$, at the limit $T \longrightarrow 0$. The slope of the noise exhibits abrupt changes every time q is an integer, or when voltage displacement eV_{dc} is a equal to a quanta $h\nu$. This is a characteristic signature of photo-assisted processes.

This signature is enhanced in the excess noise defined in eq. 1.57, highlighting that only photo-assisted processes. Furthermore, ΔS_I is more convenient to measure experimentally than raw noise, as it will be shown in chapter 4. It highlights more clearly the distribution of electron-holes toward the Fermi sea. The figure 1.7 shows the excess noise for several AC amplitudes. The curve shape has abrupt variations in the slope every $q = n$ and reveals the distribution of electron and hole in energy. For a sine excitation, as many electrons are created above the Fermi sea as holes under, the curve is symmetric regarding $V_{dc} = 0$. The

[18] At zero temperature all expression of PASN are identical and are all denoted by S.

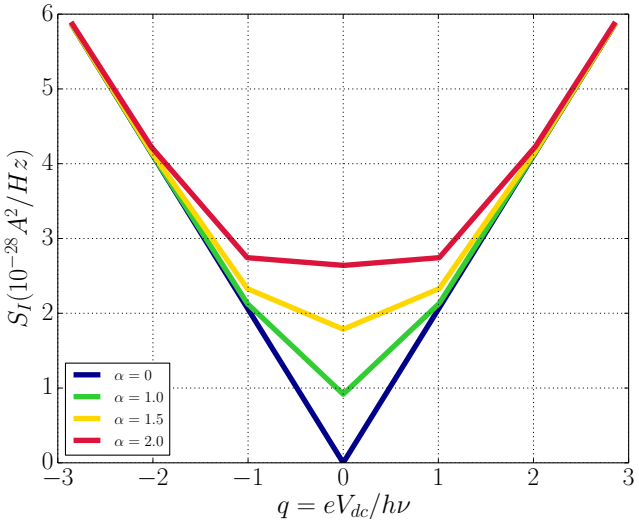

Figure 1.6: Photo-assisted shot-noise as a function of reduced charge $q = eV_{dc}/h\nu$ for several AC amplitudes. Parameters are $T = 0$ K, $D = 0.34$,$\nu = 18$ GHz.

Lorentzian profile exhibits a spectacular behaviour: no holes are created. The number of electron-hole in excess ΔN_{e-h} is denoted by ΔN_{e-h} in the left ordinate axis.

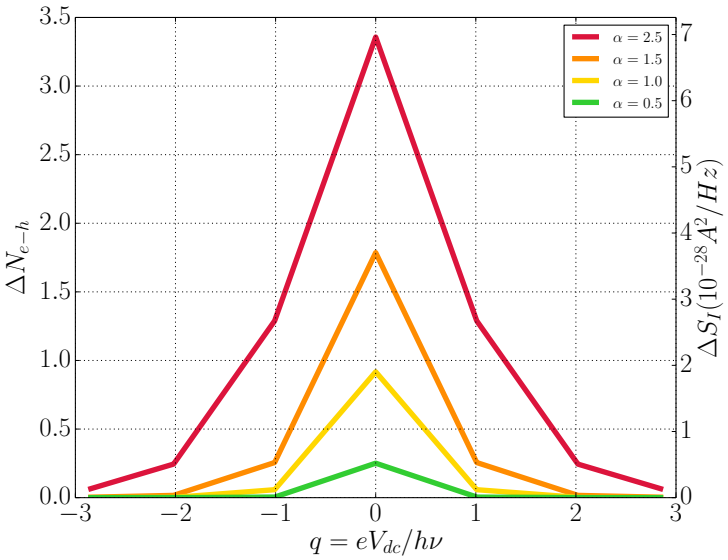

Figure 1.7: Excess noise as a function of the number of injected charges $q = eV_{dc}/h\nu$. It corresponds to the difference of the curves with the blues curves of the previous figure 1.6 : $\Delta S_I = S_I(\alpha \neq 0) - S_I(\alpha = 0)$. Parameters are $T = 0$ K, $D = 0.34$,$\nu = 18$ GHz.

The temperature of figures 1.5 1.6 and 1.7 is zero. Photo-assisted processes are sensitive with temperature increasing, which smooths the staircase structure of the Fermi sea (1.5). Changes in the slope of the photo-assisted shot-noise are softened until characteristic variations become indistinguishable. The figure 1.8 shows extra-noise ΔS_I as a

function of q for several temperatures. We use the reduced temperature, defined as:

$$\Theta = \frac{k_B T}{h\nu} \tag{1.60}$$

Parameter Θ quantizes competition between thermal disorder and photo-assisted effects in a driven Fermi-sea. Thermal effects are dominant for $\Theta > 0.1$, and it is impossible to observe typical signature at $q = n$ for larger values of Θ. Experimentally, it restricts the minimal value of frequency to $\nu > k_B T/h\Theta$. At an usual temperature of $T = 40$ mK, frequencies must be chosen above 8 GHz.

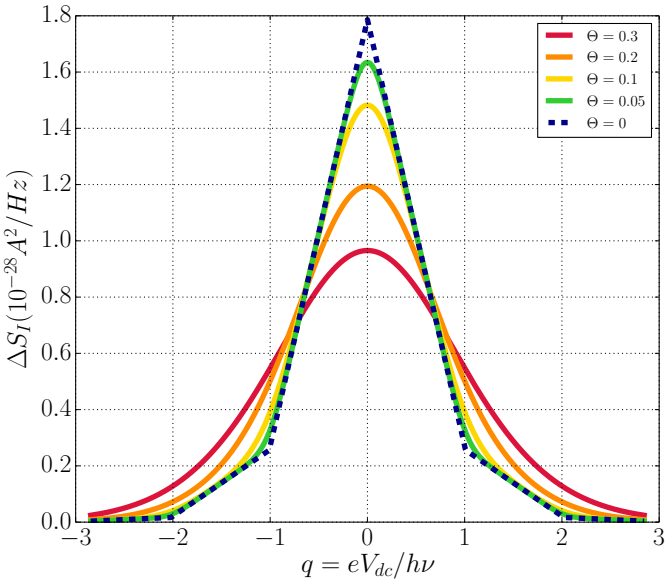

Figure 1.8: Excess noise as a function of the number of injected charges $q = eV_{dc}/h\nu$ for several values of the reduced temperature $\Theta = k_B T/h\nu$. Parameters are $\alpha = 1.5$, $D = 0.34$, $\nu = 18$ GHz.

1.2.5 Classical adiabatic regime

For a voltage $V_{ds}(t) = V_{dc} + V_{ac}\cos(2\pi\nu t)$ with an arbitrary low frequency ν, the Fermi sea is expected to be driven adiabatically. In other words, at each time t, the chemical potential in the driven reservoir is $\mu = eV_{ds}(t)$, even in the limit of $T \longrightarrow 0$. The resulting noise, denoted $S_I^{adiab.}$, corresponds to sweep and average over the curve of a DC shot-noise (in blue, in figure 1.6):

$$S_I^{adiab.} = \overline{S_I^{DC}(V_{ds}(t))} \tag{1.61}$$

As it will be shown, the quantum PASN strongly differs from this trivial, classical adiabatic regime. It does not depend on the frequency and there is no electron-hole correlations generated. Actually, the adiabatic framework is consistent with the Floquet formalism

only at very low frequencies. More precisely, the expression 1.56 tends to the average of the DC modulation:

$$\sum_{l=-\infty}^{+\infty} |p_l|^2 S_I^{DC}(V_{dc} + lh\nu/e) \quad \underset{\nu \to 0}{\longrightarrow} \quad \overline{S_I^{DC}(V_{ds}(t))} \tag{1.62}$$

In particular, it stays valid at zero temperature: in that case, frequency is compared to the amplitude of the AC excitations. It is harder to distinguish adiabatic and photo-assisted when $h\nu \ll eV_{ac}$ or $\alpha \gg 1$, illustrated in figure 1.9. At $\alpha = 1$, both curves are clearly distinct. The main difference between this classical model and the photo-assisted transport is that the changes in the slope occurs at respectively $V_{dc} = V_{ac}$ and $V_{dc} = h\nu/e$. At $\alpha = 3.0$, PASN and adiabatic noise tend to get mixed up.

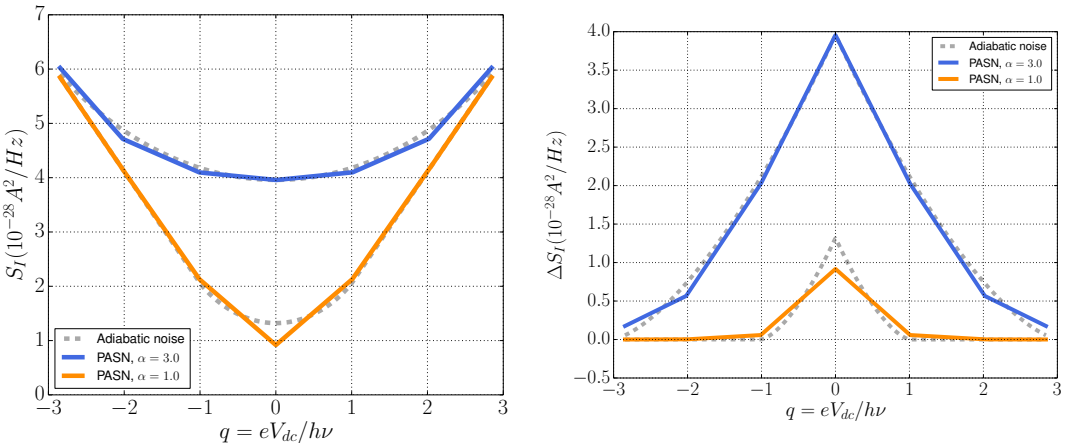

Figure 1.9: *(Left)* Photo-assisted shot-noise (coloured lines) and classical adiabatic modulation of DC shot-noise (grey dashed lines) versus reduced charge q, for $\alpha = 1$ and 3, at temperature $\Theta = 0$. *(Right)* Excess noise of a photo-assisted shot-noise (coloured lines) and of an adiabatic modulation of DC shot-noise (grey dashed lines) versus reduced charge q, for $\alpha = 1$ and 3, at temperature $T = 0$.

The difference between the adiabatic noise and the PASN is also evidenced in the curve of the noise as a function of the AC voltage amplitude V_{ac} while $V_{dc} = 0$, presented in figure 1.10. Curves are plotted at $T = 0$. The adiabatic noise is a linear function of V_{ac} whereas the PASN exhibits oscillations around the asymptotic line.

In chapter 4, we will present noise measurements as a function of the DC and AC polarisation, as shown in the figures 1.7 and 1.10. The experimental results will be compared to both the PASN and the noise deduced from the adiabatic model. It will allow us to prove that photo-assisted processes governs the physics of AC transport in quantum conductor in the quantum Hall effect regime.

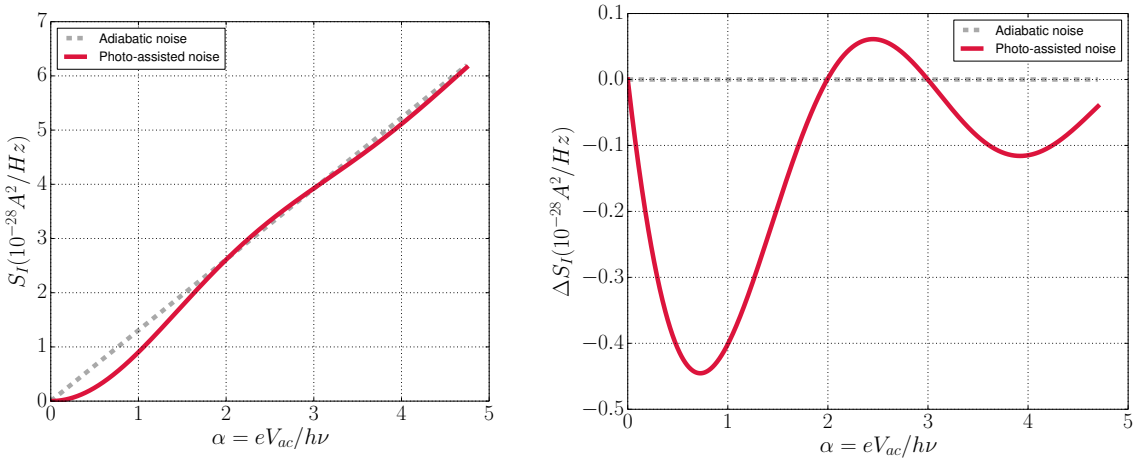

Figure 1.10: *(Left)* Photo-assisted shot-noise (red solid line) versus the reduced amplitude $\alpha = eV_{ac}/h\nu$, for $V_{dc} = 0$. The classical modulation of DCSN represented by the grey dashed line is a pure linear function of V_{ac}. Parameters are : $\nu = 18$ GHz, $T = 0$. (*Right*) Difference between the photo-assisted shot-noise and the classical noise versus the reduced amplitude α, with the same parameters. The PASN exhibits clear oscillations as a function of α.

1.3 Quantum switch

In the previous section 4.2, we described the transport properties of a quantum wire with a periodically modulated voltage applied on a contact. We propose now to study effects of a periodic modulation of the scatterer potential of a quantum wire. This problem is solved using the Landauer-Formalism applied in this chapter: the driven potential of the scatterer is reduced to a time-dependent transmission and reflection coefficients. The Floquet formalism is applied on the scattered electronic states to derive the current and its fluctuations in the wire. The main result is the presence of an additional and unavoidable noise generated by the transmission variation, even at thermal equilibrium or in the limit of zero temperature. It cannot be explained by an adiabatic modulation of the transmission of the usual thermal or shot-noise. This noise has been proposed as a meter of entanglement[76, 9, 113].

The problem can be viewed as a switching process. It corresponds to open or close an elementary quantum wire successively, connecting and disconnecting electrons propagating in the left and the right side of the scatterer. The intrinsic and fundamental noise generated by the switch can be connected with the study of electron-hole entanglement in the wire. A direct measurement of entanglement entropy is performed through current fluctuations.

This section is organized as follow. We first described the quantum switch with a time-dependent scattering matrix, and we use the Floquet formalism in order to describe the scattered electronic states. Then, we compute the current and current-current operators for the 2-contacts and 6-contacts geometries. Finally, we connect these results with the

entanglement entropy measurement proposed by Klich and Levitov[76].

1.3.1 Time-dependent scattering matrix

We first study the 2-contacts geometry presented in figure 1.2. The potential of the scatterer is modulated periodically at the frequency ν, so that scattering matrix $\mathbf{S}$ is now time-dependent[19]. The transmission and reflection coefficients are denoted $\tau \longleftrightarrow \tau(t)$ and $\rho \longleftrightarrow \rho(t)$. Despite the name "quantum switch", transmission does not reach necessary zero or one, and can take intermediate values. The scattering matrix $\mathbf{S}$ reads:

$$\mathbf{S}(t) = \begin{pmatrix} \rho(t) & \tau(t) \\ \tau(t) & -\rho(t) \end{pmatrix} \tag{1.63}$$

The unitary of $\mathbf{S}$ is still preserved, ensuring the current conservation at all time t:

$$\rho(t)^2 + \tau(t)^2 = 1 \tag{1.64}$$

The fermion operators describing the scattered outgoing states are time periodic with fundamental frequency ν. For instance, in the left side, the scatterer Fermion operator is: $\hat{\mathbf{b}}_L(t) = \rho(t)\hat{\mathbf{a}}_L + \tau(t)\hat{\mathbf{a}}_R$. Its expression in the energy domain is:

$$\begin{aligned} \hat{\mathbf{b}}_L(\varepsilon) =& \sum_l \alpha_l \hat{\mathbf{a}}_L(\varepsilon - lh\nu) + \beta_l \hat{\mathbf{a}}_R(\varepsilon - lh\nu) \\ =& \hat{\Gamma}_L(\varepsilon) + \hat{\Lambda}_R(\varepsilon) \end{aligned} \tag{1.65}$$

where $\hat{\Gamma}_L(\varepsilon) = \sum_l \alpha_l \hat{\mathbf{a}}_L(\varepsilon - lh\nu)$ and $\hat{\Lambda}_R(\varepsilon) = \sum_l \beta_l \hat{\mathbf{a}}_R(\varepsilon - lh\nu)$, and α_l and β_l are respectively the Fourier coefficients of $\rho(t)$ and $\tau(t)$:

$$\rho(t) = \sum_l \alpha_l e^{-2i\pi lh\nu} \tag{1.66}$$

$$\tau(t) = \sum_l \beta_l e^{-2i\pi lh\nu} \tag{1.67}$$

Therefore, the Fermi operator of electrons in the left side reads:

$$\hat{\Psi}_L(x_L, t) = \int \frac{d\varepsilon}{\sqrt{2\pi\hbar v(\varepsilon)}} \left(\hat{\mathbf{a}}_L(\varepsilon) e^{ik(\varepsilon)x_L} + (\hat{\Gamma}_L(\varepsilon) + \hat{\Lambda}_R(\varepsilon)) e^{-ik(\varepsilon)x_L} \right) e^{-i\varepsilon t/\hbar} \tag{1.68}$$

The quantum switch modelling is similar to the Floquet formalism presented in section 1.2.1: Floquet states are now the scattered states[93], as explained in figure 1.11. An incoming electron at a given energy ε collides the barrier and absorb ($l > 0$) or emit ($l < 0$)

[19] The first study of a time-dependent potential barrier has been done in [23] by Büttiker and Landauer and shows the absorption or emission of a quanta $h\nu$ as we will see in the following.

a quanta of energy $lh\nu$ with a probability $|\alpha_l|^2$ in reflection and $|\beta_l|^2$ in transmission. It is interesting to note that $\sum_l |\alpha_l|^2$ and $\sum_l = |\beta_l|^2$ are respectively the probability to be reflected and transmitted. The resulting structure is a presence of electron (resp. holes) above (resp. under) the Fermi sea, described by $\hat{\Gamma}_L$ and $\hat{\Lambda}_R$, which are respectively the reflected and transmitted scattered Floquet operators, defined in eq. 1.65.

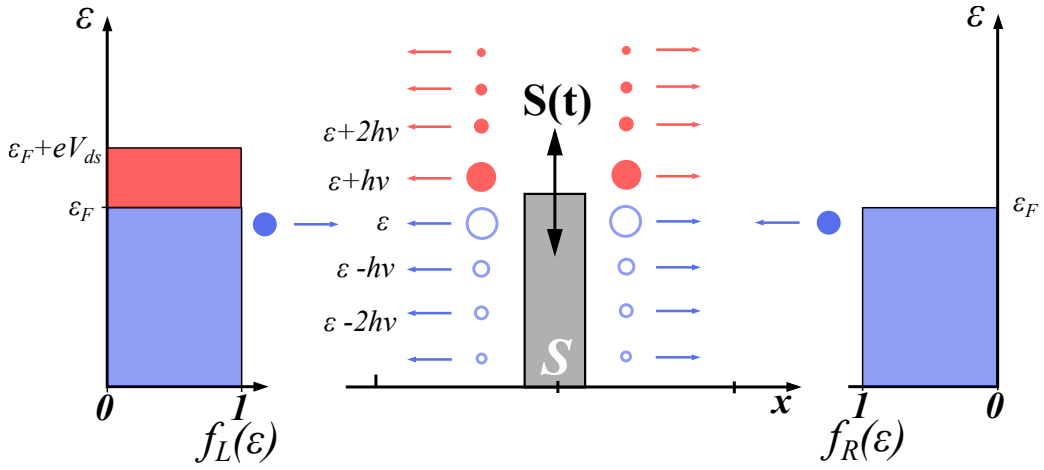

Figure 1.11: The transmission of the barrier of the QPC is time-dependent. Electrons from both reservoirs are scattered in Floquet states. A DC polarisation enables to probe the resulting entangled electron-holes excitations generated similarly to the PASN.

The current conservation implies that the number of electrons and holes generated are equal: no charges are created in the process. Similarly to the photo-assisted shot-noise presented in section 4.2, an additional DC-voltage to the left or right reservoir allows to probe the scattered state in energy. Indeed, electrons emitted at an energy $\varepsilon = \varepsilon_F + eV_{dc}$ have probability lower than one to be partitioned because a scattered electron has a probability to occupy this energy state (figure 1.11). Similarly to the PASN, we expect to observe abrupt changes in the slope of a DC shot-noise when scatterer is periodically modulated.

These definitions are easily extended to the 6-contacts geometry (figure 1.3). Coefficients of $\rho \longleftrightarrow \rho(t)$ and $\tau \longleftrightarrow \tau(t)$ are now time-dependent in the 6 matrix in eq. 1.19. Scattered Floquet operators are replaced by $\hat{\Gamma}_0$ and $\hat{\Lambda}_3$.

1.3.2 Current operator

2-contact geometry

The left current operator $\hat{\mathbf{I}}_L(x,t)$ is deduced from the definition eq. 1.3 using the Fermi operator in eq. 1.68:

$$\begin{aligned}\hat{\mathbf{I}}_L(x,t) = \frac{e}{h}\int d\varepsilon_1 d\varepsilon_2 \Big(& \hat{\mathbf{a}}_L^\dagger(\varepsilon_1)\hat{\mathbf{a}}_L(\varepsilon_2) - \hat{\Gamma}_L^\dagger(\varepsilon_1)\hat{\Gamma}_L(\varepsilon_2) - \hat{\Lambda}_R^\dagger(\varepsilon_1)\hat{\Lambda}_R(\varepsilon_2) \\ & - \hat{\Gamma}_L^\dagger(\varepsilon_1)\hat{\Lambda}_R(\varepsilon_2) - \hat{\Lambda}_R^\dagger(\varepsilon_1)\hat{\Gamma}_L(\varepsilon_2)\Big) e^{-i(\varepsilon_1-\varepsilon_2)(t-x/v_F)/\hbar}\end{aligned} \tag{1.69}$$

Only the three terms in the first line have a non-zero average. The calculation of $\langle\hat{\Gamma}_L^\dagger(\varepsilon_1)\hat{\Gamma}_L(\varepsilon_2)\rangle$ and $\langle\hat{\Lambda}_R^\dagger(\varepsilon_1)\hat{\Lambda}_R(\varepsilon_2)\rangle$ is similar to the expression in eq. 1.44. Finally, if a DC voltage polarisation V_{dc} is applied on R_L, the current $\hat{\mathbf{I}}_L(x,t)$ is:

$$\langle\hat{\mathbf{I}}_L(x,t)\rangle = \frac{2e^2}{h}|\tau(t)|^2 V_{dc} \tag{1.70}$$

The resulting current is the generalisation to a time-dependent transmission of the Landauer-Büttiker's law (eq. 1.12). Experimentally, we measure the time-average of $\tau(t)$: effect of the driven transmission on the conductance is simply the adiabatic modulation.

6-contact geometry

For the 6-contacts geometry, the incoming current $\hat{\mathbf{I}}_1$ on the contact 1 is:

$$\begin{aligned}\hat{\mathbf{I}}_1(x,t) = \frac{e}{h}\int d\varepsilon_1 d\varepsilon_2 \Big(& \hat{\mathbf{a}}_1^\dagger(\varepsilon_1)\hat{\mathbf{a}}_1(\varepsilon_2) - \hat{\Gamma}_3^\dagger(\varepsilon_1)\hat{\Gamma}_3(\varepsilon_2) - \hat{\Lambda}_1^\dagger(\varepsilon_1)\hat{\Lambda}_1(\varepsilon_2) \\ & - \hat{\Gamma}_3^\dagger(\varepsilon_1)\hat{\Lambda}_0(\varepsilon_2) - \hat{\Lambda}_0^\dagger(\varepsilon_1)\hat{\Gamma}_3(\varepsilon_2)\Big) e^{-i(\varepsilon_1-\varepsilon_2)(t-x/v_F)/\hbar}\end{aligned} \tag{1.71}$$

Currents $\hat{\mathbf{I}}_4$ is obtained by inverting index $0 \longleftrightarrow 3$. Resulting current is the also the extension of the eq. 1.28: $I_1(t) = \frac{e^2}{h}(V_1 - |\tau(t)|^2 V_0 - |\rho(t)|^2 V_3)$ and $I_4(t) = \frac{e^2}{h}(V_4 - |\tau(t)|^2 V_3 - |\rho(t)|^2 V_0)$.

1.3.3 Quantum switch noise

The calculation of noise is similar to the photo-assisted shot-noise. Starting from eq. 1.4 and using expression 1.71 of the current, we introduce, for the computation, the quantities

R_l and S_l defined as:

$$R_l = \nu \int_0^{1/\nu} dt\ e^{-2i\pi\nu lt} \rho(t)^2 \tag{1.72}$$

$$S_l = \nu \int_0^{1/\nu} dt\ e^{-2i\pi\nu lt} \rho(t)\tau(t) \tag{1.73}$$

which are the Fourier transform of $\rho^2(t)$ and $\rho(t)\tau(t)$. Using those definitions, the integrated form of quantum switch noise reads:

$$S_{I_L \times I_L} = 4\frac{2e^2}{h} \sum_{l=-\infty}^{\infty} |\delta_{l,0} - R_l|^2 \frac{lh\nu}{e^{\beta lh\nu} - 1} + \frac{|S_l|^2}{2} \left(\frac{lh\nu - eV_{dc}}{e^{\beta(lh\nu - eV_{dc})} - 1} + \frac{lh\nu + eV_{dc}}{e^{\beta(lh\nu + eV_{dc})} - 1} \right) \tag{1.74}$$

The first term, in the case of $l = 0$, can be understood as the thermal contribution. The term $|S_l|^2$ corresponds to the partitioning noise. The DC shot-noise formula in eq. 1.15 is easily recovered when $R_l = D \cdot \delta_{l,0}$ and $S_l = RD \cdot \delta_{l,0}$. Cross-correlation is $S_{I_L \times I_R} = -S_{I_L \times I_L}$.

Quantum switch in addition to a driven Fermi sea

The quantum switch theory can be extended to the case where the reservoir R_L is also simultaneously periodically driven as shown in the section 4.2. The Fermi operator $\hat{\mathbf{a}}_L$ in the expression of the current operator are replaced by the Floquet operator $\hat{\mathbf{A}}_L$ defined in eq. 1.43. A straightforward calculation gives the expression found in eq. 1.74, but the coefficients S_l read now:

$$S_l = \nu \int_0^{1/\nu} dt\ e^{-2i\pi\nu lt} \rho(t)\tau(t) e^{-i\phi(t)} \tag{1.75}$$

where the function $\phi(t)$ is the time-dependent phase of eq. 1.38 used in the Floquet formalism. The case of a pure PASN is easily recovered by taking $R_l = (1 - \tau^2)\delta_{l,0}$ and $S_l = |p_l|^2$.

A simple example: a sine modulation

We propose to illustrate the previous calculations by applying the formula 1.74 on a simple example, which has been studied in [133] using Full Counting Statistics (FCS) formalism.

We consider a sinusoidal time-evolution for the transmission and reflection coefficients [20]:

$$\rho(t) = \sin(\pi\nu t) \tag{1.76}$$

$$\tau(t) = \cos(\pi\nu t) \tag{1.77}$$

This is the simplest case for the calculation of Fourier coefficients R_l and S_l. We explicitly choose the frequency of $\rho(t)$ and $\tau(t)$ to be equal to $\nu/2$, therefore the coefficient $D(t) = |\tau(t)|^2$ is ν periodic[21] The unitary of the matrix is respected. In that case, Fourier coefficient R_l and S_l are equal to zero, except $R_0 = 1/2$, $R_{-1} = R_1 = 1/4$ and $S_{-1} = -S_1 = i/4$. The analytical expression of the noise is then:

$$\begin{aligned} S_{I_L \times I_L} = \frac{2e^2}{h}\Bigg[& k_B T + \frac{h\nu}{4}\coth\left(\frac{h\nu}{k_B T}\right) + \\ & \frac{h\nu + eV_{dc}}{8}\coth\left(\frac{h\nu + eV_{dc}}{2k_B T}\right) + \frac{h\nu - eV_{dc}}{8}\coth\left(\frac{h\nu - eV_{dc}}{2k_B T}\right)\Bigg] \end{aligned} \tag{1.78}$$

At low frequencies $\nu \longrightarrow 0$, we recover the expression of an time-averaged DC shot-noise whose transmission[22] is $D(t) = \cos^2(\pi\nu t)$. The interesting case of low temperatures ($T = 0$) and of an absence of polarisation ($V_{dc} = 0$) highlights the fundamental charge noise generated by the quantum switch:

$$S_{I_L \times I_L} = e^2\nu \tag{1.79}$$

This example shows that current fluctuations may be arbitrary large as ν is not bounded and are generated in a quantum conductor even at the equilibrium in the limit of $T = 0$.

The interpretation of this simple example can be understood in terms of electron-hole excitations, as proposed by Zhang and al. [133]. At each period, an entangled pair of a electron and a hole is created at energies respectively equal to $\pm h\nu$ around the Fermi sea and four equipossible cases can occurs: two cases where the electron and the hole move together to the right or to the left, and two cases where the electron and the hole go in opposite direction. The last situations generate the noise fluctuations: indeed, it is easy to show that at each period, the standard deviation of the charge is $\frac{1}{2}e^2$. Therefore, the

[20] Such time dependence of τ and ρ can be performed in principle but is an experimental challenge. More details are provided in chapter 2 and 5.

[21] In the experiments of the quantum switch presented in the chapter 5, we consider that the frequency ν is the frequency of the coefficient D that we experimentally measure.

[22] More precisely, at low frequency the noise becomes:

$$\begin{aligned} S_{I_L \times I_L} =& 4k_B T\frac{2e^2}{h}\left(\frac{3}{8} + \frac{1}{8}\frac{eV_{dc}}{2k_B T}\coth\left(\frac{eV_{dc}}{2k_B T}\right)\right) \\ =& 4k_B T\frac{2e^2}{h}\left(\overline{D(t)^2} + \overline{D(t)(1-D(t))}\frac{eV_{dc}}{2k_B T}\coth\left(\frac{eV_{dc}}{2k_B T}\right)\right) \end{aligned}$$

with $D(t) = \cos^2(\pi\nu t)$

current noise is simply e^2/h, by taking in account the factor 2 due to the spin degeneracy.

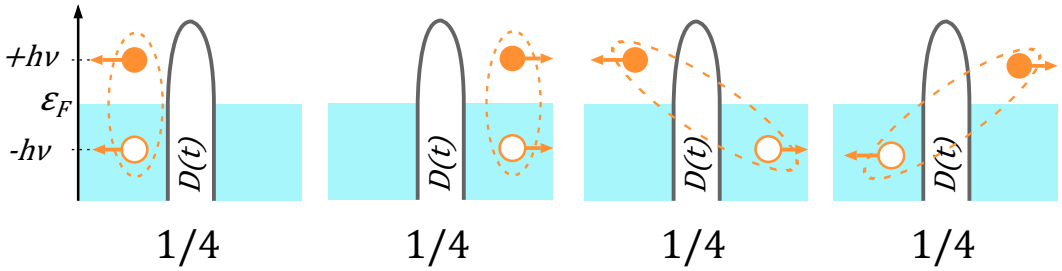

Figure 1.12: Four equipossible outcomes when $\tau(t) = \cos(\pi\nu t)$ and $\rho(t) = \sin(\pi\nu t)$ in terms of entangled pair of electron-hole. The two last cases generate current fluctuations.

1.3.4 Characteristic signatures of quantum switch noise

QS noise as a function of DC polarisation

The quantum switch as a function of DC polarisation is characterized by an additional offset in the noise level and abrupt changes in the slope at multiples of two quanta: $eV_{dc} = 2nh\nu$. It is illustrated for $V_{dc} = 0$ in the figure 1.13, left, that represents the QS noise deduced from eq. 1.74 as a function of the polarisation voltage for several frequencies. The corresponding transmission $|\tau(t)|^2$ used for the computation of Fourier coefficients R_l and S_l is represented by the blue curve in figure 1.13, right[23]. The adiabatic limit ($\nu \longrightarrow 0$) is represented by the dark blue curve and corresponds to a DC shot-noise with a modulated conductance. The offset is proportional to the frequency[24]. It is important to note that a current noise is generated even at the limit $T = 0$ in the absence of polarisation voltage.

Abrupt changes in the slope of the noise are clearly visible in the excess noise $\Delta S_I = S_I - S_I(\nu = 0)$, in figure 1.14. The slope changes every $eV_{dc}/h\nu = \pm 2n$. Odd values of l do not contribute to the noise[25] $R_{2l+1} = S_{2l+1} = 0$. The QS noise is displayed in figure 1.14 for several amplitude, A, which can be understood also as the velocity of switching. A "hard" transition between a closing (D=1) and an opened switch (D=0) generates more QS noise than a soft transition.

[23] Coefficient $\tau(t)$ is deduced from the saddle-point model of a QPC, explained in detail in chapter 2

[24] It is proportional in the limit $k_B T \ll h\nu$.

[25] $\rho^2(t)$ and $\tau(t)\rho(t)$ are periodic function with fundamental frequency 2ν. Thus, only even Fourier coefficients are not equal to zero.

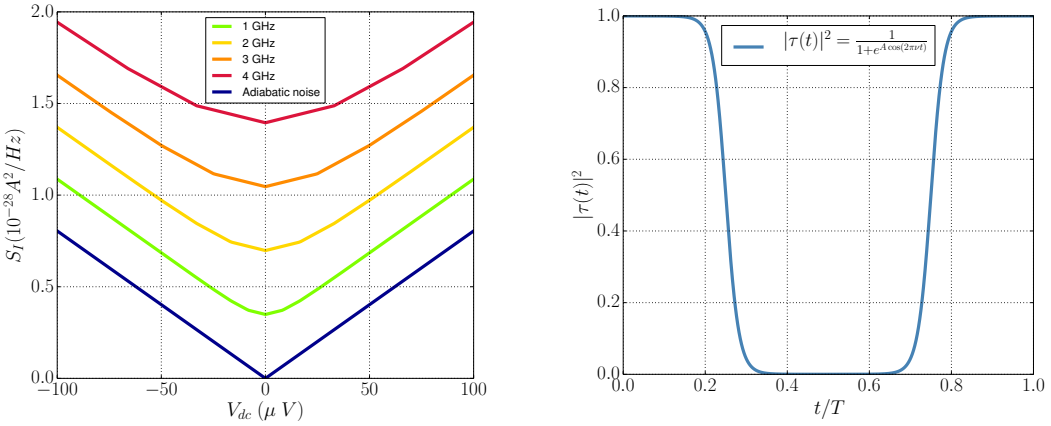

Figure 1.13: *(Left)* QS noise as a function of DC polarisation at several frequencies, in the limit $T = 0$. The blue curve is the adiabatic limit $\nu \longrightarrow 0$. Characteristic signatures of QS noise is the additional offset and abrupt changes in the slope every $eV_{dc} = 2nh\nu$. *(Right)* The transmission $|\tau(t)|^2 = 1/1 + e^{A\cos(2\pi\nu t)}$ versus time used for the QS noise computation. It is inspired from realistic transmission of QPC, modelled in [17]. Those simulations are displayed for an amplitude $A = 10$.

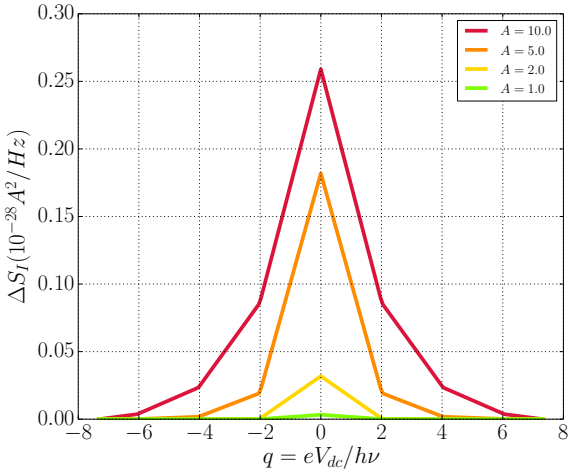

Figure 1.14: QS excess noise as a function of DC polarisation for several sweeping velocity A. QS excess noise is defined as the difference of QS noise and its adiabatic limit. It corresponds to the subtraction of the curves displayed in figure 1.13 from the blue curve. Offset generated by the QS is removed for a clear comparison.

Transmission shape dependence

Experimentally, it is interesting to perform the QS noise as a function of the mean transmission D_m, without polarisation voltage[26]. The mean transmission is defined as:

$$D_m = \nu \int_0^{1/\nu} dt \cdot |\tau(t)|^2 \tag{1.80}$$

[26] Advantages of this type of measurement are detailed in the chapter 5.

In the previous examples, the mean transmission was set to $D_m = 0.5$. We suppose here that a gate voltage denoted V_G[27] controls the transmission $D(V_G) = |\tau(V_G)|^2$. In order to generate QS noise, V_G is time dependent: $V_G(t) = V_0 + \Delta V \sin(2\pi\nu t)$. The DC voltage V_0 set the mean transmission D_m and the AC component ΔV makes the transmission time-dependent.

Examples of transmission shape versus V_G are displayed in figure 1.15, left. The green curve is deduced from the saddle point model of a QPC (presented in chapter 2). The yellow and red curves are more realistic and model respectively the 0.7 anomaly and Fabry-Perrot resonances (visible on realistic transmissions presented in chapter 3). The dashed lines are the corresponding mean transmission D_m, obtained from eq. 1.80 by using: $D(t) = D(V_G(t))$.

The QS noise is derived as a function of D_m for each transmission shape by computing the respective Fourier coefficients R_l and S_l, and displayed in the figure 1.15, right. The shape and the maximum value strongly depends on the shape of the transmission. In particular, the properties of symmetry regarding $D_m = 0.5$ are preserved in the noise, for instance in the case of the green and red curves. Conversely, the asymmetry of the yellow conductance is recovered in the corresponding QS noise. This property of symmetry will be useful for the experiment of QS performed in this thesis and allows us to discriminate the QS noise for other unwanted shot-noise.

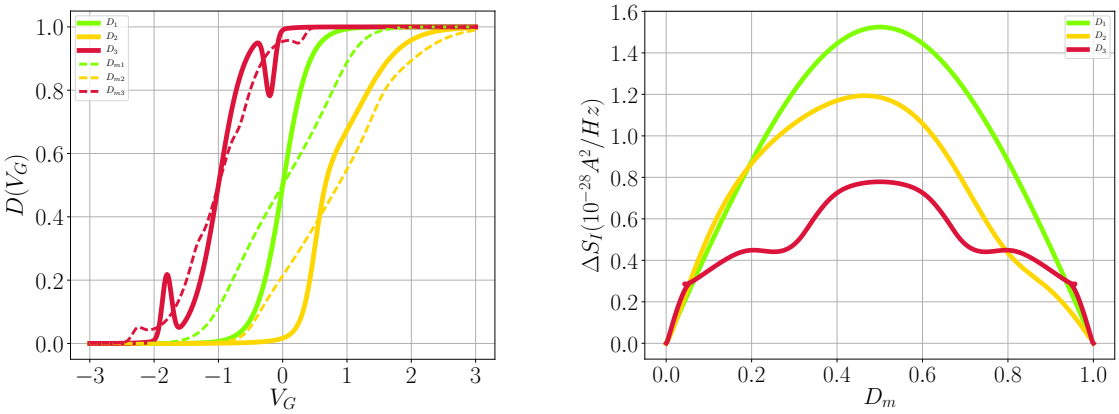

Figure 1.15: *(Left)* Model of experimental transmission as a function of the voltage V_G. Dashed lines represents the corresponding transmission with a sine modulation of V_G. (*Right*) QS noise generated in the limit $T = 0$ by the respective transmission in *(left)* as a function of D_m. The noise shape strongly depends on the transmission profile.

[27] The experimental implementation of a quantum conductor is review in the chapter 2.

1.3.5 Entanglement entropy measurement

The quantum switch problem has connections with more general physics, such as the quantum information [10] or quantum quenches[28, 30, 40]. Levitov and al. establish a direct relation between the QS noise and the entanglement entropy of the electrons in the quantum conductor[76]. Entanglement entropy describes the quantum correlation between separate part of a system. The QS problem can be described as follows: initially, the switch is opened ($D = 0$) and electrons are localized in each left and right reservoirs. Then, the switch is closed ($D = 1$) during a time w and electrons are delocalized in the full space of the quantum wire, generating entanglement between the left and the right part.

Repeating this process at a frequency ν leads to an entanglement entropy $\mathcal{S}_0$ per cycle[76, 8]. Using the Full Counting Statistic (FCS)[84], the entropy $\mathcal{S}_0$ reads[28]

$$\mathcal{S}_0 = \frac{k_B}{3} \log\left(\frac{\sin(\pi\nu w)}{\pi\nu t_0}\right) \tag{1.81}$$

where t_0 is the "cut-off" time needed to open or to close the switch. The current fluctuations through the quantum wire are connected to the entanglement entropy thanks to:

$$S_I = \frac{3e^2\nu}{k_B\pi^2}\mathcal{S}_0 = \frac{e^2\nu}{\pi^2} \log\left(\frac{\sin(\pi\nu w)}{\pi\nu t_0}\right) \tag{1.82}$$

It is interesting to compare this expression with the formula of the QS noise in eq. 1.74. The comparison between both expressions is made through numerical analysis displayed in figure 1.16. The time-dependence of the transmission used for the computation of eq. 1.74 is a square wave, with a width w and a short time cut-off $t_0 = 1/100\nu$. The figure 1.16 presents the QS noise found with the FCS (red curve) and the Landauer-Büttiker (green curve) approach, as a function of the ratio w/T, where $T = 1/\nu$. Unexpectedly, the QS noise using FCS approach is ~ 4 times lower.

[28] Fluctuations are Gaussian whereas the system switches from $D = 0$ to $D = 1$ and only the second moment, the current noise, matters.

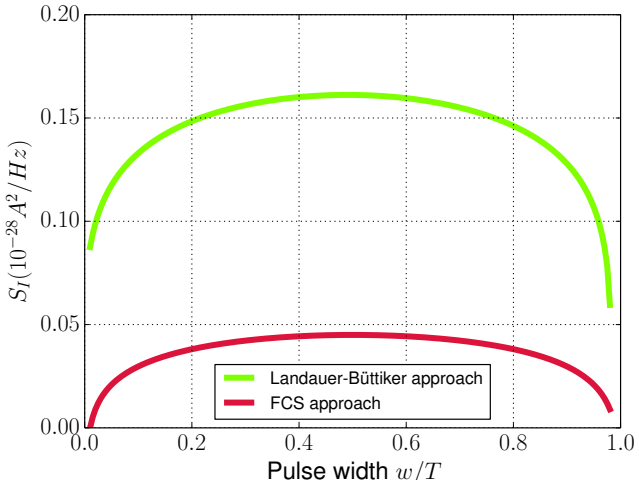

Figure 1.16: QS noise as a function of the pulse width ratio w/T deduced from the FCS (red curve) and the Landauer-Büttiker (green curve) approach. The transmission versus time is a square wave of period $T = 1/\nu$ with a width w. Parameters used are: $\nu = 500$ MHz, short-time cut-off $t_0 = 20$ ps and $T = 0$.

Conclusion

In this chapter, we provide the basic tools to understand the physics of AC transport in quantum conductors. The DC current and its fluctuations have been derived for two type of QPC geometries within the Landauer-Büttiker formalism. In addition, the Floquet scattering theory allows us to describe the properties of the charge injection in the quantum wire and of charge noise of a elementary switch. The experimental results presented in the chapter 4 and 5 will be compared to the expression of noise fluctuations for the photo-assisted shot-noise and the quantum switch noise, developed in this chapter. In the following, we propose to review the experimental implementation of quantum conductor through a QPC and how these objects are designed for our experiments.

Chapter 2

The Quantum Point Contact at GHz frequencies

The Photo-Assisted Shot Noise (PASN) and the Quantum Switch (QS) experiments are based on the Quantum Point Contact (QPC), an experimental device which implement a one-dimensional quantum conductor with a tunable barrier. A QPC is implemented from 2 Dimensional Electron Gases (2DEG) in a GaAs/AlGaAs heterostructure in which the coherence and ballistic lengths are large: the transport is ballistic and coherent, and is described by the Landauer-Büttiker formalism presented in the previous chapter. In order to create a one-dimensional quantum conductor in a 2DEG, one can use the edge channels of the quantum Hall effect. In an other way, the QPC takes advantage of the electrostatic potential of gates deposed on the GaAs surface whose the width is comparable to the Fermi wavelength[7]. It creates an electronic tunable potential barrier while the constriction confines electrons to a unidimensional motion.

Two QPCs have been made in the laboratory with electron gas grown at Cambridge university. These samples have been designed to be particularly suitable for our needs: the circuit is well-adapted for high frequency and the gate is design for the need of each experiment. This chapter presents first the two dimensional electron gas in an GaAs heterostructures and how QPC is made from a 2DEG. Then, we propose a simple model which describes the conductance shape as a function of the voltage gate for two different geometries of the gates. It allows to choose the relevant geometry for the PASN and the QS experiments. Finally, we present the improvements made in the fabrication of the 6-contacts QPC.

2.1 What is a Quantum Point Contact ?

In the previous chapter, we theoretically derived the DC and AC transport in ballistic coherent conductors. These systems are implemented in our experiments with 2 Dimensional Electron Gas (2DEG) where the electronic quantum coherence and the ballistic length are large enough for a fabrication with lithography processes. The main features of 2DEG are first presented and then we show how the 2-contacts and 6-contacts geometries for a QPC are realized from the 2DEG.

2.1.1 The 2-Dimensional Electron Gas (2DEG)

Experimental implementation

The two dimensional electron gas are artificial systems historically developed with the MOSFET (Metal Oxide Semiconductor Field Effect transistor) 50 years ago. More recently, Molecular Beam Epitaxy (MBE) machines allow the realization of high quality GaAs and $Ga_{1-x}Al_xAs$[1] heterostructures with long electron mean free path needed for the high speed electronics[90] and for quantum experiments. The samples used during this thesis have been made with the heterostructure presented in figure 2.1 (*Left*), from Cambridge University: 10 nm of GaAs, 40 nm of $Ga_{0.7}Al_{0.3}As$ doped with Silicon (n-doping), 40 nm of $Ga_{1-x}Al_xAs$ and GaAs.

In those heterostructures, the resulting energy of the conduction band as a function of the depth z is displayed in figure 2.1 with a schematic view of charge repartition in the layers[121, 122]. The main feature is the presence of a 300 meV triangular quantum well[15] at $z = 90$ nm, with a width of $l \simeq 5$ nm and quantized energy levels, separated by $\Delta E \simeq 20$ meV. The density n sets the Fermi energy ε_F between the two first energy levels such that at the limit $T = 0$, only the first energy level is occupied. An excitation energy $\Delta E - \varepsilon \simeq 10$ meV $\Leftrightarrow 100$ K is required for an electron to change its orbital: thus, at $T \ll 1$ K, the motion along z of electrons in the conduction band is completely frozen. Electrons at the interface of the heterostructure of $Ga_{0.7}Al_{0.3}As$/GaAs forms an effective 2DEG.

Quantum properties of 2DEG

The electronic quantum states in a 2DEG are well-described by a Fermi liquid. The quasi-particles near the Fermi sea behave as free particles of mass $m^* = 0.067m_e$, m_e being the electron mass in the vacuum. It is consistent with the hypothesis made in chapter 1 for the Landauer-Büttiker-Martin formalism.

[1] $Ga_{1-x}Al_xAs$ is an alloy where a ratio of x Ga atoms in the lattice are replaced by the same ratio of Al atoms.

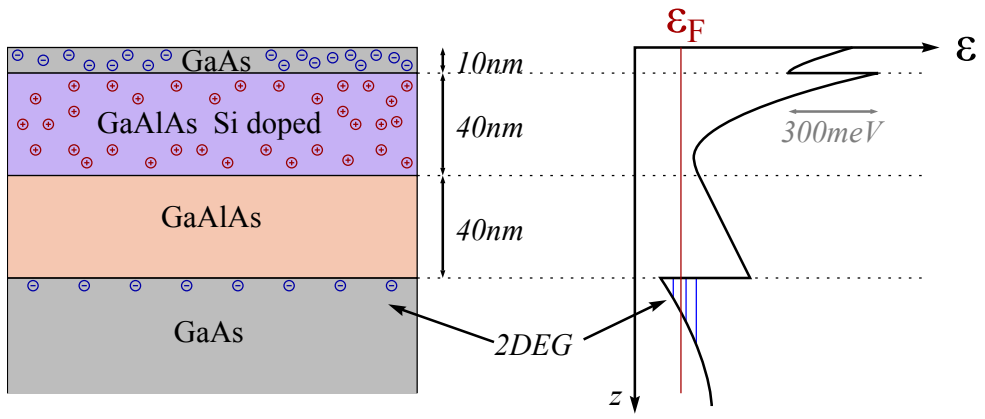

Figure 2.1: *(Left)* GaAlAs/AsGa heterostructure and charge repartition in the layers. *(Right)* Energy ε of the conduction band as a function of depth z. A 300 meV energy gaps appears at the interfaces of GaAlAs and GaAs whereas the electrostatic field resulting of the charge repartition creates a triangular quantum well between GaAlAs Si-doped and the GaAs substrate. The Fermi sea set above the first quantized energy level in the well: at low temperature, z motion of electron in the conduction band is frozen, making the 2DEG.

The Fermi energy $\varepsilon_F = \frac{\pi\hbar^2}{2m^*}n \simeq 6.5$ meV is large enough in comparison with the excitations applied in our experiments, which are typically $eV_{ds} \simeq h\nu \simeq 100\ \mu$V. Similarly, the velocity dispersion is negligible near the Fermi sea: the velocity of an electron at an energy 100 μV above the Fermi sea is only 0.6% faster[2] than the Fermi velocity v_F. It is consistent with the implicit assumptions made in the previous chapter for the computation of the noise.

Quantum coherence length: The size of the experimental devices for quantum experiments must be smaller than the coherence length of the wave function, or the quantum coherence length l_ϕ of the electrons in the 2DEG. At low temperature, the electron-phonon interaction vanishes and the decoherence is due to the thermal noise of the environment[116] which limits the life-time of quasi-particles to the characteristic time $\tau_\phi = l_\phi/v_F \simeq \frac{\hbar}{k_B T} \simeq 40\ \mu$m. It is larger than the typical size of our samples ($\sim$20 μm)[3].

[2] An electron with an energy $d\varepsilon$ above the Fermi sea has a velocity $v_F + dv$ where dv is: $dv/v_F = d\varepsilon/m^* v_F^2$.

[3] The decoherence due to electron-electrons collision limits the life-time of a quasi-particle of energy Δ to[52]:

$$\frac{1}{\tau_\phi} = \frac{\varepsilon_F}{4\pi\hbar}\left(\frac{\Delta}{\varepsilon_F}\right)^2\left(\log\left(\frac{\Delta}{\varepsilon_F}\right) - \log\left(\frac{2q_{TF}}{p_F}\right) - \log 2 - 1\right) \tag{2.1}$$

where $2q_{TF} = 2m^*e^2/\hbar^2$ is the Thomas-Fermi screening vector in 2D and $p_F = \sqrt{2m^*\varepsilon_F}/\hbar$ the Fermi momentum. In our sample, it leads to life-times of $\tau_\phi \simeq$1 ns, corresponding to coherence length of

In the integer quantum Hall effect regime, experiments performed in Mach-Zehnder interferometers reported coherence lengths of ~ 20 μm which decrease as $\propto 1/T$[107].

Ballistic length: The random distribution of the Si donors in the AsAlGa layer creates an additional random potential in the resulting electrostatic potential seen by an electron in the 2DEG[4]. In the case of a hard disorder, as represented in the figure 2.2, *(Left)*, the motion of an electron is diffusive. On the contrary, in the case of a weak disorder (figure 2.2 *(Right)*), the motion is ballistic on large distances. The mean distance travelled by electrons between two successive collisions is the ballistic length l_c: motion is ballistic (resp. diffusive) if the typical size of the sample is lower (resp. larger) than l_c. The ballistic length is related to the mobility[5] μ of electrons in the 2DEG:

$$\mu = \frac{el_c}{m^* v_F} \tag{2.2}$$

Nowadays, typical mobility is $\sim 10^6$ V^{-1}.cm^2.s^{-1} and can reach 10^7 V^{-1}.cm^2.s^{-1}[101]; in our case it is $\mu = 3 \cdot 10^6$ V^{-1}.cm^2.s^{-1} so the ballistic length is then $l_c \simeq 22$ μm, larger than the size of where the physics take place (~ 10 μm in our experiments) so that the transport is purely ballistic.

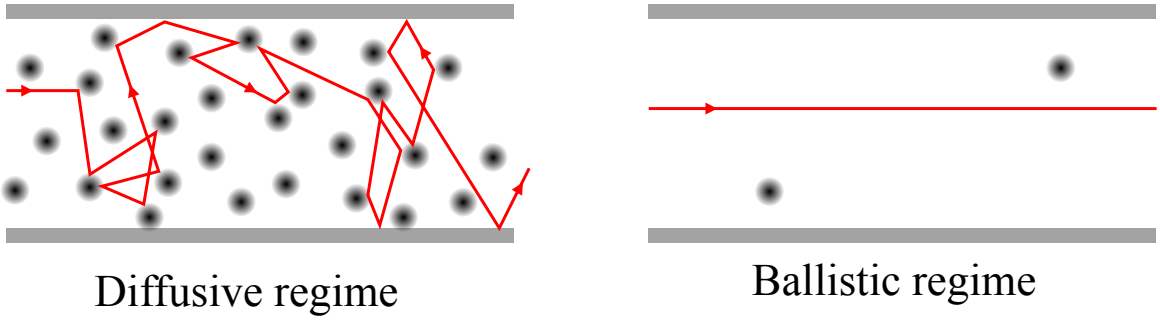

Figure 2.2: Schematic representation of trajectory for an electron in the diffusive regime *(Left)* and in the ballistic regime *(Right)*.

Note that the collisions are elastic and the quantum coherence is preserved even after several collisions: Webb and al. evidenced Aharonov-Bohm oscillations measured in a gold ring[130], showing that $l_\phi > l_c$. The mobility is related to the macroscopic resistance per square of the sample R_s. Using the same argument than in the Drüde model, one can

$\sim$200 μm, larger than observed.

[4]These fluctuations are softened by increasing the density or the distance between Si ions and the 2DEG

[5]For an charge submit to an electrical field $\vec{E}$ moving at the mean velocity $\langle\vec{v}\rangle$, the mobility is defined as $\vec{E} = \mu\langle\vec{v}\rangle$

find that R_s is related to the mobility μ and the electronic density n_s by :

$$R_s = \frac{1}{e\mu n_s} \tag{2.3}$$

The resistance per square R_s is $\sim$ 10 Ω for our samples. As a consequence, the Joule dissipation occurs (in the absence of magnetic field) when currents of few nA flow through the QPC.

2.1.2 QPC : A voltage constriction for a one dimensional channel with a tunable scatter.

How to make a QPC from a 2DEG? In the following, we review in detail the main elements of a QPC: the mesa, the ohmic contacts and the electrostatic gates represented on a schematic of the figure 2.3. We review the quantisation of conductance, evidenced by the tunable potential barrier in the 2DEG controlled by the gate voltage. Then, we detail the advantages of the 6-contacts QPC geometry presented in chapter 1 thanks to the chirality of edge channels in the quantum Hall effect.

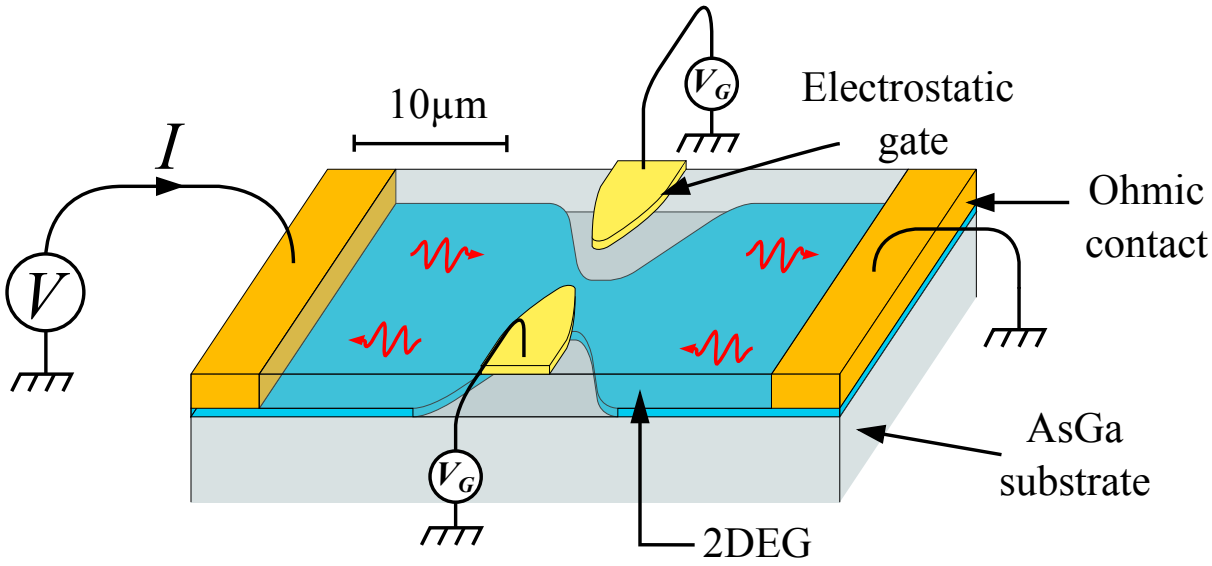

Figure 2.3: Schematic representation of a 2-contacts QPC. The 2DEG (in blue) is at $\sim$ 100 nm depth under the surface, in a restricted area called the mesa. It is electrically connected to an external circuit with ohmic contacts (in orange). Electrostatic gates (in yellow) tuned the transmission of electrons crossing the QPC with a negative voltage V_G. In the constriction, 2DEG can be considered as a quantum wire. Schematic is not on scale.

Mesa

The mesa is a spatially restricted area of the 2DEG. It has a hourglass shape which results of a large external size needed for the ohmic contact and a constriction in the central part, in order to limit the surface shared with the electrostatic gates. This constriction prevents from Schottky noise of the 2DEG electron tunnelling with the electrostatic gates through the AsGa. The name "mesa" comes from the geological term[6]: the mesa is fabricated by etching the unwanted area of AsGa with orthophosphoric acid, thus its transversal shape is similar to a geological mesa[97]. The etching must reach at least the depth of the 2DEG, 100 nm in our case, to ensure that there are no free-carriers outside of the mesa.

Its size is typically the ballistic length square, l_c^2. As mentioned in section 2.1.1, it is in our samples of the order of ~ 20 μm. This choice is justify by a compromise. A larger mesa increases the resistance per square and the collision rate with the disorder. A smaller mesa becomes harder to fabricate, in particular for the etching and the ohmic contact.

Ohmic contact

The electron gas is approximatively 100 nm under the surface of the AsGa heterostructure which is an insulator at low temperature: it is thus required to electrically connect the electron gas with a external circuit. A solution consists[7] in the diffusion of a conductor through the AsGa substrate at high temperatures, called an ohmic contact[14, 77], represented in orange in the figure 2.3. We use an alloy of Gold, Germanium and Nickel, which has a melting temperature around 450 °C, lower than these metals taken separately[8]. Fifteen minutes at 470 °C are enough to have a sufficient spreading and good electrical contact[58]. The resistance depends on the direction of the contact regarding the crystallographic axes[73, 55], therefore the ohmic contacts of our samples have a tooth shape, as shown in part 2.3.2. The typical resistance is $R_{CO} \simeq 100$ Ω at low temperatures, which is higher than the resistance per square of the mesa $R_s = 16$ Ω but negligible compared to the quantum of resistance $R_Q = \frac{h}{e^2} = 25812$ Ω.

Electrostatic gates

The electrostatic gates are metallic tips connected to an external voltage V_G deposed on the mesa. The typical size between the two gates is few hundreds of nanometres, usually 300 nm for a 100 nm deep 2DEG. A negative polarisation voltage creates an electrostatic potential for the electrons in the 2DEG, whom width is at the order of the Fermi lengh. It is the smallest element of the QPC and an electron-beam lithography is required for

[6] In geology, a mesa is an elevated area of land with a flat top and sides that are usually steep cliffs.

[7] Another possibility is to etch until the 2DEG depth and contact it with a metallic deposition without thermal diffusion.

[8] Melting point of gold and germanium are respectively 1064 and 938 °C.

the fabrication. All details about the shape, the potential created and the quantization of conductance are given in the section 2.2.

Conductance quantisation

A QPC is an experimental realization of the quantum wire described in chapter 1[127, 132]. In the constriction, the width of the electrostatic potential created by the gate voltage is of the order of the Fermi wavelength $\lambda_F = \sqrt{2\pi/n}$, so that the transversal motion of electrons is quantized by a discrete number of modes. Each mode is equivalent to an unidimensional wire of conductance $2e^2/h$. The number of modes is controlled by the height and the width of the potential barrier, through the gate voltage V_G. In the figure 2.3, QPC is polarised with a voltage V and the current flowing into it is denoted I. As explained in chapter 1, conductance of the QPC is then:

$$G = \frac{I}{V} = \frac{e^2}{h} D(V_G) = \frac{2e^2}{h} \sum_k |\tau_k(V_G)|^2 \tag{2.4}$$

where $|\tau_k(V_G)|^2$ is the transmission of the mode k. For each mode, $|\tau_k(V_G)|^2$ evolves from 0 to 1 successively with V_G. It manifests experimentally by the apparition of plateaus in the conductance curve. The figure 2.4 shows the experimental conductance $G = I/V$ as a function of V_G of a QPC[9]. The conductance increases by steps of $2e^2/h$ with V_G. Modes k of conductance $2e^2/h$ open successively while V_G increases.

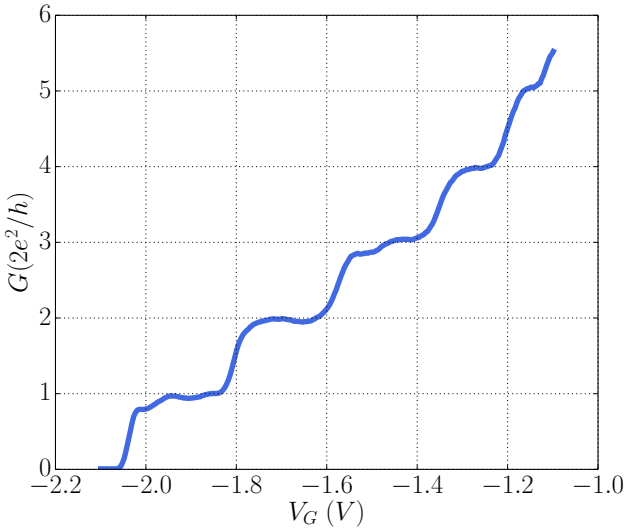

Figure 2.4: Experimental conductance of a 2-contacts QPC (sample 1) as a function of gate voltage V_G. The measurement is performed at 24 mK with no external magnetic field.

[9]The conductance curve presented in the figure 2.4 has been measured on sample 1.

QPC in the quantum Hall effect

As mentioned in the chapter 1, electrons follow unidimensional trajectories that fit closely the edges of the mesa in the quantum Hall effect. Therefore, the transport takes place in the edge channels, where the current is conserved [26, 59] and flows without dissipation[75]. A remarkable property is the chirality of edge channels, as illustrated in the figure 2.5. Incoming and outgoing electrons in each contact are spatially separated. The 6-contacts geometry presented in figure 2.5 and in chapter 1 is relevant for the measurements in the quantum hall effect regime. The voltage V_0 is applied on the contact 0, and measurement are performed through contact 4 and 1. Contacts 2 and 5 are connected to the ground. Then, relations between currents and voltages reads:

$$
\begin{aligned}
I_0 &= \frac{\nu e^2}{h} V_0 \\
I_1 &= \frac{e^2}{h}(\nu V_1 - T V_0) \\
I_2 &= -\frac{\nu e^2}{h} V_1 \\
I_3 &= 0 \\
I_4 &= \frac{e^2}{h}(\nu V_4 - R V_0) \\
I_5 &= -\frac{\nu e^2}{h} V_4
\end{aligned}
$$

where $R = \sum_k |\rho_k|^2$ and $T = \sum_k |\tau_k|^2$ are respectively the total reflection and transmission coefficients. The injected current I_0 does not depends on the voltages of other contacts and the voltages V_1 and V_4 are linear with respect of coefficients R and T, which make their calibration easier.

Moreover, edge channels in this configuration cancel correlations between contact 1 and 4. Consequently, the cross-correlation measurement $\langle I_1 I_4 \rangle$ is not sensitive to the measurement environment connected on contact 1 and 4. In particular, the cross-correlation measurement is not affected by the amplification chain. The noise calibration is also easier: the coefficient of conversion between current noise and voltage noise does not depends on the transmission, on the contrary of the 2-contacts geometry presented in figure 2.3. However, it is not possible to perform measurement with no magnetic field: in that case, contacts are short-circuited by the ground.

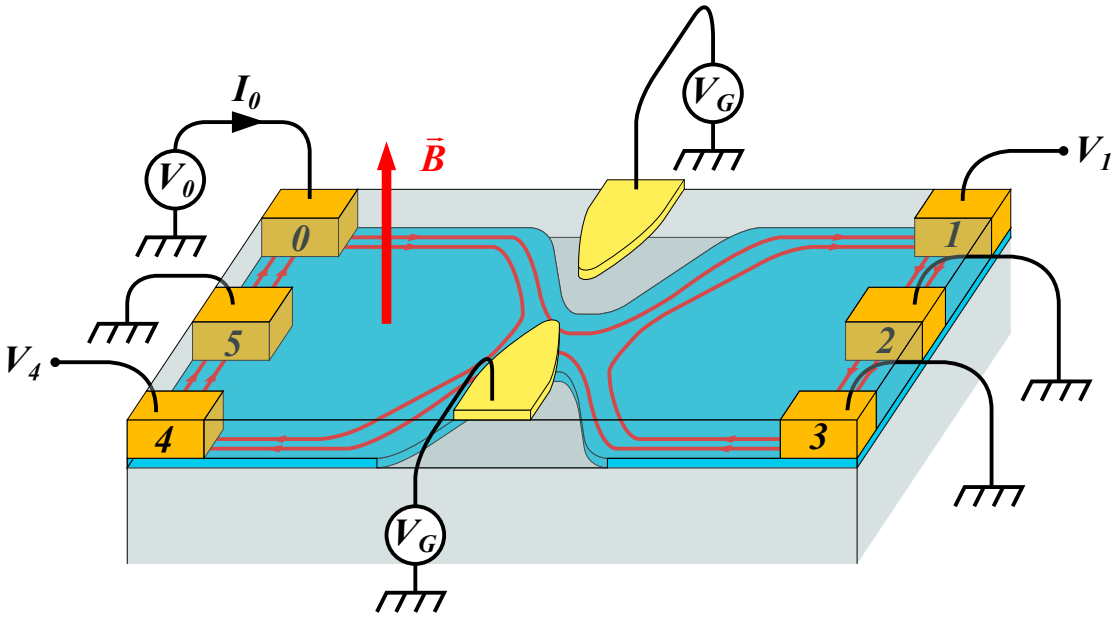

Figure 2.5: Schematic representation of a QPC under a magnetic field B with 6 ohmic contacts for quantum Hall effect for the filling factor $\nu = 2$. Edge channels are represented in red.

2.2 Electrostatic gates design

We present in this section the electrostatic gate conception. More precisely, we study the impact of the gate geometry on the curve of conductance as a function the gate voltage V_G, as shown previously in the example of the figure 2.4. It is important to decide which geometry is well adapted for the experiments performed in this thesis. For the PASN experiment the stability of the transmission is required, thus, the conductance must vary slowly with respect to V_G. On the contrary, the QS experiment requires an abrupt variation of conductance in order to close or open the switch (ie. to go from the transmission 0 to 1) with a small voltage amplitude ΔV, which reduces heating effects and increases the amount of the QS noise generated.

Two types of shapes for the gates are studied here: the sharp and the square shapes, respectively for the PASN and the QS experiments. We use a saddle-point model in order to predict qualitatively the conductance curve as a function of the gates voltage and thereby we justify the choice of the shape for each experiment. We compare the conductance deduced from this model with experimental data of two home-made QPC with sharp and square gate, whose a SEM picture is shown in the figure 2.6.

2.2.1 Electrostatic potential of the gates and saddle-point model

A negative voltage applied on the gates depletes the electronic density and creates a local potential constriction ϕ for the electrons in the 2DEG[134]. The resolution of Schrödinger's equation for an electron of the 2DEG in the potential $\phi(x, y)$ gives access to the properties of the QPC, such as the quantisation of conductance or the energy-dependence of the transmission. Here, we suppose that the plan of the 2DEG is (x, y) with x the main direction of propagation and y the main axes of the gates, transversal to the direction of propagation. The electrostatic potential $\phi(x, y)$ seen by the electrons can be computed by solving the Laplace's equation[33], but it is hard to explicit the boundary conditions of the problem[99] from the geometry of the gates shown in the figure 2.6. A self consistent treatment is required[118, 43] in order to take in account the screening effects in the 2DEG.

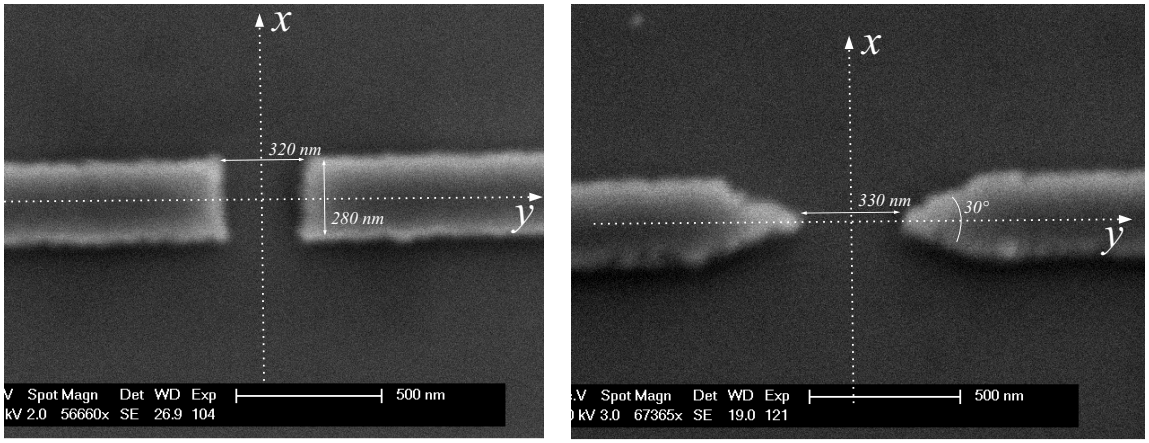

Figure 2.6: *(Left)* SEM picture of QPC with square gates. (*Right*) SEM picture of QPC with sharp gates.

We propose here to use the model proposed by Büttiker[17], describing the potential $\phi(x, y)$ near the bottleneck as a saddle point in order to justify qualitatively which shape is the well adapted for a given experiment. The transmission probabilities of crossing the potential wall along x is computed by solving Schrödinger's equation. For both geometries studied here, the potential near the centre $(x, y) = (0, 0)$ is a wall along the x direction and a well in the y direction, with a respective depth and height which depends on the voltage applied on the gate, V_G. This can be modelled by a quadratic potential:

$$\phi(x, y) = \phi_0 - \frac{1}{2}m^*\omega_x^2 x^2 + \frac{1}{2}m^*\omega_y^2 y^2 \tag{2.5}$$

The curvatures of the saddle are expressed in terms of an effective mass of electrons in the 2DEG $m^* = 0.067m_{e-}$, pulsations ω_x and ω_y and the height of the barrier ϕ_0. As we

focus only on energies close to the potential ϕ_0 at $(x, y) = (0, 0)$, high order terms are neglected. The typical width of the well is few hundreds of nanometres comparable to the Fermi wavelength $\lambda_f \simeq 50$nm, leading to a quantization of the momentum over y. As the transverse motion is frozen in that region, the QPC is considered as a unidimensional channel. For an electron moving in the x direction, the quadratic dependence of the potential gate is equivalent to an effective unidimensional potential $V_n(x)$:

$$V_n(x) = \phi_0 + \hbar\omega_y(n + 1/2) - 1/2m^*\omega_x^2 x^2, \tag{2.6}$$

with discrete levels, energetically spaced of $\hbar\omega_y$. Solving the Schrödinger's equation with potential in expression 2.5 [29, 78], conductance G through the barrier is given by:

$$G = \frac{e^2}{h}D = \frac{e^2}{h}\sum_n \frac{1}{1 + e^{-2\pi(\mu - \hbar\omega_y(n+1/2) - \phi_0)/\hbar\omega_x}} \tag{2.7}$$

where D is the transmission probability for an electron to cross the barrier and μ is the chemical potential of the reservoir of the incoming electrons. The sum operates on the total number of modes in the quantum well. The dependence on the gate voltage V_G is hidden in the parameters ϕ_0, ω_x and ω_y and not explicit in eq. 2.7.

In the case where $\omega_x \longrightarrow 0$, the effective width of the barrier diverges and the QPC becomes a perfect wave guide: the transmission of an incoming electron through the barrier is possible only if its energy E is exactly the energy of a level of the quantum well: $E = \hbar\omega_y(n + 1/2)$. For finite ω_x, the barrier can be crossed by electrons whose the incoming energy is in a narrow window around $\hbar\omega_y(n + 1/2)$: the transmission is smoothed. This has been verified in [65], where Iqbal and al. fabricated a QPC with a tunable potential ϕ thanks to six gates controlled independently in order to vary from 200 to 600 nm the effective length, which is proportional to the inverse of ω_x. Their measurements confirm that the transition between the plateaus of conductance becomes more abrupt when the effective length increase (ie. ω_x decreases). Zakka-Bajjani and al. [?] reported that a short QPC length (~ 80 μm) exhibits a smooth conductance curve. As a consequence, a square (resp. sharp) geometry is relevant for the QS experiment (resp. the PASN experiment).

2.2.2 Comparison with the experimental conductance

We compare here the experimental conductance of the QPCs whose the gates are shown in the figure 2.6: it confirms that the transmission is more abrupt for the square geometry than the sharp one. We also propose to derive an expression of the conductance deduced from the saddle-point model as a function of the gate voltage, in order to extract the

parameter of the potential $\phi(x, y)$. We assume the potential to be homothetic[10] with respect of V_G, $\phi(x, y) \propto -V_G$:

$$\phi(x, y) = -c_0 V_G - c_x V_G x^2 + c_y V_G y^2 \tag{2.8}$$

where c_x and c_y are the curvatures respectively in the x and y direction and c_0 the height of the barrier, at a given gate voltage V_G. These parameters are connected to ϕ_0, ω_x and ω_y of the saddle-point model through:

$$\omega_x = \sqrt{\frac{-2c_x V_G}{m^*}} = e_x \sqrt{-V_G} \tag{2.9}$$

$$\omega_y = \sqrt{\frac{-2c_y V_G}{m^*}} = e_y \sqrt{-V_G} \tag{2.10}$$

$$\phi_0 = -c_0 V_G = -e_0 V_G \tag{2.11}$$

where $e_x = \sqrt{2c_x/m^*}$, $e_y = \sqrt{2c_y/m^*}$, $e_0 = c_0$. We now have a direct formula of the conductance as a function of V_G and the parameters e_x, e_y and e_0 defined in 2.9, 2.10 and 2.11:

$$G(V_G) = \frac{e^2}{h} \sum_n \frac{1}{1 + e^{-2\pi \frac{\mu - \hbar(n+1/2)e_y\sqrt{-V_G} + e_0 V_G}{\hbar e_x \sqrt{-V_G}}}} \tag{2.12}$$

The figure 2.7, left, shows the measured conductance of the QPC with square gates. The measurement is performed at 25 mK, without magnetic field[11]. Similarly, the figure 2.7, right, is the measured conductance of the QPC with sharp gates (figure 2.6, right). The plateaus of quantisation clearly appears and the pinch-off voltages are ~ -0.43 V and ~ -0.65 V.

In addition, we attempt to fit those experimental conductance with the formula 2.12. The simulated conductance curves are displayed in the figures 2.7 and reproduce well the experimental data. The fitting parameters are reported in table 2.1. Note that this model does not take in account the 0.7 structure[125], visible on the conductance of the square gate.

A direct comparison between the two experimental curves evidences the difference between the two geometries. In the figure 2.8, we overlaid the experimental conductance thanks to a translation of the voltage gate V_G. The first transition is similar for square and

[10] The screening effects in the 2DEG are neglected.

[11] In QHE, conductance is computable with the saddle point model but its expression is different from formula 2.7 refbuttiker

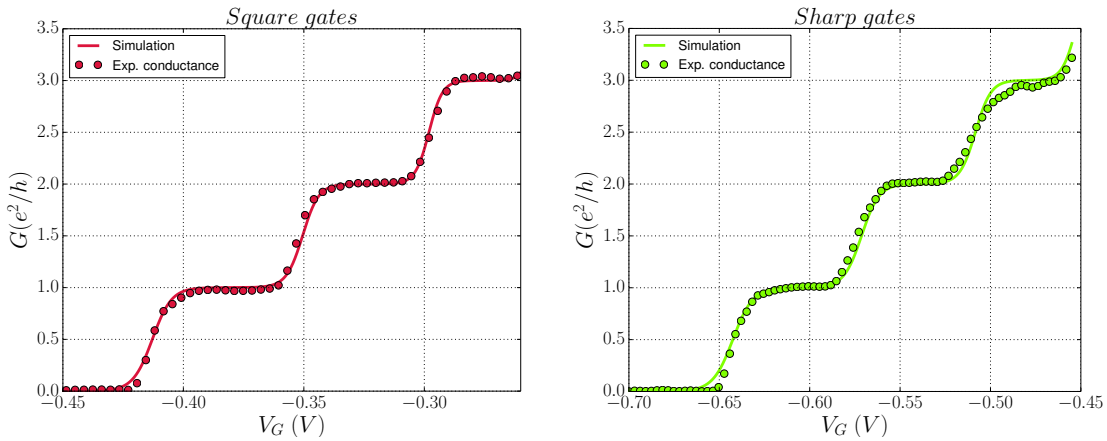

Figure 2.7: *(Left)* Experimental conductance of a QPC with square gates (red dots). The solid line represents the simulated conductance by using eq. 2.12 and the fitting parameters reported in the table 2.1. (*Right*) Same curves with sharp gates.

Experimental fit	$\hbar e_x$	$\hbar e_y$	e_0	μ
Square	1.63	4.41	40.1	18.0
Sharp	1.15	2.43	25.0	17.1

Table 2.1: Values in meV of fitting parameters e_x, e_y and e_0 for square and sharp gates, deduced from curves fitted presented in figure 2.7.

shape gates but the difference between two types of gate appears clearly for the following transitions: in square gates, the conductance is more abrupt than for the sharp gates.

The calculations in the quantum Hall effect are not presented here but described in [17]. In this regime, transmission behaviour includes the cyclotron pulsation $\omega_c = eB/m^*$ and radically differs from previous results only for strong magnetic fields. In that case, the transition is hard, with a very narrow voltage window, for both shape of gate. The choice of the shape must also considers the presence impurities in the experimental 2DEG, which are not taken in account in those calculations.

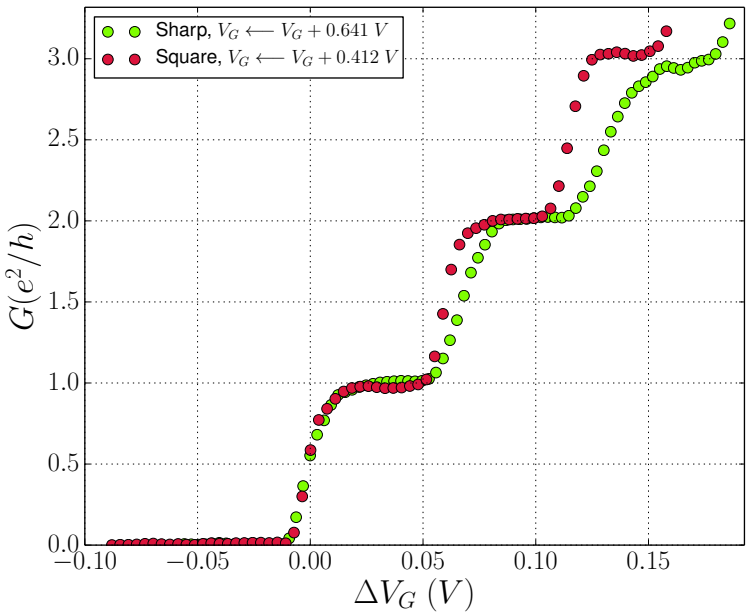

Figure 2.8: Experimental measurement of the conductance of QPC with square gate (red dots) and sharp gate (green dots), translated at 0 V in order to compare the transition between plateaus.

2.3 Sample design and fabrication

In this thesis, experiments have been performed thanks to two QPC: sample 1, made in the summer 2013 by Benoît Roche and sample 2 I made in spring 2015. The table 2.2 summarizes their characteristics. The fabrication and design of these samples have been realized entirely in our laboratory for both samples. These samples are designed in order to apply a GHz frequency on the voltage gate (resp. ohmic contacts) in the case on the QS experiment (resp. PASN experiment). We first present the sample 1 and then we describe the improvements done for the fabrication of sample 2.

Sample	1	2
Density (cm^{-2})	$1.7 \cdot 10^{11}$	$2.0 \cdot 10^{11}$
Mobility ($V^{-1}.cm^2.s^{-1}$)	$2.2 \cdot 10^6$	$3.1 \cdot 10^6$
Gates shape	Square	Square
Geometry	2 contacts	6 contacts

Table 2.2: Main features of sample 1 and sample 2.

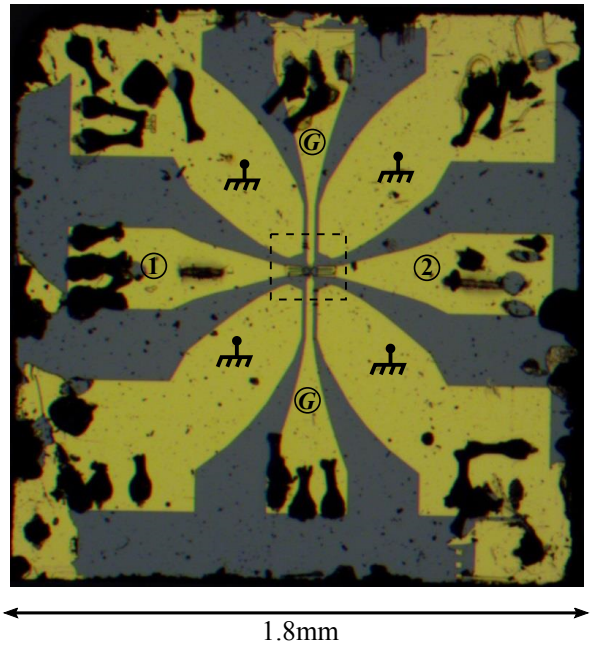

Figure 2.9: Optical image of the 2-contacts QPC sample 1. The coplanar waveguides indexed with 1 and 2 (resp. G) are connected to the two ohmic contacts (resp. to the gates) and are surrounded by ground planes. Black stains in the edge are due to aluminium micro-bounding. Dashed square correspond to the size of the SEM image in figure 2.10.

2.3.1 2-contacts QPC: sample 1

The sample 1 is a 2-contacts QPC used for the measurements of QS without magnetic field[12]. The GaAs wafer has been provided by David Richie and Ian Farrer from Cambridge University. It has a density of $n = 1.7 \cdot 10^{11}\text{cm}^{-2}$ and a mobility of $\mu = 2.2 \cdot 10^{6}\text{V}^{-1}.\text{cm}^{2}.\text{s}^{-1}$. The figure 2.9 shows the circuit of the sample. The potential of the gate is applied on the ports denoted by "**G**" and the 2 ohmic contacts are connected through the ports **1** and **2**. The circuit is made of 100 nm gold evaporated on the substrate. All lines are surrounded by ground planes which form coplanar waveguides that enable a good transmission of the RF voltages from the port to the QPC. More technical details about the propagation of RF voltages on the sample can be founded in the phD thesis of Julie Dubois [38]. The hourglass shape of the mesa and the square gates of sample 1 are clearly visible on the figure 2.10.

The results of the QS experiment that will be presented in the chapter 5 highlight two main misconceptions of this sample. Firstly, the proximity between the mesa and the gates creates a capacitive coupling, inducing AC parasitic currents heating the 2DEG.

[12]The presence of a magnetic field does not change the measurement but this 2-contacts geometry not allow to get benefit of the spatial decoupling of edge channels.

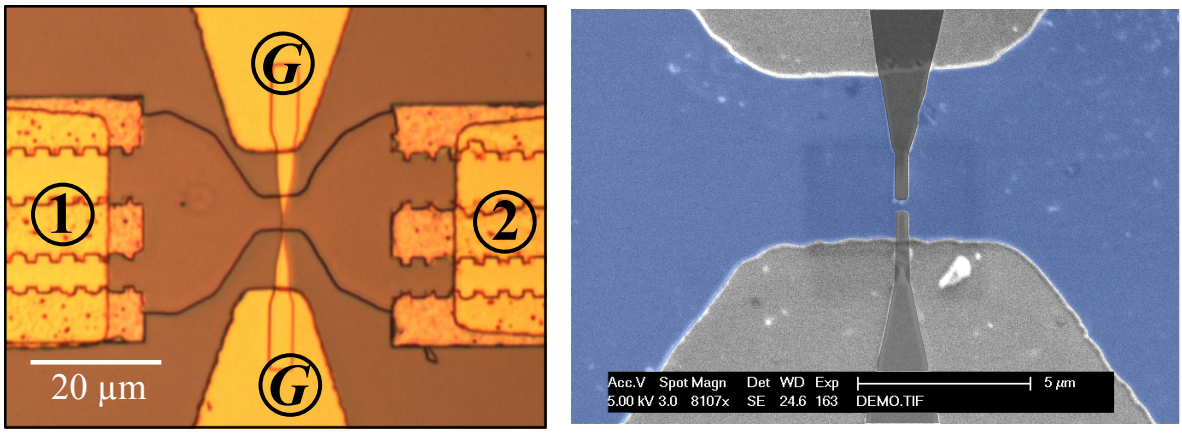

Figure 2.10: *(Left)* Optical picture of the mesa of sample sample 1, recognizable with its hourglass shape presented in figure 2.3. The coplanar waveguides indexed by 1 and 2 (resp. G) are connected to the two ohmic contacts (resp. to the gate). (*Right*) SEM picture with artificial colors of the gates of sample 1.

Those effects are enhanced by the wide size of the gate on the mesa and the absence of ground planes near the mesa. Secondly, the asymmetry of the gate regarding the mesa, which is clearly visible on the figure 2.10, left, generates additional parasitic AC drain-source voltages adding an unwanted noise. Those unwanted effects are studied in details in chapter 5 and lead us to improve the 6-contacts samples presented in the following.

2.3.2 6-contacts QPC for quantum Hall effect: Sample 2

The sample 2 is a 6-contacts QPC designed for both PASN and QS experiments in the quantum Hall effect regime and is improved in order to prevent the issues in the QS experiments. The figures 2.11, 2.12 and 2.13 show respectively the circuit, the mesa and the gates of the sample. The GaAS wafer also comes from the same team of Cambridge University, with a density of $n = 2.0{\cdot}10^{11}\text{cm}^{-2}$ and the mobility is $\mu = 3.1{\cdot}10^{6}\text{V}^{-1}.\text{cm}^{2}.\text{s}^{-1}$. The circuitry design is inspired by sample 1 for the waveguide geometry and is adapted to a 6 contact geometry for quantum Hall effect, shown in figure 2.5. It has also two main improvements near the mesa in order to reduce the effects of the capacitive coupling between the 2DEG and the gates.

Geometry design

The sample 2 is used for both QS and PASN experiments. Consequently, the ohmic contacts and the gates must be connected to coplanar waveguides for a good transmission of the RF voltages. The circuit shown in the figure 2.11 is designed in order to be the most symmetric so that the resulting shape has an octagonal symmetry, where the lines connected to the QPC are equivalent regarding the RF propagation. The exponential shape for the size reduction from 300 μm to 20 μm and the width ratio of the coplanar

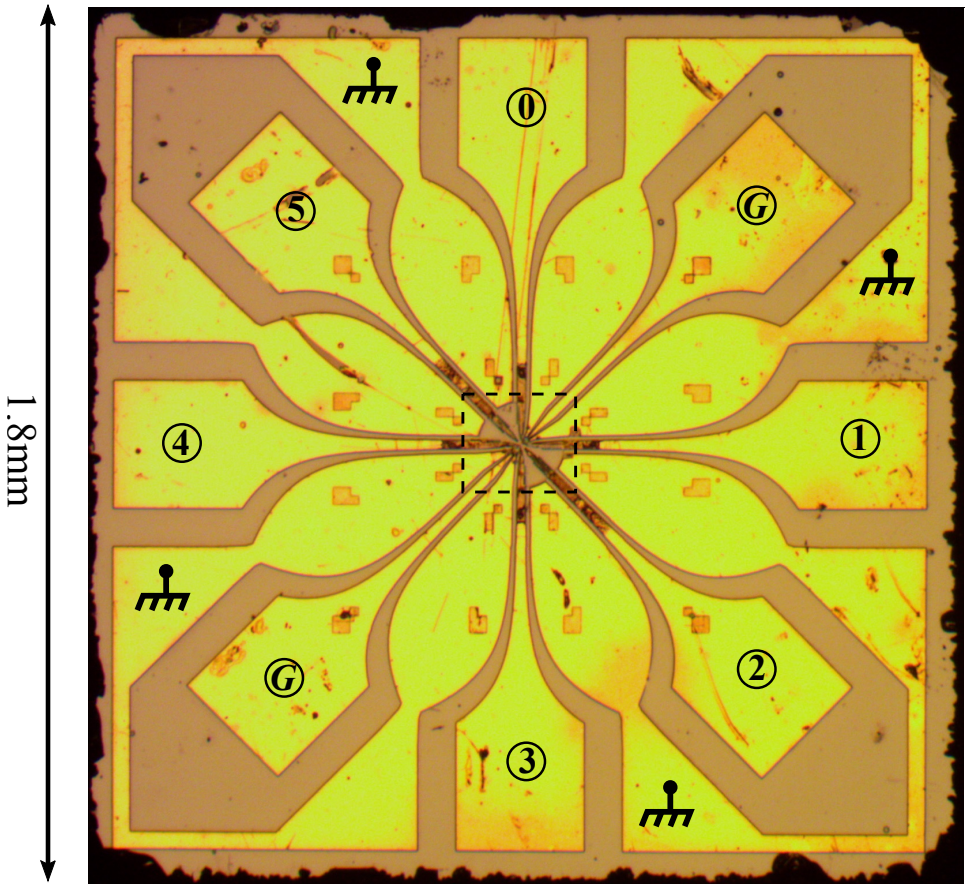

Figure 2.11: Optical image of sample 2. Lines from 0 to 6 are connected to the 6 ohmic contacts. Lines "G" are connected to the gates. The dashed square corresponds to the size of the SEM image in figure 2.12.

waveguides is inspired from those designed by Julie Dubois[38] in order to have a 50 Ω impedance matching.

The size of the mesa (figure 2.12) is larger than in the case of the sample sample 1 in order to minimize the ohmic contact resistance. The capacitive coupling between the gate and the mesa is reduced in comparison with sample 1, thanks to the extension of the ground planes around the gate lines until the mesa and the limited width of the gate to 300 nm on the mesa. Those improvements are visible on the figure 2.13.

Fabrication

For the 2-contacts samples like sample 1, the symmetry of the gates regarding the mesa is limited by the alignment accuracy between the circuit and the mesa, shown in the figure 2.10. Indeed, the fabrication of those elements is based on an optical lithography using a photomask whose alignment markers are far from the center; thus the resolution is limited to few microns[13]. Moreover, the asymmetry visible in the figure 2.10 results of the absence

[13]Using the wafer mask aligner of our clean room.

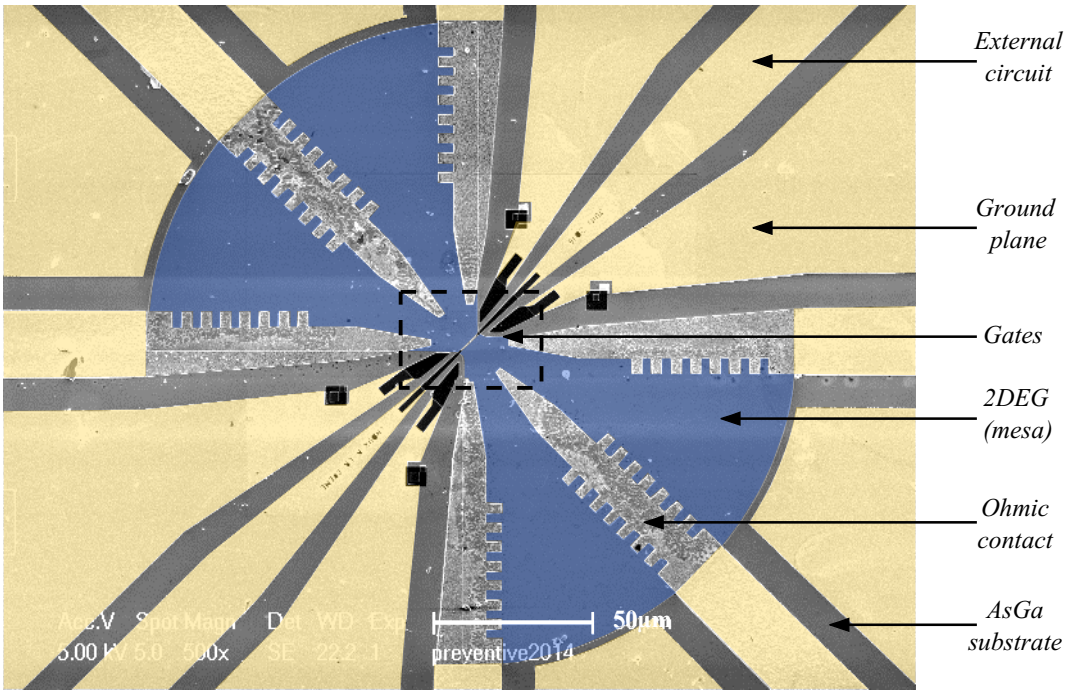

Figure 2.12: SEM image of the mesa of sample 2 with artificial colors. Blue corresponds to the 2DEG (mesa), the black to the gates (in aluminium) and the gold to the circuit in gold. Dashed square correspond to the size of the SEM image in figure 2.13.

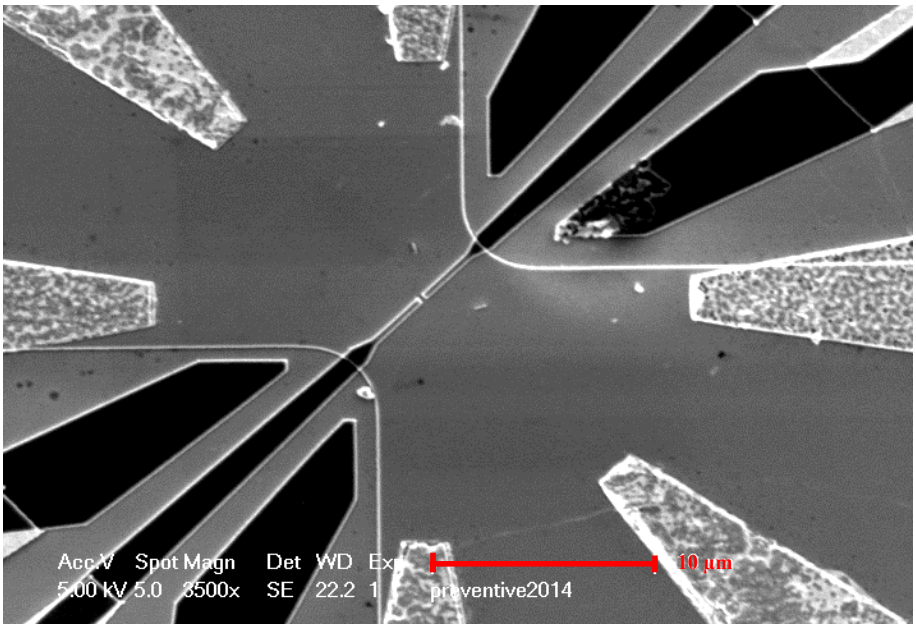

Figure 2.13: SEM image of the gates of sample 2. Black color correspond to aluminium. 300×300 nm square shape of the gate is visible.

of markers at the QPC scale near the mesa making the alignment of the gates smallest part (300 nm) hard.

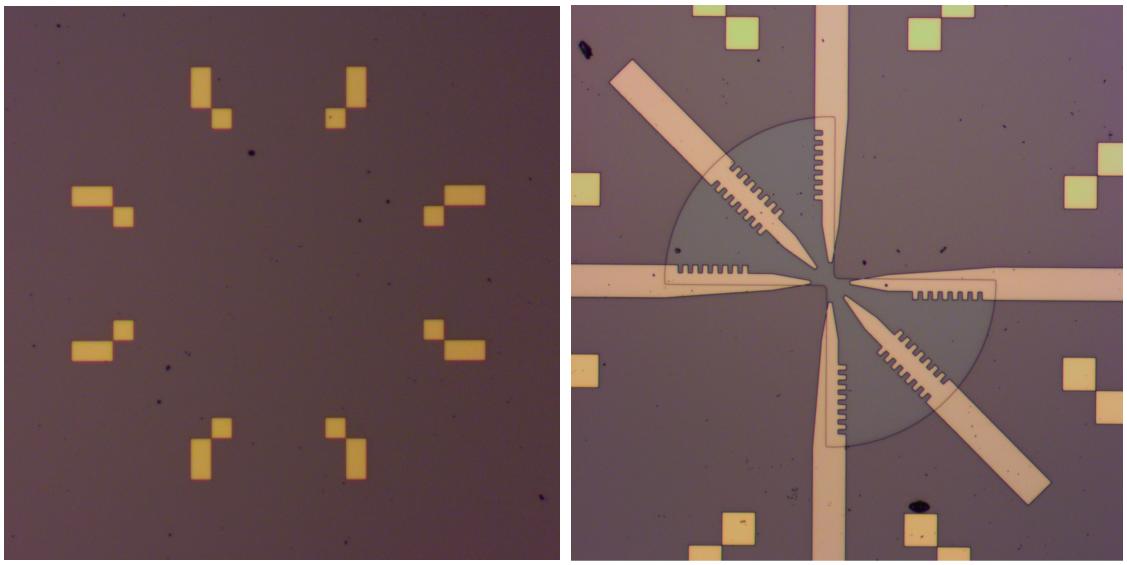

Figure 2.14: *(Left)* Optical picture of the alignment markers of sample sample 1. It is the first step for the fabrication of the 6-contacts geometry entirely made by electron beam lithography. The size of the picture is 500 μm. (*Right*) Optical picture of the same sample after the mesa etching and the ohmic contact deposition. Note that the position of these elements is highly symmetric.

The improvement of the 6-contacts QPC fabrication consists in using an electron beam lithography for all steps during the process, which is slower than the optical lithography but more accurate. The first step is to draw alignments markers on the substrate as shown in the figure 2.14, left. Then, the mesa is etched and ohmic contacts are deposed with a remarkable accuracy regarding themselves (figure 2.14, right). There are two steps of fabrication for the circuit: one at large scale with a rough resolution (>2 μm) and another around the mesa in order to place 10×10 μm markers[14] closed to the QPC. Finally, thanks to these markers, the accuracy of the position of the gates (in black in the figure 2.13) is better than in the case of the 2-contacts samples.

[14]Those markers are the four black squares near the gate line and are visible in the figure 2.12

2.4 Conclusion

Quantum experiment in one dimension theoretically studied in chapter 1 can be implemented by using a QPC. Indeed, quasi-particles in 2DEG behave like free fermions with a ballistic motion and their quantum coherence is preserved over large distances. Electrostatic gates deposed on a constriction in the shape of the 2DEG create a unidimensional motion with a potential barrier playing the role of the scatter. Electrostatic simulation of the gate and a model for the conductance gives a qualitative argument to choose the relevant shape: For the PASN experiment, sharp gate are relevant whereas for the QS experiment, we will use square gates. Finally, sample are designed to apply high frequency on the QPC with a coplanar waveguide design, for experiment without magnetic field or in quantum Hall effect.

Chapter 3

Experimental set-up

The measure of extremely low current fluctuations has been the central part of the experimental work of this thesis. We present here our experimental set-up devoted to noise measurements at low temperatures under high magnetic fields while RF voltages are applied on the samples. The measurements are performed in a helium-free cryostat designed by Cryoconcept with a 14 T magnet.

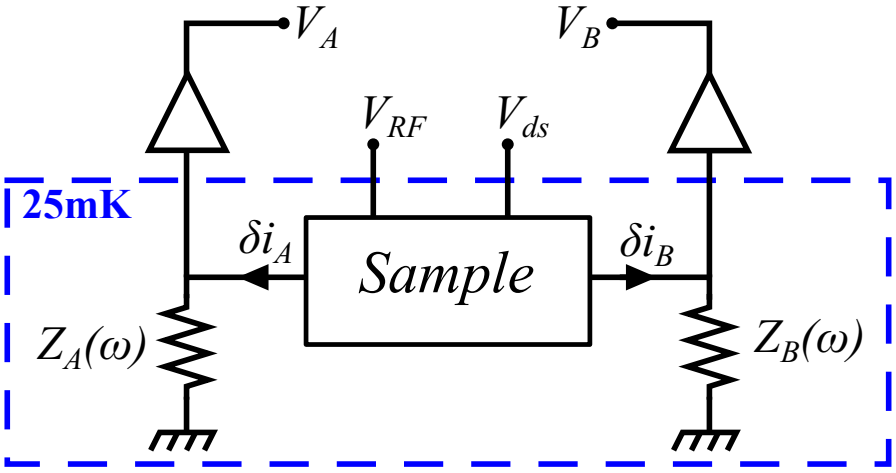

Figure 3.1: Principle of current noise measurement at low temperature. Currents fluctuations δi_A^2 and δi_B^2 emitted are independently collected by two channels A and B. RLC circuits $Z_A(\omega)$ and $Z_B(\omega)$ whose resonant frequency is ~ 2 MHz convert current fluctuations into voltage fluctuations. Auto and cross-correlations of voltages V_A and V_B are computed thanks to a digitizer of the PC. From these, an appropriate calibration of the measurement lines presented in section 3.16 allows to recover the current fluctuations emitted by the sample. Our set-up also enables to apply DC and RF voltages.

The measurement principle is described on figure 3.1, in the general case of the Photo-Assisted Shot-Noise (PASN) and the Quantum Switch (QS) experiments. Noise measurements are realized thanks to two independent channels denoted A and B. Current fluctuations δi_A and δi_B measured by channels A and B generated by the sample are converted into voltage fluctuations through the RLC resonators of impedance $Z_A(\omega)$ and

$Z_B(\omega)$, whose resonant frequency is $\sim$ 2 MHz. Both signals are amplified by amplifiers on the 4K stage and at room temperature. A digitizer performs real time measurements of voltage fluctuations V_A and V_B. They are sent to a computer which calculates the auto and cross-correlations of channels A and B. An appropriate calibration allows to recover the current noise S_I emitted by the sample from the voltages recorded.

The cross-correlation measurements of current fluctuations emitted by electronic devices at low temperatures and at the MHz regime presents several advantages. First, the $1/f$ noise generated by the amplification chain and the environment background is negligible at these frequencies[35]. Secondly, the cross-correlation directly cancels[54] the intrinsic noise of amplification chain and reduces the standard deviation by a factor $\sqrt{2}$[88]. Finally, our set-up reaches a resolution of $5 \cdot 10^{-30}$ A^2/Hz in 5 minutes approximatively in high magnetic fields for an electronic temperature of 40 mK. Many technical aspects of low-noise measurements are detailed in [53, 98].

This chapter is organized as follows. In the first section, we describe the experimental set-up for the PASN and the QS experiments in detail. Then, we focus on the description of the measurement lines (RLC, amplifiers) and of the injection line (DC and RF voltage line). The data acquisition and the improvement made in this thesis in order to increase the resolution of the noise measurement are presented in the third part . The last part is devoted to the calibration of the conductance of a QPC and the current noise.

3.1 Set-up for PASN and QS experiments

The experimental set-up is composed of two main parts: the measurement lines (section 3.2) composed of RLC impedances, the amplification chain and DC wires which are identical for both PASN and QS experiments, and the injection lines (section 3.3) composed of DC and high frequency coaxial wire in order to apply DC or RF voltages on the samples. The technical aspects about the cryostat and the thermalisation of DC and RF lines are detailed in the appendix B. We present here an overview of the set-up for the PASN and the QS experiments.

3.1.1 PASN experiment

The figure 3.2 presents a schematic of the PASN experiment. The aim is to measure the current noise of the sample 2 described in chapter 2, while voltages at GHz frequency (or RF voltages) are applied on an ohmic contact. The sample is cooled down at 25 mK in a Helium-free dilution cryostat while a 14 T superconducting coil apply a perpendicular magnetic field.

The voltage injection line is composed of two parts: DC lines for the DC voltages, V_{dc}, and RF lines[1] for GHz voltages denoted by V_{RF}. A voltage divider of ratio 1/1000 set on the 100 mK stage allows to apply DC voltages with a high accuracy ($\sim \mu$V) with no heating in the mixing chamber (on the 25 mK stage). For the PASN experiment, there is a unique RF line with three 20 dBm attenuators on the 3.6 K, 1 K and 100 mK stages in order to reduce the thermal noise coming from the 300 K environment. The 60 dBm total attenuation divides V_{RF} by a factor 1000, larger in practical because of intrinsic loss of the RF lines. The voltage source can deliver 2 V until 40 GHz, which is enough to reach at least ~ 120 μV effectively applied on the contact of the sample. In addition, a bias-tee at 25 mK adds the DC voltage V_{dc}.

The measurement is performed over two independent channels A and B, composed by two RLC resonators Z_A and Z_B and home-made cryogenic amplifiers on the 3.6 K stage and commercial amplifiers at room temperature. The voltage source V_{pol} with the 2 kΩ resistor provides the power required for the cryogenic amplifiers.

3.1.2 QS experiment

The figure 3.3 describes the main features of the QS experiment. In that case, the goal is to measure current noise generated by the high frequency voltage applied on the gates of the sample 1, described in chapter 2.

[1] In the following, RF means "radio frequencies" and refers to high frequency, in our case, frequencies above 1 GHz.

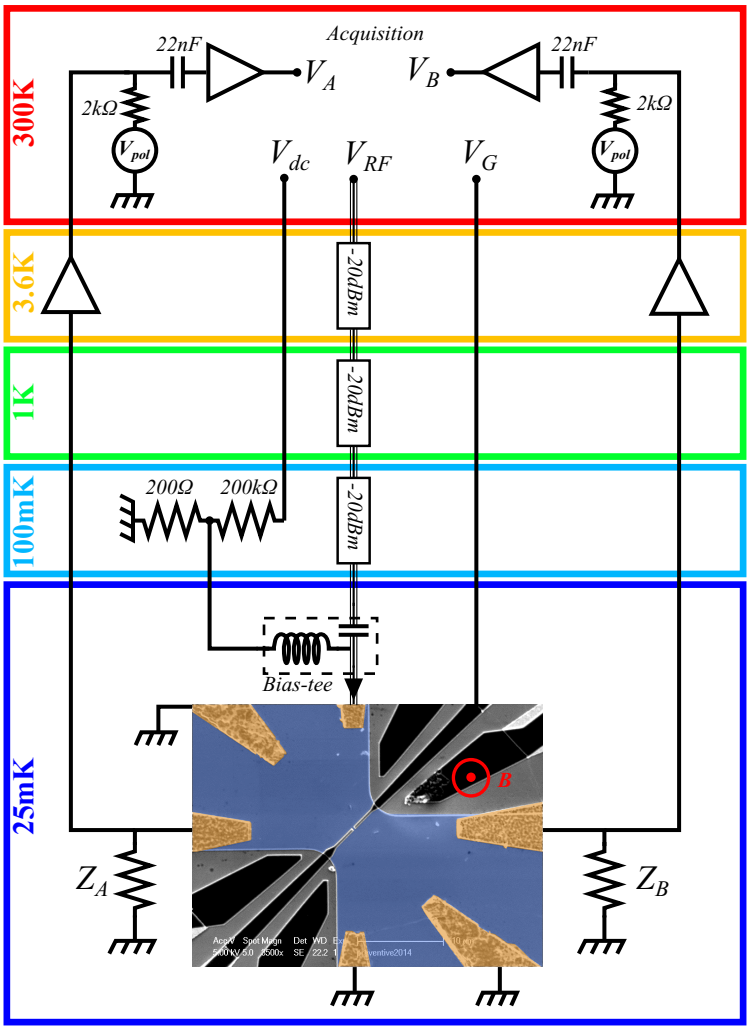

Figure 3.2: Schematic set-up of the PASN experiment. A unique high frequency line (highlight black line) is connected to the injection ohmic contact. The sample is represented by a electronic microscope image of the QPC with artificial colors : the 2DEG is in blue, ohmic contact in orange and gates in black.

The set-up is similar to the PASN experiment. The 2-contacts geometry of the sample allows us to perform the experiment either with no magnetic field or in the QHE regime. The DC-voltage line for the sample polarisation is connected to the sample through impedance Z_A. The main difference from the PASN set-up is that the gate voltage is provided through two independent RF lines in order to control its phase and amplitude with accuracy. The total attenuation is 23 dBm for each high frequency line, which is large enough to reduce the thermal noise brought from the external environmental: the transmission of the QPC is not affected for variations of gate voltage lower than 0.1 mV. Two bias-tee at 25 mK add high frequency to DC voltages for each gate. The measurement set-up is identical to the PASN experiment.

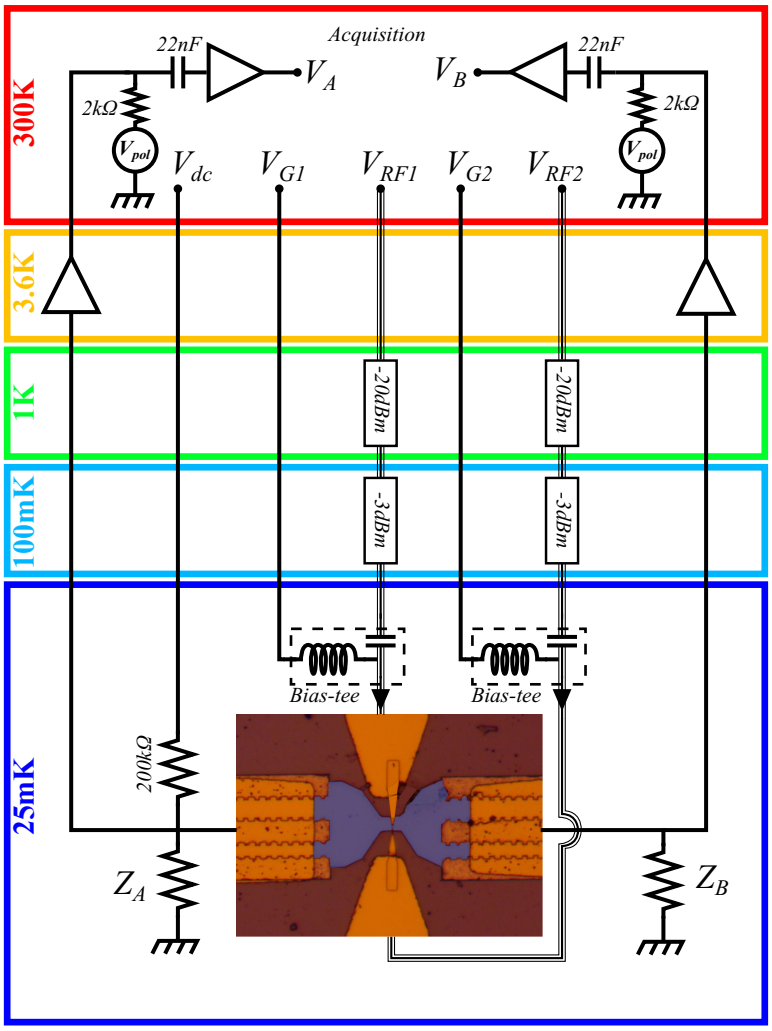

Figure 3.3: Schematic set-up of the QS experiment. In this experiment, there are two independent high frequency lines (highlight black lines) connected to the two gates. Measurement lines are identical to the PASN experiment. The sample is represented by an optical picture of the QPC. The artificial blue color correspond to the 2DEG, the upper and lower triangular yellow shape to the gates and the toothed yellow shape on the left and the right is the ohmic contact.

3.2 Measurement lines

In this part, we describe the measurement lines composed of the RLC resonators Z_A and Z_B and the amplifiers used for both the PASN and QS experiments. These elements are connected with DC wires presented in section 3.3.

3.2.1 RLC resonators

The impedances Z_A and Z_B in figures 3.2 and 3.3 are passive RLC resonators fully described in the figure 3.4. The goal of these resonators is to convert the currents I_A and

I_B coming from the sample into voltages[2] V_A and V_B in the MHz range, as proposed in [35]. In order to maximize the cross-correlation signal, the matching between the two impedances over the frequency must be as large as possible[3], in the ideal case $Z_A = Z_B$. As the linear capacitance of the wire is comparable to the capacitance of the RLC circuit, the length of the wires and the thermalisation lines must be chosen carefully. In our case, the two resonators have a close resonant frequency $f_{0,A} = 1.85$ MHz and $f_{0,B} = 1.87$ MHz and bandwidth $\Delta f \simeq 500$ kHz.

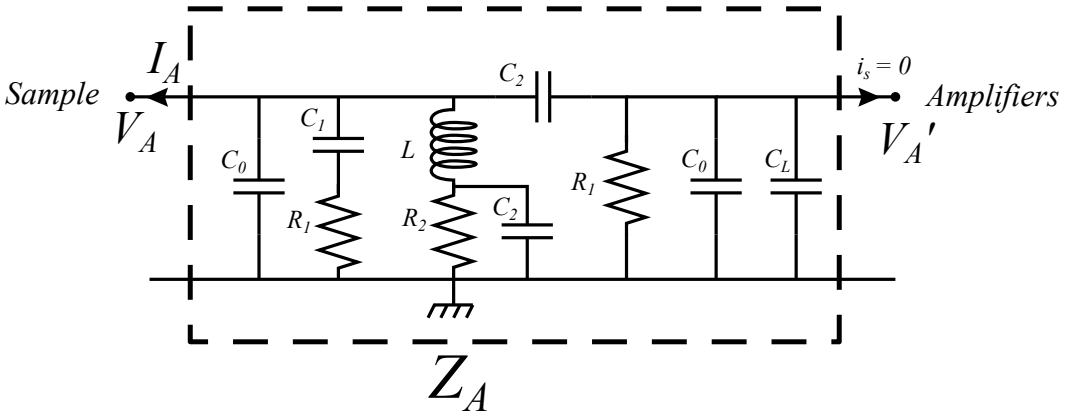

Figure 3.4: Schematic view of resonator Z_A. The values of capacitors, resistors and inductance are reported in table 3.1. The resonator Z_B is made with the same electronic components. The difference between the two circuits is mainly the wire capacitance C_L which is due to the length of the wire.

Z_A and Z_B are defined as the total impedance seen by the ohmic contacts where current fluctuations are measured. The voltages and the currents outgoing from the ohmic contact connected to the resonator Z_A are denoted V_A and I_A, so that $V_A = -Z_A I_A$. Note that the voltage V_A', at the entrance of the amplifier G_A (in figure 3.4), is not strictly equal to V_A because of the presence of the capacitance C_2; the figure 3.4 is then not strictly true. Nevertheless, at high frequencies, $V_A \simeq V_A'$ is a good approximation, and will be used for the calibration of noise measurement (see appendix C). The values of all components is given in table 3.1.

The components have been chosen for their temperature and magnetic stability. For instance, the 22 μH coil (COILCRAFT 1812CS) does not have a magnetic core and is suitable for measurement under high magnetic fields. Moreover, it has a small resistance ($\sim 10\ \Omega$) at room temperature, negligible in comparison with R_2. Resistors are made of metallic thin film (CMS 0805-size), whose resistance varies less than 10% from 300 K to 4 K or 25 mK. All capacitors are also 0805-size CMS and made from $C0G/NP0$, stable in temperature.

[2]Conversion factors between voltage and current noise are detailed in section 3.5

[3]More precisely, the real part of the cross-correlation that we measure is proportional to $\int d\omega Z_A^*(\omega) Z_B(\omega)$. Thus, this is maximum if the resonance frequencies are the closest as possible

Component	Value	
C_0	125 pF	cut DC-current coming from amplifier
C_1	9.4 nF	set accurately the resonant frequency
C_2	22.4 nF	set accurately the resonant frequency
R_1	5 kΩ	dissipate DC-current coming from amplifiers
R_2	2.5 kΩ	dissipate DC-current coming from the QPC
L	22 μH	set the frequencies measurement in MHz range
C_L	$\sim$ 90 pF	intrinsic capacitance of wires

Table 3.1: Values of components of resonators Z_A and Z_B, described in figure 3.4.

3.2.2 Amplification chain

The amplification chain is composed of two voltage-to-voltage amplifiers in series. The first is a hand made cryogenic amplifier thermally fixed to the 3.6 K stage in the cryostat. The second one is a commercial amplifier NF SA-421F5 at room temperature, powered with external battery, in order to avoid interference from DC voltage sources. It has a gain of 46 dB (×400) and a low noise density : 0.5 nV/$\sqrt{Hz}$.

Cryogenic amplifiers used for the experiments presented in this thesis have been developed by Thibaut Jullien[71]. Here we expose the principle of these amplifiers and their components; for more details, please report in Thibaut Jullien phD thesis. The principle of these amplifiers is based on the sensitivity of a High Electron Mobility Transistor resistance (HEMT) with its gate voltage (figure 3.5). A HEMT is connected toward its gate to the input of voltage δV_{in}, thus $\delta V_{in} = V_G$. The capacitance C_2 of resonators cuts DC currents coming from the sample so that V_{in} is composed of only voltage fluctuations. A polarization resistance R_{pol} imposes a current I through the HEMT, thus: $V_{HEMT} = I \cdot R_{HEMT}(V_G)$. Fluctuations of V_{in} makes the resistance R_{HEMT} fluctuates as well, in the case of small variations of V_{in} :

$$R_{HEMT}(V_G) = R_{HEMT}(V_G = 0) + \frac{\partial R}{\partial V_g}|_{V_g=0}\delta V_{in} \tag{3.1}$$

As the current is constant, voltages fluctuations of V_{in} are recovered in V_{HEMT}, multiplied by a factor :

$$V_{HEMT} = I \cdot R_{HEMT}(V_G = 0) + I \cdot \frac{\partial R}{\partial V_g}|_{V_g=0}\delta V_{in} \tag{3.2}$$

The 22 nF capacitance before the commercial amplifier at 300 K (figure 3.2 and 3.3) cuts the DC voltage. Thus, the output voltage V_{out} is :

$$V_{out} = I \cdot \frac{\partial R}{\partial V_g}|_{V_g=0}\delta V_{in} \tag{3.3}$$

The gain G of this amplifier is thus $G = g_m/g_{ds} = I \cdot \frac{\partial R}{\partial V_g}|_{V_g=0}$, where $g_m = \frac{\partial I_{ds}}{\partial V_{ds}}$ is the differential conductance and $g_{ds} = \frac{\partial I_{ds}}{\partial V_g}$ is the transconductance. G strongly depends on

the current polarisation I, the frequency of the fluctuation of δV_{in}. Both amplifiers are on the 3.6 K stage, with a good stability over temperature during time.

Transistors are two commercial HEMT in parallel. They are polarized with an external voltage source (a battery) directly through the measurement line. HEMT are well adapted for high frequency and low temperatures. Cryogenic amplifiers are realized on Copper-Kapton-Copper PCB in order to have a good thermalisation with the 3.6 K stage.

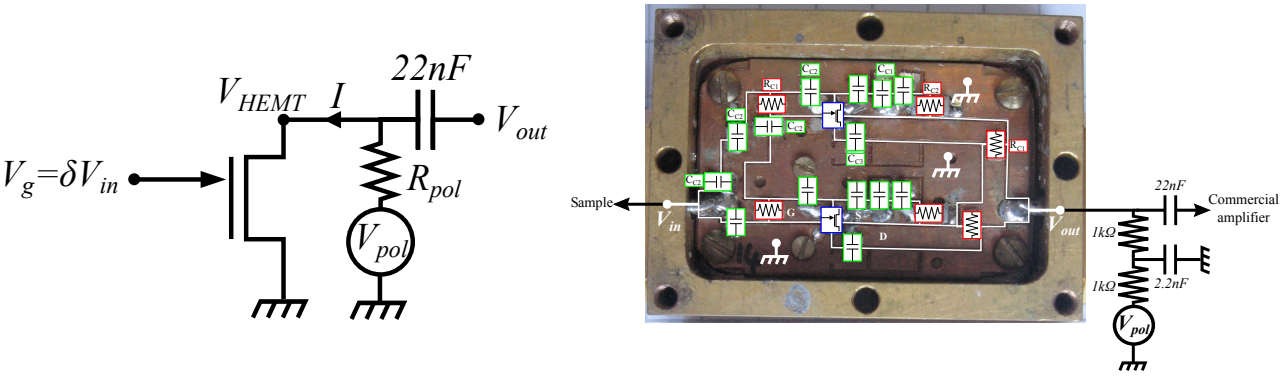

Figure 3.5: *(Left)* Schematic of cryogenic amplifier. (*Right*) Cryogenic amplifier. Values of components are : $R_{C1} = 11\ \Omega$, $R_{C2} = 200\Omega$, $C_{C1} = 22$ nF, $C_{C1} = 5$ pF and $C_{C1} = 100$ pF. Real size is 1.8 cm×2.8 cm.

In figure 3.6, the gains of each amplifier G_A and G_B are displayed as a function of voltage polarisation V_{pol}. Their maximum value is around ~ 4 but in practical, the gains are set to $G_A \simeq 3$ and $G_B \simeq 2$ for stability and a good SNR. Their intrinsic noise is ~ 3.5 nV/$\sqrt{Hz}$. The gain of amplifiers is stable under magnetic field until 9 T, thanks to a compensation coil.

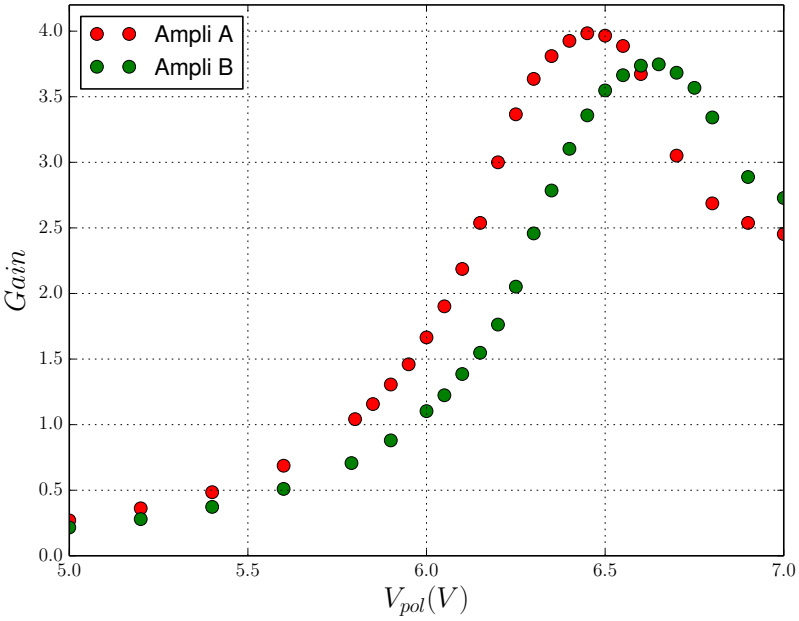

Figure 3.6: Gain of home-made amplifiers as a function of the voltage polarisation V_{pol}. The maximum value is $\sim$4 but the working range is $\sim$ 6.2 V for a good SNR.

3.3 High frequencies and DC injection lines

In this section, we present how samples are connected to DC and RF line with a good transmission, while electronic temperature is limited to 40 mK. The choice of material and the geometry of DC and RF lines components is crucial: the first issue is to limit heat transfer brought by the wire between the cryostat stages whereas inner conductor of wires[4] must be thermalised. Consequently all the wires, either DC or RF lines, are made into resistive materials.

The second issue is the thermal electromagnetic radiation[87]. All the components of the set-up (wire, attenuator, voltage source) generate a voltage noise due to Johnson-Nyquist noise or to the thermal motion of electrons in conductors. For instance, at room temperature a typical 50 Ω impedance generates large voltage fluctuations: $\sqrt{\Delta V^2} \simeq$ 130 μV, compared to the voltages applied in our experiment of few μV. These fluctuations also increase the effective electronic temperature by $k_B \Delta T \simeq e\Delta V$. The power spectral density of these voltage fluctuations over a typical impedance R at temperature T is[53]:

$$S_V(\nu) = \frac{4Rh\nu}{\exp(\frac{h\nu}{k_B T}) - 1} \tag{3.4}$$

The voltage fluctuations are then $\Delta V^2 = \int_0^\infty d\nu S_V(\nu)$. At low frequencies $h\nu \ll k_B T$, we recover the famous Johnson-Nyquist formula $S_V(\nu) = 4k_B TR$[96, 68]. For instance,

[4]Wire of DC and RF lines are coaxial wires.

300K correspond to a frequency of 7 THz, higher than the cut-off frequency of RF-lines. But for lower temperatures, the frequency dependence must be taken in account: 1 K $\leftrightarrow$ 20 GHz. The external noise radiating in the sample is drastically reduced either by to having low cut-off frequency in order to limit the contribution over the spectra (DC lines) or by decreasing the amplitude of S_V with attenuators (in the case of RF lines).

3.3.1 DC lines

The DC wires are thin coaxial cables of stainless steel and are made from LAKESHORE (CC-SS-100 Coaxial Cable). Their linear resistivity and capacitance are respectively 30 Ω/cm^{-1} and 156 pF.m^{-1}. The total resistance of the DC lines of length 1.5 m is 45Ω, which is lower than the RLC impedance (2500 Ω). By modelling these DC wires as RC circuits, the cut-off frequency is $f_c = \frac{1}{2\pi RC} \simeq 16$ MHz, just over our frequency measurement. Thus, the voltage fluctuations due to thermal noise are in the worst case $\Delta V \simeq 1$ μV and are completely negligible.

3.3.2 RF lines

At the opposite, the loss of the RF lines is weak until GHz frequencies (attenuation of 10 dBm at 12 GHz), therefore the voltage noise is directly transmitted on a large bandwidth $\Delta f \simeq 20GHz$ which corresponds to the loss specifications of the constructor. For the PASN experiments, RF lines are directly connected to the 2DEG of the sample (figure 3.2). As a consequence, the thermal noise dramatically increases the electron temperature. For the QS experiment (figure 3.3), voltage fluctuations are less critical because gates are sensitive to voltages of typically few mV. The voltage fluctuations seen at the end of RF lines on the mixing chamber can be expressed as the sum of the contribution of each impedance R_k at temperature T_k over the bandwidth $\Delta\nu$ = 20GHz, attenuated by a factor A_k[87]:

$$\Delta V_{tot}^2 = \sum_k \int_{\Delta\nu} d\nu \frac{4Rh\nu}{\exp(\frac{h\nu}{k_B T_k}) - 1} A_k \tag{3.5}$$

For the PASN experiment, three 20 dBm attenuators are set respectively on the 3.6 K, 1 K and 100 mK and are considered as a 50 Ω impedance. The 20 dBm attenuation corresponds to a reduction by a factor $A = 100$ of spectral density. The figure 3.7 shows the contribution on the sample of the the spectral density of each thermal noise source. Because of the attenuation, high temperatures (300 and 4 K) are completely negligible, and the main contribution to the thermal noise is the 100 mK stage. Summing all these contribution and integrating over frequency, we find voltage fluctuations (eq. (3.5)) of $\Delta V \simeq 1$ μV, corresponding to a temperature of T = 12 mK. It could be possible to decrease this temperature thanks to a 10 dBm attenuator on the mixing chamber in order to reduce the 100 mK noise, but it is no longer possible to apply more than 50 μV on the

sample at high frequency.

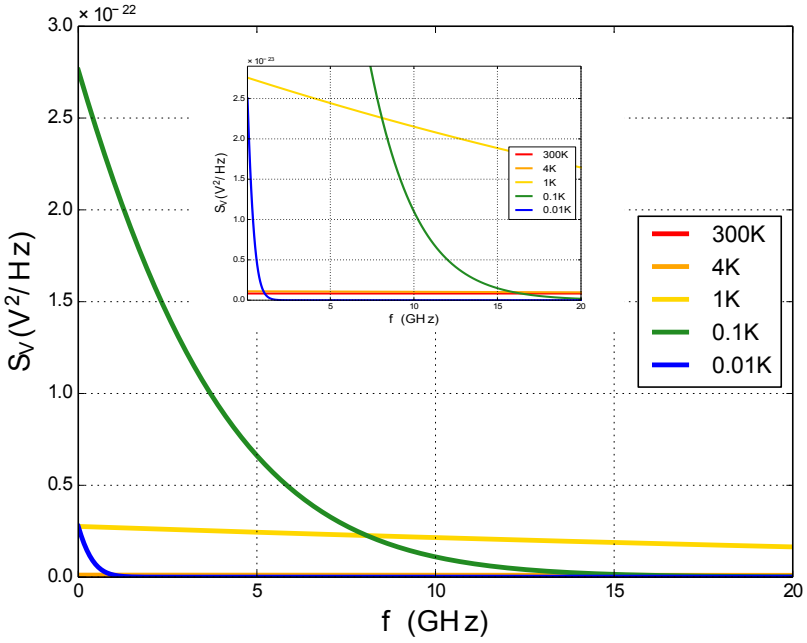

Figure 3.7: Resistors of the RF lines (for example the resistance of an attenuator is $\sim 50\ \Omega$) generates thermal fluctuations given by the formula 3.5. In this figure, we plot the power spectral density as a function of the frequency coming of these fluctuation from different resistors at several stage on the fridge, by taking in account the attenuation. The PSD of the 300 K and 4 K components are widely reduced by the attenuators (in the window). Finally, the major contribution to the thermal fluctuations is due to the 100 mK stage, where there is no attenuation in order to reach the AC amplitude required for our experiments.

Finally, RF transmission until 18 GHz is efficient. The table 3.2 gives the attenuation of RF lines for several frequencies, which remains reasonable under 20 GHz, and allows to explore the physics of dynamic quantum transport.

Frequency (GHz)	Attenuation (dBm)
6	2.4
9	2.0
10	5.5
12	10
18	13

Table 3.2: Intrinsic attenuation of RF lines for several frequencies deduced from the PASN measurements presented in chapter 4.

3.4 Data acquisition

3.4.1 Real-time acquisition

This experimental set-up allows to perform two independent and low time-consuming measures and their cross-correlation. A digitizer (Acquiris U1071A-HZ4 from agilent instruments) records simultaneously voltages V_A and V_B, presented in the figures 3.2 and 3.3 and uses a memory size of $N_s = 65472$ points at a rate of $20\text{G}\cdot\text{s}^{-1}$. In order to save time, the memory size is divided into two blocks: one stores new incoming data, a second operate fast Fourier transform (FFT) on the measured voltages in order to compute the power spectral density (PSD). The PSDs of V_A and V_B are computed from equations 3.6, 3.7 and 3.8 for respectively the auto and the cross-correlation:

$$S_{V_A \times V_A}(\omega) = \frac{1}{N_{moy}} \sum_{k=1}^{N_{moy}} \frac{\tilde{V}_{A,k}(\omega) \cdot \tilde{V}^*_{A,k}(\omega)}{\Delta f} \tag{3.6}$$

$$S_{V_B \times V_B}(\omega) = \frac{1}{N_{moy}} \sum_{k=1}^{N_{moy}} \frac{\tilde{V}_{B,k}(\omega) \cdot \tilde{V}^*_{B,k}(\omega)}{\Delta f} \tag{3.7}$$

$$S_{V_A \times V_B}(\omega) = \frac{1}{N_{moy}} \sum_{k=1}^{N_{moy}} \frac{\tilde{V}_{A,k}(\omega) \cdot \tilde{V}^*_{B,k}(\omega)}{\Delta f} \tag{3.8}$$

where $\tilde{V}_A$ and $\tilde{V}_B$ are the Fourier transform of the voltages V_A and V_B. These definitions are the discrete equivalent of those proposed in the chapter 2 for the noise theoretical calculation. Each PSD measurement is averaged N_{moy}. 32732 points of $V_A(t)$ and $V_B(t)$ at a rate of 10 $\text{G}\cdot\text{s}^{-1}$ (one measure every 3.3 ms) are measured in real-time. Therefore, the resolution of the PSD spectra is 305 kHz, from 0 to 10 MHz. The FFT are computed thanks to a C++ software with high time-efficiency: 10000 averaged PSD takes 35 s experimentally whereas a pure data acquisition needs 33 s.

The figure 3.8 shows typical PSDs for auto-correlation of channels A and B, averaged $N_{moy} = 10^5$ times. The $1/f$ noise is dominant for frequencies below 50 kHz. The main contribution is due to the noise of the amplifiers, slowly decreasing from 1 to 8 MHz. The contribution of thermal noise of impedances Z_A and Z_B is visible near 2 MHz. The noise generated by the sample in which we are interested in is a white noise: thus, the goal is to measure the additional noise that appears in the PSD.

3.4.2 Experimental resolution

The resolution of our signal, the current noise S_I, is given by the "noise of the noise" or the standard deviation σ_{S_I}. The width of the PSD curves gives an estimation of σ_{S_I} (figure 3.8) and is determined thanks to the 32400 points of the curve. We implicitly

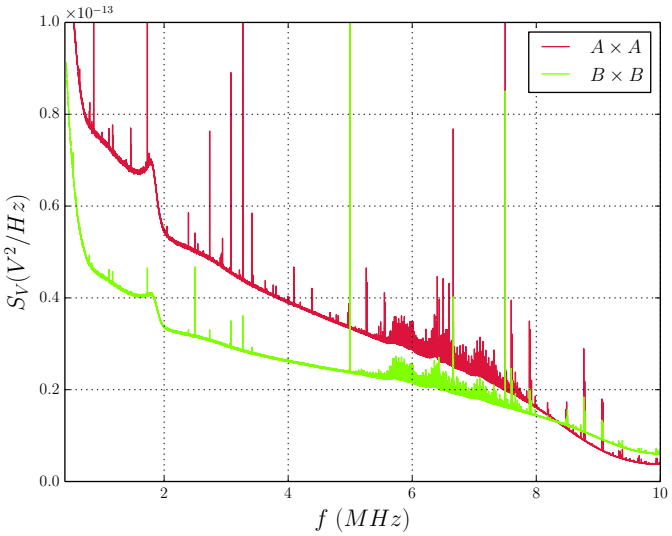

Figure 3.8: Autocorrelation PSD $S_{V,A}$ and $S_{V,B}$ over 0 to 10 MHz, with $N_{moy} = 10^5$. Main signal comes from cryogenic amplifiers. Johnson-Nyquist noise of impedances Z_A and Z_B is visible around 2 MHz. Interferences due to the external electromagnetic environment, brought by the current leads, mainly appears after 5 MHz (spikes).

suppose that there is no dependence over frequency. In figure 3.9, σ_{S_I} is displayed in logarithmic scale over the number of averages N_{moy} from 10^3 to 10^5 for channels A and B. The solid curves are linear fits whose slope for A is ~ 0.51 and ~ 0.49 for B. We can deduce that the statistics of the measurement is in a good agreement with the normal distribution $\sigma_{S_I} \propto 1/\sqrt{N_{moy}}$ until 10^5 averages.

As the interesting signal is a white noise, the noise is measured only over a bandwidth Δf centered on the resonance frequency of the RLC and averaged over $N_{freq} = \Delta f/305$ Hz=802 points (in our case, $\delta f = 245$ kHz). The effective standard deviation is then $\overline{\sigma_{S_I}} = \sigma_{S_I}/\sqrt{N_{freq}}$. In the table 3.3, we reported values of the resolution of the cross correlation, deduced from the curves of the figure 3.9. It is important to note that for large values of N_{moy}, typically $2 \cdot 10^5$, $\overline{\sigma_{S_I}}$ starts to increase because of the $1/f$ noise.

N_{moy}	time	$\overline{\sigma_{S_I}}$ (A^2/Hz)
10^3	3.3 s	$2.2 \cdot 10^{-29}$
10^4	33 s	$7.0 \cdot 10^{-30}$
10^5	5 min 30 s	$2.2 \cdot 10^{-30}$

Table 3.3: Resolution of cross-correlation noise measurements and the time required

3.4.3 Limit of noise measurements and improvements.

In practice, the noise resolution in our experiments is limited to approximatively $\overline{\sigma_{S_I}} \simeq 5 \cdot 10^{-30}$, whatever the number of averages. This issue is due to the time needed for

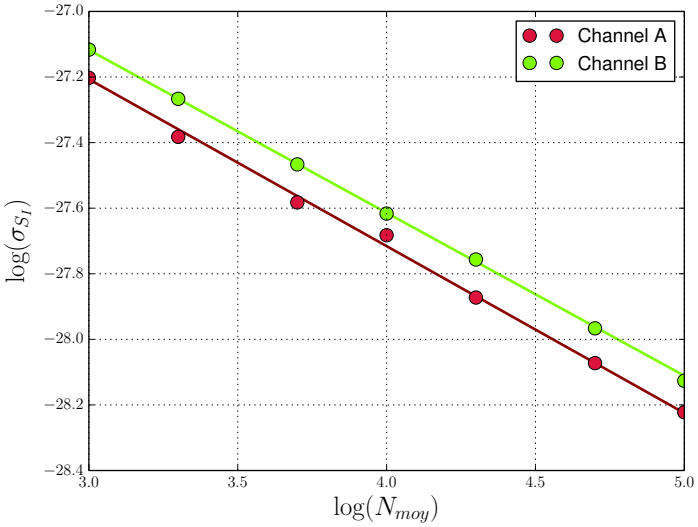

Figure 3.9: Standard deviation σ_A and σ_B of the auto-correlations, converted in current noise $S_{I,A}$ and $S_{I,B}$, as a function of the number of average N_{moy} in logarithmic scale. Continuous line are a linear fit with a 1/2 slope. The $1/\sqrt{N_{moy}}$ law is valid up to 10^5 averages.

the data acquisitions of an entire measurement: typically, a curve of DCSN of 50 points averaged 10^5 times takes 5 hours. During this time, the background noise due to external parasitics[5] vary over characteristic times of tens of minutes. It is low enough to have a good resolution for short-time measurements (<10 minutes), as shown in figure 3.9, but reduce the effective resolution of a entire noise curve.

This background noise is due to the current leads of the magnet whose the impact appears clearly on the figure 3.10, *(Left)* which shows the real part of cross-correlation PSD in the case of the PASN set-up, similarly to the figure 3.8, restricted on the interesting frequency window $f \in [1.4; 2.5]$ MHz. The green (resp. blue) curve is the PSD when currents leads are disconnected (resp. connected), whereas the average of cross-correlation noise is supposed to be zero[6]. It appears clearly that current leads bring an undesirable noise background. For safety reasons, it is not possible to let current leads disconnected[7]. This noise adds an offset $S_{I,0}$ on the total noise measurement that forbid any absolute measurement of the noise. A more disturbing effect is that $S_{I,0}$ is unstable over long times. In figure 3.10, *(Right)*, an evolution appears clearly from one day to another. Consequently, for measurements of several hours $S_{I,0}$ changes and adds an uncontrollable time-drifting on the noise that limits the resolution to $\overline{\sigma_{S_I}} \simeq 5 \cdot 10^{-30}$ A^2/Hz.

[5]These external parasitics are brought by the current leads of the magnet.

[6]These spectra have been taken with the sample 1 which is a 6-contacts QPC. As shown in chapter 1, the cross-correlation noise is $\propto D(1-D)$ and thus supposed to vanish when the QPC is completely opened or closed. In figure 3.10, QPC is closed.

[7]If a quench of the magnet occurs at high magnetic fields, it may induce hazardous voltages in the power outlets.

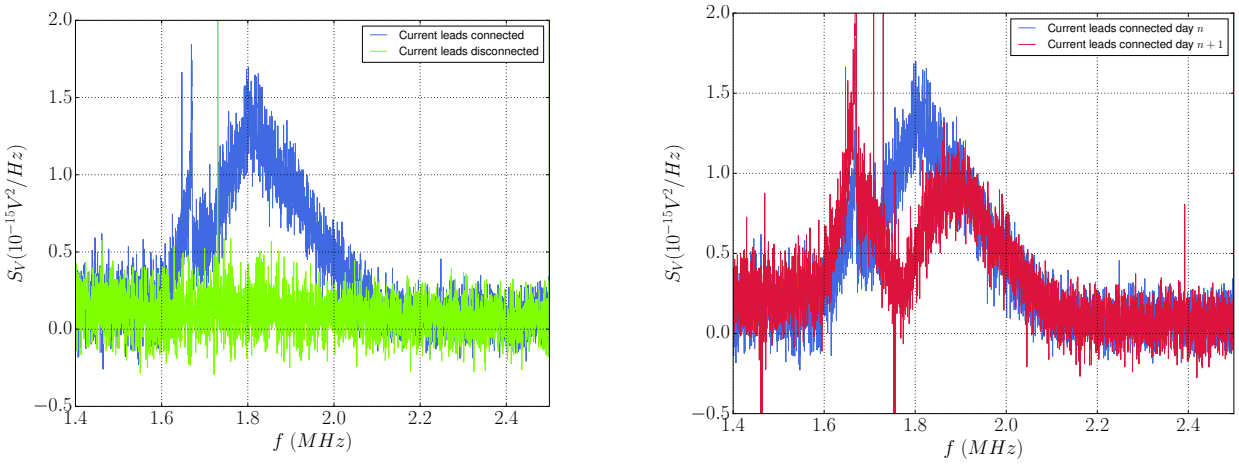

Figure 3.10: *(Left)* Cross-correlation PSD restricted to $f \in [1.4; 2.5]$ MHz. Blue (resp. green) curve corresponds to the case of connected (resp. disconnected) current leads of the magnet. *(Right)* Evolution from one day to another of cross-correlated PSD.

As the current leads play the role of big antennas between the laboratory environment and inside the cryostat, a first attempt was to isolate as much as possible the current lead and the power supply of the magnet. The power supply is protected with a Faraday-cage and the current leads with copper sleeves and ferrite blocks. It reduces sufficiently the unwanted noise and improve the resolution to $\simeq 5 \cdot 10^{-30}$ A^2/Hz.

At the end of this thesis, I developed a new measurement protocol that reduces the resolution under $1 \cdot 10^{-30}$ A^2/Hz. The idea is to perform a serie of quick low-averaged measurements, less than 1 minute for an entire curve, repeated few hundreds times. The noise background does not vary for measurements shorter than tens of minutes. As in any case we do not have access to the absolute value of the noise, the mean value of each curve is systematically removed. Finally, we obtain a cloud of points as shown in figure 3.11, *(Left)*. The mean value of this cloud appears in red dots. More interesting, it provides the effective statistics of each point. In the figure 3.11, *(Right)*, the histogram of the gathered value allows to verify that statistic is conformed to the normal distribution. In the curves presented in figure 3.11, the standard deviation of a single measurement is $\sigma = 2.06 \cdot 10^{-29}$ A^2/Hz for 10^3 averages, that corresponds to the width of the cloud. The effective standard deviation is $\sigma_{SE} = \sigma/\sqrt{N_{moy}} = 9.9{\cdot}10^{-31}$ A^2/Hz, for 430 measurements.

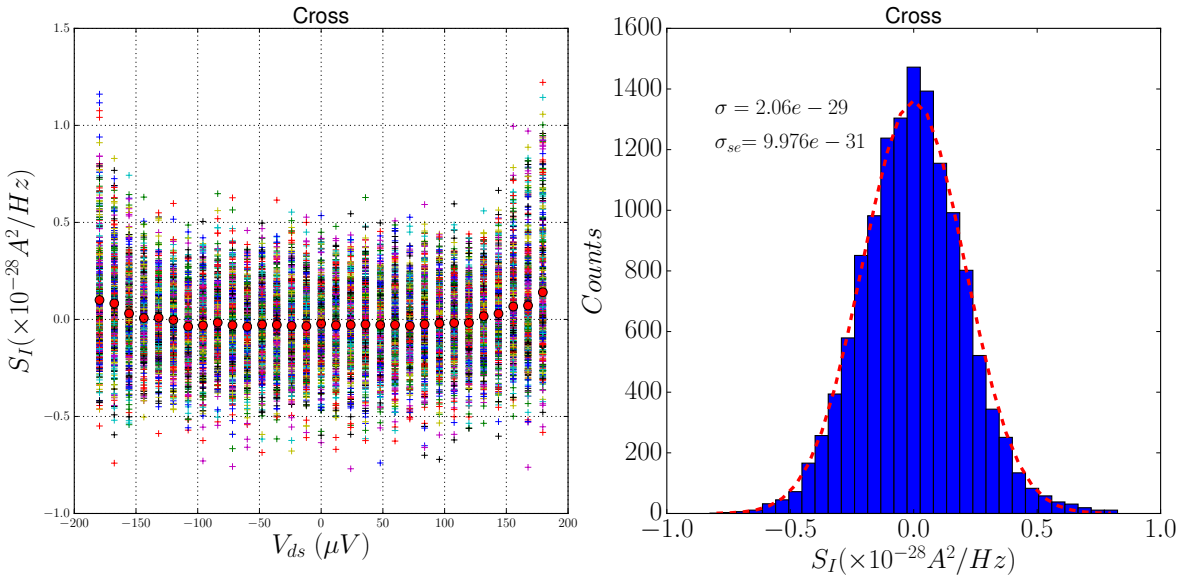

Figure 3.11: *(Left)* A noise measurement 1000 averages repeated 430 times. The cloud of points corresponds to all the results, red dots are the averages. *(Left)* Histogram of all the values (in blue). Red dashed curve represent the theoretical normal distribution with a standard deviation σ founded with the cloud of points.

3.5 Conductance and noise calibration

In this part, we explain the conductance and noise calibration procedure in order to recover the current noise from the measured voltage signals. The conductance is obtained thanks to a measurement in the MHz range and allows fast acquisition with a high SNR. The calibration of the noise in order to convert the measured voltage noise signals into the current noise generated by the sample is inspired from [35].

We focus the analysis on the PASN experiment performed on the 6-contacts geometry sample. The calibration of the 2-contact geometry is similar and is fully detailed in the phD thesis of Thibaut Jullien[71]. The figure 3.12 represents the electrical model of the experimental set-up. Ohmic contacts are indexed from 0 to 5 and their respective voltages and currents are related thanks to the Landauer-Büttiker's law, as explained in chapter 2. The contact 0 is connected to the injection line while noise measurements are performed on contacts 1 and 4. The amplification chain is reduced to a voltage gain on each channel A and B. The measured voltages are denoted V_A and V_B.

3.5.1 Calibration of the transmission and reflection coefficients

The coefficient of transmission $D = \sum_k |\tau_k|^2$ and reflection $R = \sum_k |\rho_k|^2$ of the QPC are measured with accuracy by using the noise measurement set-up as a lock-in detector. The principle is the following: an AC voltage of amplitude δV is applied on the injection

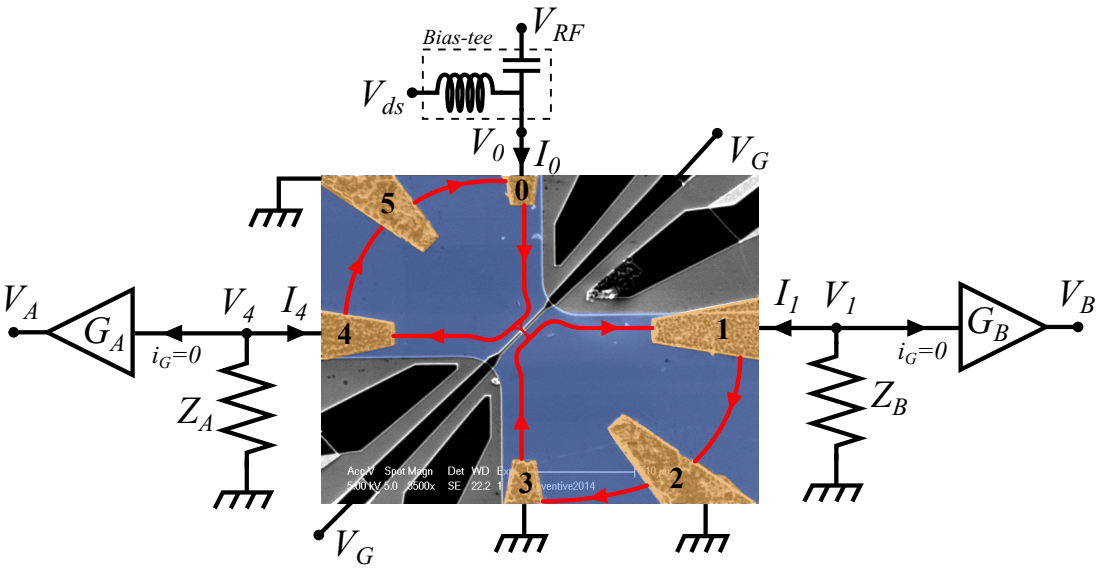

Figure 3.12: Electrical model of the experimental set-up working in the integer quantum Hall effect. The contact 0 is polarised by the voltage V_0 and the noise is measure through contacts 1 and 4. The amplification chain is reduced to voltage gains in each channel. For the noise calibration, the QPC is closed (D = 0) such as V_1 and V_4 are completely decorrelated.

contact 0,

$$V_0(t) = \delta V \cos(\omega_0 t) \tag{3.9}$$

and the amplitude of respective voltages V_A and V_B of ohmic contacts 4 and 1 are measured at the pulsation ω_0. A simple linear relation between coefficients and voltages is found thanks to the relations between voltages developed in chapter 2:

$$V_A = \frac{G_A}{1 + R_H/Z_A(\omega_0)} \frac{R}{\nu} \tag{3.10}$$

$$V_B = \frac{G_B}{1 + R_H/Z_B(\omega_0)} \frac{D}{\nu} \tag{3.11}$$

where $R_H = h/\nu e^2$ is the hall resistance, ν is the filling factor and G_A and G_B the gain of the amplification chain. The maximum values of V_A and V_B are obtained at the resonance of the impedances Z_A and Z_B thus pulsation ω_0 is chosen near ~ 1.8 MHz[8]. This measurement takes also benefit from working in the MHz range : $1/f$ noise is considerably reduced and we obtain an excellent SNR. The voltages V_A and V_B are recovered through the noise measurement presented in section 3.4:

$$V_A = \int_{\omega_0 - \delta\omega}^{\omega_0 + \delta\omega} d\omega \sqrt{S_{V,A}(\omega) \Delta f} \tag{3.12}$$

[8]The pulsation ω_0 is chosen outside of the bandwidth of measurement, in order to prevent the noise measurement from the contribution of $V_0(t) = \delta V \cos(\omega_0 t)$.

where $\delta\omega/2\pi \simeq 1$ is small in comparison with the resonance frequency in order to averaged over a narrow frequency window, minimizing the noise background. The spikes of this AC voltage appears at 1.8 MHz on figure 3.8. As we send an AC voltage, δV must be small in order to avoid to measure non-linearities of the transmission[9]. In practice, $\delta V \simeq 5$ μV verifies this requirement. In the figure 3.13, amplitudes V_A and V_B are displayed as a function of gate voltage V_G for several filling factors ν, from 1 to 6.

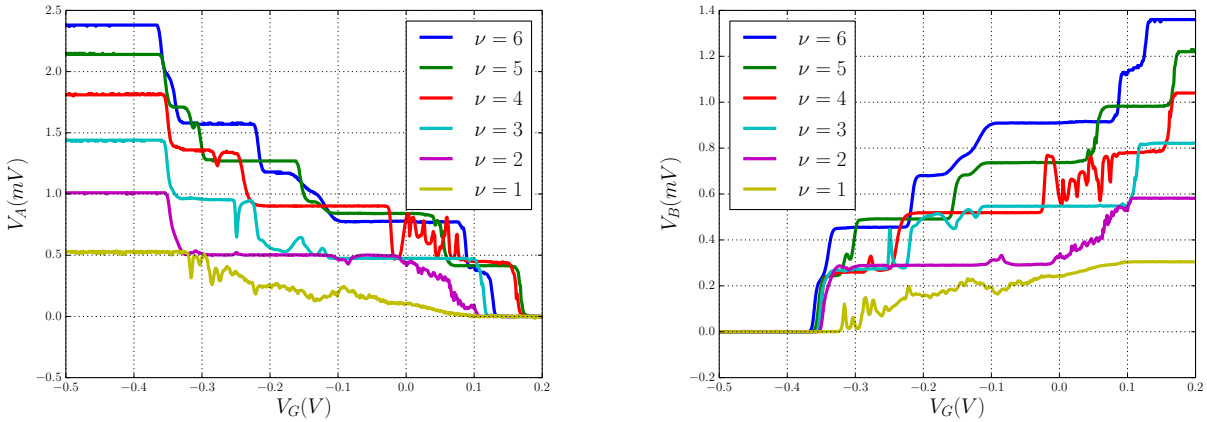

Figure 3.13: *Left*: Raw signal V_A proportional to the reflection coefficient R. Plateaus of conductance are clearly visible for each filling factor. *Right*: Raw signal V_B proportional the transmission coefficient D.

The plateaus of conductance are easily visible for each filling factor, with an excellent accuracy. The measure of a curve in the figure 3.13 takes only 30 s. As the values of δV, G_A, G_B, $Z_A(\omega_0)$ and $Z_B(\omega_0)$ are not perfectly known, coefficients R and D are calibrated according the position of plateaus, which is easy thanks to the simple linear relation between V_A (resp. V_B) and R (resp. T). The figure 3.14 shows the coefficients R and D deduced from the curves at $\nu = 4$ of figure 3.13. Measurements are in an excellent agreement with current conservation: we recover experimentally $R + D = \nu$ by using two independent measurements.

For each noise measurement, transmission is set with this calibration protocol and its stability is ensured thanks to a control feedback on the gate voltage.

3.5.2 Noise calibration

We propose a simple procedure for the calibration of the measured noise using the Johnson-Nyquist noise. Indeed, the RLC impedances and the gain of the amplification chain are not perfectly known and must be calibrated for both channels. The principle is the following: the QPC is closed ($D = 0$) and PSD are measured at several temperatures. An appropriate fit of the spectra gives access to the characteristics values of the RLC

[9]The dependence of the transmission with the energy, in this case, with the injection voltage V_0. The sample 2 has non-linearity for voltage polarization of tens of μV.

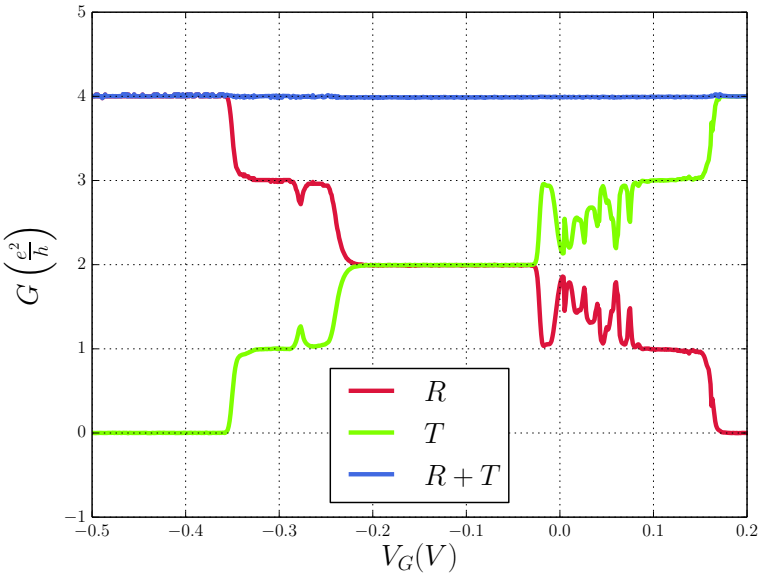

Figure 3.14: Conductance measurements for sample 2 for $\nu = 4$. R and T are respectively the reflection and transmission coefficients. Blue line correspond to the addition of the red and the blue curve.

impedance and the total gain. Then, we deduce the coefficients of conversion between the measured voltage noise S_V and the current noise S_I emitted by the sample.

Electrical description and conversion coefficient

In the case of a closed QPC, the electrical model of the QPC and the measurement lines is simplified as shown in the figure 3.15. Contacts 1 and 4 are completely decorrelated and the sample is reduced to the thermal current fluctuations of a Hall resistance R_H. The noise sources of the figure 3.15 are modelled by:

- δi_{Ga} and δi_{Gb} are the current fluctuations generated by the cryogenic amplifiers, respectively $S_{I,Ga}$ and $S_{I,Gb}$, their order of magnitude is $\sim 10^{-26} A^2/Hz$;

- δi_{Za} and δi_{Zb} are the current fluctuations due to the Johnson-Nyquist thermal noise of total impedances Z_A and Z_B, respectively $S_{I,Za}$ and $S_{I,Zb}$, their order of magnitude is $\sim 10^{-27} A^2/Hz$;

- δi_{e1} and δi_{e4} are the current fluctuations emitted by the QPC. In the case $D = 0$, their PSD is identical and corresponds to the Johnson-Nyquist noise of the Hall resistance at a temperature T. The order of magnitude is $\sim 10^{-28} A^2/Hz$.

The relation between PSD and currents is equivalent to the definition proposed in eq. 3.6, 3.7 and 3.8: $S_I = \frac{\widetilde{\delta i \delta i^*}}{\Delta f}$. By applying the current conservation law on the model in figure

3.15, we obtain a relation between current sources and the voltage measured:

$$\tilde{V}_A(\omega) = G_A Z'_A(\omega)\left(\widetilde{\delta i}_{Ga} + \widetilde{\delta i}_{Za} + \widetilde{\delta i}_{e1}\right) \tag{3.13}$$

$$\tilde{V}_B(\omega) = G_B Z'_B(\omega)\left(\widetilde{\delta i}_{Gb} + \widetilde{\delta i}_{Zb} + \widetilde{\delta i}_{e4}\right) \tag{3.14}$$

where $\tilde{V}_A(\omega)$ and $\tilde{V}_B(\omega)$ are the Fourier transform of the voltages V_A and V_B and $Z'_{A/B} = \left(\frac{1}{Z_{A/B}} + \frac{1}{R_H}\right)^{-1}$.

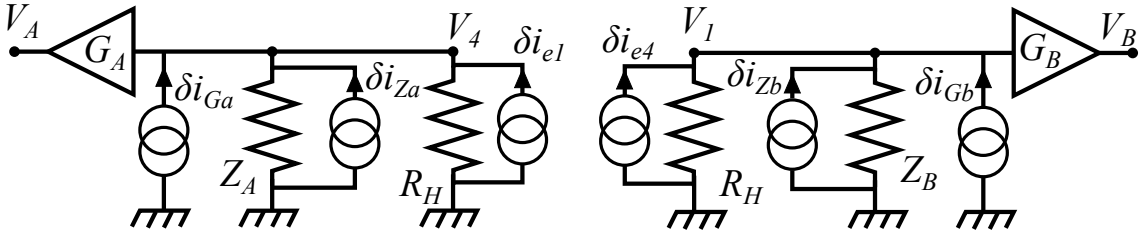

Figure 3.15: Schematic representation of current source noise. Z'_A is the total impedance $Z'_A = \left(\frac{1}{Z_A} + \frac{1}{R_H}\right)^{-1}$, where R_H is the Hall resistance. δi_{Ga}, δi_{Za} and δi_e are respectively the current fluctuations respectively due to the cryogenic amplifier, to the thermal noise of Z_A and to the sample noise.

From that, it is possible to show that the auto-correlation on channel A $S_{V,A}$, the auto-correlation on channel B $S_{V,B}$ and the cross-correlation $S_{V,A\times B}$ are:

$$S_{V_A\times V_A} = A \times A \cdot (S_{I,Ga} + S_{I,Za} + S_I) \tag{3.15}$$

$$S_{V_B\times V_B} = B \times B \cdot (S_{I,Gb} + S_{I,Zb} + S_I) \tag{3.16}$$

$$S_{V_A\times V_B} = A \times B \cdot S_I \tag{3.17}$$

where $A \times A$, $B \times B$ and $A \times B$ are respectively the conversion coefficients of the auto-correlation of channel A, the auto-correlation of channel B, and the cross-correlation. The advantage of the 6-contact geometry is the linearity relation between S_V and S_I as the measurement lines are fully decorrelated in the quantum Hall effect regime[10]. It simplifies the computation of V_A and V_B and makes disappear all parasitic contributions of the thermal and amplification noise in the cross-correlation signal. On the contrary, the conversion coefficients depends on the transmission of the QPC for the 2-contacts geometry. The coefficients $A \times A$ and $B \times B$ are real numbers and $A \times B$ is a complex number which depends on the recovering of impedances $Z_A(\omega)$ and $Z_B(\omega)$. Thus, in order to convert S_V into S_I, an accurate knowledge of all the resonator components and gain values is required. The technical calculations are detailed in the appendix C and only the main features are presented here.

[10]During the calibration, gates are supposed to be completely open are closed. Then, there is no partitioning noise.

Johnson-Nyquist noise calibration

The thermal noise generated by the impedance Z'_A and Z'_B is well-know and is given by the Johnson-Nyquist law: $S_{I,Z} = 4k_BT\Re(1/Z(\omega))$[68]. Several PSD of the auto and cross-correlation at different temperatures of the mixing chamber are measured and the noise of the cryogenic amplifiers $S_{I,Ga}$ and $S_{I,Gb}$ is removed by subtracting the noise at 25mK. The remaining noise is displayed on the figure 3.16, right and corresponds to the thermal noise generated by the RLC. The subtracted PSD ΔS are then fitted in order to extract the components of Z_A and Z_B and the gains G_A and G_B. For instance, the subtracted PSD is for channel A:

$$\Delta S_{V_A\times V_A}(\omega) = S_{V_A\times V_A}(\omega) - S_{V_A\times V_A}(\omega)\mid_{T=25mK} = 4k_B(T-T_{ref})G_A^2\Re\left[Z'_A(\omega)\right] \quad (3.18)$$

T_{ref} is the electronic temperature of the resonator when the fridge is at 24 mK which is at least the phonon temperature. This temperature is often superior to 24 mK because of the inefficient electron-phonon thermalisation process and the electromagnetic noise which is equivalent to an effective heating. T_{ref} is extracted from the equation 3.18 averaged over the frequency and linearly fitted. The result is proportional to $T - T_{ref}$:

$$\langle \Delta S_{V,A}(\omega)\rangle_{\Delta\omega} \propto (T - T_{ref}) \quad (3.19)$$

A measure of $\langle \Delta S_{V,A}(\omega)\rangle_{\Delta\omega}$ versus temperature is reported on figure (3.16, *Left*). The fit brings an estimation of T_{ref}. The reference temperature T_{ref} is reported for both channels A and B and several filling factors in the table 3.4.

ν	$T_{ref,A}$	$T_{ref,B}$
2	44mK	34mK
3	51mK	39mK
4	52mK	40mK

Table 3.4: Temperature of reference deduced from 3.19. It corresponds to the temperature of electrons in the resonators. As the QPC is closed ($D = 0$) during the calibration, the channel A (which measure the noise on the contact 4) receive the parasitic noise from the contact 0 connected to the injection line and is warmer than the contact B.

The electronic temperature in resonators T_{ref} is found higher for the channel A: as the measurement are taken QPC closed, parasitic radiations coming from the contact 0 (connected to the injection line) are transmitted on the contact 4 and not on the contact 1. An other point is the imprecision on the fit for temperatures lower than 100 mK. The recent calibrations, performed from 50 mK to 400 mK, are more accurate and we found $T_{ref} \simeq 30mK$ for both channels.

The subtracted PSD are then fitted with equation 3.18. The measured PSD are faithfully reproduced by the model and the experimental values of resonator components

are then deduced from the fitting parameters.

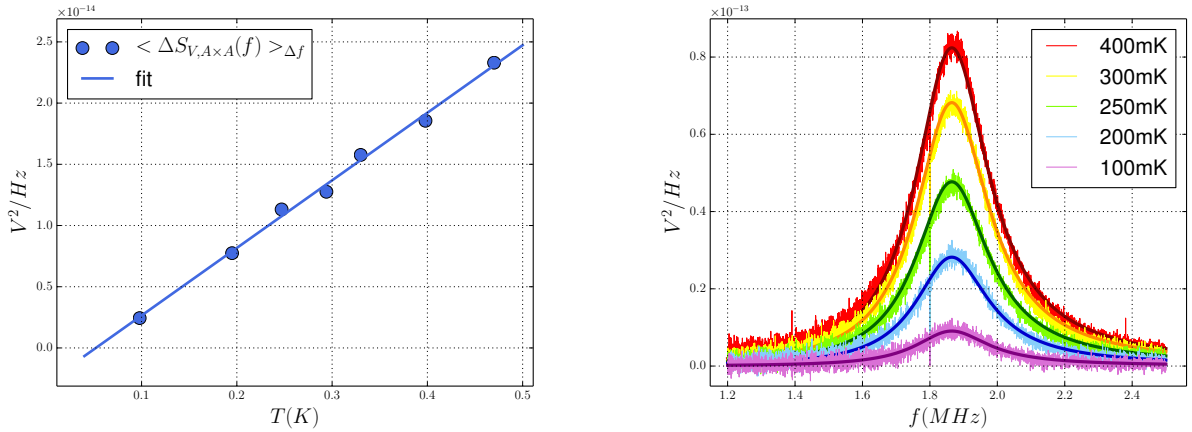

Figure 3.16: *(Left)* : average of $\Delta S_{V_A\times V_A}(\omega)$ over $f \in [1.4, 2.5]$ MHz for several temperature of the mixing chamber. The curve of the linear fit gives T_{ref} at the abscissa where $\Delta S_V = 0$. *(Right)* : Spectra $\Delta S_{V_A\times V_A}(\omega)$ for several temperature measured between 1.4-2.5 MHz and the corresponding fits plotted from eq. (3.18).

The coefficients $A\times A$, $B\times B$ and $A\times B$ computed from these parameters are reported in table 3.5. The real part of $A\times B$ is thousand times larger than its imaginary part, which is negligible. The current correlation computed in the chapter 1 are then directly deduced from the measured voltage noise: $S_{I_1\times I_1} = S_{V_A\times V_A}/A\times A$, $S_{I_4\times I_4} = S_{V_B\times V_B}/B\times B$ and $S_{I_1\times I_4} = \Re\left[S_{V_A\times V_B}\right]/\Re\left[A\times A\right]$.

ν	$A\times A(\Omega^2)$	$B\times B(\Omega^2)$	$\Re\left[A\times B\right](\Omega^2)$
2	$5.72\cdot 10^{12}$	$2.15\cdot 10^{12}$	$3.50\cdot 10^{12}$
3	$5.04\cdot 10^{12}$	$1.89\cdot 10^{12}$	$3.08\cdot 10^{12}$
4	$4.78\cdot 10^{12}$	$1.72\cdot 10^{12}$	$2.86\cdot 10^{12}$

Table 3.5: Conversion coefficients

A comparison of a calibrated experimental DC Shot-Noise with a theoretical curve allows to check directly the validity of the calibration. A DCSN performed at $\nu = 4$ at transmission $D = 0.5$ is reported in figure (3.17). The theoretical shot-noise is given by equation (3.20):

$$S_I(V_{ds}) - S_I(0) = 4k_BT\frac{e^2}{h}\left(2\nu - 1 + D^2 + R^2 + RD\frac{eV_{ds}}{2k_BT}\coth\left(\frac{eV_{ds}}{2k_BT}\right)\right) - 4k_BT\frac{e^2}{h}D \tag{3.20}$$

The experimental noise is systematically subtracted with an offset in order to set $S_I(V_{ds} = 0) = 0$. As explained above, the experimental set-up does not give access to the absolute value of the noise because of the noise background. The curvature of shot-noise

around $V_{ds} = 0$ gives access to the electronic temperature T_{e^-}, which can be used in thermometry[120]. In the case of the measurement reported in figure (3.17), we found $T_{e^-} = 35$ mK, which is really close to the reference temperature found in table 3.4. There is no dissipation in the edge channels thanks to the absence of longitudinal resistance in the regime of QHE, unlike the case of no magnetic field. The transmission D is given by the conductance curve and rectified if necessary for each point. The value of the voltage divider on the 100 mK stage has been controlled at low temperature such as the polarization voltage V_{ds} is well-known.

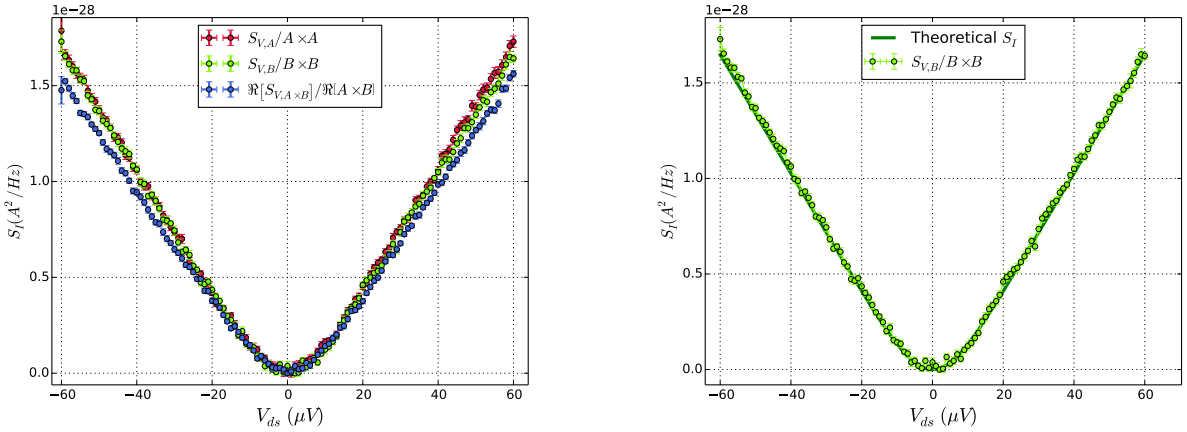

Figure 3.17: Shot-noise measurement at $D = 0.5$ and $\nu = 4$. *(Left)* : Auto and cross-correlation channels. The values at $V_{ds} = 0$ have been subtracted. *(Right)* : Channel B compared with to a theoretical shot-noise. Electronic temperature is $T_{e^-} = 35$mK.

The theoretical noise and the experimental data presented in figure 3.17 *Right* are in a good agreement. Slight differences between channels appear: it results from uncertainties in the calibration of coefficients $A \times A$, $B \times B$ and $A \times B$ presented below. The error is estimated at 8%, which is enough for the noise calibration required in the PASN experiments.

Conclusion

In this chapter, we presented the main technical aspects of the experimental set-up used in this thesis. Despite the presence of the 14 T magnetic coil which adds a parasitic noise background, we achieve to perform low noise measurements with a resolution of $5 \cdot 10^{-30}$ A^2/Hz in 5 minutes at a temperature of $\sim$40 mK while RF voltages are applied on the sample. A relevant data acquisition proposed at the end of this thesis improves the resolution to $9 \cdot 10^{-31}$ A^2/Hz and provides directly the statistics of the measurement. We also present a fast and accurate protocol for the conductance measurement, which allows us to have a feedback control on the transmission measurement.

Chapter 4

Photo-assisted shot noise in Quantum Hall Effect: experimental results

In this chapter we present the first measurement of Photo-Assisted Shot-Noise (PASN) in the Quantum Hall Effect (QHE) regime. Our experimental results are found in good agreement with the PASN predictions discussed in chapter 1 and with the similar experiments performed in the absence of magnetic field[114, 106, 69]. We first introduce the experimental measurements conditions and the data processing. Then, we show results of PASN as a function of the DC polarisation and the AC polarisation, obtained with a sine excitation, for several frequencies, RF amplitudes and for different filling factors. For all these parameters, comparison with theory clearly indicates that the PASN physics in edge channels is found similar to that observed in zero magnetic field. This opens the possibility to realize single electron source where electrons are injected in the form of levitons using periodic Lorentzian voltage pulses in the quantum Hall regime.

4.1 Experimental conditions and protocol

The aim of the experiment is the measurement of the excess shot-noise in a QPC in the quantum Hall effect regime while applying a periodic voltage on an ohmic contact. We expect to observe photo-assisted effects presented in chapter 1. In this experiment, we use the sample 2 described in chapters 2 and 3. Here, we first remind briefly the experimental set-up. Then, two raw PASN measurements illustrate the presence of an offset while most PASN features are observed in the measured noise and we explain how this offset is taken in account in the data processing for the comparison with theoretical curves.

4.1.1 Experimental set-up

The figure 5.1 shows the schematic of experimental set-up used for the PASN experiments

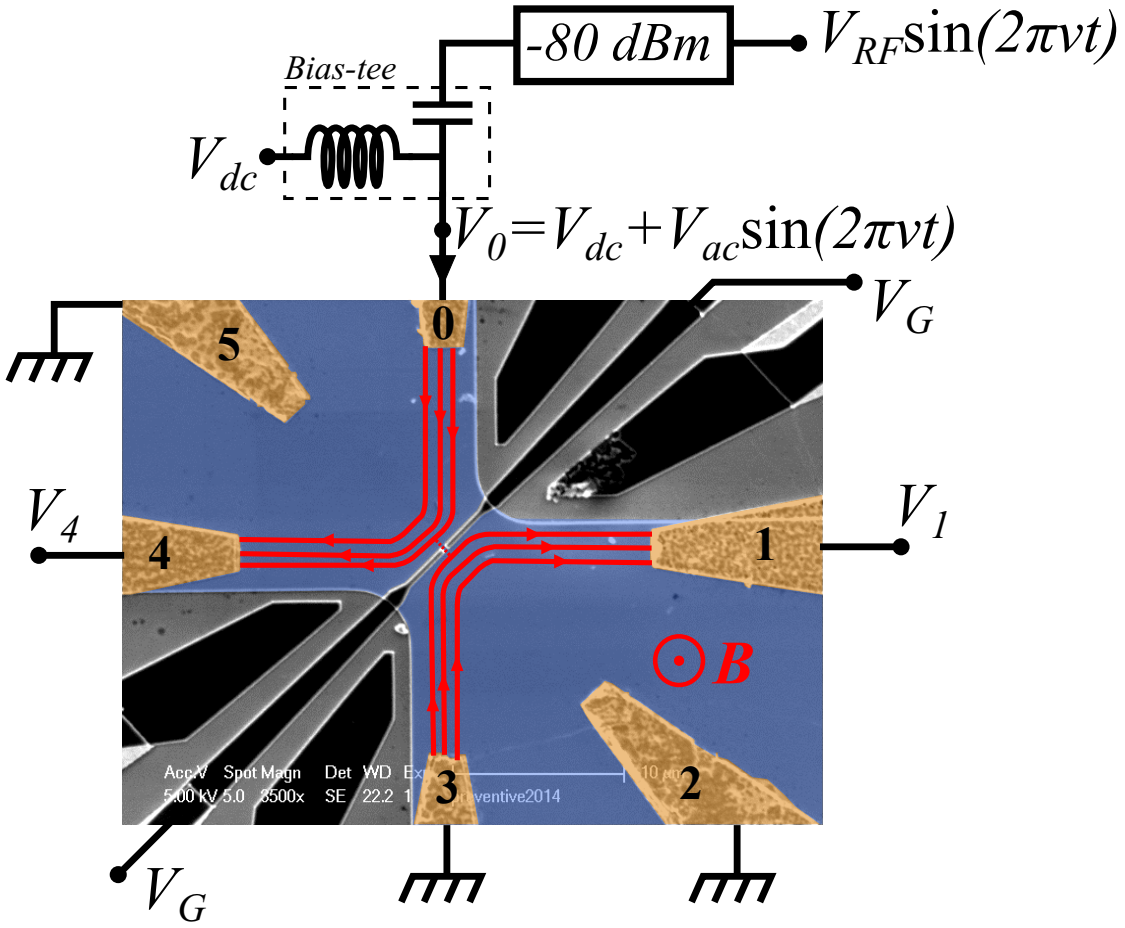

Figure 4.1: SEM picture of sample 2 used in this experiment. Voltage polarisation $V_0(t) = V_{dc} + V_{ac}\sin(2\pi\nu t)$ is applied on contact 0 thanks to a bias-tee. There is a 80 dBm attenuation on the RF line. Noise measurement is performed through contacts 1 and 4, as explained in chapter 3. Contacts 2, 3 and 5 are connected to the ground. A perpendicular magnetic field is applied in order to work at filling factor $\nu = 2$ or 3.

We apply a sine-wave voltage $V(t) = V_{dc} + V_{ac}\sin(2\pi\nu t)$ of frequency ν and amplitude

V_{ac} combined with a DC component V_{dc} on the contact 0. Practically, a bias tee allows to add the DC voltage, delivered by a Yokogawa 7651 voltage source, to the AC voltage, delivered by a RF source Agilent N5183A. As explained in chapter 3, there is a total attenuation of 80 dBm on RF lines from room temperature to the low temperature sample holder. The room temperature RF source output voltage is denoted V_{RF} and can reach 2.5 V at 20 GHz. We define k as the ratio between the effective voltage amplitude V_{ac} applied on the QPC and the voltage amplitude V_{RF} at the output of the high frequency source :

$$k = \frac{V_{ac}}{V_{RF}} \tag{4.1}$$

This factor k allows us to estimate the loss in the RF lines. Depending on the gate voltage applied on the QPC and used to reflect edge channels, the RF sample impedance is in general larger than the Hall resistance, few $k\Omega \gg 50\Omega$, which is much higher than RF line impedance. Thus, there is a quasi RF-current node at the ohmic contact and the RF-voltage amplitude is almost twice the amplitude expected if the coaxial line were terminated on a 50 Ω resistor[1]. The 80 dBm attenuation gives a voltage attenuation factor of 10^4 and the uppermost value of k is $2 \cdot 10^{-4}$ (neglecting extra RF losses, due to skin depth attenuation and uncontrolled RF-reflections) so that voltages of few hundreds of μV can be applied at high frequency.

Auto and cross-correlation measurements are performed through contact 1 and 4, whose calibration has been detailed in chapter 3. The experimental results presented in this chapter are cross-correlation measurements, except when explicitly mentioned. For simplicity, the noise is denoted S_I (instead of the notation $-S_{I_1 \times I_4}$ used in the chapter 1).

In the following, it is convenient to remind the reduced charge q and amplitude α which are the natural units for the PASN processes:

$$q = \frac{eV_{dc}}{h\nu} \tag{4.2}$$

$$\alpha = \frac{eV_{ac}}{h\nu} \tag{4.3}$$

q represents the charge injected by the DC voltage in each spin degenerate quantum edge channels during one period $1/\nu$. In these measurements, we focus on a pure sinusoidal excitation in order to verify photo-assisted properties in the quantum Hall effect. Indeed, unlike more complex time dependent excitations $V(t)$, a pure harmonic signal cannot be deformed when propagating from the RF source to the QPC, as the RF set-up response is purely linear. Consequently, the P_l coefficients that enter in PASN noise formula are

[1] In the case of voltage propagation in RF lines, if the line ends by a infinite impedance, the boundary conditions make the voltage wave amplitude at the end to be twice the initial amplitude of the wave.

well-known and given by Bessel functions :

$$P_l = |j_l(\alpha)|^2 \tag{4.4}$$

An external magnetic field is applied perpendicularly to the plane of the sample and is chosen in order to minimize the non-linear effects of the QPC DC transmission versus V_{dc}. We observe that a good regime for shot-noise measurement is at the beginning of Hall plateaus, which corresponds to $B = 2.4$ T at filling factor $\nu = 3$ and $B = 3.4$ T at $\nu = 2$.

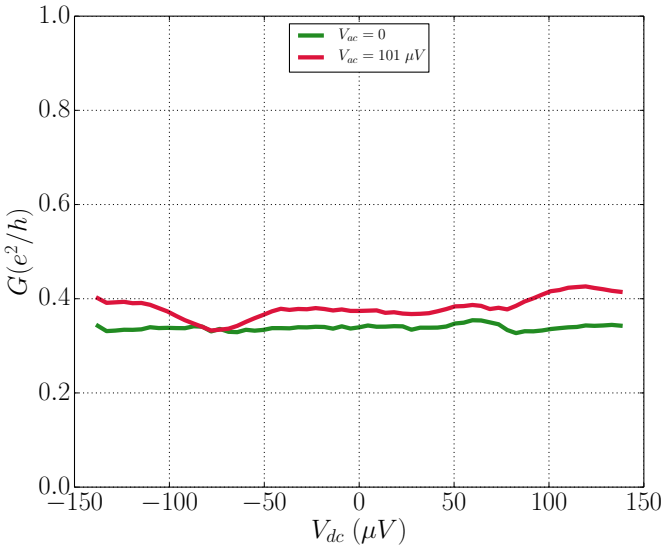

Figure 4.2: Differential conductance G of the sample in units of e^2/h with RF voltage off and on ($V_{RF} = 2.26$ V, $V_{ac} = 101$ μV) at $B = 2.4$T ($\nu = 3$). Transmission is 0.34 at $V_{dc} = 0$ and $V_{ac} = 0$.

The effective electronic temperature[2] is $T = 40$ mK and is extracted from a standard DC shot-noise (DCSN) measurements. Fortunately, the electronic temperature is weak enough to avoid a smearing of the PASN effects.

All measurements presented here have been performed at a total QPC transmission $D = 0.34$, i.e. for $\nu = 2$ (resp. 3), the edge channels 2 (resp. 3) are reflected and the last channel has a transmission 0.34. This value is chosen in order to minimize non-linearities of conductance[3]. The figure 4.2 shows the differential conductance versus DC polarisation V_{dc} for RF on and off at 18 GHz and $V_{ac} = 91$ μV and at $\nu = 3$. Measurements presented in this chapter has been taken on a period of a month, consequently due to the limited QPC stability, the differential conductance may have slightly drifted from one measure to another. Nevertheless, it keeps approximatively the same shape: the conductance

[2]Temperature of cryostat's mixing chamber is $T_{MC} = 25$ mK.
[3]Non-linearity in the transmission affects the quality of the noise measurements.

stays near 0.34 and slightly increases while RF is applied, as shown in figure 4.2. Those variations only weakly affect the shot noise, as will be explained in part 4.5.

Each point in a curve is averaged 80000 times and a noise resolution of $\sigma_{S_I} = 5 \cdot 10^{-30}$ A^2/Hz is reached, as detailed in the chapter 3.

4.1.2 Data processing of experimental results

This section presents the data processing of the experimental results. First, two examples of raw noise measurements as a function of V_{dc} are presented. They show a good agreement with the photo-assisted theory, except for an experimental offset σ in the noise level. Therefore, we propose an empirical study of this offset and we extract its dependence regarding the amplitude V_{ac}. It allows us to subtract this offset in the measurement of the noise $S_I(V_{ac})$ as a function of V_{ac} for a clear comparison with the photo-assisted theory.

Raw measurements of photo-assisted shot-noise as a function of DC polarisation

The figures 4.3 and 4.4 present two raw experimental measurements of the noise as a function of the DC polarisation, $S_I(q)$, or $S_I(V_{dc})$.

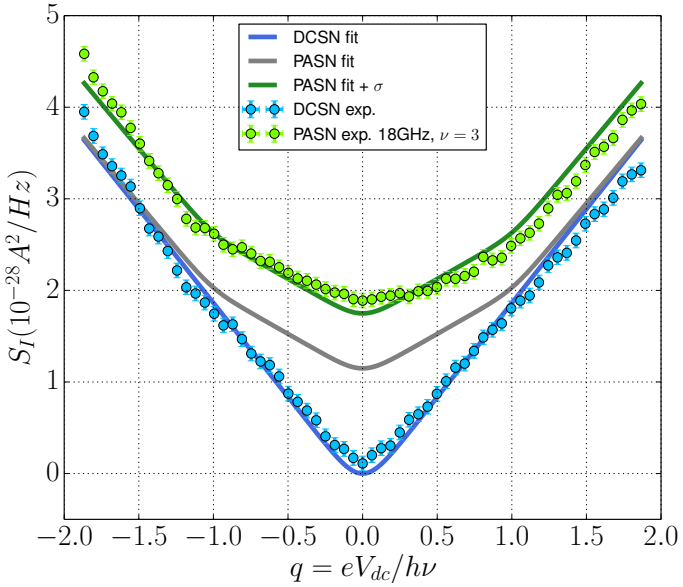

Figure 4.3: Noise measurements RF "off" (blue dots) and with RF "on" (green dots), $V_{RF} = 1.78$ V at 18 GHz and filling factor $\nu = 3$. The theoretical curve of DC Shot-noise (DCSN) is represented by the blue solid line. The theoretical photo-assisted (PASN) shot-noises curves for $\alpha = 1.51$ are represented respectively by the grey (without offset, $\sigma = 0$) and the green (with offset, $\sigma = 0.6 \cdot 10^{-28}$ A^2/Hz. Transmission : $D = 0.34$, electronic temperature: $T_e = 40$ mK. Experimental PASN is shifted compared to theoretical curve with an offset $\sigma \simeq 0.6 \cdot 10^{-28}$ A^2/Hz.

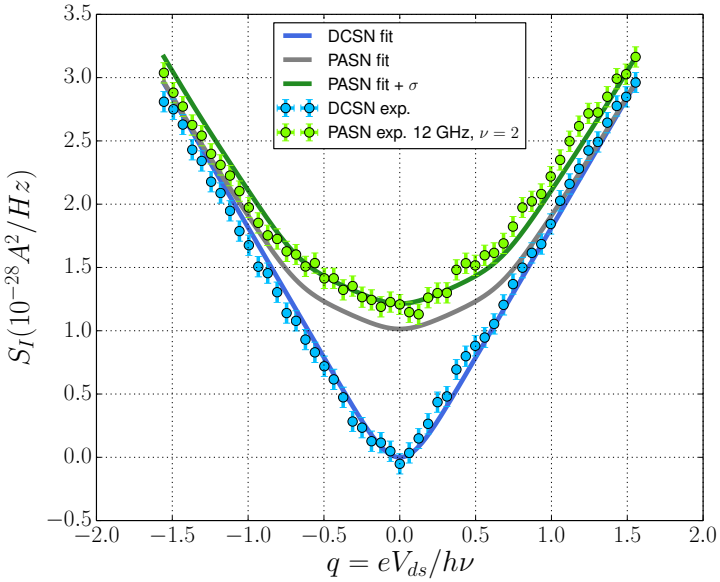

Figure 4.4: Noise measurements RF "off" (blue dots) and with RF "on" (green dots), $V_{RF} = 1.25$ V at 12 GHz and filling factor $\nu = 2$. Theoretical curves of DC Shot-noise (DCSN) and photo-assisted (PASN) shot-noise with $\alpha = 1.51$ are represented respectively with a blue and a green line. Transmission : $D = 0.34$, electronic temperature : $T_e = 40$ mK. Experimental PASN is shifted compared to theoretical curve with an offset $\sigma \simeq 0.2 \cdot 10^{-28}$ A^2/Hz.

The measured noise with (resp. without) RF voltages is represented by the green (resp. blue) dots. The parameters used are $V_{RF} = 1.78$ V at 18 GHz with a filling factor $\nu = 3$ in the figure 4.3 and $V_{RF} = 1.25$ V at 12 GHz with a filling factor $\nu = 2$ in the figure 4.4.

As explained in chapter 3, we do not have access to the absolute value of noise[4] S_I. In order to remove the unavoidable background noise, the measured DCSN is artificially set at zero at $V_{dc} = 0$. Thus, blue curves and dots verify $S_{I,DC}(0) = 0$. The measurements with RF voltages (in green) are performed simultaneously to the DC measurement (in blue) for each point, thus the distance between them is well known and the same amount of background noise is removed for both.

Empirical additional offset

The measurements without RF are fitted with a DCSN represented by the blue lines in the figures 4.3 and 4.4, and a good agreement is found with the data and no fitting parameter is used[5]. Simulations of PASN represented by the grey lines are computed with

[4] Absolute value of noise corresponds to a thermal term. Thus, it is not an issue for highlighting photo-assisted signatures in the noise, measured through its variations versus V_{dc} and V_{ac}.

[5] The thermal noise has been removed in order to recover the noise set at zero at $V_{dc} = 0$.

realistic parameters in order to reproduce the data in a first attempt[6]. We observe that the experimental data does not approach asymptotically the DCSN unlike the theoretical curves.

A second attempt consists in adding an offset σ to the curves of the theoretical PASN, which are represented by the solid green curves. Thanks to this additional offset a good agreement is founded between the data and the PASN model for both measurements at 12 and 18 GHz.

The effective AC voltage amplitude V_{ac} applied across the QPC and the observed offset σ are extracted from the fitting of the PASN measurements for a wide set of parameters (RF amplitude, frequency, filling factor). The measurements at low frequency (ie. $<$12 GHz) are not presented here. Then, the values of σ as a function of V_{ac} are reported in the figure 4.5 and we observe empirically that this offset does not depend on the frequency or the filling factor, but increases with respect to the amplitude V_{ac}.

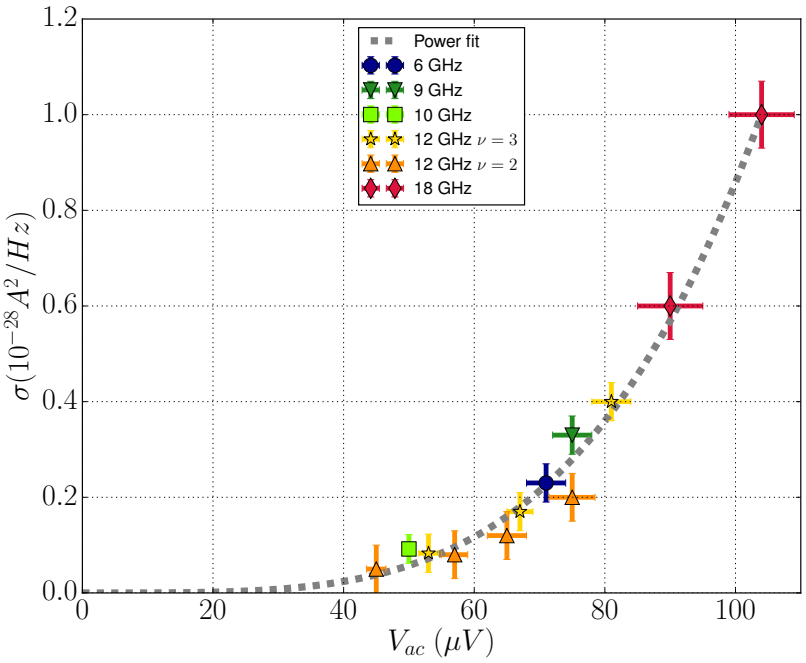

Figure 4.5: Observed offset as a function of V_{ac} in addition to the expected noise level measured in the cross-correlation σ. It is extracted from the fits of the $\Delta S_I(V_{dc})$ measurements.

More details of σ will be provided later in the section 4.5. From now, this offset is considered as a empirical law and is modelled by a power law:

$$\sigma(V_{ac}) = 1.36 \cdot 10^{-36} V_{ac}^{3.9} \tag{4.5}$$

[6]Similarly to the DCSN, thermal noise has been removed in the fitting function.

where V_{ac} is given in μV. It is important to note that the power 3.9 is a purely empirical law and is not based on physical considerations.

Finally, we empirically notice that the presence of this offset in the noise measurements and its dependence with respect to the AC voltage amplitude is understood. In the following, σ will be systematically removed from the measured noise. Furthermore, this analysis will be helpful in order to remove this additional noise from the measured noise $S_I(V_{ac})$ as a function of AC voltage amplitude, for a clear comparison with the theoretical models.

4.2 Results of excess noise measurement as a function of DC and AC polarisation

We present in this chapter noise measurements as a function of the DC polarisation, denoted $S_I(V_{dc})$ or $S_I(q)$, and as a function of the AC polarisation, $S_I(V_{ac})$ or $S_I(\alpha)$ when zero DC bias ($q = 0$) is applied. These two independent types of measurements give two determinations of the effective voltage V_{ac} applied across the QPC and should be consistent.

We first present the experimental results of the excess noise $\Delta S_I(V_{dc})$ as a function of the DC polarisation at several frequencies, amplitudes and at filling factors 2 and 3. A comparison with the photo-assisted model presented in the chapter 1 exhibits the clear quantum signature in the measured noise. Then, the subtraction of the quantity σ from the measured noise $S_I(V_{ac})$ is found consistent with the theoretical curves.

4.2.1 PASN as a function of DC polarisation

Excess noise measurements

The results of PASN measurements versus V_{dc} are presented as a noise in excess ΔS_I. As explained in chapter 1, ΔS_I is defined as the difference of the PASN and the DCSN:

$$\Delta S_I = S_I^{PASN} - S_I^{DCSN} = S_I(V_{dc}, V_{ac} \neq 0) - S_I(V_{dc}, V_{ac} = 0) \tag{4.6}$$

The experimental excess noise is obtained by subtracting the noise without RF voltages from the noise with RF voltage. This differential measure has several advantages:

- The small deviation between the theory and the measurement of PASN and DCSN neutralise themselves thanks the subtraction;
- The absolute value of noise is not required;
- The determination of the fitting parameters α (or V_{ac}) and σ is more convenient.

The measured noise is also expressed in terms of the excess number of electron-hole ΔN_{e-h}, which is defined as:

$$\Delta N_{e-h} = \frac{\Delta S_I(V_{dc})}{\frac{e^2}{h} D(1-D) h\nu}, \tag{4.7}$$

The excess number of electron-holes is the natural unit of the excess noise as it depends only on the $|p_l|^2 = |j_l|^2$ distribution.

The theoretical $\Delta S_I(V_{dc})$ used for the comparison[7] with the data differs from the

[7] Summation over l in eq. 4.8 goes from $-\infty$ to ∞. In practical, fitting are performed with least squares method with $l \in [-8; 8]$. It is reasonable because for $\alpha < l - 1$, Bessel functions becomes negligible : $|j_l(\alpha)|^2 \ll 1$.

expression found in chapter 1 by the offset σ:

$$\begin{aligned}\Delta S_I(V_{dc}) = 4k_BT\frac{e^2}{h}D(1-D)\left(1+\sum_{l=-\infty}^{\infty}|j_l(\alpha)|^2\frac{eV_{dc}+lh\nu}{2k_BT}\coth\left(\frac{eV_{dc}+lh\nu}{2k_BT}\right)\right)\\ -4k_BT\frac{e^2}{h}D(1-D)\left(1+\frac{eV_{dc}}{2k_BT}\coth\left(\frac{eV_{dc}}{2k_BT}\right)\right)-\sigma\end{aligned} \tag{4.8}$$

The fitting parameters are the reduced amplitude $\alpha = eV_{ac}/h\nu$ and offset σ.

Experimental results

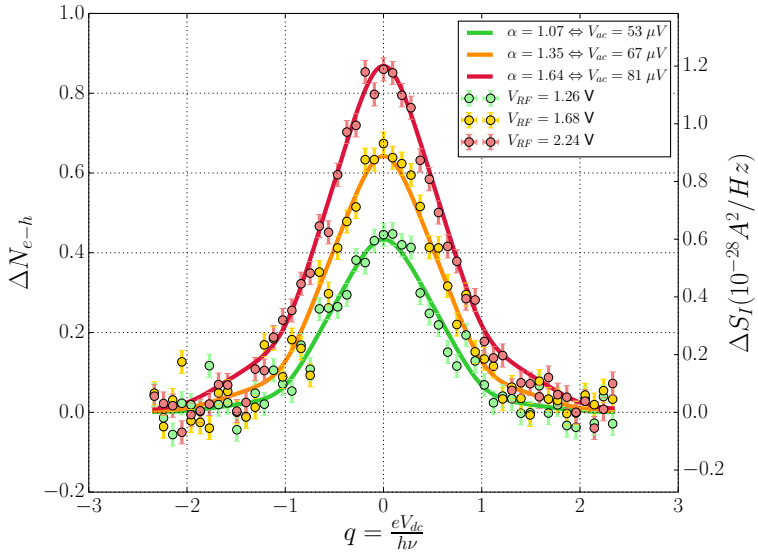

Figure 4.6: Reduced noise ΔN_{e-h} at 12 GHz for several RF voltage V_{RF}. Corresponding PASN fit (continuous line) has one fitting parameter, α. Transmission is $D = 0.34$ at filling factor $\nu = 3$. Offset has been removed from experimental data for a clear comparison between amplitudes.

Figures 4.6, 4.7 and 4.8 shows experimental excess noise $\Delta S_I(V_{dc})$ for several amplitudes V_{RF}, frequencies and filling factors (12 and 18 GHz, $\nu = 2, 3$). The offset σ has been removed from the data for a clear comparison between the different curves. The theoretical PASNs deduced from eq. 4.8 with the appropriate fitting parameters are represented by the solid curves.

It is important to note that the set of fitting parameters[8] (α, σ) that reproduce a PASN curve is unique[9], so that it is impossible to obtain the same fit by using another set of parameters. The PASN model reproduces faithfully the measured excess noise in the

[8]Each set (α, σ) can be recovered in the figure 4.5.

[9]If the transmission D is fixed. In our case, D is set independently with a good accuracy through conductance measurements.

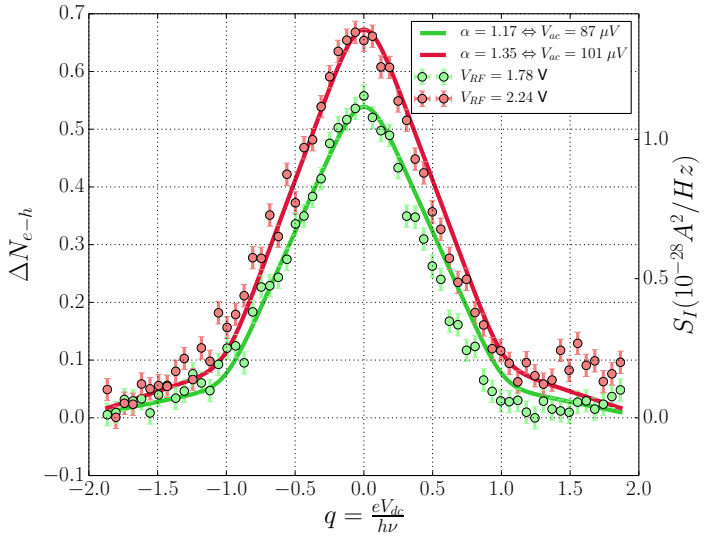

Figure 4.7: Reduced noise ΔN_{e-h} at 18 GHz for several RF voltage V_{RF}. Corresponding PASN fit (continuous line) has one fitting parameter, α. Transmission is $D = 0.34$ at filling factor $\nu = 3$. Offset has been removed from experimental data for a clear comparison between amplitudes.

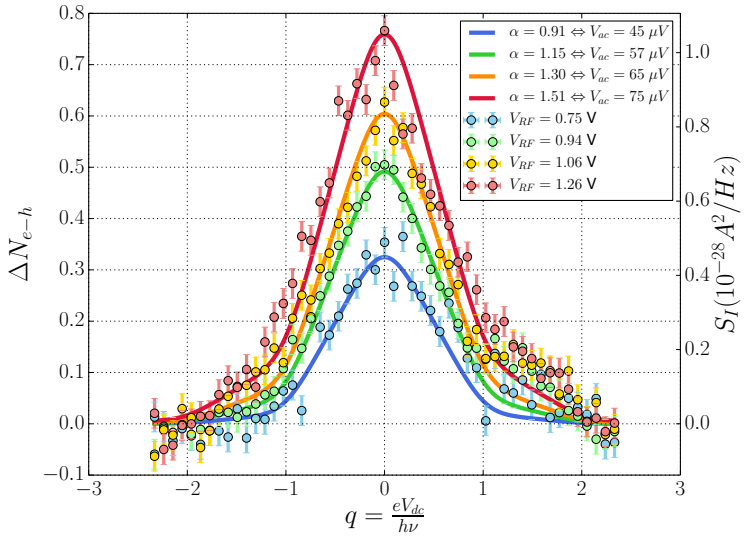

Figure 4.8: Reduced noise ΔN_{e-h} at 12 GHz for several RF voltage V_{RF}. Corresponding PASN fit (continuous line) has one fitting parameter, α. Transmission is $D = 0.34$ at filling factor $\nu = 2$. Offset has been removed from experimental data for a clear comparison between amplitudes.

curves presented here. Moreover, the expected breaks in the noise slope at $q = \pm 1$ are clearly visible, especially at 18 GHz in the figure 4.7: indeed, the reduced temperature $\Theta = 0.046$ is the weakest of those measurements. It highlights a signature of photo-assisted processes for two filling factors and two frequencies. We report in table 4.1 fixed

and fitting parameters of all measurements performed.

ν	Frequency (GHz)	V_{RF} (V)	V_{ac} (μV)	α	σ (10^{-28} A^2/Hz)
2	12	0.74	45	0.91	0.05
2	12	0.94	57	1.15	0.08
2	12	1.06	65	1.30	0.12
2	12	1.26	75	1.51	0.20
3	6	0.47	71	2.89	0.04
3	9	0.47	75	2.03	0.04
3	10	0.47	50	1.22	0.03
3	12	1.26	53	1.07	0.08
3	12	1.68	67	1.35	0.17
3	12	2.24	81	1.64	0.40
3	18	1.78	90	1.17	0.60
3	18	2.26	101	1.35	1.0

Table 4.1: Summary of parameters of the measured excess noise $\Delta S_I(V_{dc})$. Columns 1, 2 and 3 report the parameters fixed by the experimenter. The fitting parameters $V_{ac} = \alpha h\nu/e$ and σ extracted from experimental data fitted with eq. 4.8 are reported in columns 4 and 5.

4.2.2 Noise $S_I(V_{ac})$ as a function of AC voltage amplitude

Here, we present the noise measurement as a function of AC voltage amplitude, $S_I(V_{ac})$ without DC polarisation. It corresponds to the value for $V_{.dc} = 0$ of $\Delta S_I(V_{dc})$ curves previously studied. In the chapter 1, it has been shown that photo-assisted shot-noise versus V_{ac} presents typical oscillations, even at the limit $T = 0$, whereas the classical model is a linear function of V_{ac} (figure 1.10).

Offset subtraction and fitting function

The measured noise $S_I(V_{ac})$ includes a contribution of the offset σ, which must be removed from the experimental data for a comparison with the PASN model. In order to remove this additional noise, we proceed as follows.

The AC voltage amplitude is actually controlled through RF source amplitude V_{RF}, thus the noise is measured as a function of V_{RF} whereas the effective amplitude V_{ac} applied on the QPC is unknown as it depends on the factor[10] $k = V_{ac}/V_{RF}$. Therefore, the values of σ of the figure 4.5 has to be converted in terms of V_{RF} for each measurement. The empirical law of eq. 4.5 as a function of V_{RF} and k reads:

$$\sigma(V_{RF}) = 1.36 \cdot 10^{-30} \left(\frac{V_{RF}}{k}\right)^{3.9} = a \cdot V_{RF}^{3.9} \tag{4.9}$$

[10]The factor k depends on the transmission of the RF line which is unknown.

where parameter a is determined by the values of σ versus V_{RF} extracted from table 4.1, for each frequency and filling factor. We report the values of a corresponding to the measurements presented in part 4.2.1:

- 12 GHz, $\nu = 3$: $\sigma(V_{RF}) = 1.81 \cdot 10^{-30} \cdot V_{RF}^{3.9}$
- 18 GHz, $\nu = 3$: $\sigma(V_{RF}) = 4.66 \cdot 10^{-30} \cdot V_{RF}^{3.9}$
- 12 GHz, $\nu = 2$: $\sigma(V_{RF}) = 9.20 \cdot 10^{-30} \cdot V_{RF}^{3.9}$

where V_{RF} is given in Volts. The subtraction of the experimental noise $S_I(V_{RF})$ with the additional noise $\sigma(V_{RF})$ is denoted $\tilde{S}_I(V_{RF})$:

$$\tilde{S}_I(V_{RF}) = S_I(V_{RF}) - \sigma(V_{RF}) \tag{4.10}$$

$\tilde{S}_I(V_{RF})$ is the relevant quantity for a comparison with the theory than the raw data. Then, the data are compared with:

$$\begin{aligned}\tilde{S}_I(V_{RF}) = 4k_BT\frac{e^2}{h}D(1-D)\left(1+\sum_{l=-\infty}^{\infty}|j_l\left(k\frac{eV_{RF}}{h\nu}\right)|^2\frac{lh\nu}{2k_BT}\coth\left(\frac{lh\nu}{2k_BT}\right)\right) \\ - 4k_BT\frac{2e^2}{h}D(1-D)\end{aligned} \tag{4.11}$$

The thermal term $4k_BT\frac{2e^2}{h}D(1-D)$ is removed in order to set the noise at zero[11] when $V_{RF} = 0$. Eq. 4.11 corresponds to the formula of eq. 4.8, at $V_{dc} = 0$ as a function of the AC amplitude: $\alpha = k\frac{eV_{RF}}{h\nu}$. The fitting parameter here is coefficient factor k, reported in the legend of the figures.

Experimental results

The figures 4.9, 4.10 and 4.11 show raw experimental data $S_I(V_{RF})$ (grey) and transformed data $\tilde{S}_I(V_{RF})$ (color dots) at several frequencies and filling factors. The contribution of σ becomes important for noise levels greater than $1.0 \cdot 10^{-28}$ A^2/Hz. It is certainly overestimated at 18 GHz in figure 4.10, in which $\tilde{S}_I(V_{RF})$ decreases.

The maximum value of the curves in figure 4.6, 4.7 and 4.8 of the measure of $\Delta S_I(V_{dc})$ at $V_{dc} = 0$ are represented by the coloured diamonds[12] and are consistent with $\tilde{S}_I(V_{RF})$, except for measurement at 18 GHz, in which the offset is probably overestimated.

The theoretical noise deduced from eq. 4.11 represented by the solid lines are in a good agreement with the data. The typical oscillations of $S_I(V_{ac})$ curves shown in chapter 1 are not visible for $\alpha = eV_{ac}/h\nu < 2$, which is not reached in those measurements. However, the curvature for low V_{ac} is clearly visible and is a signature of the photo-assisted processes.

[11] Similarly to measurements in part 4.1.2, the background noise is removed in order to set noise at zero at zero voltage : $S_I(V_{ac} = 0) = 0$.

[12] It corresponds to values without the offset: $\Delta S_I(V_{dc} = 0) - \sigma$

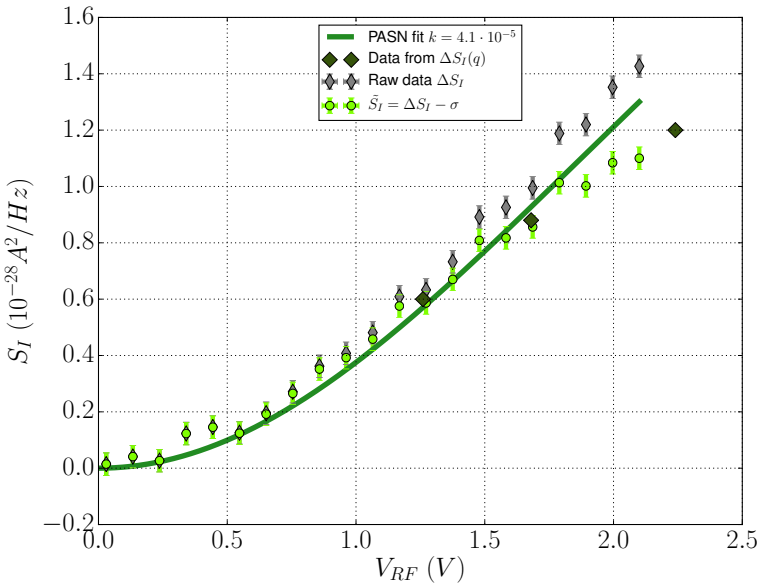

Figure 4.9: Experimental data (green dots) of noise $S_I(V_{RF})$ at $V_{dc} = 0$ with the corresponding PASN fit (green line). The diamonds represents the data $S_I(V_{ds} = 0)$ of the measurement presented in the figure 4.6. Frequency is 12 GHz, transmission $D = 0.34$, electronic temperature 40 mK, filling factor $\nu = 3$. The only fitting parameter is the attenuation coefficient $k = V_{ac}/V_{source}$.

The values of the fitting parameter k are reported in table 4.2 (third column). Similarly, we report in the second column the values of V_{ac} in terms of $k' = V_{ac}/V_{RF}$ deduced from the fit of $\Delta S_I(V_{dc})$ in the section 4.2.1 and are found consistent.

ν	Frequency (GHz)	$k' = V_{ac}/V_{RF}$ ($\times 10^{-5}$)	k ($\times 10^{-5}$) (fitting par.)
2	12	6.0	6.1
2	12	6.1	
2	12	6.1	
2	12	6.0	
3	12	4.2	4.1
3	12	4.0	
3	12	3.6	
3	18	4.9	4.3
3	18	4.5	

Table 4.2: Comparison between the coefficients $k = \frac{V_{ac}}{V_{RF}}$ deduced from the measurements of $\Delta S_I(V_{dc})$ (second column) and $\tilde{S}_I(V_{RF})$ (third column). Those are deduced from the comparison between the data and the PASN model in eq. 4.8 and 4.11.

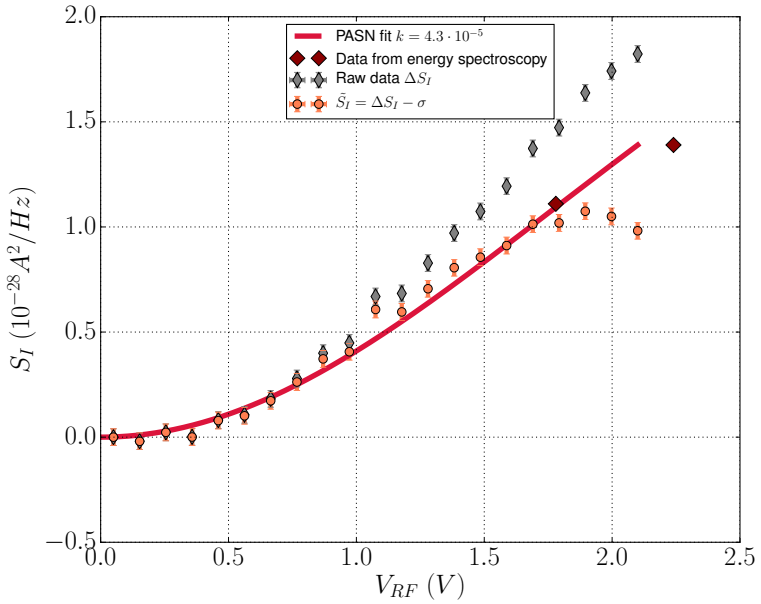

Figure 4.10: Experimental data (red dots) of noise $S_I(V_{RF})$ at $V_{dc} = 0$ with the corresponding PASN fit (red line). The diamonds represents the data $S_I(V_{ds} = 0)$ of the measurement presented in the figure 4.7. Frequency is 18 GHz, transmission $D = 0.34$, electronic temperature 40 mK, filling factor $\nu = 3$. The only fitting parameter is the attenuation coefficient $k = V_{ac}/V_{source}$.

4.3 Study of effective voltage V_{ac} for several filling factors

We propose to review the ratio $k = V_{ac}/V_{RF}$ between the RF source voltage and the effective AC voltage applied on the QPC at $\nu = 2$, $\nu = 3$ and $\nu = 4$. At a given frequency, the transmission of the RF lines does not vary with the magnetic field[13], thus a difference between the coefficients k for different filling factors must occurs on the sample level and not on the experimental set-up.

We report in the figures 4.12 and 4.13 amplitude on the QPC V_{ac} versus voltage of the RF source at $\nu = 4$, $\nu = 3$ and $\nu = 2$ (coloured dots) at respectively 12 and 18 GHz. The solid lines are linear fits deduced from those points, their slope is denoted k similarly to the definition proposed in eq. 4.1. Some of the points are extracted from data presented in the section 4.2, while others from results not shown here. At 18 GHz, there is no dependence on the filling factor: all the values follows the linear law of slope $k = 4.7 \cdot 10^{-5}$. It is comparable to the value of $4.3 \cdot 10^{-5}$ deduced from the fitting function of the measurements of $S_I(V_{ac})$. On the contrary, at 12 GHz, filling factor $\nu = 3$ gives a

[13]The coaxial wires of the RF line are made of non-magnetic material, so that no mechanical stress is applied when the field increases RF transmission is sensitive to the geometry of the wire. A mechanical stress applied on it can change notably the transmission and reflection coefficients.

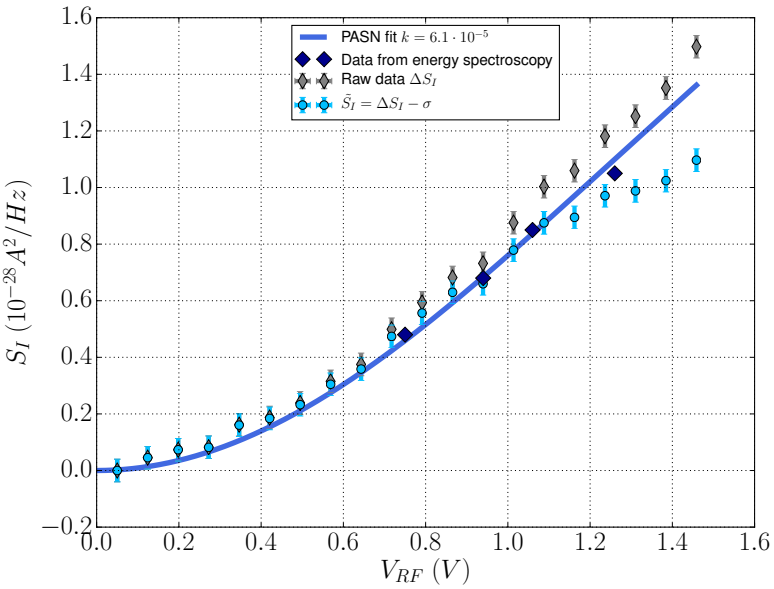

Figure 4.11: Experimental data (blue dots) of noise $S_I(V_{RF})$ at $V_{dc} = 0$ with the corresponding PASN fit (blue line). The diamonds represents the data $S_I(V_{ds} = 0)$ of the measurement presented in the figure 4.8. Frequency is 12 GHz, transmission $D = 0.34$, electronic temperature 40 mK, filling factor $\nu = 2$. The only fitting parameter is the attenuation coefficient $k = V_{ac}/V_{source}$.

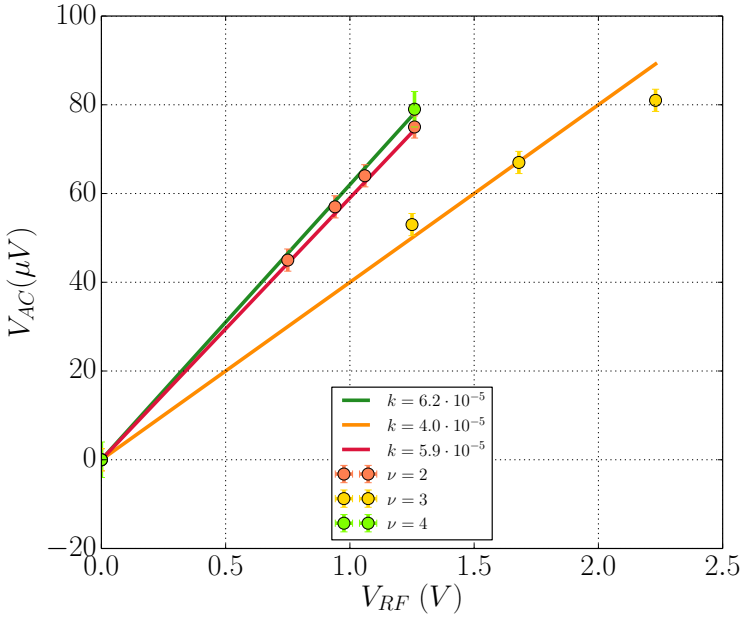

Figure 4.12: Amplitude V_{ac} as a function of RF source voltage V_{RF}, deduced from $\Delta S_I(V_{dc})$ measurement with PASN fitting function, for several filling factor. Frequency is 12 GHz. Continuous lines are linear fit with their respective slope denoted k.

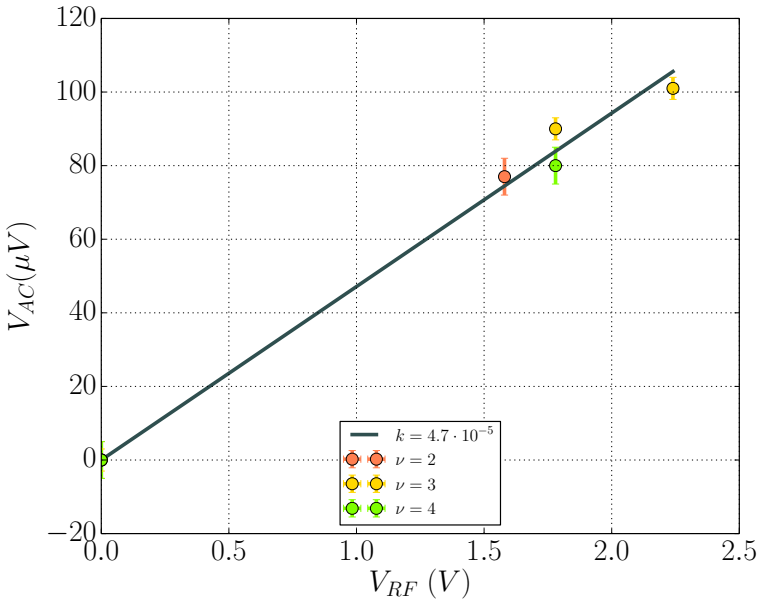

Figure 4.13: Amplitude V_{ac} as a function of RF source voltage V_{RF}, deduced from $\Delta S_I(V_{dc})$ measurement with PASN fitting function, for several filling factor. Frequency is 18 GHz. Continuous lines are linear fit with their respective slope denoted k.

coefficient of $k = 4.0 \cdot 10^{-5}$ while at $\nu = 2, 4$, $k \simeq 6.0 \cdot 10^{-5}$.

4.4 Comparison with a classical model

In this section, we propose to compare the experimental results of $\Delta S_I(V_{dc})$ and $\tilde{S}_I(V_{ac})$ presented previously in 4.2 with a classical model, which corresponds to the adiabatic modulation of a DCSN. This comparison with this classical model highlights that our measurements cannot be explained without photo-assisted processes.

4.4.1 Classical noise

The data presented in the following are the same as those presented in part 4.2 and are now compared to the average of a sine modulation of DC shot-noise (written in the second line of eq. 4.8), due to the voltage modulation of contact 0: $V_0(t) = V_{dc} + V_{ac}\cos(2\pi\nu t)$. The expression of the classical (or adiabatic) noise reads:

$$S_{I,adiab.} = \nu \int_0^{\frac{1}{\nu}} dt S_I(V_0(t)) \tag{4.12}$$

Thus, following this picture, the excess noise is:

$$\begin{aligned}\Delta S_{I,adiab.} = {} & 4k_BT\frac{e^2}{h}D(1-D)\nu\int_0^{\frac{1}{\nu}} dt\ \frac{eV_{dc}+eV_{ac}\cos(2\pi\nu t)}{2k_BT}\coth\left(\frac{eV_{dc}+eV_{ac}\cos(2\pi\nu t)}{2k_BT}\right) \\ & - 4k_BT\frac{e^2}{h}D(1-D)\frac{eV_{dc}}{2k_BT}\coth\left(\frac{eV_{dc}}{2k_BT}\right)+\sigma\end{aligned} \tag{4.13}$$

The fitting parameters are the AC amplitude V_{ac} and the offset σ. The adiabatic noise in excess does not exhibit signatures in the slope of the noise at $q \pm 1$ but has a continuous derivative, even at the limit $T = 0$. Nevertheless, the pyramidal shape of the adiabatic noise is similar to the PASN, which makes the distinction of the classical and PASN model hard for $\alpha > 2.5$ or $\nu < 10$ GHz. Thus, the comparison is done at 18 GHz in the figure 4.14 which shows the classical model represented by the dashed lines and the measured noise versus V_{dc}.

At $V_{dc} = 0$, the data and the best fit deduced from the eq. 4.13 (dashed lines) clearly differs from each other, as shown in the chapter 1. Moreover, the fit does not reproduce the abrupt change in the slope of the experimental curve that occurs at $V_{dc} = 73\ \mu$V (i.e. $q = 1$).

4.4.2 Noise $S_I(V_{ac})$ as a function of AC voltage amplitude

We compare here the measured noise $S_I(V_{ac})$ with the classical model by following the same procedure done in the section 4.2.2 in order to remove the additional noise due to

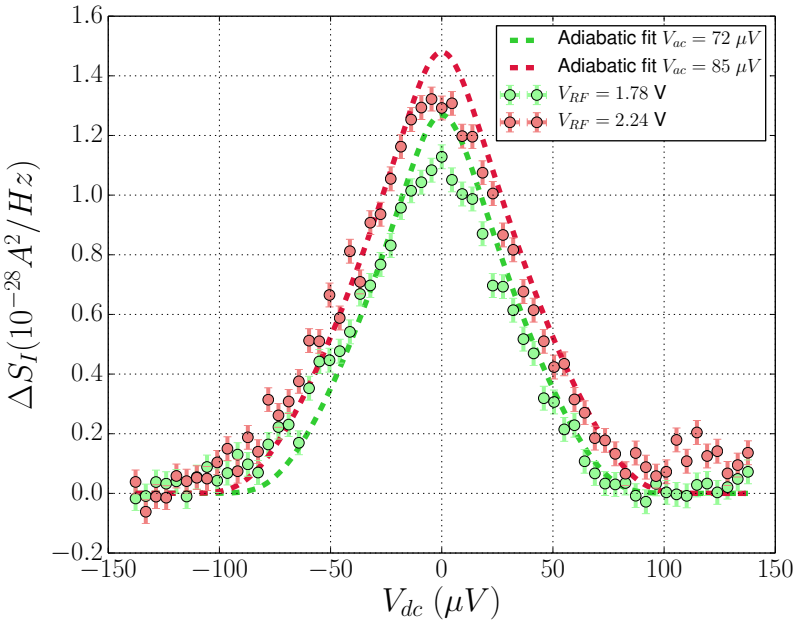

Figure 4.14: Comparison between experimental data $\Delta S_I(V_{dc})$ (coloured dots) and a classical model defined in 4.13 (dashed lines), parameters are: 18 GHz, $\nu = 3$. The fit does not reproduce as well the data than the photo-assisted theory.

the offset. In this case, the offset σ is modelled as a power[14] 4.2 versus V_{RF}. Thus, the empirical law of σ are:

- 12 GHz, $\nu = 3$: $\sigma(V_{RF}) = 1.62 \cdot 10^{-30} \cdot V_{RF}^{4.2}$
- 18 GHz, $\nu = 3$: $\sigma(V_{RF}) = 4.12 \cdot 10^{-30} \cdot V_{RF}^{4.2}$
- 12 GHz, $\nu = 2$: $\sigma(V_{RF}) = 9.02 \cdot 10^{-30} \cdot V_{RF}^{4.2}$

where V_{RF} is given in Volts. The figure 4.15 shows raw experimental data $S_I(V_{RF})$ (grey) and transformed data $\tilde{S}_I(V_{RF})$ defined in eq. 4.10 (color dots) at 18 GHz at filling factor $\nu = 3$. Again, σ is overestimated at 18 GHz in figure 4.10, where $\tilde{S}_I(V_{RF})$ decreases. The dashed line represents the theoretical adiabatic noise, which is:

$$S_{I,adiab.}(V_{RF}) = 4k_BT\frac{e^2}{h}D(1-D)\nu\int_0^{\frac{1}{\nu}} dt\left(1 + \frac{ekV_{RF}\cos(2\pi\nu t)}{2k_BT}\coth\left(\frac{ekV_{RF}\cos(2\pi\nu t)}{2k_BT}\right)\right) - 4k_BT\frac{2e^2}{h}D(1-D) \tag{4.14}$$

[14] In the framework of the adiabatic model value of V_{ac} fitted are lower than in the adiabatic fit. Variation of offset σ as a function of V_{ac} is more abrupt and follows a 4.2 power law.

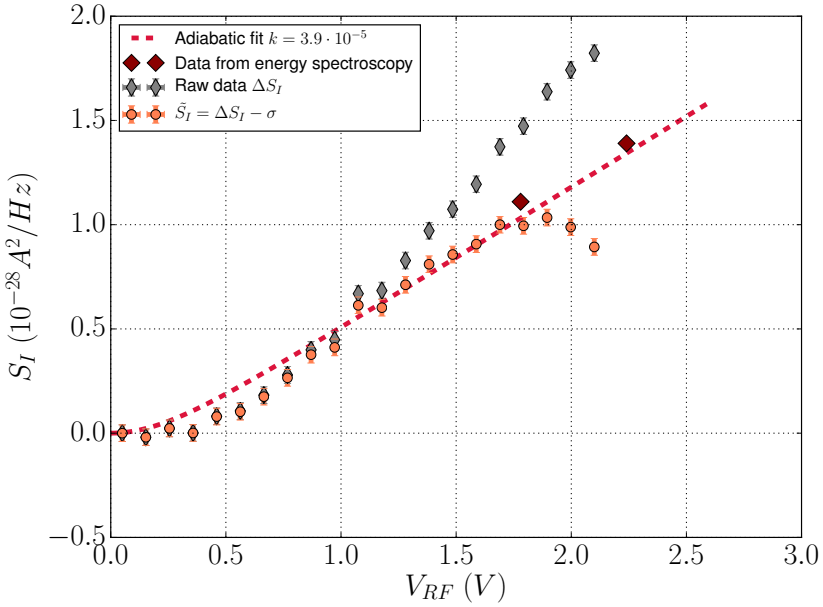

Figure 4.15: Experimental data (red dots) of noise $S_I(V_{RF})$ at $V_{dc} = 0$ with the corresponding adiabatic fit (dashed red line). Frequency is 18 GHz, transmission $D = 0.34$, electronic temperature 40 mK, filling factor $\nu = 3$. The only fitting parameter is the attenuation coefficient $k = V_{ac}/V_{source}$.

The measured noise $\tilde{S}_I(V_{RF})$ follows the asymptomatic linear evolution of the classical model with a good agreement but does not reproduce the typical curvature of the data for $V_{RF} < 1.0$ V. This illustrates that the PASN notably differs from the adiabatic noise for $V_{ac} \simeq h\nu/e$ but approaches it at large AC modulations.

ν	Frequency (GHz)	$k' = V_{ac}/V_{RF}$ ($\times 10^{-5}$)	k ($\times 10^{-5}$) (fitting par.)
2	12	5.2	4.9
2	12	5.4	
2	12	5.7	
2	12	5.2	
3	12	3.3	3.5
3	12	3.5	
3	12	3.5	
3	18	4.0	3.9
3	18	3.8	

Table 4.3: Comparison between the coefficients $k = \frac{V_{ac}}{V_{RF}}$ deduced from the measurements of $\Delta S_I(V_{dc})$ (second column) and $\tilde{S}_I(V_{RF})$ (third column). Those are deduced from the comparison between the data and the PASN model in eq. 4.13 and 4.14.

The values of the fitting parameter k are reported in table 4.3 (third column) with the values of $k' = V_{ac}/V_{RF}$, deduced from the fitting parameters of $\Delta S_I(V_{dc})$ in the second column. Coefficients k and k' reported are found consistent between each other despite

smaller than in the case of the PASN model. Finally, the most relevant comparison with the models is the shape of the curves. In particular, the data notably differs with the adiabatic model for $\alpha = 1$, as shown in the figure 4.15. The temperature is small enough for a clear distinction between PASN and classical models.

4.5 Experimental offset in PASN measurements in the QHE regime

The experimental measurements presented in 4.2 are clearly in a good agreement with the photo-assisted theory, except from the offset σ highlighted in the section 4.1.2. Yet, similar measurements of PASN performed without magnetic field [114, 106, 69] do not exhibit an offset in the excess noise. Here, we attempt to pinpoint the origin of σ found in our experiments.

4.5.1 Offset in the auto and cross-correlation

The offset is clearly visible in the measurements of the excess noise $\Delta S_I(V_{dc})$, performed according to an "on-off" procedure: the noise is successively measured with a finite RF voltage of amplitude V_{ac}^{on} and then with the minimum value delivered by the RF source: $V_{ac}^{off} < 1\ \mu$V[15], which ensures that no PASN is generated.

The figure 4.16 presents the measurements of the autocorrelations[16] denoted $A \times A$ and $B \times B$ and of the cross-correlation $A \times B$, at 18 GHz and $\alpha = 1.4$. An offset in noise appears clearly and is similar for $A \times B$ and $B \times B$, and is larger for $A \times A$:

$$\sigma_{A\times A} \simeq 1.5 \cdot 10^{-28}\ \text{A}^2/\text{Hz} \tag{4.15}$$

$$\sigma_{A\times B} \simeq \sigma_{B\times B} \simeq 1.0 \cdot 10^{-28}\ \text{A}^2/\text{Hz} \tag{4.16}$$

4.5.2 Review of possible sources of noise

We propose to review several hypothesis in order to understand this additional offset.

Additional partitioning noise

An extra partitioning noise could be generated by a DC current, called rectification current, resulting in the combination of the AC drain-source voltage and the energy-dependent transmission of the QPC, as it will be discussed later in chapter 5. However, this shot-noise would add the same amount of noise in the auto and the cross-correlation, which is not the case.

[15] During the "on-off" procedure, the "off" measurement is done at -20 dBm power, which is typically a hundred times lower than the power "on" and the GHz voltage applied can be considered to be 0. It allows us to avoid parasitics noises induced by switching off the RF source while experiment is running.

[16] As detailed in figure 5.1, channel A (respectively B) measures reflected (transmitted) currents.

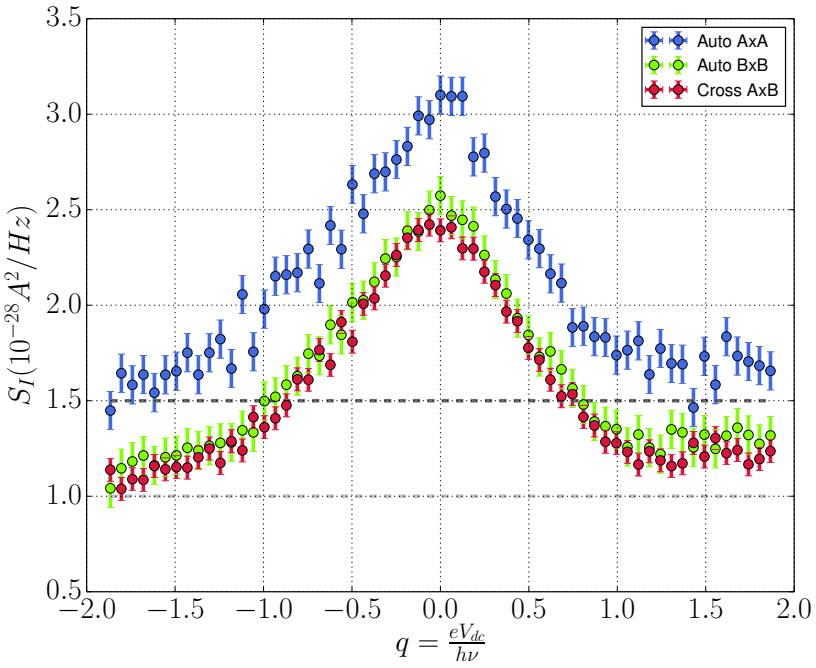

Figure 4.16: Measurements of noise $\Delta S_I = \Delta N_{e-h} \cdot S_{I0}$ for auto-correlation of channels A and B and cross correlation. Frequency is 18 GHz, $\alpha = 1.4$, transmission $D = 0.34$, filling factor $\nu = 3$. Grey lines indicate offsets σ_A and σ_B.

Transmission variation

In the figure 4.2, we saw that the transmission varies from 0.34 to 0.4 and therefore makes the partitioning factor $D(1-D)$ increase from 0.2244 to 0.24. This variation corresponds to add in the cross correlation an amount of $\simeq 1.2 \cdot 10^{-29}$ A^2/Hz, ten times lower than the effective offset reported in figure 4.16 under same the conditions. Consequently, the variation of the transmission cannot explain the offset.

Heating

The electronic temperature is $T = 40$ mK but RF voltages applied on the contact 0 may increase the temperature of electrons emitted by this contact: $T_0 = T + \Delta T_0$. Similarly, dissipation can indirectly heat the contact 3: $T_3 = T + \Delta T_3$. Then, using the expression of DCSN developed in the chapter 1, the thermal part of the cross-correlation noise reads:

$$S_{I_1 \times I_4} = \frac{4e^2}{h} k_B R D (T_0 + T_3) + S_I^{part.} \tag{4.17}$$

where R and D are the coefficients of reflection and transmission and $S_I^{part.}$ is the term of partitioning noise not developed here[17]. In the hypothesis of heating, the offset $\sigma_{A\times B}$ in

[17] The offset σ cannot be explained by partitioning noise because it doesn't depend on V_{dc}.

the cross-correlation thus corresponds to the noise due to the extra temperatures:

$$\sigma_{A\times B} = 4\frac{e^2}{h}k_B RD(\Delta T_0 + \Delta T_3) \tag{4.18}$$

By using the value of offset from figure 4.16 measured for a transmission $D = 0.34$, we obtain:

$$\Delta T_0 + \Delta T_3 = 210 \text{ mK} \tag{4.19}$$

Those temperatures increase are large compared to the base temperature. Indeed, even in the case of a homogeneous heating, $\Delta T_0 = \Delta T_3 = 105$ mK, the electronic temperature goes up to 140 mK which make the photo-assisted processes vanish. The purple curve in the figure 4.17 is a simulation of PASN with a temperature of $T = 145$ mK and does not reproduce the data presented in the figure 4.7, on the contrary to the dark blue curve which represents a PASN at 40 mK. Thus, heating seems not a relevant cause of the noise offset.

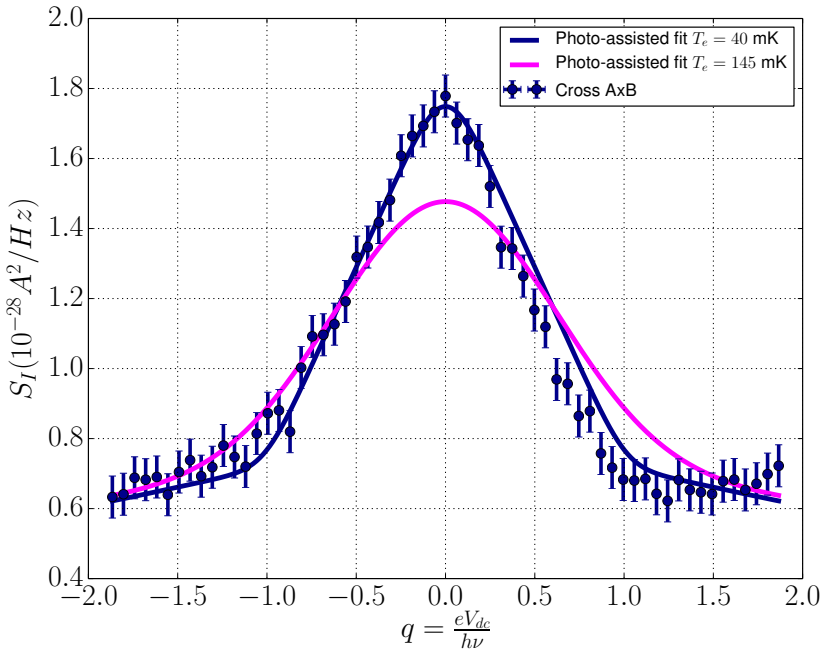

Figure 4.17: Cross-correlation PASN measurement at 18 GHz and $\alpha = 1.4$ (Blue dots). PASN fit with $T_e = 40$ mK (blue line). PASN fit with $T_e = 145$ mK (purple line). The experimental results are not relevant with a electronic temperature of 145 mK.

External white noise

Another hypothesis is an external white-noise source, for instance the RF source, connected to the contact 0, generating an additional noise while RF is applied. This assump-

tion seems wrong for two reasons. First, it leads to extremely large values of injected noise. Indeed, the amount of noise of the offset is $\sim 10^{-28}$ A^2/Hz, equivalent to a voltage noise source of $S_{V,ext} = (h/\nu e^2)^2\sigma$ applied on the contact 0. Because of the -80 dBm attenuation, it corresponds to an external white noise of 10^{-13} V^2/Hz injected[18]. For comparison, the data-sheet of Agilent N5183A specifies an intrinsic noise of -113 dBc between 250 kHz to 250 MHz, so σ does not result of the RF source.

Secondly, this hypothesis is inconsistent with the different values of σ regarding the auto or cross-correlation, no matters the nature of this external white noise source. Suppose this parasitic source is connected to the contact 0 and inserts an additional noise which reads:

$$\sigma_{A\times A} \propto (2\nu - 1 + R^2) \cdot S_{I,ext} \tag{4.20}$$

$$\sigma_{B\times B} \propto D^2 \cdot S_{I,ext} \tag{4.21}$$

$$\sigma_{A\times B} \propto RD \cdot S_{I,ext} \tag{4.22}$$

where $S_{I,ext}$ is the spectral density of external white noise source. At filling factor $\nu = 3$, $\sigma_{A\times A} = 2.66 S_{I,ext}$, $\sigma_{A\times A} = 0.12 S_{I,ext}$ and $\sigma_{A\times A} = 0.22 S_{I,ext}$, which is not consistent with the results 4.16. An external white noise source cannot describe this offset.

Environment interferences

In the chapter 3, we reported the presence of interferences in Power Spectral Density (PSD) measurements due to the electromagnetic environment: for instance, the cross-correlation PSD at the equilibrium is finite, because of the the unavoidable background noise removed in the data processing, as explained in part 4.1.2. The RF source is connected to electrical background of the experimental set-up and we cannot exclude the fact that it inserts an additional noise which increases regarding RF voltages. But σ depends only on V_{ac} and not on V_{RF}, which is clearly visible in table 4.1. As V_{ac} is the local voltage applied on the QPC, it suggests that this effect occurs at the QPC scale and not at the experimental set-up scale.

[18] It corresponds to voltage fluctuation of ~ 80 mV on the 10 MHz passband. In comparison, thermal noise for a 50 Ω impedance at 300 K has a spectral power of $8{\cdot}10^{-19}$ V^2/Hz and 9 μV voltage fluctuations.

4.6 Conclusion

The first measurements of photo-assisted shot-noise in quantum Hall effect, for a large set of parameters, have been reported here. More precisely, we performed two independent types of measurements: the excess noise as a function of the DC polarisation, $\Delta S_I(V_{dc})$, and the noise as a function of AC voltage amplitude, $S_I(V_{ac})$.

We observe the presence of an additional noise, appearing as an offset in the $\Delta S_I(V_{dc})$ measurements. This was not reported in the experiments performed without magnetic field[71]. A thorough investigation shows that this offset depends only on the effective AC amplitude applied on the QPC V_{ac}.

Except from this experimental offset, the fitting parameters extracted from the noise measurements as a function of DC voltage $\Delta S_I(V_{dc})$ are consistent with those founded with the measurement of noise as a function of AC polarisation, $S_I(V_{ac})$. The theoretical curves of PASN are in good agreement with the experimental data, especially at a frequency of 18 GHz, where the photo-assisted processes are dominant in comparison to the thermal effects. Moreover, the characteristic signatures of photo-assisted processes show that experimental results cannot be explain with an adiabatic model.

Chapter 5

Quantum switch noise: experimental results

The experimental quantum signatures of the Photo-Assisted Shot-Noise (PASN) have been shown in the previous chapter. In this part, we present the experimental results of the current noise generated by a switched quantum conductor: a Quantum Switch (QS). A QS is implemented by pulsing the gate voltage of a Quantum Point Contact (QPC): an elementary conductance channel is opened and closed at GHz frequencies, connecting and disconnecting two quantum systems, here the two side of a quantum conductor, creating an uncertainty in the number of particles initially delocalized between the two systems. Their fast separation thus generates a fundamental noise due to the projection of the particle number on the left or the right side as recently discussed in [76]. From the theoretical framework developed in chapter 1, we expect to measure current fluctuations of the order of $S_{I,QS} \simeq 10^{-29}$ A^2/Hz. Measuring this noise is an experimental challenge: for comparison, it is ten times lower than the PASN presented in the previous chapter.

The chapter is organized as follows. In section 1, we first present experimental details and the measurement protocol, allowing us to discriminate the noise generated by the QS from other sources of noise. Then, we present in section 2 measurements performed without magnetic field. Experimental results are found in a good agreement with the expected theoretical framework developed in chapter 1, showing that QS noise is experimentally observed. To account for capacitive effects not included in the ideal theoretical model, the coupling between the electrostatic gate and the 2 Dimensional Electron Gas (2DEG) of the QPC is modelled in section 3. Finally, in section 4, QS experiments are reported in the Quantum Hall Effect (QHE) where the pulsed QPC conductance exhibits an unexpected behaviour.

5.1 Experimental protocol

The goal of the experiment is the measurement of the intrinsic noise of a quantum switch. It is implemented by modulating the gate voltage of a QPC at GHz frequencies, in which noise generated is measurable with our experimental set-up.

5.1.1 Experimental set-up

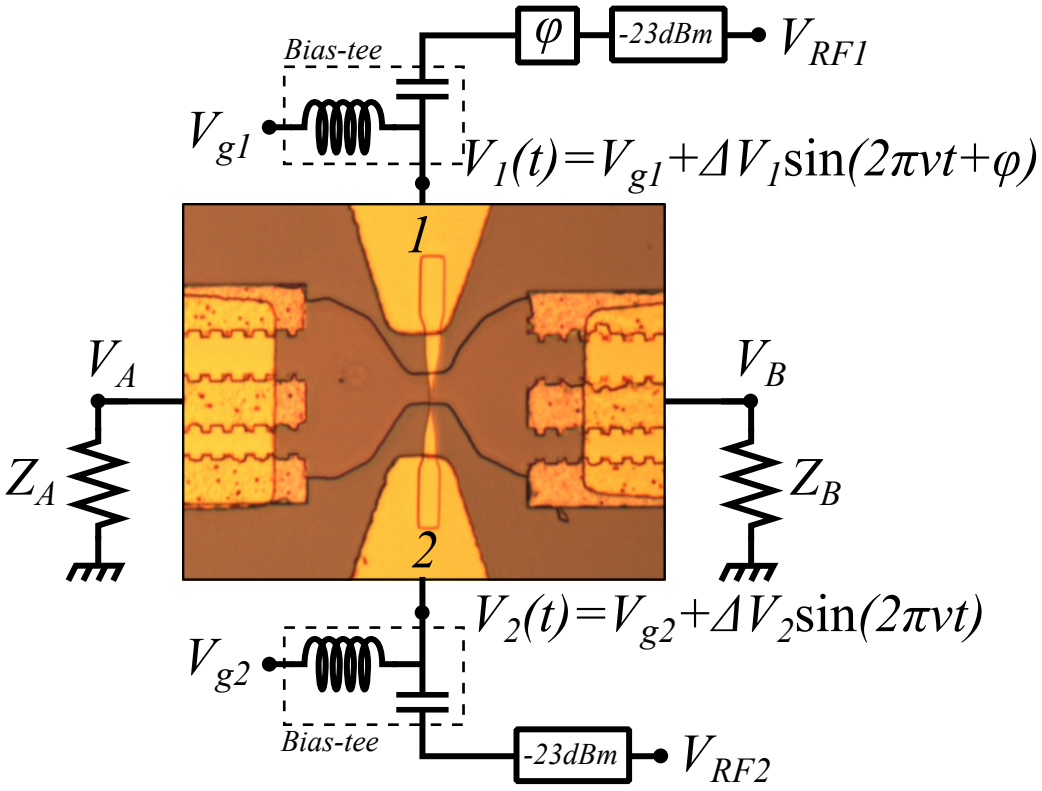

Figure 5.1: Simplified schematic of the quantum switch set-up. The picture in the center is an optical image of sample 1 presented in chapter 2. Noise measurements are performed through voltages V_A and V_B of the two ohmic contacts (gold structures at left and right sides). Periodic voltages $V_1(t)$ and $V_2(t)$ are applied on each gate (gold triangular shape on the top and the bottom) thanks to a bias-tee. There are two attenuators of -3 and -20 dBm in each RF line in order to reduce the thermal noise from 300 K. A phase shift module allows us to control the phase difference between $V_1(t)$ and $V_2(t)$.

The experimental set-up is similar to the PASN experiments, except that high frequencies lines are now connected to the gate of the QPC. The QS experiment is implemented as follows: a DC voltage applied on the gate controls the mean transmission of a conduction channel, while an additional AC voltage varies the transmission between 0 and 1 at GHz frequencies. This corresponds to opening and closing a quantum wire of conductance $2e^2/h$[1]: an elementary quantum switch.

[1] Conductance of a channel is e^2/h in the quantum Hall effect.

A reminder of the experimental set-up of the experiment is presented on figure 5.1. The 2-contacts QPC used here is the sample 1 presented in chapter 2. Measurements are performed without magnetic field (in section 5.2) and in the quantum Hall effect regime (in section 5.4). Voltages V_A and V_B give access to current fluctuations S_I generated by the sample through impedance Z_A and Z_B, as explained in chapter 3.

Thanks to two bias-tee, the two gates of the QPC (denoted by index 1 and 2) are polarised with DC voltages V_{g1} and V_{g2}, in addition to high frequency voltages of amplitude ΔV_1 and ΔV_2 at the frequency ν . The resulting total voltages $V_1(t)$ and $V_2(t)$ (figure 5.1) are applied independently on each gate. We used two synchronised RF sources (Agilent N5183A and Anritsu 69147B) while a phase shifter in line 1 sets their relative phase. Thus, we control separately DC voltage, AC amplitude and phase shift of the RF voltages applied on the gates (figure 5.1).

The base electronic temperature is 36 mK without magnetic field and is 50 mK in the QHE regime. Heating effects due to the RF pulses will be discussed in detail in section 5.3.2. Noise is calibrated with Johnson-Nyquist noise, as presented in chapter 3. The noise measurements presented in the following are averaged 40000 times. Error bar is $\sim 2 \cdot 10^{-30}$ A^2/Hz.

5.1.2 Principle of measurement

The noise generated by the Quantum Switch, or QS noise, is small in comparison with the DC shot-noise or the thermal noise, therefore its experimental signature must be clearly discriminated. A first attempt is to perform a DC Shot-noise (DCSN) while transmission is pulsed at GHz frequencies. As shown in chapter 1, the QS noise appears in this experiment through an offset in the noise level and with abrupt changes in the slope, similarly to the PASN. However, this measurement of DCSN is not relevant experimentally for two reasons. Firstly, as explained in chapter 3, we do not have access to the absolute value of the noise while many parameters change when gates are pulsed (mean transmission D, temperature, parasitic current). Secondly, abrupt changes in the slope of the DCSN vanishes quickly with temperature increasing.

We propose here to measure the QS noise as a function of the transmission of the QPC without DC voltage polarisation. More precisely, we proceed as follows:

- A sine voltage of frequency ν is applied with the same amplitude $\Delta V = \Delta V_1 = \Delta V_2$ on both gates.

- The noise measurement is performed as a function of the mean transmission D_m of the QPC, controlled by the DC voltage $V_G = V_{g1} = V_{g2}$.

This procedure presents several advantages in order to experimentally evidence the QS noise, illustrated in the following by a simulation which is helpful for the understanding

of the experimental results.

Mean transmission

The mean transmission D_m corresponds to the averaged transmission of the QPC when the gates are pulsed. In the figure 5.2, the schematic shape of the transmission D (without pulsing) as a function of the gate voltage V_G is represented by the black solid line. The transmission is time-dependent thanks to the sine modulation $\Delta V \sin(2\pi\nu t)$ applied on the gate voltage in addition to V_G, so that its mean value D_m is[2]:

$$D_m(V_G) = \nu \int_0^{1/\nu} dt\ D(V_G + \Delta V \sin(2\pi\nu t)) \tag{5.1}$$

According to the protocol, the noise is measured while D_m varies from the case of an opened switch ($V_G < -1.5$ V, $D_m = 0$) to the case of a closed switch ($V_G = -1.1$ V, $D_m = 1$).

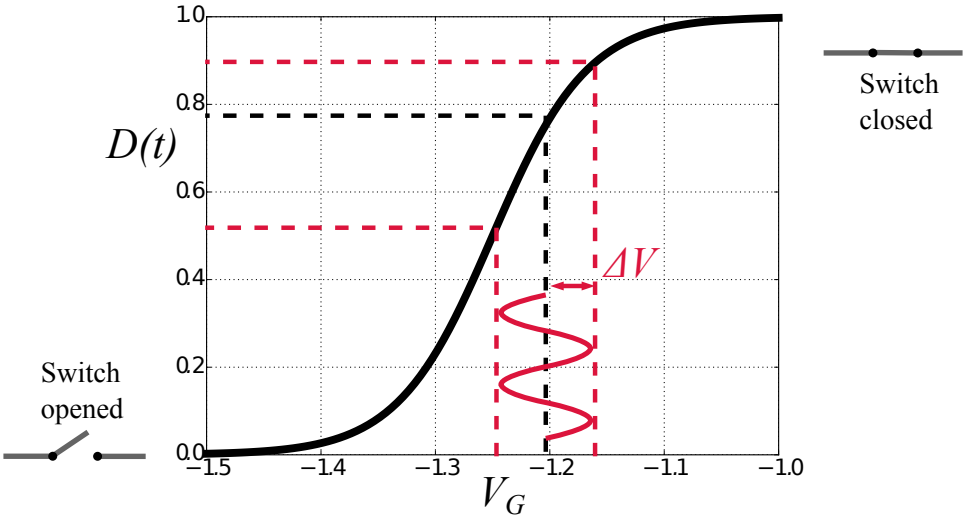

Figure 5.2: Black curve is a simulation of the QPC transmission $D(V_G)$ versus DC gate voltage V_G, using the saddle point model [17] presented in the chapter 2. A sine voltage $\Delta V_G \sin(2\pi\nu t)$ in addition to V_G leads to an oscillating transmission $D(V_G + \Delta V \sin(2\pi\nu t))$ between a closed QPC ($D = 0$, switch opened) and a opened QPC ($D = 1$, switch closed). In this case, an amplitude of 250 mV is required in order to open and close completely the switch.

[2] As shown in chapter 2, the current reads in the case of a modulation of the transmission: $I = \frac{2e^2}{h}|\tau(t)|^2 V_{dc}$. Therefore, the transmission measured at low frequency is the average of $|\tau(t)|^2$.

Simulation of the QS noise as a function of the mean transmission

The QS noise as a function of D_m without polarisation voltage is simulated thanks to the theoretical framework developed in chapter 1 and is displayed in the figure 5.5, left. The temperature used in these simulations is 250 mK, which corresponds to the typical temperature measured experimentally[3]. The total noise, represented by the solid line, is composed of the QS noise, S_I^{QS}, and the Johnson-Nyquist noise (or thermal noise), $S_I^{th.}$ given by:

$$S_I^{th.} = \nu \int_0^{1/\nu} dt\ 4k_BT\frac{2e^2}{h}D(t) = 4k_BT\frac{2e^2}{h}D_m \tag{5.2}$$

Thus, $S_I^{th.}$, represented by the dashed line, is a linear function of D_m while the total noise is slightly curved by the additional QS noise S_I^{QS}. Therefore, the QS noise corresponds to the excess noise, $\Delta S_I(D_m)$, defined by:

$$\Delta S_I(D_m) = S_I(D_m) - S_I^{th.}(D_m) \tag{5.3}$$

The simulated excess noise $\Delta S_I(D_m)$ is displayed in the figure 5.3 for several amplitudes of modulation ΔV: the parabolic shape is the signature of the expected quantum switch. Finally, the measurement of the noise as a function of D_m is relevant for two reasons:

- It is experimentally convenient to extract the excess noise ΔS_I from the total measured noise by subtracting the linear contribution of the thermal noise versus D_m;
- despite the unavoidable heating effects which make the QS noise vanish, the excess noise reaches amplitude of $\Delta S_I \simeq 10^{-29}$ A^2/Hz and is measurable by our experimental set-up for the usual experimental conditions.

It is important to note that the curves of QS noise simulated of figure 5.3 are obtained using the Büttiker saddle-point model[17] of transmission detailed in chapter 2, where ΔS_I is symmetric at $D_m = 0.5$. Realistic transmissions depart from this model and impact ΔS_I versus D_m. Each experimental curve is therefore compared to the transmission actually measured during the noise data acquisition.

[3]Those heating effects detailed in section 5.3.2

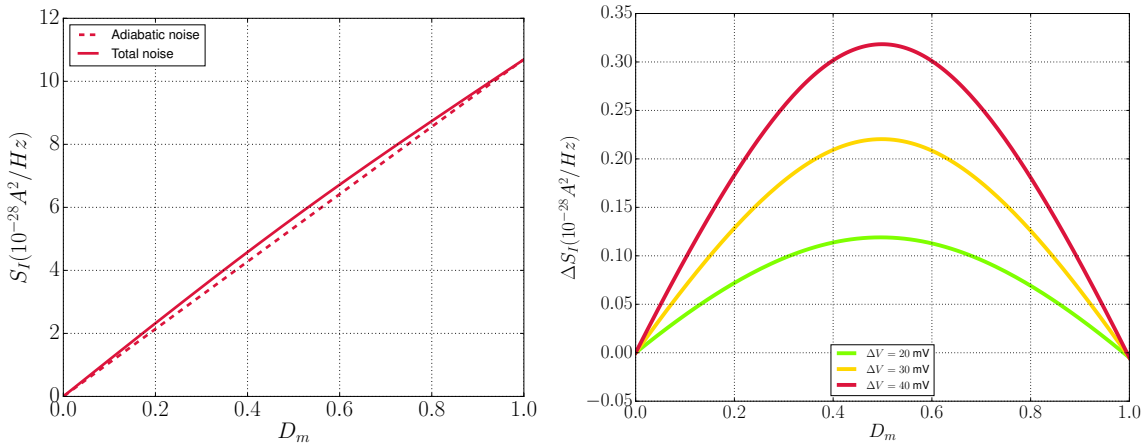

Figure 5.3: *(Left)* Total noise (solid line) generated by the quantum switch and adiabatic noise (dashed line) as a function of mean transmission D_m. Noise is composed of the thermal contribution which is linear with respect D_m and the QS noise which has a parabolic shape. (*Right*) Difference between total and thermal noise or excess noise of the quantum switch ΔS_I for several amplitudes ΔV_G as a function of the transmission D_m. Parameters for both figures are : $\nu = 6.15$ GHz, $\Delta V = 40$ mV, noise is deduced from eq. 1.74 and from the conductance plotted in figure 5.2. The excess noise is symmetric towards $D_m = 0.5$ because the conductance profile used is also symmetric. Temperature is $T = 250$ mK.

5.2 Results without magnetic field

We present here the experimental results of the quantum switch noise obtained without magnetic field. We first present the effect of the RF voltage on the transmission which gives access to a calibration of the amplitude of the voltage applied on the gates required in order to simulate the QS noise. Then, we present the noise measurements for several RF amplitudes and phase shifts. A comparison with the theory developed in chapter 1 and a classical model allows us to evidence the Quantum Switch signatures in our measurements.

5.2.1 Transmission measurements as a calibration for the RF voltage amplitude

In order to compare the excess noise measurements with QS simulations, the value of the effective amplitude ΔV of the sine voltage applied on the gates is required. The calibration of ΔV is performed thanks to the measured transmission versus V_G of the QPC for a given RF voltage V_{RF}, which corresponds to the mean transmission D_m defined in eq. 5.1. The attenuation of the RF lines is then deduced from the ratio $\Delta V/V_{RF}$. The figure 5.4 presents the experimental measurement of the transmission D without RF (green dots) and the transmission D_m with RF (red dots). The amplitude and the frequency of RF source are $V_{RF} = 1.26$ V and $\nu = 6.15$ GHz. The measured temperature is 299 mK,

however we observed that the transmission stays unchanged until few hundreds of mK.

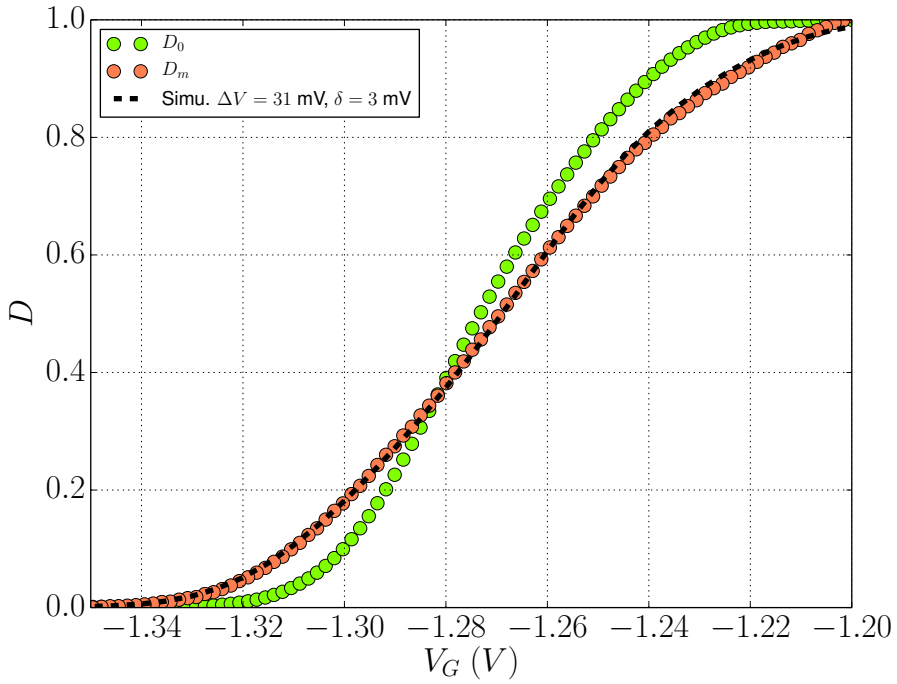

Figure 5.4: Transmission of the QPC between transmission $D = 0$ and $D = 1$. Transmission D (resp. D_m) without (resp. with) RF voltage applied on the gates is represented by the green dots (resp. red dots). Dashed black line is a simulation of the conductance with RF pulsing using eq. 5.4 with $\Delta V = 31$ mV and $\delta V = 3$ mV. This shift δV is required for a good fit of the curve and is explained by non-linearities in appendix A. Parameters are : $V_{RF} = 1.26$ V, $\nu = 6.15$ GHz, $T = 299$ mK and $\Delta\varphi = \pi$.

The effect of RF on the experimental transmission is an expected smoothing and a slight translation versus the voltage, denoted by δV. This shift δV is explained by the transmission non-linearities and is detailed in appendix A. Then, the mean transmission D_m is simulated from the measured transmission D from the expression in eq.5.1:

$$D_m(V_G) = \nu \int_0^{1/\nu} dt \; D\left(V_G + \delta V + \Delta V \sin\left(2\pi\nu t\right)\right) \tag{5.4}$$

with the additional voltage shift δV. The dashed black line of the figure 5.4 is the simulation of D_m for an amplitude voltage $\Delta V = 31$ mV and $\delta V = 3$ mV and is in a good agreement with the experimental mean transmission D_m.

These measurements provide the effective voltage amplitude ΔV for a given voltage V_{RF} delivered by the RF source. We deduce from that the ratio k, defined as:

$$k = \frac{\Delta V}{V_{RF}} = 0.025 \tag{5.5}$$

It corresponds to a total attenuation of 32 dBm at $\nu = 6.15$ GHz. The intrinsic attenuation of the RF line is thus 9 dBm (at 6.15 GHz), the remaining 23 dBm are provided by the attenuators, as shown in figure 5.1.

5.2.2 Experimental excess noise

We present the QS noise measurements performed by following the experimental protocol proposed in section 5.1.2. The amplifiers noise is systematically subtracted[4]. Figure 5.5 shows the total noise as a function of D_m without RF pulsing (green dots) and with RF pulsing (red dots). Each point is taken at regular voltages steps of V_G, and as D_m is a non-monotonic function of V_G, they are concentrated at $D_m = 0$ and $D_m = 1$. Each noise measurement is preceded by transmission measurements D_m, whose shape versus V_G is identical to those presented in the figure 5.4.

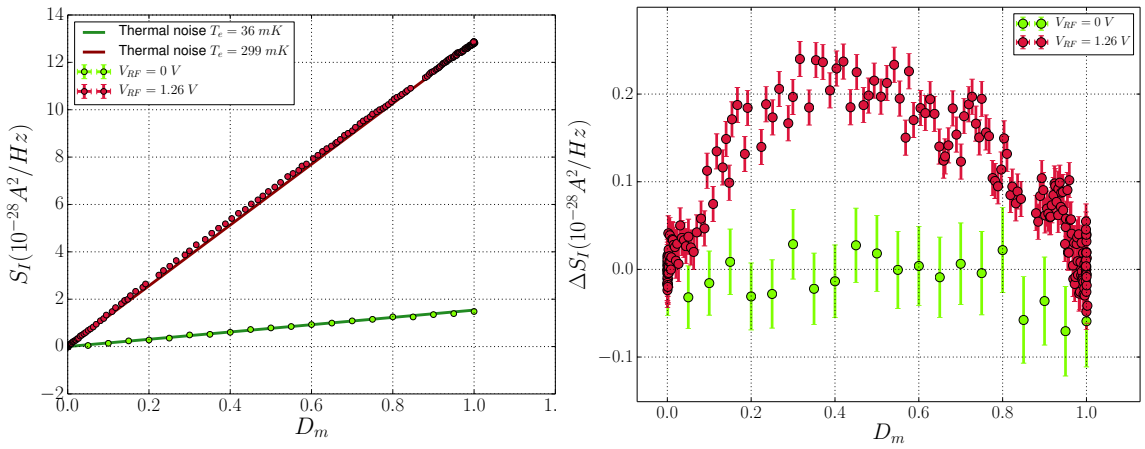

Figure 5.5: *(Left)* Measured noise as a function of mean transmission D_m, without RF pulsing (green dots) and with RF pulsing (red dots). Parameters are : $V_{RF} = 1.26$ V, ν =6.15 GHz, $\Delta\varphi = \pi$, no magnetic field. The solid lines represents the thermal noise: $S_I^{th.} = 4k_BT\frac{2e^2}{h}D_m$ at 36 mK (green line) and 299 mK (red line). A deviation appears for RF pulsing between experimental points and adiabatic limit, that corresponds to the QS noise. (*Right*) Excess noise as a function of mean transmission D_m, without RF pulsing (green dots) and with RF pulsing (red dots). RF pulsing adds an excess noise in addition to the thermal noise.

The dominant contribution is clearly the Johnson-Nyquist noise that evolves linearly with D_m (as shown in eq. 5.2), represented by the red and green solid lines. Temperatures of 36 mK and 299 mK are deduced respectively from the measurement without RF pulsing

[4]It is equivalent to a noise generated by an impedance of conductance $2D_me^2/h$ at a temperature -49 mK. Indeed, amplifiers add a positive contribution in the cross-correlation measurement in the 2-contacts QPC while noise emitted by the sample (QS, Johnson-Nyquist) is negative, as shown in chapter 1.

(green dots) and with RF pulsing (red dots). The main effect of RF pulsing is a global increase of the electronic temperature and it will be explained in detail in section 5.3.2. The heating found here is understood and will be described later in figure 5.10. As shown in the simulations of figure 5.3, a small deviation between total noise and Johnson-Nyquist noise is visible for the RF pulsing measurement.

By subtracting each curve of figure 5.5 by the Johnson-Nyquist noise *(right)*, we get the excess noise as a function of D_m, *(left)*. This shows the clear effect of the pulsing gate appears in the "ON" measurement similar to the quantum switch noise presented in part 5.3.

5.2.3 Comparison with simulations of QS and classical noise

These experimental noise measurements are compared with simulations of the QS model presented in the chapter 1, in which the strong dependence of the QS noise on the shape of the transmission versus V_G has been highlighted. Therefore, we use the experimental transmission D in order to simulate the time-dependence of the reflection and transmission coefficients, which are required for the computation of the QS noise[5]. We present here the excess noise measurement and the corresponding simulations for two phase shifts $\Delta\varphi = \pi$ and 0 and for two values of RF voltage $V_{RF} = 0.63$ and 1.26 V.

Quantum switch and photo-assisted shot-noise model

The excess noise presented in figure 5.5 (red dots) is reported in figure 5.6. A straightforward simulation with the case that takes only the modulation of the transmission (pure QS limit) is represented by the red dashed curve. There are no fitting parameters: we use the voltage amplitude $\Delta V = 31$ mV deduced from the calibration of section 5.2.1 and the temperature of 299 mK extracted from the thermal noise in section 5.2.2. The measured noise is larger by a factor ~ 2 than the expected noise.

The missing contribution is explained by adding a parasitic AC drain-source voltage applied on the QPC denoted:

$$V_{ds}(t) = V_{ac}\cos(2\pi\nu t) \tag{5.6}$$

The amplitude of $V_{ds}(t)$ is denoted V_{ac} and has the same frequency of the gate voltage.

[5]For a given transmission $D(V_G)$, reflection and transmission coefficients are given by $\rho(t) = \sqrt{1 - D(V_G + V_{ac}\sin(2\pi\nu t))}$ and $\tau(t) = \sqrt{D(V_G + V_{ac}\sin(2\pi\nu t))}$. Then, the simulation of the excess noise generated by the QS switch is computed from the formula:

$$\Delta S_I = 4\frac{2e^2}{h}\sum_{l=-\infty}^{\infty} 2|\delta_{l,0} - R_l|^2\frac{lh\nu}{e^{\beta lh\nu}-1} + |S_l|^2\left(\frac{lh\nu - eV_{dc}}{e^{\beta(lh\nu - eV_{dc})}-1} + \frac{lh\nu + eV_{dc}}{e^{\beta(lh\nu + eV_{dc})}-1}\right) - 4k_BT\frac{e^2}{h}D_m$$

where coefficients R_l and S_l are respectively the Fourier coefficients of respectively $\rho^2(t)$ and $\tau(t)\rho(t)$

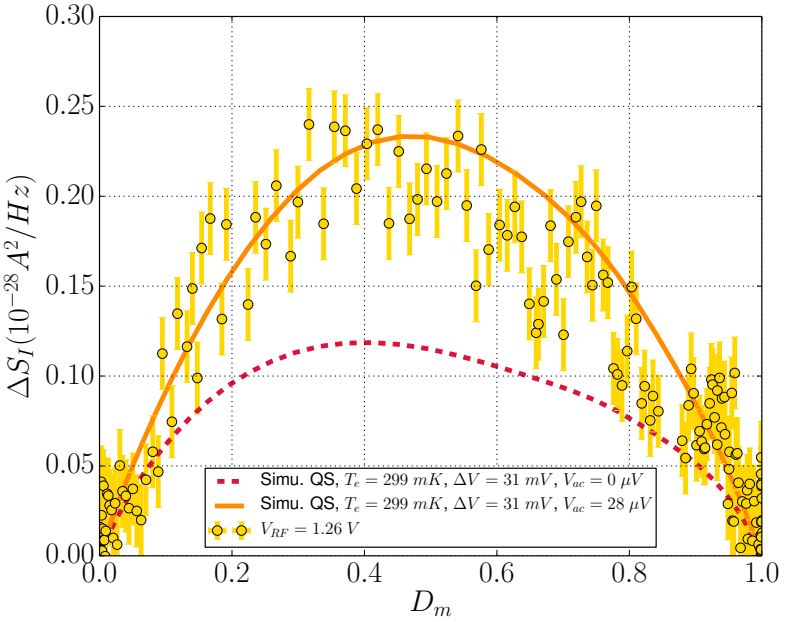

Figure 5.6: Excess noise ΔS_I as a function of mean transmission D_m. Measurement is performed at V_{RF} = 1.26 V, ν =6.15 GHz, $\Delta\varphi = \pi$. The red dashed curve represents an ideal QS limit (no voltage bias across the QPC) with $\Delta V = 31mV$, T_e = 299 mK. The yellow solid curve represents the QS model including the parasitic drain-source AC modulation of amplitude $V_{ac} = 25\ \mu$V

It generates a Photo-Assisted Shot-Noise (PASN). The yellow solid curve represents a simulation with an AC polarisation of amplitude $V_{ac} = 25\ \mu$V which provides the best fit. A good agreement is found between the model and the experimental data. The presence of this parasitic voltage is discussed in the next section 5.3.3. For the following measurements, the amplitude of $V_{ds}(t)$ is the fitting parameter of the QS model.

Phase shift and amplitude dependence

We present in the figure 5.7, left, the experimental excess noise for different phase shifts φ_1 and φ_2, whose difference[6] is $\Delta\varphi = \varphi_2 - \varphi_1 = \pi$. The noise amplitude varies by $\sim$ 20% and is maximum if gates are modulated in phase: $\Delta\varphi = 0$ (orange dots) and minimal for $\Delta\varphi = \pi$ (green dots). The fits deduced from the simulated QS noise are in a good agreement with the experimental data. This indicates that the phase shift introduced is equivalent to vary the effective amplitude of the gate voltage between two values: $\Delta V = 31$ and 35 mV.

[6]Relative phase shift is between φ_2 and φ_1 is controlled by the experimentalist with the phase shifter.

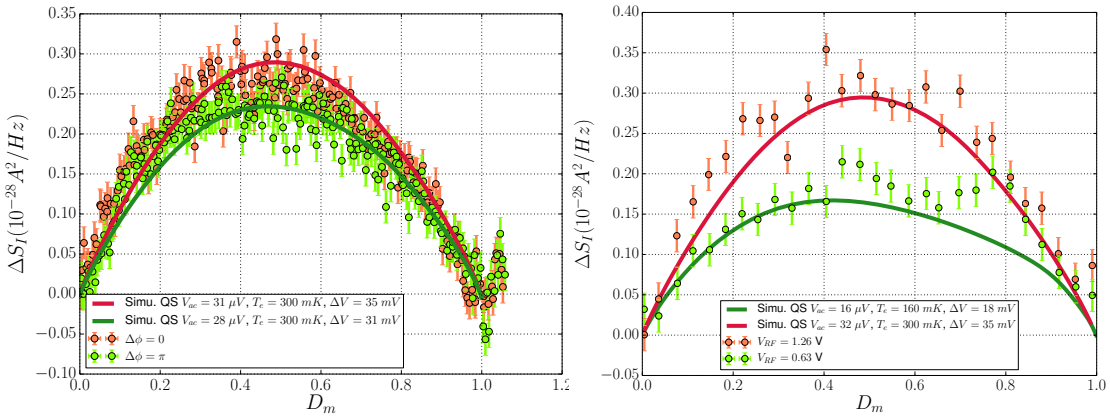

Figure 5.7: *(Left)* Excess noise ΔS_I as a function of D_m for two phase shifts. Orange dots corresponds to $\Delta\varphi = 0$ and green dots to $\Delta\varphi = \pi$. Parameters are : $V_{RF} = 1.26$ V, ν =6.15 GHz. *(Right)* Excess-noise ΔS_I as a function of D_m for $V_{RF} = 0.63$ V (green dots) and $V_{RF} = 1.26$ V (in orange). Parameters are : $\Delta\varphi = 0$, ν =6.15 GHz

The figure 5.7, right, shows similar measurements but for two different RF amplitudes, a first one at $V_{RF} = 0.63$ V and a second one at twice this value: $V_{RF} = 1.26$ V (phase shift is set at $\Delta\varphi = 0$ in both cases). Because of the linearity of the RF lines, we expect to recover the ratio 2 : 1 in the effective amplitude of modulation ΔV used in the simulations in order to fit the measurements. As shown later in section 5.3.2, the parasitic voltage V_{ds} is also linear with respect V_{RF}[7]. The simulations represented by the solid lines and the data are in a good agreement, with the expected values of amplitudes: $\Delta V^{(red)} = 2 \times \Delta V^{(green)}$ and $V_{ds}^{(red)} = 2 \times V_{ds}^{(green)}$. Note that the lower temperature of 160 mK extracted from the measurement at $V_{RF} = 0.63$ V is in agreement with the curve in figure 5.10.

Comparison with the classical model

One can ask if the classical model presented in the chapter 4 could also explain the excess noise as a function of D_m. The excess noise of the adiabatic model is the DC shot-noise averaged over a period, with a time dependent transmission $D(t) = D(V_G + \Delta V \cos(2\pi\nu t))$ and the AC drain-source voltage $V_{ds}(t)$. It reads:

$$\Delta S_I = 4k_BT\frac{e^2}{h}\nu\int_0^{1/\nu} dt\ \left(D(t)^2 + D(t)(1-D(t))\frac{eV_{ds}(t)}{2k_BT}\coth\left(\frac{eV_{ds}(t)}{2k_BT}\right)\right) - 4k_BT\frac{2e^2}{h}D_m \tag{5.7}$$

The figure 5.8 displays the QS noise measurement at $V_{RF} = 1.26$ V and $\Delta\varphi = 0$ and the curves deduced from eq. 5.7 represented by the grey solid curves, for $V_{ac} = 41\ \mu$V and

[7] The unwanted voltage V_{ds} is created by a capacitive coupling between the gate and the 2DEG, and thus is linear with respect V_{RF}.

55 μV. For an amplitude $V_{ac} = 55$ μV (grey diamonds), the classical model is in a good agreement with the experimental data only for $D_m > 0.2$, and only for $D > 0.5$ when using $V_{ac} = 41$ μV. The simulation of QS noise combined with PASN (red curve) reproduces nicely the entire experimental curve, unlike the classical model, which describes only a part of it.

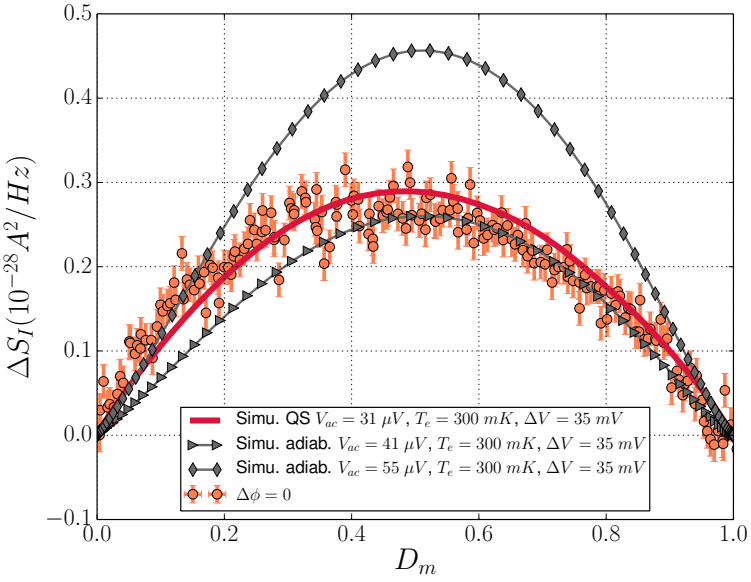

Figure 5.8: Excess noise ΔS_I as a function of mean transmission D_m. Measurement is performed at $V_{RF} = 1.26$ V, ν =6.15 GHz, $\Delta\varphi = 0$. Solid red line represent the QS noise simulation with $\Delta V = 35$ mV, $T_e = 299$ mK and $V_{ac} = 31$ μV. The classical model is represented by the grey lines for $V_{ac} = 41$ and 55 μV.

The data presented in the figure 5.8 illustrate the asymmetry of QS noise regarding $D_m = 0.5$. Indeed, the experimental transmission of the QPC, shown in figure 5.4, is also not symmetric regarding $D_m = 0.5$: the transmission varies more rapidly for $D_m < 0.5$ than for $D_m > 0.5$ and thus the QS noise is larger for $D_m < 0.5$. On the contrary, adiabatic noise appears symmetrical with respect of $D_m = 0.5$ (similar to the $D(1-D)$ curve). This non-symmetrical behaviour of the experimental results is recovered in the examples of theoretical curves presented in the chapter 1 and shows a clear evidence of the fundamental QS noise in our measurements.

5.2.4 Conclusion

We experimentally observe an excess noise when the transmission of a QPC is pulsed at the GHz frequency. The QS noise combined with a photo-assisted shot-noise generated by an extra drain-source voltage $V_{ac}(t)$ agrees well with the experimental results for several parameters. In particular, the asymmetry of the noise versus the mean transmission D_m is

only described when including a full quantum QS noise model, as predicted in the chapter 1. The classical adiabatic model model is symmetric regarding $D_m = 1/2$ and does not reproduce the experimental curves.

5.3 Effects of capacitive coupling between electrostatic gates and 2DEG in the absence of magnetic field

In the previous section 5.2, we have seen that the measured noise is not fully described by a pure QS noise as proposed in the protocol. Indeed, we observed in the experimental results that a part of the noise is due to the shot-noise created by a parasitic AC drain-source voltage. In addition, the temperature increases from 36 to hundreds of mK.

In this part, we propose to explain these effects by an unavoidable capacitive coupling between the 2 Dimensional Electron Gas (2DEG) and the gates pulsed at high frequencies, which creates AC currents in the 2DEG. These currents increase the electronic temperature and, if not symmetrical regarding the gates, add the unwanted AC polarisation.

We first present a simple electrical model of the QPC. Then, the capacitive coupling and the AC currents are estimated thanks to the temperature increase. Finally, the order of magnitude of the unwanted AC drain-source voltage is deduced from the effects of transmission non-linearities and is consistent with the values used in the previous section to analyse the QS data.

5.3.1 Electrical model of QPC

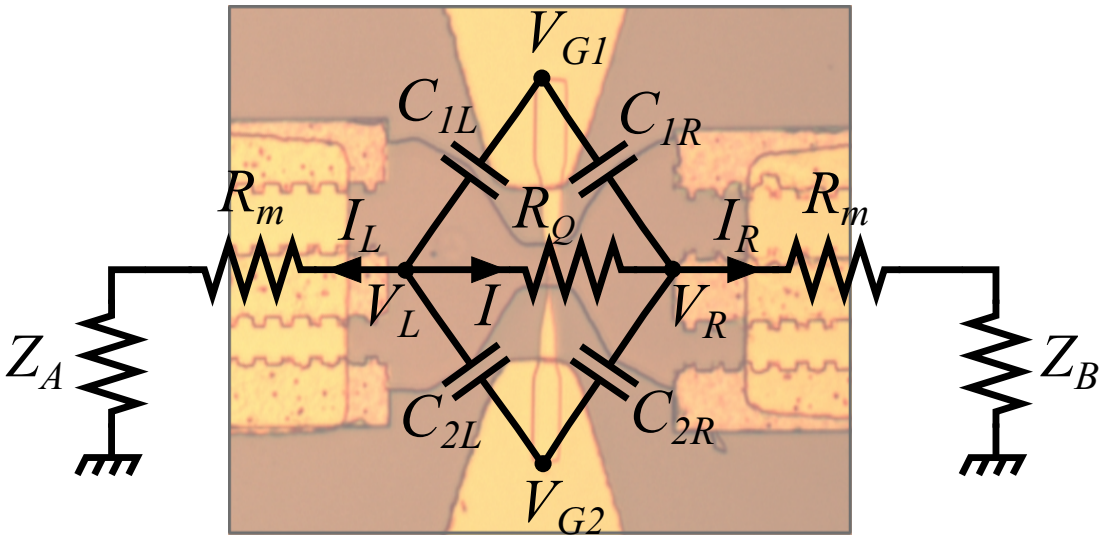

Figure 5.9: Electrical model of the QPC. Effect of GHz voltages, V_{G1} and V_{G2} applied on the gates is modelled with capacitances C_{L1}, C_{L2}, C_{R1} and C_{R2}. $R_m \simeq 150\ \Omega$ is the resistance of the mesa and of the ohmic contacts. The resistance of the QPC is $R_Q = \frac{2h}{e^2 D}$, at least 12906 Ω. Z_A ans Z_B are the measurement impedances of the RLC resonators and are negligible at GHz frequencies.

We propose an electrical description of the QPC at GHz frequencies, presented in figure 5.9. The capacitive coupling due to the proximity between the 2DEG and the gates

generates AC voltages V_L (respectively V_R) on the left (resp. right) side of the mesa, at the same frequency. Those voltages induce depletion currents I_R and I_L, increasing the electronic temperature, and their imbalance creates an AC current I through the QPC. An accurate description of this coupling is non-trivial because of the geometry of the mesa. It can be modelled, as a good approximation, by simple capacitances between the mesa and the gate (figure 5.9). These effects are detailed in the following sections 5.3.2 and 5.3.3.

5.3.2 Estimation of the capacitive coupling and the depletion currents

We propose here to estimate the coupling capacitances and the induced AC voltages through the electronic temperature increase. The depletion currents $I_{R/L}$ flow mainly in the 2DEG and the ohmic contacts[8], modelled by the resistance R_m, generating a Joule dissipation. The temperature increase due to this dissipation is presented in the figure 5.10 as a function of voltage V_{RF} of the RF source at 6.15 GHz. It is deduced from a pure Johnson-Nyquist noise measurement at transmission[9] $D = D_m = 1$. Electronic temperature starts from 36 mK (no pulsing) to 450 mK when 2.5 V are delivered by the RF source, which corresponds to an AC amplitude of 63 mV applied on the gates[10].

From this measurement, we deduce an estimation of currents $I_{L/R}$ thanks to the Wiedemann-Franz's law[11]. The non-trivial geometry of the mesa makes difficult to describe with accuracy the distribution of currents and temperature in the 2DEG. However, for $T \gg 36$ mK, the integrated form of the Wiedemann-Franz's law gives a linear relation between the current amplitudes $I_{L/R,0}$ and the temperature:[12]

$$I_{L/R,0} \simeq \frac{T_e\sqrt{\mathcal{L}}}{R_m} \tag{5.9}$$

At $V_{RF} = 2.5$ V, depletion currents are $I_{L/R,0} \simeq 5 \cdot 10^{-7}$ A, which are large values in comparison to the nano-ampere found in the usual shot-noise experiments. Note that

[8]The resistance of the QPC is much larger than the resistance R_m of the mesa + the ohmic contacts. Thus, current I must be small compared to $I_{R/L}$.

[9]When $D = 1$, there is no contribution in the noise of quantum switch or partitioning.

[10]The value of 63 mV is obtained from the calibration of ΔV presented in section 5.2.1

[11]More precisely, for the temperature range considered here, the heat transfer is carried by electron diffusion in the lead[104]. For $T < 4$ K, this process is dominant compared to electron-phonon cooling and is described by the the Wiedemann-Franz's law[3]:

$$\phi_{WF} = -\sigma\mathcal{L}T_e\nabla T_e \tag{5.8}$$

where ϕ_{WF} is the local heat flow, σ the conductivity of the mesa, $\mathcal{L} = \frac{\pi^2 k_B^2}{3e^2}$ is the Wiedemann-Franz's constant. More details about the heating effects can be found in [91].

[12]In the case of a uniform dissipation, the Wiedemann-Franz's law and the first law of thermodynamics connect the electronic temperature in the 2DEG and the current. It reads: $T = \sqrt{T_0^2 + R_m I/\mathcal{L}}$.

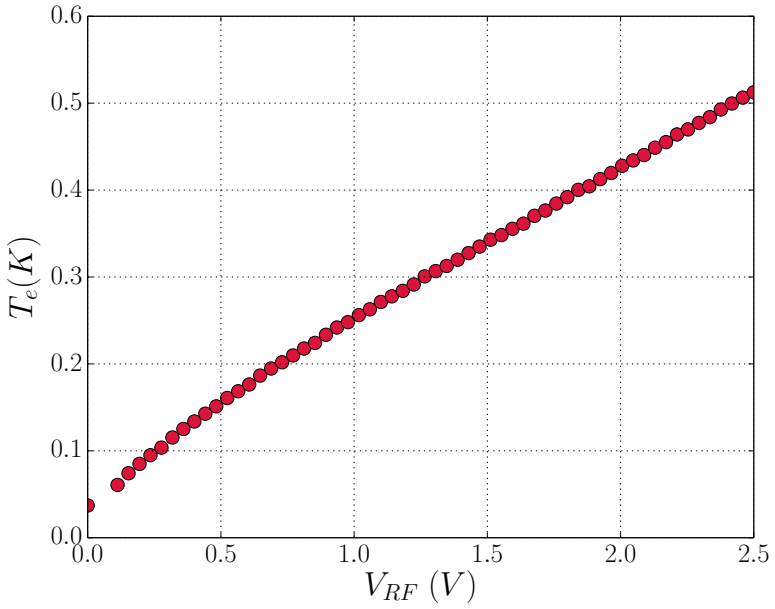

Figure 5.10: Electronic temperature in the QPC as a function of RF voltage source V_{RF} at 6.15 GHz, deduced from Johnson-Nyquist noise on the plateau $D = 1$. Effective voltage applied on the gates is 63 mV when $V_{RF} = 2.5$ V.

current amplitudes $I_{L/R,0}$ computed with eq. (5.9) are rough estimations, which do not take in account the asymmetry between the left and the right sides of the QPC.

It is reasonable to suppose that the capacitance impedance $1/C_{L/R}\omega$ is large compared to R_m at GHz frequencies. Thus, by following the electrical model in figure 5.9, the current is related to the gate voltage V_G by:

$$I_{L/R} = jC_{L/R}\omega\Delta V \tag{5.10}$$

At $V_{RF} = 2.5$ V, the effective amplitude on the gate is $\Delta V = 63$ mV, so that the value of the capacitances are:

$$C_{L1/2} \simeq C_{R1/2} \simeq 0.20 \text{ fF} \tag{5.11}$$

It is consistent with the value of the typical geometric capacitance of QPC[47]. Finally, the capacitive coupling induces voltages of amplitude $V_{L/R} = R_m I_{L/R} \simeq 75$ μV, applied on both sides of the QPC, and phase shifted by $\pi/2$ compared to the gate voltage. However, this analysis based on the study of the temperature increase does not provide a description of the asymmetry between the capacitance of the left and the right side of the mesa. This asymmetry is required in order to explain the presence of the drain-source voltage $V_{ds}(t)$, which has been introduced to model the QS noise and gives a good agreement with the noise data presented in 5.2.3.

5.3.3 Photo-assisted current as a consequence of the induced AC polarisation

In order to check the hypothesis of the drain-source voltage parasitic modulation, we seek for other manifestations of $V_{ds}(t)$. They can be found in the DC current induced by the combined $V_{ds}(t)$ and transmission modulation and by the rectification due to the energy dependent transmission of the QPC. This presence of a DC current, also called photo-current, has been evidenced in the phD thesis of Julie Dubois[38, 39], by taking in account the non-linearity of a QPC polarised with an AC voltage. Similarly, we propose to study the energy dependence of the transmission of the sample 1 used in the QS experiments. From that, photo-assisted current is simulated for several amplitudes of V_{ds} and is compared to the experimental measurement of I_{dc}.

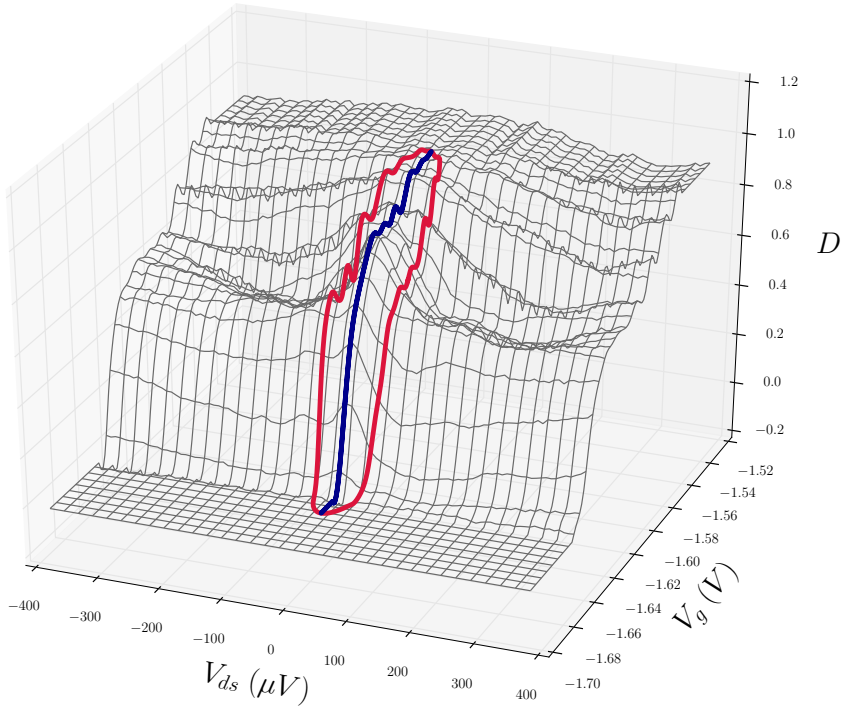

Figure 5.11: Map of the transmission $D(V_G, V_{ds})$ as a function of the voltage gate V_G and the voltage difference V_{ds} applied on the QPC. Blue curve represents the conductance with $V_{ds} = 0$. The case of pulsed gates corresponds the red path, which is an ellipse in the (V_G, V_{ds}) plane. No magnetic field is applied in this measurement.

The figure 5.11 shows the map of the experimental transmission of sample 1 between

plateaus 0 and 1 as a function of the gate voltage V_G and the drain-source voltage V_{ds}. In the case of a pure QS experiment, without polarisation, the trajectory of the conductance in this 3D map is represented by the blue solid line in the figure 5.11. In the case of a finite drain-source voltage induced by the asymmetry of the capacitive coupling, V_G and V_{ds} are phase-shifted by $\pi/2$ and the trajectory is now described by an ellipse (solid red line). A rectified current I_{dc} is created if the added contributions of the instantaneous currents $I(t) = G(t)V_{ds}(t)$ during a period is finite. On the trajectory represented by the solid red line, I_{dc} reads:

$$I_{dc} = \nu \int_0^{1/\nu} dt \cdot \frac{2e^2}{h} D\big(V_G + \Delta V \sin(2\pi\nu t); V_{ac}\cos(2\pi\nu t)\big) \cdot V_{ac}\cos(2\pi\nu t) \tag{5.12}$$

where V_{ac} is the amplitude of the drain-source voltage and $D(V_G, V_{ds})$ is the transmission of the QPC as a function of V_{ds} and V_G. The figure 5.12 represents the rectified current as a function of the amplitudes of the gate voltage ΔV and the drain-source voltage V_{ac}. It is obtained by computing the expression 5.12 for given values of $(\Delta V; V_{ac})$ versus the DC gate voltage V_G and by taking the maximum value of $|I_{dc}|$.

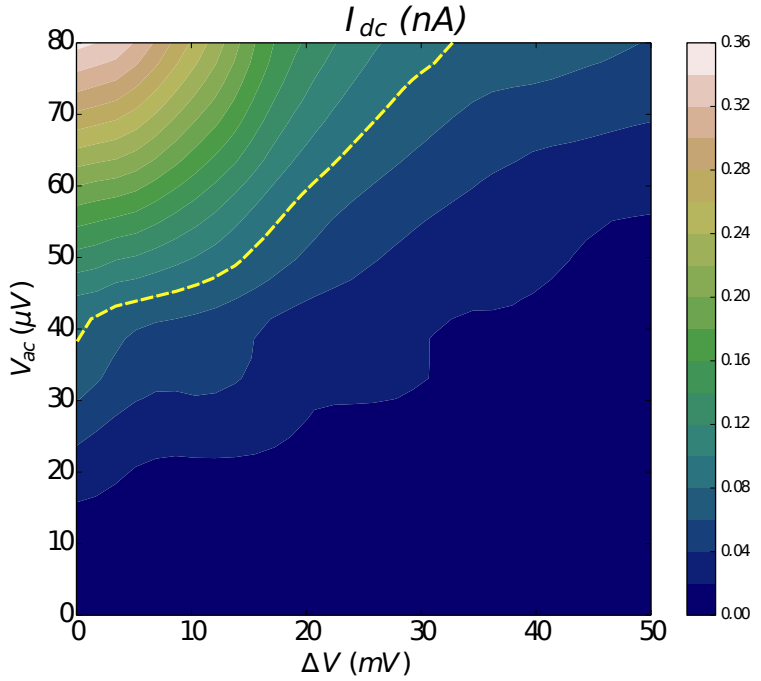

Figure 5.12: Map of the maximal value of DC current I_{dc}, as a function of the amplitude of gate voltage V_G and amplitude of polarisation voltage V_{ds}, computed from eq. 5.12. This DC current is generated by the combination of the AC drain-source voltage $V_{ds}(t) = V_{ac}\sin(2\pi\nu t)$ and the non-linearities of the transmission, presented in the figure 5.11. The yellow dashed line represents the level where $I_{dc} = 0.08$ nA, values found in the measurement of the DC current.

Are these simulations consistent with the experimental DC current measured in paral-

lel to the noise measurement? Experimental I_{dc} are shown in the figure 5.13 as a function of the mean transmission for relative gate voltage phase shift $\varphi = 0$ and $\varphi = \pi$. These measurement have been performed in parallel to noise measurement reported in the figure 5.6. It reaches a maximum value of $\sim 7 \cdot 10^{-11}$ A in both cases, which is small in comparison with the depletion currents.

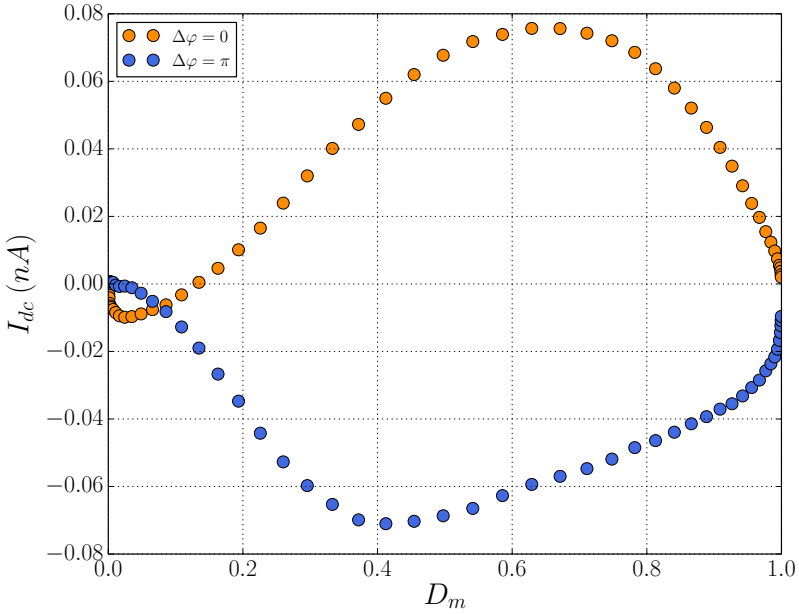

Figure 5.13: Experimental DC current I flowing through the QPC as a function of the average transmission D_m, for phase shifts $\Delta\varphi = 0, \pi$. Parameters are: $V_{RF} = 1.26$ V (on the gates: $\Delta V = 31$ mV) at $\nu = 6.15$ GHz. This DC current generated when gates are pulsed results of the AC drain-source voltage combined with the energy dependence of the transmission.

The yellow dashed curve in figure 5.12 represents the values of (V_G, V_{ds}) for which the amplitude of the simulated photo-current is $I_{DC} = 0.08$ nA. It corresponds to drain-source voltages of $40 - 80$ μV, consistent with the values used in the simulations of the QS noise presented in section 5.2. It is important to say that between the measurement of the map of transmission in figure 5.11 and the measurement of the QS noise presented in the following, the sample has been warm-up and the transmission $D(V_G, V_{ds})$ has been modified[13]. Consequently, the values of DC current found in the map 5.12 may differ from those measured in the noise experiment in 5.13.

Finally, we evidenced that the presence of an experimental DC current is explained only by an AC drain-source voltage $V_{ds}(t)$, induced by the asymmetrical capacitive coupling between the gates and the 2DEG. The amplitudes of V_{ac} are found consistent with

[13]In particular, the conductance shape versus V_G has strongly changed. For instance, map of conductance presented 5.11 shows a QPC completly closed at $V_G = -1.6$ V whereas it is closed at -1.4 V in the conductance profile 5.4.

the values used in the QS noise simulations and the capacitance found in section 5.3.2.

5.3.4 Perspectives

The quality of QS noise measurements can be enhanced by reducing the capacitive coupling between the 2DEG and the gates, in order to reduce the heating effects and the AC drain-source voltage. A first idea is to design sample with a ground plane around the gate voltage and as much as possible symmetric regarding the 2DEG. These improvements have been done for sample 2 presented in chapter 2.

A second idea is to perform the QS experiment in the quantum Hall effect. Because of the spatial separation of edge channels between incoming and outgoing electron, heating effects are reduced. Furthermore, the coupling between gate and 2DEG is decreased as the edge channel capacitance is smaller than the bulk 2DEG at $B = 0$.

5.4 Results in QHE

In this section, we present the measurements of Quantum Switch noise in the quantum Hall effect. We expect that in the QHE, the parasitic capacitive coupling will be reduced: indeed, the conduction no longer occurs in the bulk of the sample, but on the narrow edge channels, localized along the sample edges. A second advantage of using the QHE regime is the chiral propagation which strongly reduces the parasitic heating effects as explained below.

5.4.1 Mean transmission of the switch

Experimental observations

Previously, in section 5.2.1, in the absence of magnetic field, the mean conductance under AC modulation was in a good agreement with the predictions where using a simulation with $D(V_G)$ measured in DC when V_G is modulated at GHz frequencies gives a result for D_m consistent with observations. In the QHE regime, we observe a surprisingly different behaviour.

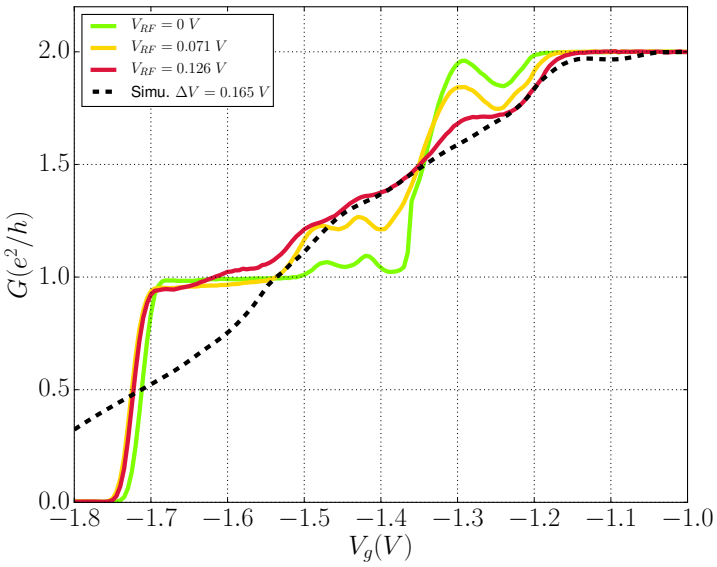

Figure 5.14: Conductance in units of e^2/h at filling factor $\nu = 3$ and at frequency 15.75 GHz. Only the two first plateaus are shown. The green line is the transmission "off", without RF pulsing the gates. The yellow and red lines are the transmission while RF voltage is "on", at respectively $V_{RF} = 71$ and 126 mV. The dashed black line represents an adiabatic simulation of the conductance "off", using eq. 5.4, using an amplitude ΔV=160 mV.

In figure 5.14, experimental curves of the transmission as a function of V_G are shown for several modulation amplitudes V_{RF}, at frequency 15.75 GHz and at $B = 2.32$ T,

corresponding to a filling factor $\nu = 3$. We focus on the two first plateaus of conductance[14]; the entire curve will be presented later in the figure 5.15.

Unexpectedly, the transmission variation widens between plateaus 1 and 2 in large proportions by comparison with the experiments performed without magnetic field, whereas voltage amplitude delivered by the RF source is lower[15]. The dashed black line represents the simulation of the mean transmission computed from the green curve without RF modulation, using the eq. 5.4 in the same way as done in the section 5.2.1. Surprisingly, a reasonable fit of the curve between plateaus 1 and 2 is found with an amplitude of the gate voltage of $\Delta V = 0.126$ V. By comparison, the voltage delivered by the RF source is 0.126 V, and by taking in account the minimal -23 dBm attenuation, the maximum value of ΔV would be, in principle, 20 mV! On the contrary, the transmission between the plateaus 0 and 1 seems unaffected by the modulation, whatever the amplitude, excepted a shift of few mV.

Modulation for filling factors 1, 2 and 3

This effect is studied for the filling factors $\nu = 1,\ 2,\ 3$. In figure 5.15, at filling factor $\nu = 3$, the three expected conductance plateaus are observed without RF modulation (dark green curve). The conductance between plateaus 2 and 3 is shown strongly modulated .

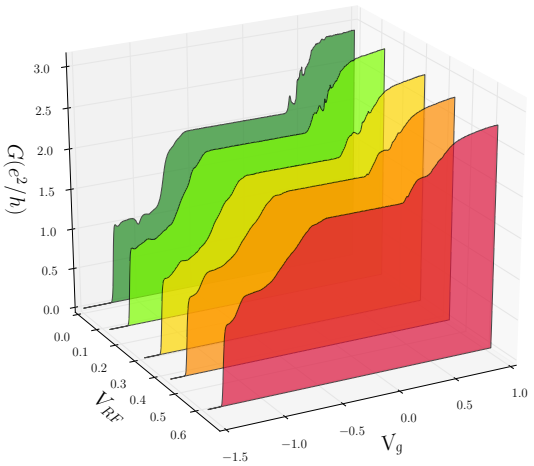

Figure 5.15: Conductance at filling factor $\nu = 3$ as a function of V_G (in V), for several modulation V_{RF} (in V). The green curve corresponds to $V_{RF} = 0$. Frequency of modulation is 15.75 GHz.

[14]Term "plateau n" means the plateau corresponding to a value of ne^2/h in the conductance curve.
[15]Typically, voltage delivered by RF source were of the order of ∼1 V in the section 5.2.

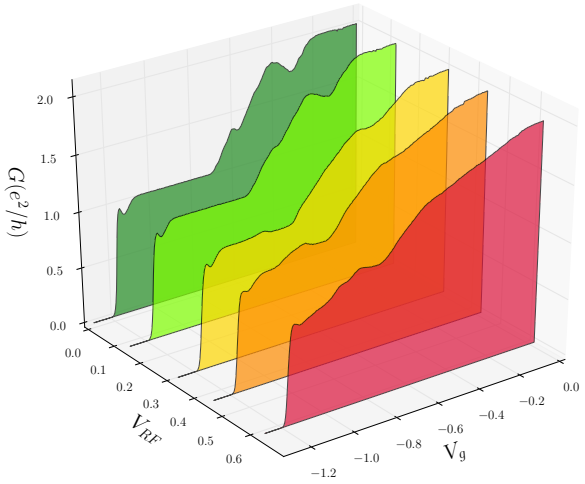

Figure 5.16: Conductance at filling factor $\nu = 2$ as a function of V_G (in V), for several modulation V_{RF} (in V). The green curve corresponds to $V_{RF} = 0$.

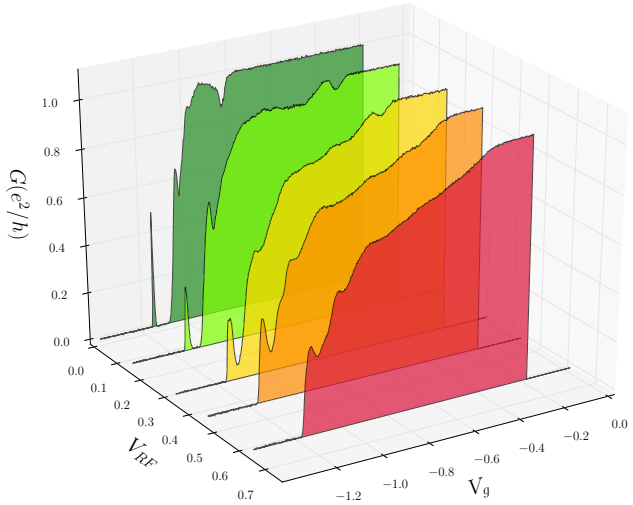

Figure 5.17: Conductance at filling factor $\nu = 1$ as a function of V_G (in V), for several modulation V_{RF} (in V). The green curve corresponds to $V_{RF} = 0$.

Similarly, the transmission curves at filling factor $\nu = 2$ presented in figure 5.16 exhibits a strong modulation between the platean 1 and 2 while it is weakly affected between 0 and 1.

In the case of the filling factor $\nu = 1$, where there is a unique plateau of conductance, one can ask if the transmission is strongly or weakly modulated. It is in a intermediate situation as shown in the figure 5.17: a strong modulation occurs for transmission close to 1, while the slope is still abrupt when the QPC is pinched-off.

Description of the large modulation of the transmission

We observed that the transmission with pulsing gates cannot be simulated from the DC curve of $D(V_G)$, where the effects of the modulation are stronger than at $B = 0$. We propose here a description of this phenomenon thanks to the dynamical properties of a quantum circuit.

A conductance channel is modelled as shown in figure 5.18[16, 27, 103]. Gate voltage controls the electrostatic potential $U(t)$ in the 2DEG cavity through the geometrical capacitance C_G[16]. The channel is modelled as a quantum RC circuit: $C_Q = \tau e^2/h$ is the quantum capacitance[5, 4], where τ is the time of travelling through the QPC and is typically $\sim$ fF and R_Q is the charge-relaxation resistance (or Büttiker's resistance). This model has been verified by Gabelli and al. [46].

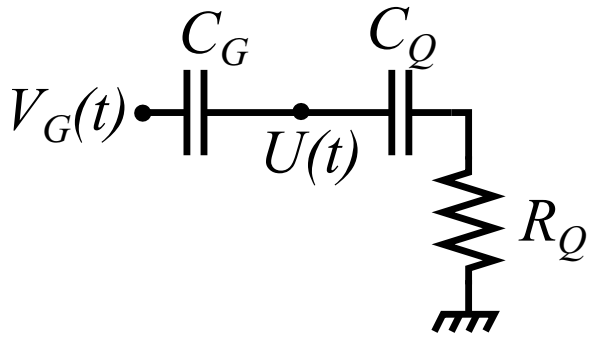

Figure 5.18: Charge relaxation in the coherent RC circuit of the 2DEG. $U(t)$ is the electrostatic potential in the 2DEG cavity. Geometrical capacitance is denoted C_G and corresponds to the capacitance presented in the model 5.9. C_Q is the quantum capacitance and $R_Q = h/2e^2$ the charge-relaxation resistance (or Büttiker's resistance).

The case of several channels N_{ch} in parallel corresponds to the situation of N_{ch} wire modelled by (C_Q, R_Q) in parallel between $U(t)$ and the ground in the schematic of the figure 5.18, and the quantum capacitance is then $C_Q = N_{ch}\tau e^2/h$. At $B = 0$, the number of modes is large in the 2DEG and $C_Q \gg C_G$. At frequency $\omega \ll 1/R_Q C_Q$, the electrostatic potential in the cavity without magnetic field reads:

$$U_{B=0} \simeq \frac{C_G}{C_Q} V_G \simeq 10^{-3} V_G \tag{5.13}$$

[16]The capacitance C_G corresponds to the capacitance presented in the model of figure 5.9. For simplicity, we assume here that $C_{L1} = C_{R1} = C_{L2} = C_{R2} = C_G$. It has been estimated to 0.2 fF in section 5.3.2

The gate potential is screened and the potential seen by the electrons is smaller. On the contrary, in QHE the number of modes is reduced to the filling factor ν and there is less screening. The potential U is then a fraction of the gate potential at high frequency:

$$U_{QHE} = \frac{C_G}{C_G + C_Q} V_G \simeq V_G \tag{5.14}$$

The effective voltage seen by the electron is thus similar to the gate voltage $V_G(t)$ and the effect of the modulation is several order of magnitudes larger in the QHE than without magnetic field.

5.4.2 QS Noise measurements

We present here the results of noise measurements performed in QHE for quantum switch experiments. We follow the experimental protocol proposed in section 5.1.2: the transmission and the noise without drain-source voltage are measured as a function of D_m while the gates are pulsed. The measurements are performed from the plateau 0 to the plateau 2 of transmission, in order to study the effects of the spectacular modulation shown in the previous part. Intuitively, we expect to observe two "bumps" in the excess noise, similar to what was founded previously, with maxima at transmission $D_m = 0.5$ and 1.5 and minima on the plateaus, at $D_m = 0$, 1 and 2.

Two technical points must be mentioned here: first, the electronic temperature in quantum switch experiments in QHE rose to 50 mK, after the installation of the magnetic coil[17]. Secondly, for technical reasons, it was not possible to perform DC current measurements in QHE similar to those presented in 5.3.3.

Total noise and absence of heating

The figure 5.19, left, presents the total noise S_I as a function of D_m from 0 to 2 for several phase shifts between the gates. The filling factor is $\nu = 3$, the frequency is 7 GHz and the amplitude delivered by the RF source is $V_{RF} = 112$ mV. A pure thermal noise of 50 mK is represented by the grey straight curve. The first interesting fact is the absence of RF heating: all experimental curves intersect at $D_m = 2$ with the 50 mK thermal contribution. This contrasts with the $B = 0$ experiments, presented in figure 5.5. The absence of heating in the QHE regime was expected as mentioned above and be explained by:

[17] Temperature was 36 mK without the presence of the magnet, which has been set in the cryostat after the QS experiments without magnetic field. Electronic temperature has been improved to 40 mK for the PASN experiments.

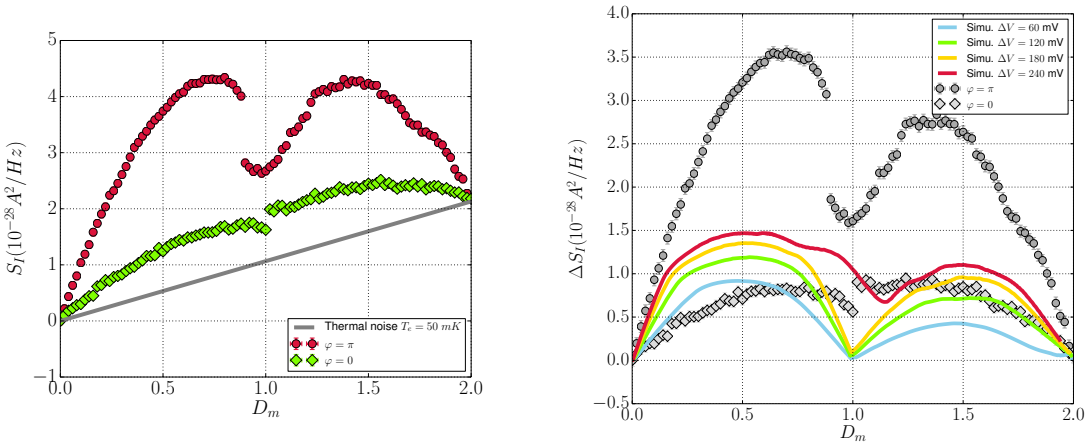

Figure 5.19: *(Left)* Total noise S_I as a function of the mean transmission D_m for the phase shifts $\varphi = 0$ and π. Parameters are : filling factor $\nu = 3$, $V_{RF} = 112$ mV, frequency 7 GHz. Grey line represents a thermal noise of 50 mK. (*Right*) Deduced excess noise ΔS_I from the same data. The coloured lines represent pure QS noise simulations (without drain-source voltage), for several modulation amplitude ΔV.

- Incoming and outgoing electrons are spatially separated, so that thermalisation between them vanishes. In the case of a heating due to the pulsed gates, outgoing electrons, do not interact with the cold incoming electrons;

- The dissipation does not occur in edge channels but only in the contacts;

The excess noise ΔS_I deduced from the data of figure 5.19, left is displayed in the figure 5.19, right. The phase shift seems to play an equivalent role to the RF modulation ΔV. Pure QS noise (without drain-source voltage) simulations computed with the transmission curves in figure 5.14 are represented by the solid coloured curves for amplitude modulations ΔV from 60 to 240 mV. Those theoretical curves do not predict the same amount of noise than observed, even for large modulation amplitudes ΔV.

Asymmetry of the capacitive coupling

Here, we would like to see if the measured noise can be described by including the PASN effects. Indeed, the excess noise measured presented in the figure 5.19, right, strongly depends on the phase shift between the voltage applied on the gates, which are asymmetric regarding the top and the bottom of the mesa, clearly visible in the figure 5.20. This suggests that in QHE voltages induced across the QPC contribute to the noise generated.

In the quantum Hall effect, edge channels follow the equipotential lines of the potential landscape on the edge of the sample, as represented in figure 5.20. More precisely, an incoming (resp. outgoing) edge channel from the left (resp. from the right) follows the edge of the top gate (resp. the bottom gate)[18]. Consequently, an edge channel coming

[18]Reversing the magnetic field is equivalent to permute the left/right and top/bottom.

from the left has a capacitive coupling only with the top gate and the edge channel coming from the right only with the bottom gate.

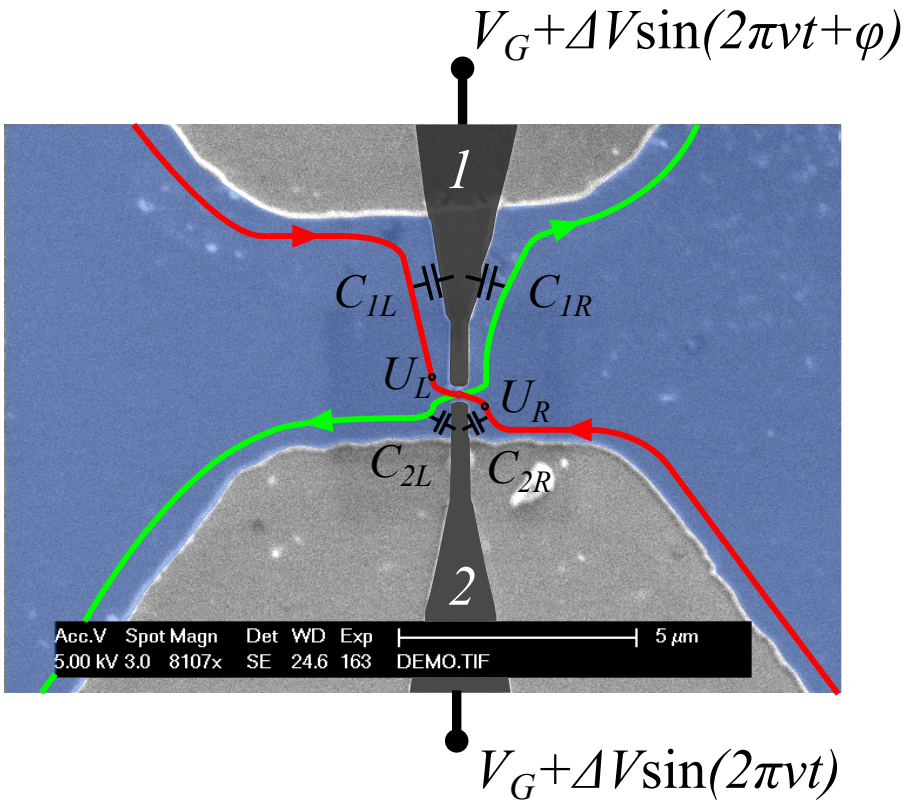

Figure 5.20: SEM picture of the gates of the QPC with artificial colors. Mesa is in blue, gates are in grey. The top-bottom asymmetry of the gates is clearly visible. Edge channels of incoming (resp. outgoing) electrons are represented in red (resp. in green). Capacitive coupling between incoming edges channels and the gate is modelled with capacitance C_{1L} and C_{2R} and generates polarisation voltage $V_{ds} = V_1 - V_2$. Phase shift between gate 1 and 2 driven the polarisation amplitude V_{ds}.

The voltages $V_1(t) = V_G + \Delta V \sin(2\pi\nu t + \varphi)$ and $V_2(t) = V_G + \Delta V \sin(2\pi\nu t)$ are applied respectively on the top and the bottom gate while the phase shift φ is controlled by the phase-shifter. Thus, the amplitude of the intern AC potentials U_L and U_R of the incoming left and right edge channels, which are generated by the capacitive coupling are:

$$U_L \propto (jC_{1L}\omega + 1/R_Q)\Delta V$$
$$U_R \propto (jC_{2R}\omega + 1/R_Q)\Delta V$$

where $\omega = 2\pi\nu$, C_{1L} and C_{2R} are the capacitance between the gate and the edge channel, as represented in figure 5.20. This induces an effective drain-source voltage V_{ds} across the QPC is then:

$$V_{ds}(t) = U_L \cos(2\pi\nu t + \varphi + \phi_0) - U_R \cos(2\pi\nu t + \phi_0) \tag{5.15}$$

where ϕ_0 is the phase shift due to the charge relaxation R_Q, for simplicity we suppose $\phi_0 = 0$ in the following. The amplitude modulation of V_{ds} with respect to φ (maximum at $\varphi = \pi$ and minimum at $\varphi = 0$) is expected to be recovered in the noise simulation.

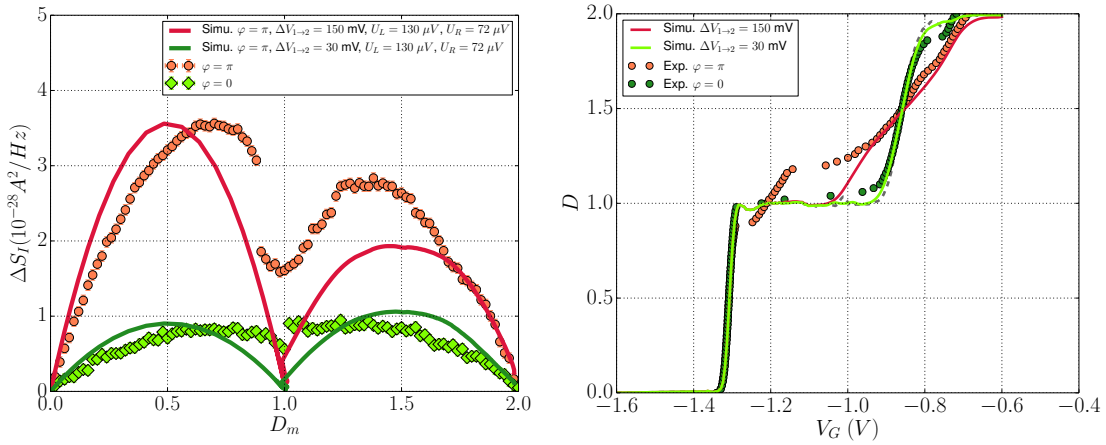

Figure 5.21: *(Left)* Excess noise ΔS_I as a function of the mean transmission for the phase shifts $\varphi = 0$ and π. Parameters are: filling factor $\nu = 3$, $V_{RF} = 112$ mV, frequency 7 GHz. The combination of QS noise and PASN simulations are represented by the coloured solid lines, with $\Delta V_{0\to1} = 0$ and $U_L = 150\ \mu$V and $U_R = 72\ \mu$V for the two phase shifts. The difference comes from the difference in the modulation between the first and the second plateaus : $\Delta V_{1\to2} = 30$ mV at $\varphi = 0$ and $\Delta V_{1\to2} = 150$ mV at $\varphi = \pi$, according to the conductance curves presented in the right figure. (*Right*) Experimental transmission curves (dots), measured simultaneously with the noise presented in left. The simulations use two different gate voltage modulations $\Delta V_{1\to2}$ for each phase shift in order to describe accurately the modulation in the QHE. In both case, there is no modulation between the plateaus 0 and 1: $\Delta V_{0\to1} = 0$. The transmission without RF pulsing is represented by the grey dashed line.

The figure 5.21, left, displays the same measurements compared with simulations of the QS noise combined with PASN, for the phase shifts $\varphi = 0$ (red dots and solid lines) and $\varphi = \pi$ (green dots and solid lines). The fitting parameters are the amplitudes of the AC potentials defined in eq. 5.15: $U_L = 130\ \mu$V and $U_R = 72\ \mu$V. The amplitude of the gate voltage ΔV is decomposed on $\Delta V_{0\to1}$ and $\Delta V_{1\to2}$, which are respectively the amplitude of modulation between the plateaus 0 and 1 and between the plateaus 1 and 2. This decomposition describes more accurately the transmission curves in QHE, where the modulation is stronger for $D_m > 1$ than for $D_m < 1$. The values $\Delta V_{1\to2} = 150$ mV at $\varphi = \pi$ and $\Delta V_{1\to2} = 30$ mV at $\varphi = 0$ are extracted from a simulation of the conductance represented by the solid line in the figure 5.21, right, while the modulation $\Delta V_{0\to1} = 0$ for both cases.

The noise simulations allow us to recover an amount of noise in a better agreement than a pure QS noise proposed in the figure 5.19,right , while only the parameter φ, which

appears in the definition of the drain-source voltage in eq. 5.15, is different between the two curves. Furthermore, we succeed to reproduce the lower amount of noise for $D_m \in [1;2]$ at $\varphi = \pi$. Surprisingly, this highlights the fact that the combination of the QS noise and the PASN can generates a lower noise than a pure PASN[19] for some set of parameters[20].

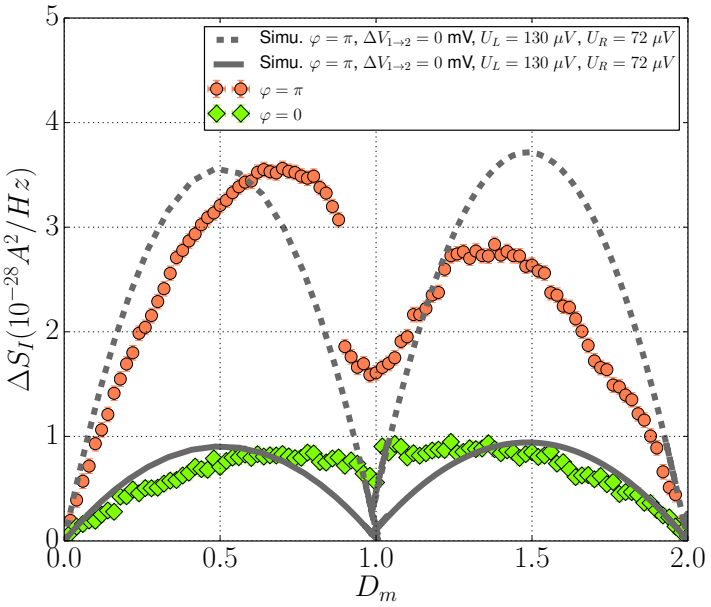

Figure 5.22: Same experimental curve than the figure 5.21 (green and red dots). Solid coloured lines represent simulation of a pure PASN ($\Delta V_{0\to1} = \Delta V_{1\to2} = 0$) using $U_L = 150\ \mu$V and $U_R = 72\ \mu$V for the two phase shifts. Unlike the simulations using a combination of QS and PASN presented in the figure 5.21, a pure PASN do not reproduce the difference of noise level between the two bumps.

This effect is evidenced by a comparison with a PASN only, presented in the figure 5.22: if we assume that transmission modulations are zero in both cases $\Delta V_{0\to1} = \Delta V_{1\to2} = 0$, then the simulated curves show two "bumps" but with the approximatively the same level of noise unlike the experimental points. Finally, only the QS noise can explain the difference of the noise level between the two "bumps", lower for $D_m \in [1;2]$.

[19]For $D_m \in [0;1]$, the gate modulation is taken to zero $\Delta V_{0\to1} = 0$ so that only PASN occurs with $U_L = 130\ \mu$V and $U_R = 72\ \mu$V, while for $D_m \in [1;2]$, there is the QS and the PASN: $\Delta V_{1\to2} = 130$ mV.

[20]In the case without magnetic field presented in the section 5.2, the amplitudes of the drain-source voltage and the gate modulation amplitude were found smaller than in the simulations of 5.21 and the combination of PASN and QS was greater than pure PASN or QS taken separately.

5.5 Conclusion

We have investigated the current noise generated by the most elementary switch on a quantum conductor by pulsing at the GHz the voltage of the gates of a QPC. In the experiments performed without magnetic field, we found that the noise measurements are faithfully reproduced by the predicted QS noise, combined with a PASN resulting from a parasitic drain-source voltage across the QPC. On the contrary, a classical model does not describe the data, demonstrating that only the QS model developed in the chapter 1 explains our observations. The temperature increase and the DC current flowing through the QPC are fully understood by a thorough investigation, which confirms that a capacitive coupling between the gates and the 2DEG generates this unavoidable drain-source voltage. In the QHE regime, we observe a surprising stronger modulation of the transmission, which can be explained by the quantum capacitance and the charge relaxation of a conductance channel. Similarly, the noise measurements in the QHE are described by the combination of the QS and the PASN noise. These experiments presented in this chapter, performed under a wide set of parameters, evidence the universality of the noise of the quantum switch.

Conclusion and perspectives

Conclusion

This thesis has explored the dynamics of AC transport in ballistic coherent circuit through two experiments: the study of the Photo-Assisted Shot-Noise in the Quantum Hall Effect and the current fluctuations of a Quantum Switch.

The main achievements of this thesis are: the first measurement of the Photo-Assisted Shot-Noise under magnetic field for a sine excitation, which demonstrates the validity of the photo-assisted process in the integer Quantum Hall Effect; the first experimental measurement of the current fluctuations generated by a Quantum Switch. We review the work accomplished in the following.

Overview

Theoretical analysis

In the first chapter, we presented the main features of the DC transport by applying the Landauer-Martin-Büttiker formalism and derived the current and noise correlations for the 2-contacts and 6-contacts QPC geometries. Then, AC transport is first studied in the case of an alternative voltage applied on the lead of a quantum wire: we used the Floquet formalism in order to describe the electronic states, which become in a superposition of electrons and holes shifted by quanta $lh\nu$, respectively above and below the Fermi sea. This allows us to obtain the formula for the Photo-Assisted Shot-Noise and the extra number of electron-hole pairs generated by a sine excitation. Finally, we applied the Floquet formalism on the states scattered by the potential barrier of the QPC, when its transmission $D(t)$ is a periodic function of time: this provides the generalisation of the Quantum Switch problem to the case of arbitrary transmissions shape, where the switch is not completely closed ($D < 1$) or opened ($D > 0$). The noise generated by the switching process is derived in the general case for both geometries. We also present a simple example in which the noise reads, with no drain-source voltage and in the limit of $T = 0$: $S_I = 2e^2\nu$, showing that current fluctuations are intrinsic to the QS process.

Design and fabrication of QPC

After the theoretical study of the transport in coherent ballistic conductors, the chapter 2 presents the experimental implementation using 2 Dimensional Electron Gases in GaAs heterostructures. We briefly reminded their properties of quantum coherence and large ballistic lengths and we described how a Quantum Point Contact is realized from a 2DEG. Then, we presented a simple model for the design of the gates in order to choose the relevant geometry for each experiment. We connected the curvatures of the electrostatic potential of the saddle point model to the gate voltage and we deduced the conductance shape versus the voltage gate for square and sharp gates. The results obtained were in a good agreement with the experimental conductance of home-made QPC, showing that sharp (resp. square) gates were well adapted for the PASN (resp. QS) experiment. Therefore, we explained the conception of the 6-contacts sample designed for high frequency voltages and the improvement provided in comparison with the 2-contacts sample. This sample has been entirely realized in our laboratory, and we provided several improvements in comparison with the previous 2-contacts samples, particularly during the fabrication process.

Experimental set-up

The chapter 3 is devoted to the presentation of the experimental set-up. We started by an overview of the PASN and the QS experiments, showing that the noise measurement set-up is similar for both. The noise is measured in the MHz range in order to go beyond the $1/f$ noise by using a RLC circuit and home-made amplifiers. Thanks to thermalisation of the RF lines, we were able to send high frequency voltages with a good transmission meanwhile the electronic temperature reaches 40 mK. The data acquisition process gives access to both auto and cross-correlation of the noise with a resolution of $5 \cdot 10^{-30}$ A^2/Hz in 5 minutes. This resolution is limited by the parasitic interferences due to the presence of the magnetic coil and we proposed an efficient procedure in order to improve the resolution of the noise measurement to $9 \cdot 10^{-31}$ A^2/Hz in the same amount of time. Then, we presented the calibration of the conductance, measured with a excellent SNR ratio, and the calibration of the noise measurement performed thanks to the Johnson-Nyquist noise. Comparisons with theoretical DC shot-noise curves gave excellent agreements with the calibrated noise.

Photo-Assisted Shot-Noise in the integer Quantum Hall Effect

We reported in the chapter 4 the measurements of the Photo-Assisted Shot-Noise of a sine excitation in the integer Quantum Hall Effect. A first study of PASN as a function of the DC polarisation, $S_I(V_{dc})$ shown that data are well fitted with the model developed in chapter 1, except from an offset in the noise when RF voltages are applied. Therefore,

we performed the measurement of excess noise $\Delta S_I(V_{dc})$ at 12 and 18 GHz and for filling factors $\nu = 2$, 3, which are found in good agreement with the expected theory. More precisely, the abrupt changes in the noise slope at $q = eV_{dc}/h\nu$ are clearly visible and reflect to absorption or emission of quanta $lh\nu$ characteristic of photo-assisted processes. We completed the study thanks to the measurement of the noise as a function of the AC polarisation with no bias, also well described by the PASN model and giving access to consistent values of the effective AC voltage applied on the sample. The validity of the photo-assisted theory is confirmed thanks to a comparison with a classical model, which cannot reproduce as well the data. These experiments are the first step required for the generation of voltage pulses composed of several harmonics in the QHE regime, for instance Lorentzian pulses in order to inject levitons in edge channels.

Quantum switch

We presented in chapter 5 the first measurements of the noise of a Quantum Switch. It is implemented on a QPC transmitting a single mode whose gates are pulsed at GHz frequencies. At finite temperatures, we shown that the measure of the excess noise as a function of the mean transmission D_m is the most relevant quantity in order to analyse the QS noise. Despite the temperature increase (up to 300 mK) and the presence of a parasitic AC voltage bias, the measured noise performed with no magnetic field were faithfully reproduced by the QS theory combined with an additional PASN. Furthermore, only this model succeeded to describe the asymmetry of the data regarding D_m, whereas a classical model is purely symmetric and thus can not explain the measured noise. Thanks to a thorough investigation, the heating effects and the parasitic AC voltage are explained by a asymmetric capacitive coupling between the gates and the left and the right sides of the mesa. The measured DC current across the QPC is another manifestation of this capacitive coupling. Then, we also performed the measurement of the QS noise in the QHE regime in which heating effects vanish because of the absence of dissipation in the edge channels. On the contrary to the case of no magnetic field, we observe a modulation of the conductance much larger than expected, explained by the dynamical screening effect modelled by the quantum capacitance in a channel of conduction. The measured noise is also in a good agreement with the model of the QS noise combined with the PASN, by taking in account the huge modulation of the transmission. Finally, the measured noise in those experiments is a good agreement with the QS theory for a wide set of parameters.

Suggested improvements

In hindsight, the theoretical analysis and the experimental results reported in this manuscript leads us to propose some suggested improvements for the future experiments based on the Photo-Assisted Shot-Noise or the Quantum Switch.

Concerning technical aspects, the resolution in the noise measurement and the electronic temperature worsened after the installation of the 14-T magnet in the cryostat and huge amount of work has been done in order to reach the performances required for the measurements presented in this thesis ($5 \cdot 10^{-30}$ A^2/Hz and 40 mK). The procedure presented in chapter 3, which consists of dividing a single measurement into many short low-averaged measurements allows to improve the resolution below $5 \cdot 10^{-31}$ A^2/Hz without any technical modification of the experimental set-up. A low pass filter connected in the current leads in order to reduce the background noise would certainly enhance those performances.

The experiments performed during this thesis evidenced the intrinsic noise of the Quantum Switch but it has been shown that a part of the measured noise is due to an additional unwanted PASN. Thanks to the improvements of the fabrication processes (see chapter 2), the capacitive coupling responsible of parasitics AC voltages and currents in the 2DEG should be strongly reduced for the sample 2 and the signature of the QS noise should be clearer. Another improvement would be the reduction of the width of the mesa in order to minimise the capacitive coupling.

Perspectives

In this thesis, we focused on the dynamics of quantum transport for sine excitations paving the way for the implementation of Lorentzian excitations that would be generated by several harmonics whose relative phases and amplitudes are well controlled[71]. The PASN experiments presented in this manuscript confirm the possibility of injecting levitons in the integer Quantum Hall Effect for a clean on-demand electron source. The levitons in QHE are expected to preserve their coherence over tens of microns as their energy are close to the Fermi sea, which make them good candidate for quantum computation with flying qu-bits[64]. The total charge carried by a leviton is set by the experimentalist and it is possible to explore the transport in quantum conductors with fractional charge pulses (in the integer QHE)[48, 92, 62].

In the case of the Quantum Switch experiments, it has been shown that for a peculiar shape of the time-dependent transmission of the QPC[21], it generates a minimal noise[32, 117] and neutral levitons pairs, which are expected to be entangled[32]. This is a experimental challenge as the transmission is indirectly controlled by the gate voltage. Quantum switches could also play a role in quantum circuits by controlling the path of flying-qubits in edge channels. For instance, one can imagine a single electron detector based on the charge detection in a quantum trap, whose opening or closing is made by a Quantum Switch.

[21] More precisely, the coefficient of transmission is $\tau(t) = sin\phi(t)$ where $\phi(t)$ correspond to the phase used for the Levitons production.

Another challenging perspective is to extend the dynamics of transport in Fermi liquid studied here to the case of Luttinger liquids, for instance in the edge channels under the regime of the Fractional Quantum Hall Effect at the filling factor $\nu = 1/3$, well understood[80]. A first step would be to recover the PASN signatures in the noise slope similar to the integer QHE[31, 111], but every multiple of the reduced charge $q^* = e^* V_{dc}/h\nu$, e^* being the fractional charge of the excitations in this regime[131]. The generation of levitons carrying the fractional charge e^* has been proposed in [105]: it occurs for reflected levitons in the case of weak backscattering[112, 34]. Furthermore, fractional levitons are supposed to be anyons[2] and one can imagine HOM experiments like in which we explore the anyonic statistic, neither bosonic nor fermionic!

Appendix A

Effect of the energy dependence on the measurement of the mean transmission

We explain in this part how the measured mean transmission D_m departs from its definition of eq.5.1, shown in the chapter 5, part 5.2.1, in the light of the transmission energy dependence. In that case, the transmission is both a function of the gate voltage V_G and the drain-source voltage V_{ds}: $D(V_G, V_{ds})$, whose a map as a function of V_G and V_{ds} is displayed in the figure 5.11. When the gate are pulsed, the path followed during a period is an ellipse as explained in 5.3.3, represented by a red curve. Therefore, the average of the transmission D_m over a period is then given by:

$$D_m(V_G) = \nu \int_0^{1/\nu} dt \cdot D\big(V_G + \Delta V \sin(2\pi\nu t); V_{ac}\cos(2\pi\nu t)\big) \tag{A.1}$$

where $V_{ds} = V_{ac}\cos(2\pi\nu t)$. The effect of this energy-dependence is to shift the mean transmission from the expected curve if the QPC was linear. The figure B.1 presents the mean transmission (red solid curve) simulated from eq. A.1 with a drain-source voltage of amplitude 25 μV and the mean tranmission in the absence of V_{ds}. The effect of the energy-dependence can be model in a good approxiamtion as a shift in the gate voltage. It allows to reproduce faithfully the mean transmission and to deduce the effective amplitude applied on the gate ΔV for the calibration.

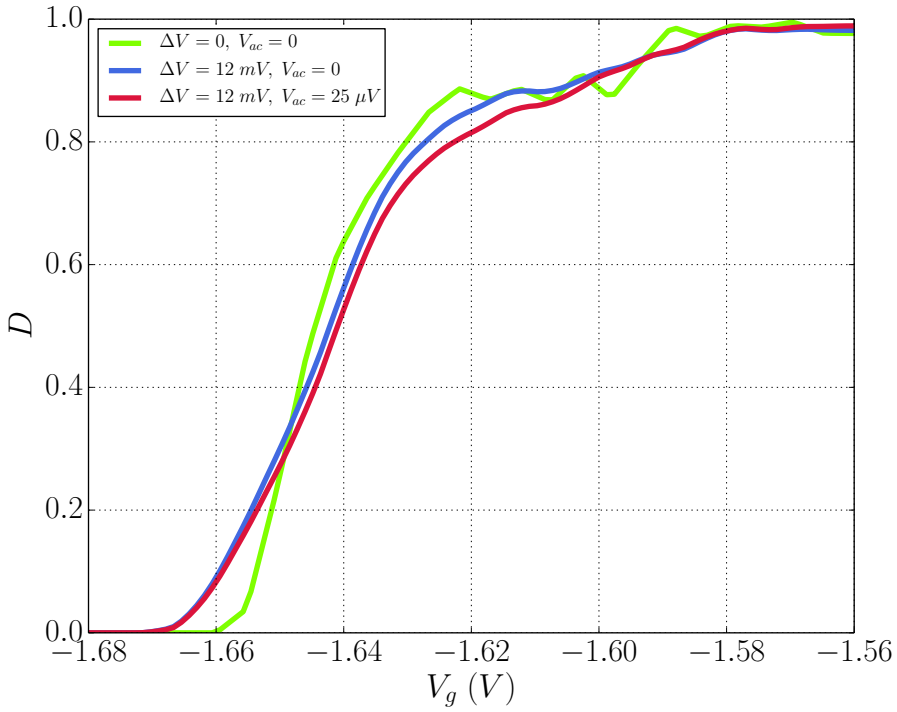

Figure A.1: Transmission of the QPC without RF pulsing (green), with RF pulsing $\Delta V = 12$ mV and no polarisation (blue) and with RF pulsing $\Delta V = 12$ mV and an amplitude drain-source voltage $V_{ds} = 25\ \mu$V, simulated from eq. A.1 and the map of transmission 5.11. The main effect of the energy dependence of the transmission can be modelled by a shift of the transmission.

Appendix B

Low temperatures technical aspects

B.1 Cryostat

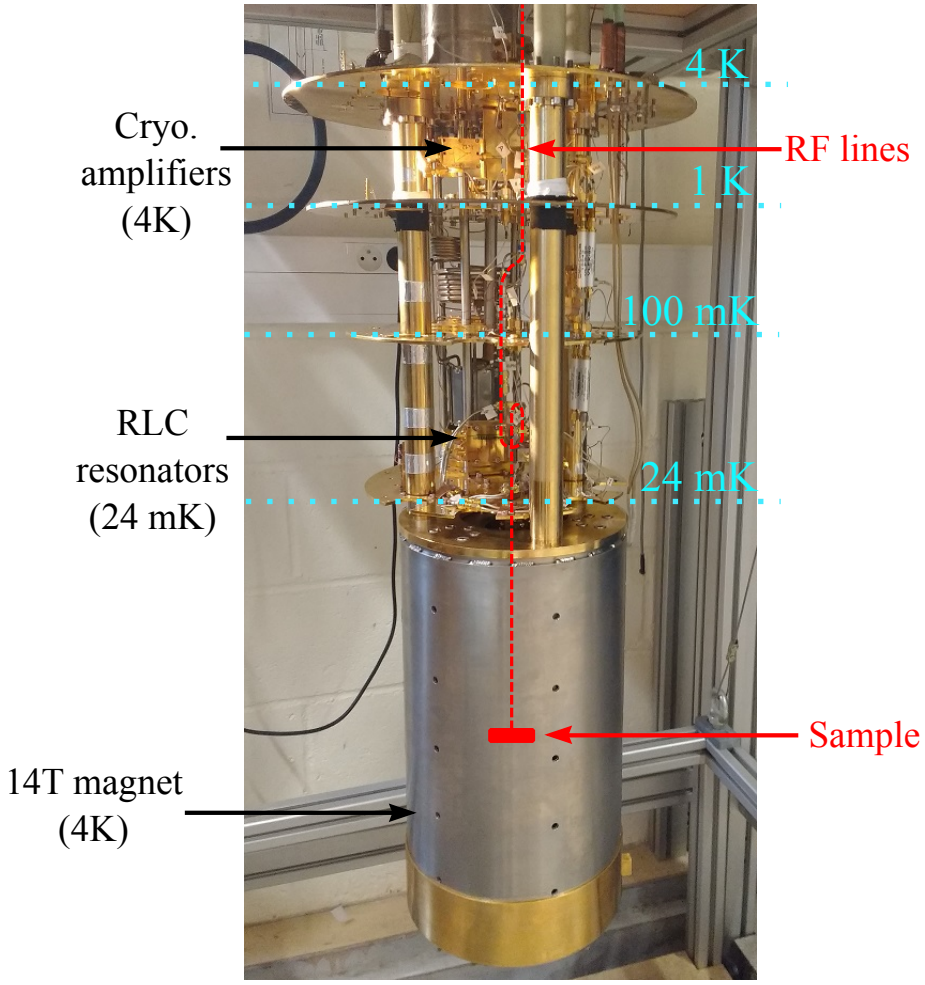

Figure B.1: Helium-free crysotat used for the experiments presented in this thesis. The main stages from 4 K to 24 mK are clearly visible. The sample is set in the magnet (on the bottom) at the maximum of magnetic field.

The cryostat is a helium-free cryostat made by Cryoconcept. The 14 T magnet has been installed in February 2014 after Quantum Switch experiments performed with no magnetic field. The electronic temperature increases from 16 to 24 mK with the presence of the magnet. It is limited by the absence of shield between the magnet at 4 K and the sample thermally connected to the mixing chamber.

The pulse tube is a PT410 from Cryomech developing a power of 1.0W at 4.2 K. 36 hours are required to reach 24 mK from room temperature. The magnet is thermalised on the 4 K stage whose temperarature is typically 3.6 K, low enough to reach 14 T in 2 hours. Pneumatic dampers limit mechanical vibrations generated by the compressor and the rotary valve of the pulse tube. More details about the characterisation of the vibration and techniques in order to prevent parasitic voltage and current noise are details in [72].

B.2 RF lines: materials, thermalisation

B.2.1 Materials

The RF lines used for our experiments are home-made coaxial wires of diameter 2.2 mm with SMA connectors and dielectric made of PTFE. The characteristic impedence is 50 Ω caracteristic imepdance. The material for the inner and outer conductors is silver-plated stainless steel (from 300 to 1 K), Niobium-Titanium (from 100 mK to 24 mK) and copper (24 mK) in order to minimize heat transfer between stages. The table (B.1) gives an estimation of the thermal power transfered between stages due to coaxial wire compared with the cooling power.

Stage	Material	Heat transfer	Cooling power
300K → 60K	SSS	50mW	20W
60K → 3.6K	SSS	40mW	0.5W
3.6K → 1K	SSS	10μW	3mW
1K → 100 mK	SSS	1μW	500μW
100mK → 25mK	Nb-Ti	>1pW	2μW

Table B.1: Power of cooling and heat transfer between stages. SSS means "silver-plated stainless steel" and "Nb-Ti" niobium titanium.

We use a silver-plated stainless steel coaxial wire between the stages from 300K to 100mK. The inner conductor is "silver-plated", meaning that the core of stainless steel is covered of a thin silver coat. Indeed, the electric field propagates only on the surface of the conductor (the skin depth is $\delta \simeq 500\mu$m, it highly decreases the attenuation, going from 32.7dB·m^{-1} (at 300 K and 10GHz) with only steel, to 11.7dB·m^{-1}(at 300 K and 10GHz) with sliver-plated steel.

The cooling power of the mixing chamber is $P_{BM} \simeq 2\mu$W and one must be careful to the thermal power provided by the wires. Thus, we use superconducting of Ni-Ti

cable between 100mK and 25mK stage to minimize as much as possible heat transfer. The thermal conductivity of a superconductor is similar to a insulator crystal: $\kappa_{NiTi} \propto T^3$ which decreases dramatically at low temperatures. The heat transfer is then: $P_{NiTi} = \frac{\lambda_{NiTi}(T^4_{100mK} - T^4_{25mK})}{4L}$, where L is the length of the wire in cm and $\lambda_{NiTi} = 7.23 \cdot 10^{-8}$W.cm.K^{-4} and is negligible in comparison with the cooling power of the mixing chamber.

B.2.2 Thermalisation

The outer conductor of the RF lines are thermalised thanks to the SMA-connectors crossing each stage of the fridge and oxygen-free copper blocks where the wire is strongly attached. These are visible on the figure B.2. It also reduces the mechanical vibrations and thus prevents from induced voltages in the presence of high magnetic field. The thermalisation of the inner conductor of RF wires mainly occurs through the resistance of the attenuators set on the RF lines. More details are provided on the phD manuscript of J. Gabelli [45].

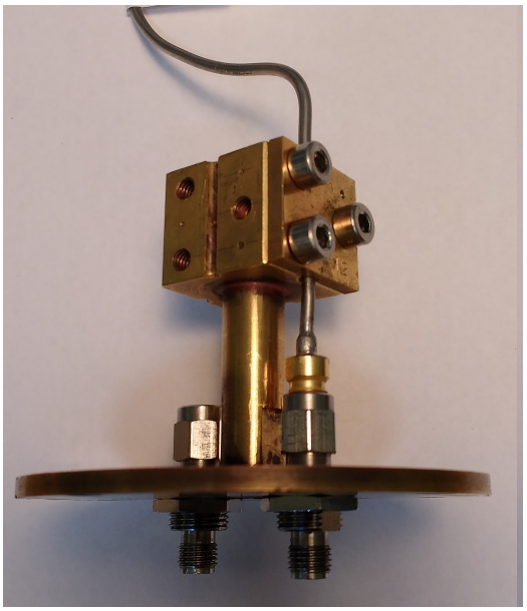

Figure B.2: Thermalisation of the outer conductor of RF wires.

B.3 Thermalisation of DC lines

At low temperatures, the thermal conductivity of the dielectric decreasing as T^2, thus the thermalization of DC lines is critical. Therefore, the inner conductor of the DC lines is connected into a board of copper-teflon-copper confined into a copper box at 25mK for an efficient thermalisation, as represented in the figure B.3. The gradient of temperature

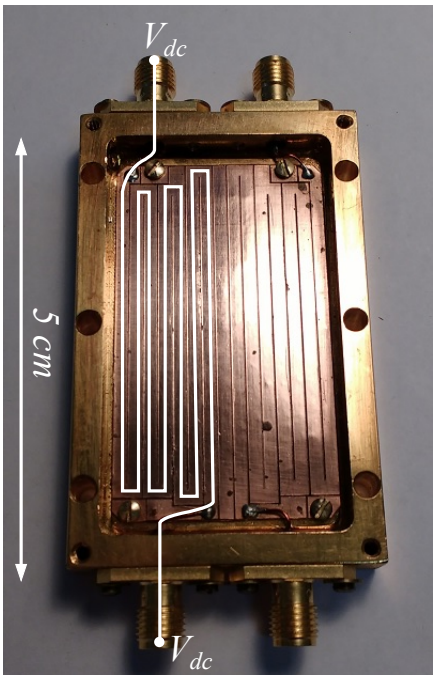

Figure B.3: Thermalisation for two DC lines. Total length of thermalization is 35cm.

decreases exponentially with a caracteristic length l_{th} given by[45]:

$$l_{th} = \sqrt{\delta_{Cu}\delta_{Te}\frac{\lambda_{Cu}}{\lambda_{Te}}}, \tag{B.1}$$

where λ_{Cu} and λ_{Te} are the thermal conductivity of copper and teflon. For temperatures belox 10K, $\lambda_{Cu} \simeq 10T\text{W.cm}^{-1}\text{.K}^{-1}$ and $\lambda_{Cu} \simeq 30 \cdot 10^{-6}T^2\text{W.cm}^{-1}\text{.K}^{-1}$. At $T = 25mK$, $l_{th} \simeq 15$ cm. In order to maximize the thermalisation in the smallest device, the line as a zigzag pattern and the total length of the copper is 35cm.

Appendix C

Noise calibration

We describe here the determination of the conversion coefficients for calibration of the noise measurement presented in part 3.5. The aim is to recover the interesting noise S_I emitted by the sample from the measured voltage noises through channels A and B. To achieve this, we first show that the conversion coefficients $A \times A$, $B \times B$ and $A \times B$ are proportional to the modulus square of the RLC impedance. Then, the values of the RLC components are deduced by fitting thermal Johnson-Nyquist noise and allow to compute the conversion coefficients. The notation in the following are the same of those used in part 3.5.

We remind that the voltages V_A and V_B measured are:

$$\tilde{V}_A(\omega) = G_A Z_A(\omega) \left(\widetilde{\delta i}_{Ga} + \widetilde{\delta i}_{Za} + \widetilde{\delta i}_e \right) \tag{C.1}$$

$$\tilde{V}_B(\omega) = G_B Z_B(\omega) \left(\widetilde{\delta i}_{Gb} + \widetilde{\delta i}_{Zb} - \widetilde{\delta i}_e \right) \tag{C.2}$$

Therefore, the auto-correlation computed for the channel A is:

$$\begin{aligned} S_{V_A \times V_A}(\omega) &= \frac{\overline{\tilde{V}_A(\omega)\tilde{V}_A^*(\omega)}}{\Delta f} \\ &= \frac{G_A^2 \mid Z_A(\omega) \mid^2 \left(\overline{\mid \widetilde{\delta i}_{Ga} \mid^2} + \overline{\mid \widetilde{\delta i}_{Za} \mid^2} + \overline{\mid \widetilde{\delta i}_e \mid^2} \right)}{\Delta f} \\ &= G_A^2 \mid Z_A(\omega) \mid^2 (S_{I,Ga} + S_{I,Za} + S_I) \end{aligned} \tag{C.3}$$

For the channel B :

$$S_{V,B \times B}(\omega) = G_B^2 \mid Z_B(\omega) \mid^2 (S_{I,Gb} + S_{I,Zb} + S_I) \tag{C.4}$$

And the cross-correlation between channels A and B is:

$$S_{V,A \times B}(\omega) = -G_A G_B Z_A(\omega) Z_B^*(\omega) S_I \tag{C.5}$$

The measured noise is averaged over a frequency range $\Delta f_m = 2\pi\Delta\omega_m$ centered on the resonance of the RLC circuit:

$$\langle S_{V,A\times A}(\omega)\rangle_{\Delta f_m} = G_A^2 \int_{\Delta\omega_m} d\omega \mid Z_A(\omega) \mid^2 (S_{I,Ga} + S_{I,Za} + S_I) \tag{C.6}$$

$$\langle S_{V_B\times V_B}(\omega)\rangle_{\Delta f_m} = G_B^2 \int_{\Delta\omega_m} d\omega \mid Z_B(\omega) \mid^2 (S_{I,Gb} + S_{I,Zb} + S_I) \tag{C.7}$$

$$\langle S_{V_A\times V_B}(\omega)\rangle_{\Delta f_m} = -G_A G_B \int_{\Delta\omega_m} d\omega Z_A(\omega) Z_B^*(\omega) S_I \tag{C.8}$$

Therefore, the current-voltage conversation coefficients are for each channel:

$$A \times A = G_A^2 \int_{\Delta\omega_m} d\omega \mid Z_A(\omega) \mid^2 \tag{C.9}$$

$$B \times B = G_B^2 \int_{\Delta\omega_m} d\omega \mid Z_B(\omega) \mid^2 \tag{C.10}$$

$$A \times B = G_A G_B \int_{\Delta\omega_m} d\omega Z_A(\omega) Z_B^*(\omega) \tag{C.11}$$

These coefficients cannot be computed directly from the Johnson-Nyquist noise presented in 3.5, which gives access only to the real part of the RLC impedance. The PSD as a function of temperature presented in the figure 3.16 are fitted with the following function:

$$\Delta S_{V,A\times A}(\omega) = \frac{4k_B(T - T_{ref})G_A^2 R_{eq,A}(1 - LC_2\omega^2)^2}{(1 - LC_2\omega^2)^2 + (R_{eq,A}C_{eq,A}\omega + R_{eq,A}C_2\omega - R_{eq,A}LC_2C_{eq,A}\omega^3)^2} \tag{C.12}$$

It corresponds to the impedance of the RLC impedance presented in the figure C.1 at MHz frequencies. Fixed parameters are: $L = 22.4$ μH and $C_2 = 22.4$ nF. C_{eq}, R_{eq} and G_A are the fitting parameters. We report below the values found for several filling factors ν in table (C.1).

ν	$R_{eq,A}(\Omega)$	$C_{eq,A}$(pF)	G_A
2	1954	336	1393
3	1800	336	1394
4	1741	335	1400
ν	$R_{eq,B}(\Omega)$	$C_{eq,B}$(pF)	G_B
2	2008	332	836
3	1898	331	820
4	1730	331	844

Table C.1: Fitting parameters

Finally, these values of the components allow to compute the conversion coeffients defined in eq. C.9, C.10 and C.11 given in 3.5.

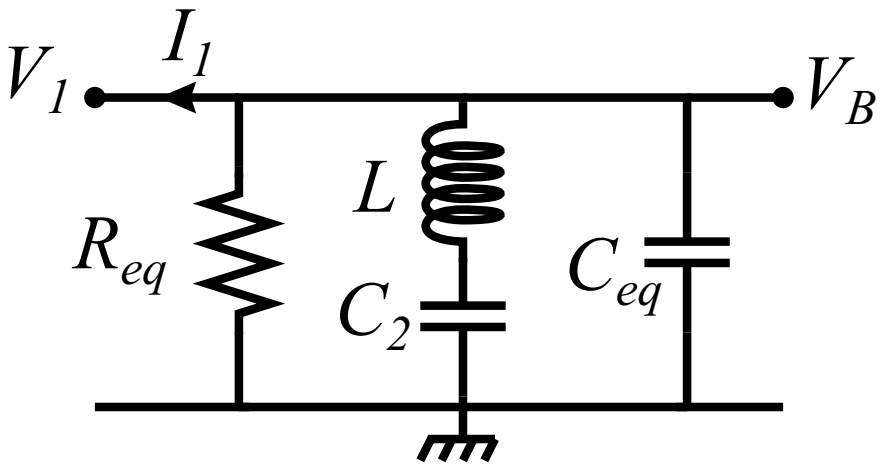

Figure C.1: Equivalent circuit of the RLC impedance presented in the figure 3.4 at MHz frequencies.

Appendix D

Table of symbols

Symbol	Definition
$\hbar$	Reduced Planck constant
k_B	Boltzmann constant
e	Elementary charge
T	Electronic temperature
β	$1/k_BT$
ν	Filling factor/Frequency
	(The distinction is mentioned when necessary)
B	Magnetic field
f_α	Fermi distribution of a reservoir α
$\hat{\mathbf{a}}_\alpha$	Annihilation operator in the lead α
$\mathbf{S}$	Scattering matrix
$\hat{I}_\alpha$	Current operator of in the lead α
ρ, τ	Amplitude of reflection and transmission

Table D.1: List of symbols

Symbol	Definition
D, R	Coefficient of reflection and transmission, $D = \|\tau\|^2$, $R = \|\rho\|^2$
v_F	Fermi velocity
λ_F	Fermi wavelength
ε_F	Fermi energy
$\Delta S_I(V_{ac})$	Excess noise as a function of V_{dc}
$S_I(V_{ac})$	Noise as a function of V_{ac}
p_l	Photo-assisted amplitude
j_l	l^{th}-Bessel function
ΔN_{e-h}	Excess electron-hole number
q	$eV_{dc}/h\nu$
α	$eV_{ac}/h\nu$
V_{RF}	Voltage delivered by the RF source
k	RF line losses coefficient
ΔV	Amplitude of AC voltage applied on the gates
R_l, S_l	Photo-assisted scattering probabilities
D_m	Mean transmission

Table D.2: List of symbols

Acronym	Definition
QPC	Quantum Point Contact
QHE	Quantum Hall Effect
PASN	Photo-Assisted Shot-Noise
DCSN	DC Shot-Noise
QS	Quantum Switch
2DEG	2 Dimensional Electron gas
PSD	Power Spectral Density
RF	Radio Frequency
HEMT	High Electronic Mobility Transistor
SEM	Scanning Electron Microscopy
SNR	Signal-to-Noise Ratio

Table D.3: Acronym list

Bibliography

[1] C. Altimiras, F. Portier, and P. Joyez. Interacting electrodynamics of short coherent conductors in quantum circuits. *Phys. Rev. X*, 6:031002, Jul 2016.

[2] Daniel Arovas, John R Schrieffer, and Frank Wilczek. Fractional statistics and the quantum hall effect. *Physical review letters*, 53(7):722, 1984.

[3] Neil W Ashcroft and N David Mermin. Solid state physics. 1976.

[4] RC Ashoori, HL Stormer, JS Weiner, LN Pfeiffer, KW Baldwin, and KW West. N-electron ground state energies of a quantum dot in magnetic field. *Physical review letters*, 71(4):613, 1993.

[5] RC Ashoori, HL Stormer, JS Weiner, LN Pfeiffer, SJ Pearton, KW Baldwin, and KW West. Single-electron capacitance spectroscopy of discrete quantum levels. *Physical review letters*, 68(20):3088, 1992.

[6] Alain Aspect, Philippe Grangier, and Gérard Roger. Experimental tests of realistic local theories via bell's theorem. *Phys. Rev. Lett.*, 47:460–463, Aug 1981.

[7] Carlo Beenakker and H van Houten. Quantum point contacts. In *Nanostructures and mesoscopic systems: proceedings of the international symposium, Santa Fe, New Mexico*, 1991.

[8] CWJ Beenakker. Proc. int. school phys. e. fermi. 2006.

[9] CWJ Beenakker, C Emary, M Kindermann, and JL Van Velsen. Proposal for production and detection of entangled electron-hole pairs in a degenerate electron gas. *Physical review letters*, 91(14):147901, 2003.

[10] Charles H Bennett, Herbert J Bernstein, Sandu Popescu, and Benjamin Schumacher. Concentrating partial entanglement by local operations. *Physical Review A*, 53(4):2046, 1996.

[11] Laure-Hélène Bize-Reydellet. *Bruit quantique électronique et photons micro-ondes*. PhD thesis, Université Pierre et Marie Curie-Paris VI, 2003.

[12] Erwann Bocquillon, Vincent Freulon, J-M Berroir, Pascal Degiovanni, Bernard Plaçais, A Cavanna, Yong Jin, and Gwendal Fève. Coherence and indistinguishability of single electrons emitted by independent sources. *Science*, 339(6123):1054–1057, 2013.

[13] Erwann Bocquillon, FD Parmentier, Charles Grenier, J-M Berroir, Pascal Degiovanni, DC Glattli, Bernard Plaçais, A Cavanna, Yong Jin, and Gwendal Fève. Electron quantum optics: partitioning electrons one by one. *Physical Review Letters*, 108(19):196803, 2012.

[14] Norman Braslau. Ohmic contacts to gaas. *Thin Solid Films*, 104(3-4):391–397, 1983.

[15] Henrik Bruus and Karsten Flensberg. *Many body quantumm theory in condensed matter physics*. Oxford Graduate Texts, 2002.

[16] M. Büttiker, H. Thomas, and A. Prêtre. Mesoscopic capacitors. *Physics Letters A*, 180(4):364 – 369, 1993.

[17] M. Büttiker. Quantized transmission of a saddle-point constriction. *Phys. Rev. B*, 41:7906–7909, Apr 1990.

[18] M Büttiker. Scattering theory of thermal and excess noise in open conductors. *Physical review letters*, 65(23):2901, 1990.

[19] M. Büttiker. Scattering theory of current and intensity noise correlations in conductors and wave guides. *Phys. Rev. B*, 46:12485–12507, Nov 1992.

[20] M Büttiker. Time-dependent current partition in mesoscopic conductors. *Il Nuovo Cimento B (1971-1996)*, 110(5):509–522, 1995.

[21] M. Büttiker, Y. Imry, R. Landauer, and S. Pinhas. Generalized many-channel conductance formula with application to small rings. *Phys. Rev. B*, 31:6207–6215, May 1985.

[22] M Büttiker, Y Imry, R Landauer, and S Pinhas. Generalized many-channel conductance formula with application to small rings. *Physical Review B*, 31(10):6207, 1985.

[23] M. Büttiker and R. Landauer. Traversal time for tunneling. *Phys. Rev. Lett.*, 49:1739–1742, Dec 1982.

[24] M. Büttiker, A. Prêtre, and H. Thomas. Admittance of small conductors. *Phys. Rev. Lett.*, 71:465–465, Jul 1993.

[25] M Büttiker, A Prêtre, and H Thomas. Dynamic conductance and the scattering matrix of small conductors. *Physical review letters*, 70(26):4114, 1993.

[26] Markus Büttiker. Absence of backscattering in the quantum hall effect in multiprobe conductors. *Physical Review B*, 38(14):9375, 1988.

[27] Markus Buttiker. Capacitance, admittance, and rectification properties of small conductors. *Journal of Physics: Condensed Matter*, 5(50):9361, 1993.

[28] Pasquale Calabrese and John Cardy. Evolution of entanglement entropy in one-dimensional systems. *Journal of Statistical Mechanics: Theory and Experiment*, 2005(04):P04010, 2005.

[29] J. N. L. Connor, T. Uzer, R. A. Marcus, and A. D. Smith. Eigenvalues of the schrödinger equation for a periodic potential with nonperiodic boundary conditions: A uniform semiclassical analysis. *The Journal of Chemical Physics*, 80(10):5095–5106, 1984.

[30] Marcus Cramer, Christopher M Dawson, Jens Eisert, and Tobias J Osborne. Exact relaxation in a class of nonequilibrium quantum lattice systems. *Physical Review Letters*, 100(3):030602, 2008.

[31] Adeline Crépieux, Pierre Devillard, and Thierry Martin. Photoassisted current and shot noise in the fractional quantum hall effect. *Phys. Rev. B*, 69:205302, May 2004.

[32] David Dasenbrook and Christian Flindt. Dynamical generation and detection of entanglement in neutral leviton pairs. *Physical Review B*, 92(16):161412, 2015.

[33] John H. Davies, Ivan A. Larkin, and E. V. Sukhorukov. Modeling the patterned two dimensional electron gas: Electrostatics. *Journal of Applied Physics*, 77(9):4504–4512, 1995.

[34] R De-Picciotto, M Reznikov, M Heiblum, V Umansky, G Bunin, and D Mahalu. Direct observation of a fractional charge. *Physica B: Condensed Matter*, 249:395–400, 1998.

[35] L DiCarlo, Y Zhang, DT McClure, CM Marcus, LN Pfeiffer, and KW West. System for measuring auto-and cross correlation of current noise at low temperatures. *Review of scientific instruments*, 77(7):073906, 2006.

[36] Bernard Diu, Bernard Roulet, Claudine Guthmann, and Danielle Lederer. *Eléments de physique statistique*. Hermann, 1989.

[37] J. Dubois, T. Jullien, F. Portier, P. Roche, A. Cavanna, Y. Jin, W. Wegscheider, P. Roulleau, and D. C. Glattli. Minimal-excitation states for electron quantum optics using levitons. *Nature*, 502(7473):659–663, 2013.

[38] Julie Dubois. *Towards a n-electron source based on Lorentzian voltage pulses.* Theses, Université Pierre et Marie Curie - Paris VI, October 2012.

[39] Julie Dubois, Thibaut Jullien, Charles Grenier, Pascal Degiovanni, Preden Roulleau, and DC Glattli. Integer and fractional charge lorentzian voltage pulses analyzed in the framework of photon-assisted shot noise. *Physical Review B*, 88(8):085301, 2013.

[40] Jens Eisert and Tobias J Osborne. General entanglement scaling laws from time evolution. *Physical review letters*, 97(15):150404, 2006.

[41] G. Fève, A. Mahé, J.-M. Berroir, T. Kontos, B. Plaçais, D. C. Glattli, A. Cavanna, B. Etienne, and Y. Jin. An on-demand coherent single-electron source. *Science*, 316(5828):1169–1172, 2007.

[42] Richard Feynman, Leighton Robert, and Sands Matthew. *Le cours de physique de Feynman - Mécanique quantique.* Dunod, 2004.

[43] G. Fiori, G. Iannaccone, and M. Macucci. Modeling of shallow quantum point contacts defined on algaas/gaas heterostructures: The effect of surface states. *Journal of Computational Electronics*, 1(1):39–42, 2002.

[44] Gaston Floquet. Sur les équations différentielles linéaires à coefficients périodiques. In *Annales scientifiques de l'École normale supérieure*, volume 12, pages 47–88, 1883.

[45] Julien Gabelli. *Evidence of quantum coherence in dynamical electronic transport.* Theses, Université Pierre et Marie Curie - Paris VI, January 2006.

[46] Julien Gabelli, Gwendal Fève, J-M Berroir, Bernard Plaçais, A Cavanna, Bernard Etienne, Yong Jin, and DC Glattli. Violation of kirchhoff's laws for a coherent rc circuit. *Science*, 313(5786):499–502, 2006.

[47] Julien Gabelli, Gwendal Fève, Jean-Marc Berroir, and Bernard Plaçais. A coherent rc circuit. *Reports on Progress in Physics*, 75(12):126504, 2012.

[48] Benoit Gaury and Xavier Waintal. Dynamical control of interference using voltage pulses in the quantum regime. *Nature communications*, 5, 2014.

[49] Benoit Gaury, Joseph Weston, Matthieu Santin, Manuel Houzet, Christoph Groth, and Xavier Waintal. Numerical simulations of time-resolved quantum electronics.

Physics Reports, 534(1):1 – 37, 2014. Numerical simulations of time-resolved quantum electronics.

[50] Benoit Gaury, Joseph Weston, and Xavier Waintal. Stopping electrons with radio-frequency pulses in the quantum hall regime. *Phys. Rev. B*, 90:161305, Oct 2014.

[51] L. J. Geerligs, V. F. Anderegg, P. A. M. Holweg, J. E. Mooij, H. Pothier, D. Esteve, C. Urbina, and M. H. Devoret. Frequency-locked turnstile device for single electrons. *Phys. Rev. Lett.*, 64:2691–2694, May 1990.

[52] Gabriele F Giuliani and John J Quinn. Lifetime of a quasiparticle in a two-dimensional electron gas. *Physical Review B*, 26(8):4421, 1982.

[53] DC Glattli. Quantum shot noise of conductors and general noise measurement methods. *The European Physical Journal-Special Topics*, 172(1):163–179, 2009.

[54] DC Glattli, P Jacques, A Kumar, P Pari, and L Saminadayar. A noise detection scheme with 10 mk noise temperature resolution for semiconductor single electron tunneling devices. *Journal of Applied Physics*, 81(11):7350–7356, 1997.

[55] Oktay Göktaş, Jochen Weber, Jürgen Weis, and Klaus von Klitzing. Alloyed ohmic contacts to two-dimensional electron system in algaas/gaas heterostructures down to submicron length scale. *Physica E: Low-dimensional Systems and Nanostructures*, 40(5):1579–1581, 2008.

[56] Ch Grenier, Julie Dubois, Thibaut Jullien, Preden Roulleau, DC Glattli, and Pascal Degiovanni. Fractionalization of minimal excitations in integer quantum hall edge channels. *Physical Review B*, 88(8):085302, 2013.

[57] Ch Grenier, Rémy Hervé, Erwann Bocquillon, François D Parmentier, Bernard Plaçais, Jean-Marc Berroir, Gwendal Fève, and Pascal Degiovanni. Single-electron quantum tomography in quantum hall edge channels. *New Journal of Physics*, 13(9):093007, 2011.

[58] RP Gupta and WS Khokle. Gallium-vacancy-dependent diffusion model of ohmic contacts to gaas. *Solid-state electronics*, 28(8):823–830, 1985.

[59] Bertrand I Halperin. Quantized hall conductance, current-carrying edge states, and the existence of extended states in a two-dimensional disordered potential. *Physical Review B*, 25(4):2185, 1982.

[60] M. Heiblum, M. I. Nathan, D. C. Thomas, and C. M. Knoedler. Direct observation of ballistic transport in gaas. *Phys. Rev. Lett.*, 55:2200–2203, Nov 1985.

[61] Sylvain Hermelin, Shintaro Takada, Michihisa Yamamoto, Seigo Tarucha, Andreas D Wieck, Laurent Saminadayar, Christopher Bäuerle, and Tristan Meunier. Electrons surfing on a sound wave as a platform for quantum optics with flying electrons. *Nature*, 477(7365):435–438, 2011.

[62] Patrick P Hofer and Christian Flindt. Mach-zehnder interferometry with periodic voltage pulses. *Physical Review B*, 90(23):235416, 2014.

[63] C. K. Hong, Z. Y. Ou, and L. Mandel. Measurement of subpicosecond time intervals between two photons by interference. *Phys. Rev. Lett.*, 59:2044–2046, Nov 1987.

[64] Radu Ionicioiu, Gehan Amaratunga, and Florin Udrea. Quantum computation with ballistic electrons. *International Journal of Modern Physics B*, 15(02):125–133, 2001.

[65] M. J. Iqbal, J. P. de. Jong, D. Reuter, A. D. Wieck, and C. H. van der Wal. Split gate quantum point contacts with tunable channel length. *Journal of Applied Physics*, 113(2):024507, 2013.

[66] DA Ivanov, HW Lee, and LS Levitov. Coherent states of alternating current. *Physical Review B*, 56(11):6839, 1997.

[67] Yang Ji, Yunchul Chung, D Sprinzak, M Heiblum, D Mahalu, and Hadas Shtrikman. An electronic mach–zehnder interferometer. *Nature*, 422(6930):415–418, 2003.

[68] John Bertrand Johnson. Thermal agitation of electricity in conductors. *Physical review*, 32(1):97, 1928.

[69] Y Jompol, P Roulleau, T Jullien, B Roche, I Farrer, DA Ritchie, and DC Glattli. Detecting noise with shot noise using on-chip photon detector. *Nature communications*, 6, 2015.

[70] T Jullien, P Roulleau, B Roche, A Cavanna, Y Jin, and DC Glattli. Quantum tomography of an electron. *Nature*, 514(7524):603–607, 2014.

[71] Thibaut Jullien. *Mesoscopic few-electron voltage pulse source.* Theses, Université Paris Sud - Paris XI, April 2014.

[72] Rachpon Kalra, Arne Laucht, Juan Pablo Dehollain, Daniel Bar, Solomon Freer, Stephanie Simmons, Juha T Muhonen, and Andrea Morello. Vibration-induced electrical noise in a cryogen-free dilution refrigerator: Characterization, mitigation, and impact on qubit coherence. *Review of Scientific Instruments*, 87(7):073905, 2016.

[73] M Kamada, T Suzuki, F Nakamura, Y Mori, and M Arai. Investigation of orientation effect on contact resistance in selectively doped algaas/gaas heterostructures. *Applied physics letters*, 49(19):1263–1265, 1986.

[74] J Keeling, I Klich, and LS Levitov. Minimal excitation states of electrons in one-dimensional wires. *Physical review letters*, 97(11):116403, 2006.

[75] U Klass, W Dietsche, K Von Klitzing, and K Ploog. Imaging of the dissipation in quantum-hall-effect experiments. *Zeitschrift für Physik B Condensed Matter*, 82(3):351–354, 1991.

[76] Israel Klich and Leonid Levitov. Quantum noise as an entanglement meter. *Phys. Rev. Lett.*, 102:100502, Mar 2009.

[77] EJ Koop, MJ Iqbal, F Limbach, M Boute, BJ Van Wees, D Reuter, AD Wieck, BJ Kooi, and CH Van Der Wal. On the annealing mechanism of auge/ni/au ohmic contacts to a two-dimensional electron gas in gaas/alxga1- xas heterostructures. *Semiconductor Science and Technology*, 28(2):025006, 2013.

[78] Lifchitz Landau. *Mécanique quantique, tome 3 : Théorie non relativiste.* Ellipse, 1967.

[79] Rolf Landauer. Johnson-nyquist noise derived from quantum mechanical transmission. *Physica D: Nonlinear Phenomena*, 38(1-3):226–229, 1989.

[80] Robert B Laughlin. Anomalous quantum hall effect: an incompressible quantum fluid with fractionally charged excitations. *Physical Review Letters*, 50(18):1395, 1983.

[81] A. V. Lebedev, G. B. Lesovik, and G. Blatter. Generating spin-entangled electron pairs in normal conductors using voltage pulses. *Phys. Rev. B*, 72:245314, Dec 2005.

[82] GB Lesovik and LS Levitov. Noise in an ac biased junction: Nonstationary aharonov-bohm effect. *Physical review letters*, 72(4):538, 1994.

[83] Leonid S Levitov, Hyunwoo Lee, and Gordey B Lesovik. Electron counting statistics and coherent states of electric current. *Journal of Mathematical Physics*, 37(10):4845–4866, 1996.

[84] LS Levitov and GB Lesovik. Charge distribution in quantum shot noise. *JETP LETTERS C/C OF PIS'MA V ZHURNAL EKSPERIMENTAL'NOI TEORETICHESKOI FIZIKI*, 58:230–230, 1993.

[85] T Martin. Noise in mesoscopic physics nanophysics: Coherence and transport ed h bouchiat, y gefen, s guéron, g montambaux and j dalibard, 2005.

[86] Th. Martin and R. Landauer. Wave-packet approach to noise in multichannel mesoscopic systems. *Phys. Rev. B*, 45:1742–1755, Jan 1992.

[87] John M Martinis and M Nahum. Effect of environmental noise on the accuracy of coulomb-blockade devices. *Physical Review B*, 48(24):18316, 1993.

[88] Jacques Max. *Méthodes et techniques de traitement du signal et application aux mesures physiques. Tome 2.* Masson, 1981.

[89] RPG McNeil, M Kataoka, CJB Ford, CHW Barnes, D Anderson, GAC Jones, I Farrer, and DA Ritchie. On-demand single-electron transfer between distant quantum dots. *Nature*, 477(7365):439–442, 2011.

[90] Takashi Mimura, Satoshi Hiyamizu, Toshio Fujii, and Kazuo Nanbu. A new field-effect transistor with selectively doped gaas/n-alxga1-xas heterojunctions. *Japanese journal of applied physics*, 19(5):L225, 1980.

[91] Anurag Mittal, RG Wheeler, MW Keller, DE Prober, and RN Sacks. Electron-phonon scattering rates in gaas/algaas 2deg samples below 0.5 k. *Surface Science*, 361:537–541, 1996.

[92] Michael Moskalets. Fractionally charged zero-energy single-particle excitations in a driven fermi sea. *Physical Review Letters*, 117(4):046801, 2016.

[93] Mykhaylo Moskalets and M Büttiker. Floquet scattering theory of quantum pumps. *Physical Review B*, 66(20):205320, 2002.

[94] Mykhaylo Moskalets and Markus Büttiker. Time-resolved noise of adiabatic quantum pumps. *Physical Review B*, 75(3):035315, 2007.

[95] Michael A Nielsen and Isaac Chuang. *Quantum computation and quantum information.* AAPT, 2002.

[96] Harry Nyquist. Thermal agitation of electric charge in conductors. *Physical review*, 32(1):110, 1928.

[97] K Owusu-Sekyere, AM Chang, and TY Chang. Fabrication of gatable submicron channels in al x ga1- x as-gaas heterostructures. *Applied physics letters*, 52(15):1246–1248, 1988.

[98] François Parmentier. Low noise measurements, 2016.

[99] Claude Pasquier. *Transport quantique balistique et monoelectronique dans des nanostructures d'arseniure de gallium.* PhD thesis, 1994. Thèse de doctorat dirigée par Glattli, Denis-Christian Physique Paris 11 1994.

[100] Morten Holm Pedersen and Markus Büttiker. Scattering theory of photon-assisted electron transport. *Physical Review B*, 58(19):12993, 1998.

[101] Loren Pfeiffer, K. W. West, H. L. Stormer, and K. W. Baldwin. Electron mobilities exceeding 107cm2/vs in modulation doped gaas. *Applied Physics Letters*, 55(18):1888 1890, 1989.

[102] H. Pothier, P. Lafarge, P.F. Orfila, C. Urbina, D. Esteve, and M.H. Devoret. Single electron pump fabricated with ultrasmall normal tunnel junctions. *Physica B: Condensed Matter*, 169(1):573 – 574, 1991.

[103] A Prêtre, H Thomas, and M Büttiker. Dynamic admittance of mesoscopic conductors: Discrete-potential model. *Physical Review B*, 54(11):8130, 1996.

[104] Peter J Price. Hot electrons in a gaas heterolayer at low temperature. *Journal of Applied Physics*, 53(10):6863–6866, 1982.

[105] Jérôme Rech, Dario Ferraro, Thibaut Jonckheere, Luca Vannucci, Maura Sassetti, and Thierry Martin. Minimal excitations in the fractional quantum hall regime. *Physical Review Letters*, 118(7):076801, 2017.

[106] L-H Reydellet, P Roche, DC Glattli, B Etienne, and Yun Jin. Quantum partition noise of photon-created electron-hole pairs. *Physical review letters*, 90(17):176803, 2003.

[107] Preden Roulleau, F Portier, P Roche, A Cavanna, G Faini, U Gennser, and D Mailly. Direct measurement of the coherence length of edge states in the integer quantum hall regime. *Physical Review Letters*, 100(12):126802, 2008.

[108] Valentin S Rychkov, Mikhail L Polianski, and Markus Büttiker. Photon-assisted electron-hole shot noise in multiterminal conductors. *Physical Review B*, 72(15):155326, 2005.

[109] Ines Safi. Time-dependent transport in arbitrary extended driven tunnel junctions. *arXiv preprint arXiv:1401.5950*, 2014.

[110] Ines Safi and Philippe Joyez. Time-dependent theory of nonlinear response and current fluctuations. *Phys. Rev. B*, 84:205129, Nov 2011.

[111] Ines Safi and Eugene V Sukhorukov. Determination of tunneling charge via current measurements. *EPL (Europhysics Letters)*, 91(6):67008, 2010.

[112] L Saminadayar, DC Glattli, Y Jin, and B c-m Etienne. Observation of the e/3 fractionally charged laughlin quasiparticle. *Physical Review Letters*, 79(13):2526, 1997.

[113] P Samuelsson, EV Sukhorukov, and M Büttiker. Orbital entanglement and violation of bell inequalities in mesoscopic conductors. *Physical review letters*, 91(15):157002, 2003.

[114] RJ Schoelkopf, PJ Burke, AA Kozhevnikov, DE Prober, and MJ Rooks. Frequency dependence of shot noise in a diffusive mesoscopic conductor. *Physical review letters*, 78(17):3370, 1997.

[115] RJ Schoelkopf, AA Kozhevnikov, DE Prober, and MJ Rooks. Observation of "photon-assisted" shot noise in a phase-coherent conductor. *Physical review letters*, 80(11):2437, 1998.

[116] Georg Seelig and Markus Büttiker. Charge-fluctuation-induced dephasing in a gated mesoscopic interferometer. *Physical Review B*, 64(24):245313, 2001.

[117] Yu Sherkunov, Jin Zhang, N d'Ambrumenil, and B Muzykantskii. Optimal electron entangler and single-electron source at low temperatures. *Physical Review B*, 80(4):041313, 2009.

[118] A. Siddiki and F. Marquardt. Self consistent calculation of the electron distribution near a quantum point contact in the integer quantum hall effect. *Phys. Rev. B*, 75:045325, Jan 2007.

[119] H Francis Song, Stephan Rachel, Christian Flindt, Israel Klich, Nicolas Laflorencie, and Karyn Le Hur. Bipartite fluctuations as a probe of many-body entanglement. *Physical Review B*, 85(3):035409, 2012.

[120] Lafe Spietz, RJ Schoelkopf, and Patrick Pari. Shot noise thermometry down to 10 mk. *Applied physics letters*, 89(18):183123, 2006.

[121] H. L. Störmer. Electron mobilities in modulation doped GaAs (AlGa)As heterostructures. *Surface Science*, 132:519 526, September 1983.

[122] HL Störmer, R Dingle, AC Gossard, W Wiegmann, and MD Sturge. Two-dimensional electron gas at differentially doped gaas–al x ga1- x as heterojunction interface. *Journal of Vacuum Science and Technology*, 16(5):1517–1519, 1979.

[123] Horst L Stormer, Daniel C Tsui, and Arthur C Gossard. The fractional quantum hall effect. *Reviews of Modern Physics*, 71(2):S298, 1999.

[124] H. L. Störmer, R. Dingle, A. C. Gossard, W. Wiegmann, and M. D. Sturge. Two-dimensional electron gas at differentially doped gaas-alxga1-xas heterojunction interface. *Journal of Vacuum Science and Technology*, 16(5):1517–1519, 1979.

[125] K. J. Thomas, J. T. Nicholls, N. J. Appleyard, M. Y. Simmons, M. Pepper, D. R. Mace, W. R. Tribe, and D. A. Ritchie. Interaction effects in a one-dimensional constriction. *Phys. Rev. B*, 58:4846–4852, Aug 1998.

[126] T. J. Thornton, M. Pepper, H. Ahmed, D. Andrews, and G. J. Davies. One-dimensional conduction in the 2d electron gas of a gaas-algaas heterojunction. *Phys. Rev. Lett.*, 56:1198–1201, Mar 1986.

[127] B. J. van Wees, H. van Houten, C. W. J. Beenakker, J. G. Williamson, L. P. Kouwenhoven, D. van der Marel, and C. T. Foxon. Quantized conductance of point contacts in a two-dimensional electron gas. *Phys. Rev. Lett.*, 60:848–850, Feb 1988.

[128] Mihajlo Vanević, Yuli V Nazarov, and Wolfgang Belzig. Elementary events of electron transfer in a voltage-driven quantum point contact. *Physical review letters*, 99(7):076601, 2007.

[129] Mihajlo Vanević, Yuli V Nazarov, and Wolfgang Belzig. Elementary charge-transfer processes in mesoscopic conductors. *Physical Review B*, 78(24):245308, 2008.

[130] R. A. Webb, S. Washburn, C. P. Umbach, and R. B. Laibowitz. Observation of aharonov-bohm oscillations in normal-metal rings. *Phys. Rev. Lett.*, 54:2696–2699, Jun 1985.

[131] Xiao-Gang Wen. Chiral luttinger liquid and the edge excitations in the fractional quantum hall states. *Physical Review B*, 41(18):12838, 1990.

[132] D A Wharam, T J Thornton, R Newbury, M Pepper, H Ahmed, J E F Frost, D G Hasko, D C Peacock, D A Ritchie, and G A C Jones. One-dimensional transport and the quantisation of the ballistic resistance. *Journal of Physics C: Solid State Physics*, 21(8):L209, 1988.

[133] Jin Zhang, Yury Sherkunov, Nicholas d'Ambrumenil, and Boris Muzykantskii. Full counting statistics of quantum point contacts with time-dependent transparency. *Physical Review B*, 80(24):245308, 2009.

[134] H. Z. Zheng, H. P. Wei, D. C. Tsui, and G. Weimann. Gate-controlled transport in narrow gaas/$al_xga_{1-x}as$ heterostructures. *Phys. Rev. B*, 34:5635–5638, Oct 1986.

Titre : Dynamique quantique dans des conducteurs balistiques et cohérents : interrupteur quantique et transport photo-assisté

Mots clefs : Source d'électron, Interrupteur quantique, Bruit de grenaille

Résumé : La compréhension de la dynamique du transport électronique dans des conducteurs balistiques et cohérents est indispensable à la réalisation d'expériences d'optique électronique ou de calcul quantique à partir de « flying qu-bits ». La première étape est de pouvoir injecter en régime d'effet Hall quantique un électron dans la mer de Fermi sans excitation supplémentaire : un léviton, dont les propriétés remarquables ont été expérimentalement démontrées sans champ magnétique [1], ainsi que contrôler sa trajectoire à l'aide d'interrupteurs quantiques. Dans ce travail de thèse, nous avons réalisé l'étape préliminaire qui valide la possibilité de créer des lévitons en régime d'effet Hall Quantique : cela consiste à démontrer la validité de la théorie de bruit photo-assisté dans ce régime, en utilisant une excitation sinusoïdale et monochromatique, plus simple et plus contrôlée, que celle conduisant aux lévitons. En outre, nous avons étudié lors de la thèse le phénomène physiquement relié de l'interrupteur quantique élémentaire, qui est l'ouverture et la fermeture très soudaine d'un canal de conduction élémentaire. Ce phénomène, qui pose la question fondamentale « Que se passe-t-il lorsque que la mer de Fermi est spatialement coupée en deux ? », génère un bruit intrinsèque de charge[2] que nous avons mis en évidence et donne une mesure théorique de l'entropie d'intrication quantique.

[1] J. Dubois, T. Jullien, F. Portier, P. Roche, A. Cavanna, Y. Jin, W. Wegscheider, P. Roulleau, and D. C. Glattli. minimal-excitation states for electron quantum optics using levitons. Nature, 502(7473), October 2013.

[2] Israel Klich and Leonid Levitov, Phys. Rev. Lett. 102, 100502 (2009)

Title : Quantum dynamics of ballistic coherent conductors: Quantum switch and Photo-assisted transport.

Keywords : On-demand electron source, Quantum Switch, Shot-noise

Abstract : The study of dynamic electronic transport in ballistic coherent conductor is required for the implementation of electron quantum optics experiments or the quantum computation by using "flying qu-bits". The first step is to be able to inject in the quantum Hall effect a single electron without any additional excitations in the conductor: a Leviton, whose remarkable properties have been experimentally observed without magnetic field [1], and to control its trajectory thanks to a quantum switch. During this thesis, we confirmed the possibility to implement a leviton in the quantum Hall effect, by demonstrating the validity of the photo-assisted shot-noise theory in this regime: we use a sine excitation which is simpler to implement than a lorentzian excitation required for Levitons. We also studied a new effect described by the photo-assisted theory: a quantum switch, which is the sudden closing and opening of an elementary channel of conduction. This generates an intrinsic charge noise [2] that we have evidenced and enable us to answer the general question: "What are the effects of a spatial separation of the Fermi sea?". Furthermore, this charge noise provides a theoretical measurement of the entanglement entropy.

Université Paris-Saclay
Espace Technologique / Immeuble Discovery
Route de l'Orme aux Merisiers RD 128 / 91190 Saint-Aubin, France